

DISSERTATION

EVALUATION OF DOSE ENHANCEMENT DUE TO CUATSM UPTAKE IN HYPOXIC
ENVIRONMENTS WITH EXTERNAL RADIATION

Submitted by

Stephen K. Martinez

Department of Environmental and Radiological Health Sciences

In partial fulfillment of the requirements

For the Degree of Doctor of Philosophy

Colorado State University

Fort Collins, Colorado

Fall 2019

Doctoral Committee:

Advisor: Del Leary

Keara Boss

Alexander Brandl

Susan De Long

Takamitsu Kato

Copyright by Stephen K. Martinez 2019
All Rights Reserved

ABSTRACT

EVALUATION OF DOSE ENHANCEMENT DUE TO CuATSM UPTAKE IN HYPOXIC ENVIRONMENTS WITH EXTERNAL RADIATION

Most solid tumors contain areas of chronic hypoxia caused by limited diffusion of oxygen from tumor microvasculature. Hypoxic regions have been found to be radioresistant and their presence results in a worse prognosis for tumor control. Metal radiosensitizers have been employed to alleviate the radioresistance in hypoxic tumors by increasing dose through additional photoelectrons and Auger cascades. In recent years, gold nanoparticles (GNP) have been explored for their potential as an enhancer of external beam radiation and become the standard-bearer for the treatment modality; however, GNP have lower cellular uptake in anoxic and hypoxic conditions than under normoxic conditions. Additionally, the large size of nanoparticles decreases their diffusivity, reducing their ability to penetrate into tumor tissue distant from vasculature.

The chelator diacetylbis (N(4)-methylthiosemicarbazonato) copper II (CuATSM) provides the potential to overcome the hypoxic barrier by preferentially depositing copper into tumor regions previously inaccessible to treatment. The characteristics of CuATSM have led to its utilization in positron emission tomography (PET) imaging of hypoxic regions. These PET images have also been investigated as a method for dose painting, amplification of intensity modulated radiation therapy (IMRT) dose to hypoxic regions. Additionally, radioactive $^{64}\text{CuATSM}$ has been investigated for implementation in brachytherapy for hypoxic tumors. The Auger electrons ejected upon decay of the radioisotope have been shown to be highly damaging

to DNA. The intention of this study is to evaluate the potential of CuATSM as an external beam radiosensitizer.

This project investigates radiosensitization of CuATSM by Monte Carlo (MC) modeling of different energy external beam spectra available clinically with Electron Gamma Shower (EGSnrc) and Geometry and Tracking (Geant4) and evaluating dose enhancement with CuATSM. These MC models are informed by and evaluated against cell models. Research indicates that CuATSM at high concentrations with low energy photons has efficacy for enhancing dose in hypoxic tumor regions.

ACKNOWLEDGMENTS

Throughout the writing of this dissertation I have received a great deal of support and assistance. I would like to thank Dr. Leary for allowing me to participate in his lab and whose expertise was invaluable in the formulating of the research topic and methodology. I would also like to thank my committee: Dr. Kato, for allowing me to work in his lab, and for his guidance and mentorship; Dr. De Long, for allowing me to use her equipment, and advisement; Dr. Brandl for guidance and mentorship; and Dr. Boss for supporting my project with resources and advice. Several faculty were valuable with their suggestions and assistance: Dr. Johnson, Dr. Sudowe, Dr. Larue, Dr. Genik, Dr. Wiese & Dr. Weil from the Environmental and Radiological Health Sciences department. Additional faculty at Colorado State University who were valuable mentors: Dr. Turk, Dr. Wilson, Dr. Biedron, Dr. Azimi-Sadjadi, Dr. Rice & Dr. Chen. From outside CSU: Dr. Kanesalingam, Dr. Parsons & Dr. Robar.

DEDICATION

For the people who helped me get here, but weren't here to cross the finish line with me. Mom, thank you, I hope I made you proud.

TABLE OF CONTENTS

ABSTRACT.....	ii
ACKNOWLEDGMENTS.....	iv
DEDICATION.....	v
LIST OF TABLES.....	ix
LIST OF FIGURES.....	x
EXECUTIVE SUMMARY.....	1
CHAPTER 1 – INTRODUCTION.....	8
1.1 Interaction of Radiation with Matter.....	8
1.2 External Beam Radiation Therapy with X-ray Photons.....	10
1.3 The Role of Tumor Hypoxia in Radiation Therapy.....	12
1.4 Radiation Enhancement.....	17
1.5 Fenton-like Reaction of Copper in Reactive Oxygen Species Production.....	23
1.6 Nanoparticles as a Mechanism for Dose Enhancement.....	25
1.7 The Role of CuATSM as a Hypoxic Tracer.....	27
1.8 CuATSM in Radiation Therapy.....	31
CHAPTER 2 - MONTE CARLO EVALUATION OF METAL DOSE ENHANCEMENT WITH EXTERNAL PHOTON BEAM SPECTRA.....	33
2.1 Introduction.....	33
2.2 Analytical Attenuation and Energy Absorption of Metal Solutions.....	37
2.3 Monte Carlo as a Tool for Dose Prediction.....	40
2.4 Electron Gamma Shower (EGSnrc) Monte Carlo Codes.....	41
BEAMnrc.....	42
DOSXYZnrc.....	43
FLURZnrc.....	43
2.5 External Radiation Beam Models.....	44
Varian Clinac Linear Accelerator.....	45
Megavoltage Imaging Spectra.....	48
Small Animal Orthovoltage Spectra.....	50
External Beam Spectra.....	52
Percentage Depth Dose.....	55
Field Size and Shape.....	57
Benchmarking Trilogy Model to Varian Trilogy.....	59
2.6 Dose Enhancement in Various Metals.....	59
Dose Enhancement with Concentration of Metal Solution.....	61
Dose Enhancement with Depth in Phantom.....	65
2.7 Electron Spectra Enhancement with Metal.....	69
Photoelectrons and Emission of Auger Electron/Fluorescent Photon upon Atomic Relaxation.....	73
2.8 Discussion.....	78

CHAPTER 3 – CuATSM DOSE ENHANCEMENT IN HYPOXIC TUMOR MODEL WITH ORTHOVOLTAGE TREATMENT.....	80
3.1 Introduction.....	80
Orthovoltage Arcs.....	82
3.2 Monte Carlo Dose Prediction Compared to Analytical Models.....	83
3.3 Hypoxic Tumor Model.....	86
3.4 Dose Enhancement with CuATSM or GNP in Hypoxic Tumor.....	90
3.5 Orthovoltage Arcs.....	94
3.6 Hypoxic Boost.....	96
3.7 Discussion.....	103
 CHAPTER 4 – LABORATORY EVALUATION OF THE RADIOSENSITIZATION OF COPPER (CuATSM) IN DNA AND MAMMALIAN CELLS.....	 106
4.1 Introduction.....	106
4.2 Background.....	108
Cell Culture.....	109
Cell Survival Curves.....	110
4.3 DNA Strand Break Assay.....	112
4.4 CuATSM Toxicity.....	116
4.5 Radiosensitization of CHO Cells with CuATSM.....	121
4.6 Discussion.....	125
 CHAPTER 5 – NANOSCALE MONTE CARLO ASSESSMENT OF DOSIMETRY AND RADIOCHEMICAL YIELD IN CELLULAR MODEL.....	 129
5.1 Introduction.....	129
5.2 Geant4-DNA.....	134
Pdb4dna.....	136
Chem4.....	136
5.3 Simulation Design.....	140
Mammalian Cell Geometry.....	140
Electron Spectra.....	141
5.4 Microdosimetric Model.....	143
5.5 Radiochemical Yield Model.....	153
5.6 Discussion.....	158
 CHAPTER 6 – CONCLUSIONS.....	 161
 REFERENCES.....	 172
 APPENDIX A.....	 210
A.1 PEGS4 Materials for BEAMnrc Models.....	210
A.2 BEAMnrc Input Code for Trilogy Model.....	211
A.3 BEAMnrc Input Code for Imaging Model.....	218
A.4 BEAMnrc Input Code for SARRP Model.....	220
A.5 PEGS4 File for DOSXYZnrc Simulations.....	223

A.6	DOSXYZnrc Sample Input File.....	226
A.7	Silver and Gadolinium Dose Enhancement Factors.....	227
A.8	Maximum DEF for Non-radioactive Metals with Imaging Beam.....	228
A.9	Silver and Gadolinium DEF with Depth.....	228
A.10	FLURZnrc Sample Input File.....	229
A.11	Electron Spectra Output for Silver and Gadolinium.....	231
A.12	Electron Origin Output for Gold, Silver, Gadolinium.....	232
APPENDIX B.....		235
B.1	Percentage Depth Dose in Tissues with differing Effective Atomic Numbers....	235
B.2	PEGS4 File for Hypoxic Tumor Model Simulations.....	235
B.3	Hypoxic Tumor Model DOSXYZnrc Sample File.....	236
B.4	Dose Enhancement in Hypoxic Tumor Model with Imaging Beam Spectra.....	237
B.5	Dose Enhancement of Various Tissues with CuATSM High and SARRP.....	238
B.6	Isodose Comparison of Boost Treatments.....	238
APPENDIX C.....		239
C.1	Benchmarking Data for Examples.....	239
C.2	PEGS4 Data for Electron Spectra.....	241
C.3	Plot of Copper Compartment Concentration with CuATSM.....	245
C.4	Example Run File for Microdosimetry.....	245
C.5	Example Run File for Chemical Species.....	246
LIST OF ABBREVIATIONS.....		247

LIST OF TABLES

1.1	Characteristics of an ideal hypoxic tracer, from Fleming, et al. 2015.....	28
2.1	EGSnrc parameters for all simulations.....	46
2.2	Summary of components used to define the Trilogy model.....	48
2.3	Summary of components used to define the Imaging model.....	51
2.4	Summary of components used to define the SARRP model.....	53
3.1	Concentrations of gold (GNP) with initial injection concentration of 1.35 g/kg in normoxic and anoxic tissue.....	88
3.2	Concentrations of copper as deposited by CuATSM with a range of initial injected concentrations, and their simulated uptake in normoxic and anoxic tissues.....	90
3.3	Concentrations of copper and gold from a hybrid scenario combining GNP and CuATSM.....	93
3.4	Dose metrics for three boost techniques: MV, Copper (dose enhanced) orthovoltage, Tissue (non-enhanced) orthovoltage.....	103
5.1	List of G4DNA physics processes for DNA extension.....	135
5.2	Intermolecular reactions and reaction rates within the G4DNA chemical model....	139

LIST OF FIGURES

1.1	Tumor interiors develop regions of hypoxia and anoxia when the growth rate of tumor tissue outpaces the rate at which vasculature forms.....	14
1.2	Mass attenuation of copper as a function of photon energy plotted from 1 keV to 20 MeV.....	19
1.3	Chart of mass attenuation coefficient by energy and metal elements with increasing atomic number.....	20
1.4	Collision mass stopping power for electrons as a function of electron energy in liquid water.....	21
1.5	Summary of the theoretical framework by which metal particles act to enhance DNA damage with external radiation.....	22
1.6	Fluorescence X-ray vs. Auger electron yield in K-shell by atomic number.....	23
1.7	Proposed mechanism for hypoxic cellular trapping of copper as deposited by CuATSM.....	31
2.1	Monte Carlo simulation of copper dose enhancement with monoenergetic photon beams compared to spectral photons.....	36
2.2	Mass attenuation coefficients of selected metals.....	37
2.3	Energy absorption in metal solution phantom for copper solutions normalized to water.....	40
2.4	Varian Trilogy linac head model with scale in centimeters.....	47
2.5	Megavoltage imaging beam spectra model with scale in centimeters.....	50
2.6	An orthovoltage energy source (225 kVp) with scale in centimeters.....	52
2.7	Photon energy spectra for beam models.....	54
2.8	Percentage depth dose for beam models.....	56
2.9	Crossplane profile for beam models.....	58
2.10	Benchmarking of Trilogy MC Model to VTH Varian Trilogy linac.....	59
2.11	Geometry for simulation of dose in voxelized phantom, not to scale.....	60
2.12	Dose enhancement evaluation of copper ($Z=29$) by concentration.....	62
2.13	Dose enhancement evaluation of gold ($Z=79$) by concentration.....	63

2.14	Maximum dose enhancement comparison of four metals (copper, silver, gadolinium, and gold).....	65
2.15	Geometry for dose simulation with metal solution layer at increasing depths (not to scale).....	66
2.16	Evaluation of maximum DEF for a copper solution layer (concentration 100 g/kg) at increasing depths within a water phantom.....	67
2.17	Evaluation of maximum DEF for a gold solution layer (concentration 100 g/kg) at increasing depths within a water phantom.....	68
2.18	Electron fluence as a function of depth in phantom with metal solution layer at between 20 mm and 30 mm.....	71
2.19	Three photon beam models are used as the input to evaluate electron yield amplification in metal solution layer.....	72
2.20	Electron and photon origin tracking with modified DOSXYZnrc code 10 ⁶ histories.....	75
2.21	Comparison of Auger emission from gold and copper.....	77
2.22	Fluorescence vs Auger electron yield from the L3-shell.....	78
3.1	Hypoxic cell survival with irradiation.....	80
3.2	Hypoxic tumor model geometry with phantom representing section of body containing a tumor with normoxic and hypoxic regions.....	89
3.3	Dose enhancement factor in hypoxic tumor model with GNP.....	91
3.4	Dose enhancement factor in hypoxic tumor model with CuATSM.....	92
3.5	Mixture of GNP in normoxic tissue with CuATSM in hypoxic tissue to create a uniform dose distribution.....	93
3.6	Large tumor model with hypoxic core and skin layer.....	95
3.7	Dose deposition within large hypoxic tumor with orthovoltage arcs.....	95
3.8	Image dataset used to evaluate hypoxic boost.....	98
3.9	Treatment fields for bulk irradiation and boost.....	99
3.10	Calculated dose for bulk treatment and boost displayed with color wash.....	100
3.11	Dose volume histograms used to evaluate the efficacy of copper boosted orthovoltage.....	102
4.1	Chinese hamster ovary cells in cell culture.....	110
4.2	Gel image for viral DNA single-strand break assay.....	113

4.3	Six metal salts analyzed for radiosensitization: (Fe, Al, Ag, Ni, Co, and Cu).....	114
4.4	Radiosensitization with copper at various concentrations and beam energies.....	115
4.5	Growth inhibition with DMSO.....	118
4.6	CHO cell alterations from CuATSM.....	119
4.7	Growth inhibition with CuATSM.....	120
4.8	Film analysis for 6-well plate irradiation.....	123
4.9	Cell survival with CHO exposed to CuATSM and PXI orthovoltage radiation.....	124
5.1	Differences in electron track structure resulting from differences in energy cutoff.....	130
5.2	Track structure evolution of an individual electron and the resultant secondary electron creation is shown over the timespan of 0.001ps to 0.01ps.....	132
5.3	Geometrical model of compact tetranucleosome implemented for pdb4dna simulation of energy deposition and strand breaks.....	136
5.4	Chemical species generation, diffusion, and mutual interaction to create different species.....	138
5.5	Cell dimensions rationale.....	141
5.6	The electron spectra used for input to the microdosimetric models.....	142
5.7	Solid angles from distances within the nucleus and cytoplasm to the DNA fragment.....	145
5.8	Representation of microdosimetry irradiation scheme within geometry.....	146
5.9	Energy deposition by energy window (1-1000 eV) from nucleus and cytoplasm with equal distribution of CuATSM (50/50) in each cellular compartment.....	148
5.10	Comparison between the 50/50 case and the XC case, with $5(10^7)$ histories normalized to NXC.....	149
5.11	DNA strand break definition.....	150
5.12	DNA strand break comparison between 50/50 copper spectra and XC spectra with $5E7$ histories normalized to NXC.....	151
5.13	Enhancement factors for copper spectra.....	152
5.14	Representation of radiochemical irradiation scheme within geometry.....	154
5.15	Time based evaluation of radiochemical species yield for the 50/50 case.....	155

EXECUTIVE SUMMARY

The objective of the work presented is to determine if: *Copper ATSM (diacetyl-bis N4-methylthiosemicarbazone) can be used as a radiosensitizer with external beam radiation*. That objective is investigated through the completion of the following specific aims.

Macroscopic dose enhancement is evaluated with copper and other metals using external beam radiation models. CuATSM uptake into hypoxic tumor is used to create a model and evaluate the dose enhancement in simulated tumors. Radiosensitization by copper is evaluated using DNA and cellular laboratory experiments. Microscopic dose quantities is investigated at the cellular scale to determine alternative contributions to cell death mechanisms.

SA1. Model the dose enhancement of various metal radiosensitizers.

Radiation therapy is a cancer treatment that has become principle because of its noninvasive application. A negative consequence of radiation is that secondary tumors may arise from non-target energy deposition. Metal radiosensitizers have been considered as a method to concentrate energy into tumor targets to increase dose and decrease non-target healthy tissue and organ dose. Previous research has investigated several metals including gold, copper, silver, and gadolinium in the form of nanoparticles and found these metals to enhance dose both in computer and animal models. However, an area that has not been systematically explored is the response of metal radiosensitizers to external beam spectra commonly available in radiation therapy.

External beam spectra are modeled using electron gamma shower (EGSnrc) Monte Carlo software. A model was created corresponding to a 6 MV Varian Trilogy linear accelerator (linac) that is a common energy and treatment in radiation therapy. Additionally, a carbon target altered linac was modeled, mirroring developments in radiation technology to enable MV (2.35 MV) imaging spectra onboard traditional linacs. Finally, an orthovoltage X-ray model (225 kVp), was created based on a small animal research radiation platform (SARRP) provided by Xstrahl. These sources were then used to irradiate water phantoms with layers of metal solutions. Gold, silver, copper, and gadolinium were each evaluated for several concentrations from 10^{-4} to 10^{-1} to evaluate the relationship of dose amplification with metal atomic number, concentration and external beam spectra. Depth of the metal solution layer was also varied to investigate the effects of photon depletion and beam hardening on dose enhancement. Dose from photon irradiation is intricately tied to kerma and the electron spectra created by the photons as they transit media. The resulting electron spectra was evaluated for each metal in the same geometrical configuration. Auger electrons was also enumerated in each metal as they are a critical mechanism of DNA damage in the theory of radiosensitization by metals.

Radiosensitization by metal has previously been found to occur with correlations strongly related to the photoelectric effect at low energies due to the (atomic number) Z^3 dependency. Additionally, the probability of the photoelectric interaction increases at lower energies. Therefore, lower energy photon spectra and higher Z materials are each expected to lead to higher dose enhancement. For example, it is expected that the SARRP (orthovoltage) energy will lead to a higher dose enhancement than the Trilogy (6 MV) for all metals. Similarly, it is expected that the higher atomic number gold ($Z=79$) will have a higher dose enhancement than silver ($Z=47$) for all external beam energies. Metal solution concentration will affect the effective

atomic number of the material being irradiated, therefore it is expected that increasing metal concentration will increase dose enhancement. Radiation spectra are composed of many photon energies and low energy photons have less penetration than high energy photons. Therefore, depth of inhomogeneity is also expected to affect radiosensitization. Electron spectra are expected to increase in yield with atomic number, as is Auger electron production.

SA2. Estimate the dose enhancement within a hypoxic tumor model.

Of the metals previously mentioned as potential radiosensitizers, the indication would be that gold ($Z=79$) would be the best option for future research, and in fact, the radiosensitivity research community has invested most research into GNP for that reason. Physical dose enhancement, however, is only part of the consideration for an actual radiation treatment. Toxicity of the metal is a concern, especially for systemic injections. Additionally, it is important to evaluate the actual tumor uptake of the particle under investigation, and in this respect GNP have some limitations. Specifically, GNP have decreased uptake in hypoxic cells. Most tumors contain micro-regions of hypoxic tissue that is radioresistant. It is assumed that without uptake into hypoxic regions, GNP would not radiosensitize those critical tumor areas. Alternatively, the hypoxic tracer molecule CuATSM has been shown to have an increased uptake in hypoxic cells. In order to sensitize the critical hypoxic regions in tumor, CuATSM will be considered for its radiosensitizing potential.

Radiation spectra will be used to model irradiation of a simple hypoxic core tumor model. Dose enhancement will be evaluated in a tumor model with GNP and concentrations decreased within hypoxic regions. CuATSM will be evaluated as a radiosensitizer with several injected concentrations based on literature with increased uptake in hypoxic regions.

Orthovoltage photon radiation is not often a treatment consideration for large tumors where hypoxic regions would form because of its shallow penetration into tissue. Models will evaluate the possibility of using focused irradiation arcs to increase dose to hypoxic cores without significant surface tissue dose.

Radiosensitization with gold and copper will be found (SA1) for several concentrations of each metal. Previous research has indicated a decrease of GNP uptake of up to 3.4 times in hypoxic tissue. Distant from vasculature, GNP have limited diffusion and uptake in hypoxic tissue could decrease to zero. Furthermore, in certain cell lines an increase of 9 times has been observed for CuATSM. Therefore, the expected outcome for GNP would have a high dose enhancement in normoxic tissue that decreases substantially in the hypoxic core region. Conversely, CuATSM would be expected to have a low dose enhancement in normoxic regions that would increase in hypoxic regions.

CuATSM and GNP have complementary strengths in normoxic and hypoxic tissue uptake. Therefore, a combination of the two radiosensitizers will be evaluated as a mechanism for uniformly enhancing dose in tumors. It is expected that there is a concentration of copper for which the dose enhancement in hypoxic tissue would match the level of GNP in normoxic tissue. That concentration will be determined from previous data, and a simulation will evaluate the dose enhancement of that concentration.

Orthovoltage irradiation from numerous angles will be evaluated in Monte Carlo models to determine the feasibility of treating deeply in large tumors. A proof-of-concept with orthovoltage arcs will be evaluated in a canine osteosarcoma tumor. Patient data in DICOM form will be imported into treatment planning software utilizing orthovoltage photons, and irradiation

modeled in regions defined as hypoxic by CuATSM PET study. Resulting dose will be combined with standard 6 MV 3-D treatment plan dose to demonstrate planning target volume (PTV) coverage with hypoxic treatment volume (HTV) boost.

SA3. Verify radiosensitization by copper in laboratory investigations.

In order to evaluate the application of CuATSM as a radiation sensitizer it is important to test its ability to radiosensitize *in vivo* and *in vitro*. Viral DNA is a useful tool to evaluate single stranded DNA breaks that occur as a result of irradiation. In preliminary studies, copper (CuCl_2) was indicated to have potential as a radiosensitizer. CuATSM has been investigated in several cell lines as a hypoxic tracer and radiotheranostic. Studies have indicated that CuATSM has a high differential uptake between hypoxic and normoxic conditions in certain cancer cell-lines. Uptake into cells is critical in radiosensitization because proximity of the radiosensitizer to DNA increases the fluence and hit frequency of highly damaging ionizing radiation. Enhanced cell kill from comparative survival curves will provide additional proof of concept for how CuATSM might be used as a hypoxic tissue radiosensitizer.

Copper, in the form of CuCl_2 was investigated as a radiosensitizer by mixing copper solution at three different concentrations with viral DNA and exposing to two types of external beam radiation. Subsequently, the DNA was stained and run through gel electrophoresis to measure the amount of DNA single strand breaks (SSB) induced with copper. The external beam radiation sources investigated will be 6 MV Varian Trilogy, and 225 kVp XRAD SmART to evaluate energy spectra differences. Additionally, survival curves will be produced using Chinese hamster ovary (CHO) cells exposed to CuATSM and irradiated with orthovoltage radiation energies at several doses. Cellular toxicity will be investigated by determining the

maximum concentration of CuATSM and DMSO incubated with cells. ATSM, as a chelate, will act to detach cells from the surface of the culture vessel they are grown in. For that reason, this experiment will utilize Coulter counting of a large number of cells. Hypoxia will be induced in some samples by exposure to a hypoxic environment in an anoxic chamber with O₂ concentration below 10 ppm.

CuCl₂ has been shown to be a radiosensitizer in previous studies, it is therefore expected that within the viral DNA investigations, copper will similarly be shown to enhance SSB at a higher rate with irradiation than without. Additionally, it is expected that orthovoltage, with a lower energy spectrum than 6 MV, will result in more SSB with copper present because of the higher probability of photoelectric effect at low energy. CuATSM is expected to have a higher uptake, and therefore higher dose enhancement, in hypoxic cells. It is possible that radiation enhancement by CuATSM in this experiment will exceed expectations established in macroscopic Monte Carlo studies because of the additional action of copper to enhance damage to DNA through the creation of reactive oxygen species (ROS) through Fenton reactions.

SA4. Evaluate the microdosimetric enhancement of CuATSM in cell models.

The goal of this investigation will be to evaluate the dose enhancement of CuATSM with external beam radiation at very low energies and small spatial scale. The evidence from the preceding investigations (SA1-3) are believed to implicate the dose enhancement potential of CuATSM, however it is expected that the dosimetric enhancement will not fully account for cell death. DNA ionization can occur at low incident energy (7.5 – 10 eV), and therefore it is informative to investigate low energy depositions for potential biological damage. Biological response in radiation is related to dose, but direct interaction with DNA only accounts for about a

third of total damage. Previous research has found that even without a physical mechanism for dose enhancement (proton therapy) GNP still produce radiosensitization by increasing damage to DNA in part by indirect generation of reactive oxygen species (ROS). Therefore, it is possible that the greater cell sensitization of copper *in vivo* may also be attributable to ROS.

To more accurately interpret the radiobiological damage to cells by CuATSM radiosensitization, radiation will be tracked using low energy track structure Monte Carlo models. A Monte Carlo cell model will be created with electron spectra informed by copper concentration in nuclear and cytoplasm compartments from literature. Microscopic dose enhancement factor (mDEF) will be calculated based on the electron spectra as well as an estimation of single strand breaks (SSB) and double strand breaks (DSB) in a simple DNA model. Molecular yield of ROS will be calculated to evaluate the effect of copper altered electron spectra on creation of chemical species.

Previous research has indicated that copper is a radiosensitizer of hypoxic cells at concentrations lower than were able to be predicted at a macroscopic level (SA1). The goal of this experiment is to determine the degree to which that discrepancy comes from dose differences at a microscopic level. It is expected that the microscopic dose enhancement will provide some evidence of the gap between macroscopic dose and cell survival, but that it will not completely elucidate the difference. ROS molecule creation differences between copper and water electron spectra may also provide some insights, however, a full understanding of the factors that lead to cell survival differences, including the physical, chemical and biological contributions is beyond the scope of this investigation.

CHAPTER 1

INTRODUCTION

1.1 – Interaction of Radiation with Matter

Malignant tumors are one of the most frequent causes of death worldwide, which has led to significant attention from the scientific community [1-4]. Radiation therapy has been an attractive option in treatment of cancers because of its noninvasive nature compared to other treatment options, such as surgery, and its capability for targeting disease more precisely than chemotherapy [6]. Radiation encompasses several sources that can be used for therapeutic treatment including external beam photons, electrons, heavy-ions, and internally placed brachytherapy sources.

When radiation is utilized in health and medicine, a chief consideration is the behavior it exhibits in its interaction with matter [189]. Radiation of sufficient energy, termed ionizing radiation, is capable of causing ionization. Ionization, is the forced removal of electrons from molecules by external irradiation, as opposed to excitation, which imparts energy to an atom leaving it in an excited state. When ionization occurs in DNA or other critical cell components, it may result in damage that if not repaired may lead to death of the cell.

Photon radiation, in the form of either x-rays or γ -rays is uncharged and interacts with matter in infrequent exchanges of large energy transfers. Each photon has a relatively small likelihood of interacting with matter at any point, and therefore has a theoretically infinite range. The interaction path of an individual photon is unknowable *a priori*, but the behavior of many photons can be characterized statistically by the probability per unit distance that the photon will

interact within an infinitesimal thickness dl of material [190]. The change in number of photons due to absorption within media from an initial N particles is:

$$\frac{dN}{dl} = -\mu N \quad (1.1)$$

Where μ is the linear attenuation coefficient, or macroscopic cross-section. It is an empirically derived quantity dependent on material and photon energy and commonly tabulated in radiation resources [191]. The linear attenuation coefficient quantifies the probability of photon interaction per unit distance traveled with dimension of inverse length [cm^{-1}]. It accounts for the number of atoms in a cubic centimeter volume of material and the probability of a photon being scattered or absorbed from the nucleus or electron of one of the atoms in the material. By integrating Equation (1.1), it is seen that photons will be attenuated exponentially as they traverse through matter of thickness L :

$$\frac{N_L}{N_0} = e^{-\mu L} \quad (1.2)$$

The value of the linear attenuation coefficient for a material depends on the density of the material [112, 192]. Normalizing the linear attenuation coefficient by the material's density ρ , removes the material density dependence. Therefore, the mass attenuation coefficient, denoted by μ/ρ , is more commonly presented.

Photons deposit energy in matter indirectly, by liberating electrons through ionization [193]. Electrons are charged particles, and interact with matter directly through Coulomb-force interactions with the atoms of media. In some cases this interaction results in the ionization of the atoms' electrons, releasing them as δ -rays, which can cause further ionization in the medium. Electrons can also interact with the nuclei of atoms causing deflections in the path of the

electron; a substantial deceleration of the electron results in the emission of electromagnetic radiation in the x-ray energy range, termed a Bremsstrahlung photon.

The path and interactions of an individual particle are inherently stochastic, however, nonstochastic quantities can be determined from the expectation values of stochastic quantities to predict outcomes by calculation. The kinetic energy deposited per unit mass through local collisions (collision kerma) in a gas is related to the number of ionization events by:

$$(K_c)_{air} = X * \left(\frac{\bar{W}}{e}\right)_{air} \quad (1.3)$$

Where \bar{W} , is the mean energy expended in a gas per ion pair formed, and the exposure (X) is the total charge of ions produced in air when all electrons liberated by photons come to a stop:

$$X = \frac{dQ}{dm} [C/kg] \quad (1.4)$$

Collision kerma is a critical measurement in radiation therapy, because under conditions of charged particle equilibrium (CPE) it is equivalent to absorbed dose, D :

$$D \stackrel{CPE}{=} K_c \quad (1.5)$$

Absorbed dose is the radiological construct most often used to estimate the risk associated with radiation exposure. Absorbed dose is the average energy absorbed per unit mass of a target for any ionizing radiation [193].

1.2 – External Beam Radiation Therapy with Orthovoltage Photons

External beam photon therapy has been the focal point for radiation therapy because of the availability of linear accelerators in oncology clinics capable of delivering highly conformal treatments with megavoltage (MV) energy [5-6]. Typical treatment consists of 3-dimensional

image guidance with computed tomography (CT) and/or positron emitting tomography (PET) to determine tumor location and extent with high resolution medical imaging slices. Additionally, radiation can be modulated with multi-leaf collimators (MLC) to deliver pre-calculated photon fluence dynamically to the region of interest. Before 1950, however, most radiotherapy was limited to lower energy x-rays up to 300 peak kilovoltage (kVp) [93].

Effective radiation treatment depends on damage to DNA in tumor cells leading to mitotic death [13]. Damage is related to photon fluence and thus total absorbed dose to the tumor cells. Photons damage DNA both by directly cleaving bonds, and indirectly by radiolysis of water molecules within the cells resulting in reactive oxygen species (ROS) that damage DNA through chemical interaction. Increasing dose to tumors is essential in increasing tumor control probability (TCP) and therefore enhancing effectiveness of treatment [14-15, 31].

Contrarily, dose that is received by normal tissue is undesirable in therapies and can lead to increased normal tissue complication probability (NTCP) [7]. Typically, limitations on dose deliverable to the tumor is restricted to normal tissue damage tolerance. Radiation complications can be severe in the normal tissues of patients, resulting in a range of effects from mild erythema to paralysis or death [97]. Unfortunately, irradiation of normal tissue is inevitable in radiation treatment of deep tumors with photons [8-9]. Techniques capable of widening the therapeutic window between TCP and NTCP with radiosensitized tissue improving local dose enhancement are frequently pursued [10-12].

Radiation treatment currently employs MV energy ranges because high energy photons, having lower probability of interaction, are more penetrating, and can treat more deeply than lower energy x-rays. However, modern research into small animal treatments has encouraged

renewed interest into orthovoltage (150-500 kVp) energy x-rays [195]. Orthovoltage is suitable for the shallow treatments in small animals at a considerably lower cost. Orthovoltage energy photons also have attractive physical qualities. High energy photons result in dose buildup at heterogeneous media interfaces and increased penumbra due to substantial range of secondary electrons [47, 324-325]. Low energy photon beams, alternatively, have narrow penumbra and can deliver constricted dose distributions. Orthovoltage energy photons are also of renewed interest because of the dose enhancement potential of radiosensitizers, which have increased photon interaction cross-sections for high atomic number materials [104].

1.3 – The Role of Tumor Hypoxia in Radiation Therapy

The term hypoxia describes the lower oxygen conditions present in tumors from the levels available in normoxic tissue regions [156]. Hypoxia is generally defined as having oxygen levels below 5 mmHg compared to the oxygen levels in normal tissues (40-60 mmHg) [119]. Low oxygen conditions can occur throughout the body, especially areas of the gastrointestinal tract. Hypoxia is differentiated from those areas in normal tissue because even at low oxygen levels the normal tissue is still able to support itself, hypoxic tumors on the other hand are not stable [156]. Hypoxic regions have been associated with genetic instability and aggressive phenotype which correlate with tumor metastasis risk [119].

Low oxygen levels were implicated as a factor in tumors as early as 1928 by Warburg [157]. Although the causation mechanism was misunderstood, it was found that tumor cells survive low oxygen environments by increasing levels of anaerobic respiration, producing lactic acid as an indicating byproduct. The tumor microenvironment is another region that exhibits pathological hypoxia and appears to play a key role in communication with the tumor to promote

cell survival and propagation [119]. Tumor interiors develop dynamic gradients of oxygen distribution as the rapid cell proliferation outpaces the rate of angiogenesis [16-18]. Hypoxia occurs in most solid tumors because of several factors leading to an imbalance between oxygen supply and consumption that occurs as cell proliferation outpaces the formation of new vasculature [110, 119]. Tumor cells tolerate hypoxia because in many cases the partially or totally inactivated p53 gene reduces the reaction of cells to external stresses [85, 159]. Most solid tumors contain areas of chronic hypoxia caused by limited diffusion of oxygen from tumor microvasculature [110] (Figure 1.1).

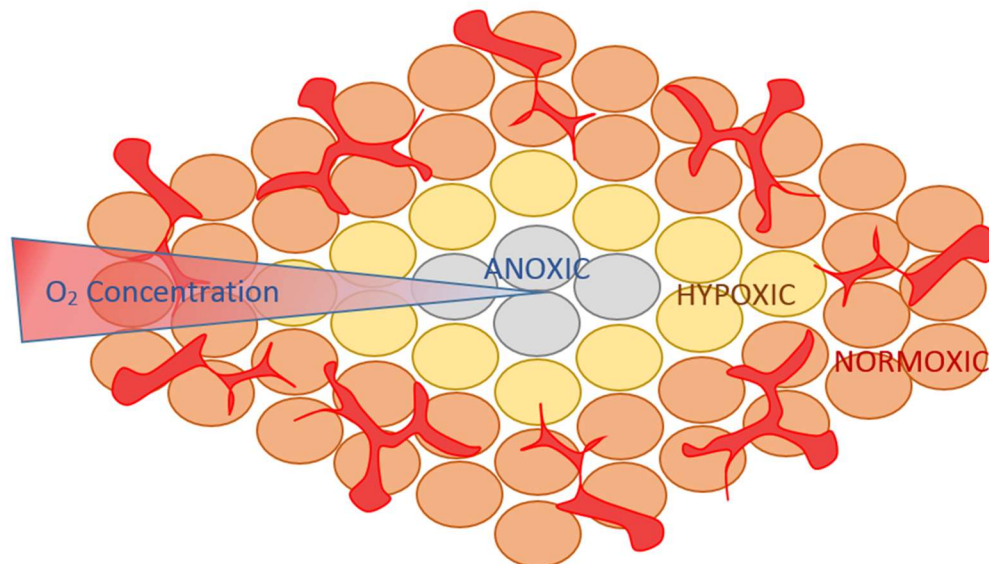


Figure 1.1 - Tumor interiors develop regions of hypoxia and anoxia when the growth rate of tumor tissue outpaces the rate at which new vasculature forms. Tissue regions with less vasculature have fewer oxygen-providing pathways and diffusion of oxygen from vascular tissue is limited across successive cell layers.

Hypoxia can be classified into three types; chronic, acute, and cycling. Chronic hypoxia, also known as diffusion limited hypoxia, was the earliest to be characterized by Thomlinson and Gray in 1955 [22]. It occurs as the result of high oxygen consumption by metabolically active tumor cells in close proximity to vessels, decreasing the amount of available oxygen distant from

vasculature. The distance that oxygen can diffuse is about 70 μm from the capillary, although that distance is dependent on whether the region of capillary is in the arterial or venous region and the rate of tumor metabolism [158]. For example, in phosphorescence life-time imaging in window chamber studies oxygen diffusion was found to 100 μm [168]. The scope of effects of chronic hypoxic conditions are tumor size associated, and larger tumors tend to have higher accumulation of DNA breaks and replication errors by decreasing synthesis of homologous recombination proteins, thus leading to a higher likelihood of genetic instability and mutation [170]. Chronic hypoxia is also exacerbated by tumor and treatment associated anemia and carbon monoxide.

Acute hypoxia, also known as perfusion-related hypoxia is the brief exposure to hypoxic conditions from minutes to 72 hours, which occurs from insufficient blood flow [156]. Brown et al., were the first to identify this type of hypoxia in 1979 [160]. It occurs as a result of transient openings and closings of tumor blood vessels and the resulting changes in blood flow rate [158]. Microcirculatory pathophysiology causes functional abnormalities in vasculature such as arteriovenal shunts, blind ends, and breaks in vessel walls [158]. Tumor vasculature is characterized as permeable, dilated, elongated, and tortuous causing blood flow irregularities and increased interstitial fluid pressure on lymphatics limiting drainage [110]. Temporal occlusion of blood vessels from emboli and blood clots can also cause acute hypoxia [161]. In cases where temporal variations of better or worse oxygenation occurs in a region, the term cycling hypoxia is applied [162].

Goodall et al., were among the earliest researchers to characterize a cycling blood flow occurring in tumors in 1965 [163]. Cycling hypoxia is a prominent feature of the tumor microcirculation and approximately 20% of tumor cells experience cycling hypoxia in certain

cancer types [164]. Cycling hypoxia occurs generally as a result of fluctuations in erythrocyte flux, which is in turn caused by functional changes in vascular geometry such as transient occlusion or narrowing of vasculature that result in differences among cycling frequencies [95]. Cycling frequency can vary from a few cycles per minute to days [164]. High frequency cycles have been attributed to changes in perfusion, erythrocyte flux, vascular occlusion, and vascular intussusception [95, 110]. Low frequency cycles on the other hand are often attributed to changes in the vascular network structure that occurs during angiogenesis or blood vessel remodeling [95, 110]. Cycling is also not strictly a vasculature adjacent phenomenon as it can also occur as distant as 130 μm from vasculature [166].

Hypoxic radioresistance is a well-established trait of cancer, which was discovered as early as the 1920's, although earlier observations may have provided baselines for these discoveries [14]. Systematic evaluations of tumor cells indicated resistance to ionizing radiation for those cells exposed to anaerobic conditions during radiation exposure, compared to those in aerobic conditions [167]. Irradiation with photons requires the creation of reactive oxygen species (ROS) to stabilize damage by secondary electrons initiated by photons. An explanatory mechanism for decreased efficacy of ionizing radiation in hypoxia is that without oxygen and other ROS, DNA damage is less permanent [20-21]. Additionally, hypoxia changes the cell cycle distribution in the population which leads to altered responses to radiation therapy which can have a greater effect than the lack of fixation [110, 158].

At oxygen levels below 10 mmHg, gene expression of hypoxia-regulated genes downstream of hypoxia-inducible factors (HIF) increase. HIF-1 and HIF-2 are heterodimeric transcription factors that act as important factors for cell adaptation to hypoxia. They are associated with downstream expression of genes that regulate a wide variety of cellular

mechanisms and metabolism that lead to malignant and metastatic phenotype including metastasis and immune evasion [110]. Furthermore, ROS resulting from the electron transport chain damage surrounding cells, and result in oxidative stress within tumor [23-24]. Tumor cells under these conditions are more likely to metastasize and spread to other parts of the body [28-30]. Metastasis increases the stage of cancer and results in the disease becoming more difficult to treat and leading to diminished outcomes [25, 84].

HIF can affect the rates of angiogenesis, cell proliferation, differentiation, and apoptosis. Additionally, HIF-1 regulates glycolysis and pyruvate metabolism, while HIF-2 regulates fatty acid metabolism [156]. HIF-1 and HIF-2 are oxygen sensitive molecules that under normoxic conditions have their alpha subunit bound by prolyl hydroxylase (PHP) enzymes, subsequently promoting E3 ubiquitin ligase bonding, and promoting degradation. PHP is activated by also binding to oxygen, so without its presence, HIF-1 and HIF-2 are allowed to function and activate other genes [171]. Hypoxia and HIF have also been associated with inhibition of anti-tumor mechanisms and in the facilitation of immune escape. For example, the vasculature endothelial growth factor (VEGF) as well as epithelial-mesenchymal transition (EMT) are regulated by HIF and can facilitate the formation of new vessels, alter nutrient and oxygen conditions in the tumor, alter cell adhesion, and allow for cancer cell detachment and migration [172]. Increased levels of HIF-1 and HIF-2 are poor prognostic indicators associated with increased mortality [169]. Radiation treatment can act as an initiator for HIF-1 activity coinciding with reoxygenation with ROS acting in part to preserve HIF-1 [110]. Radiation therapy interacts in a complex way with HIF-1. HIF-1 can act as a radiosensitizer by promoting tumor metabolism, proliferation, and apoptosis. On the other hand, by promoting endothelial cell survival, it can act to enhance radioresistance [110].

1.4 – Radiation Enhancement

A primary consideration in the field of radiation therapy has been to find ways to identify and overcome radioresistance within hypoxic tissue regions [19-20, 154]. Enormous progress has been made limiting dose to normal tissues through advanced collimation and modulation techniques [6, 31]. Additionally, standard practice has evolved to challenge hypoxia by delivering doses in numerous successive fractions. Fractionation reduces the size of the tumor by removing exterior layers, allowing oxygen to diffuse farther into the tumor and become radiosensitive to successive radiation fractions [32-34]. Radiosensitization techniques aim to improve radiation treatments by increasing dose to tumor for each treatment, thereby increasing tumor control. Alternatively, peripheral dose can be lowered accordingly as radiosensitizers will keep dose consistent in the tumor while lowering dose to normal tissues.

One form of radiosensitization that has been explored to treat hypoxic tumors is increasing the atomic number (Z) within the tumor tissue [11-12, 37-39]. Investigations have established that high- Z elements in low energy x-ray beams (< 100 keV) result in increased dose due to the photoelectric effect [40-42]. The measurable quantity to evaluate the efficacy of radioenhancers is dose enhancement factor (DEF) defined as:

$$DEF = \frac{\text{Dose with Radiosensitizer}}{\text{Dose without Radiosensitizer}} \quad (1.6)$$

Materials that have a large photoabsorption cross-section increase the probability of interaction with the atoms in the material [189]:

$$\frac{\mu}{\rho} = \frac{\tau}{\rho} + \frac{\sigma}{\rho} + \frac{\kappa}{\rho} + \frac{\sigma_R}{\rho} \quad (1.7)$$

Where, τ/ρ is the contribution of the photoelectric effect, σ/ρ is that of the Compton effect, κ/ρ that of pair production, and σ_R/ρ is that of Rayleigh scattering. High- Z radiosensitizers effectively increase dose when added to tissue by increasing the probability of interacting with photons through the photoelectric interaction [11, 40]:

$$\frac{\tau}{\rho} \propto \left(\frac{Z}{h\nu}\right)^3 \quad (cm^2/g) \quad (1.8)$$

The probability of emission of photoelectrons is proportional to the third power of atomic number and inversely proportional to the third power of the photon energy [113] (Figure 1.2).

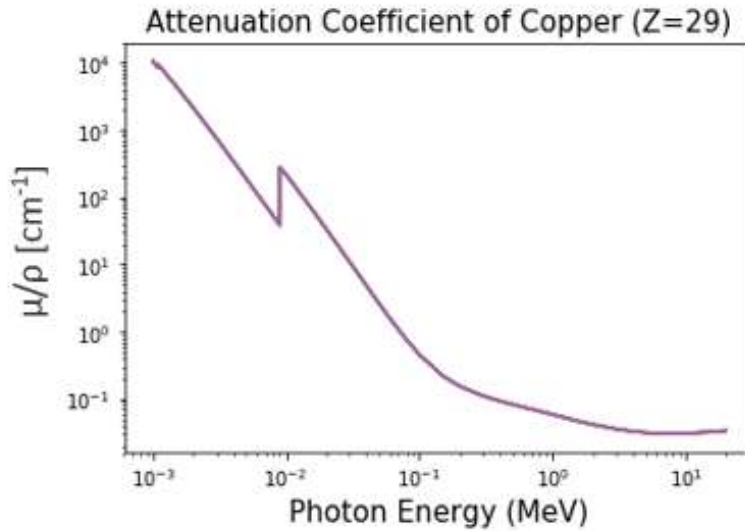


Figure 1.2 - Mass attenuation of copper as a function of photon energy plotted from 1 keV to 20 MeV. Cross-section increases with decreased energy. The spikes at 8.979 keV (K-edge) and at 1.096 keV (L1-edge) are the energy of resonance of the inner electron shells for copper.

The probability of photoionization is also increased at photon energies that overlap the absorption edge of the inner-shell electrons in the element [104]. This is demonstrated in Figure (1.2) at ~10 keV where the K-edge greatly increases the absorption due to the energy being

appropriate to interact with electrons within the K-shell. The interplay between atomic number, energies, and absorption shell dependence is illustrated in Figure (1.3).

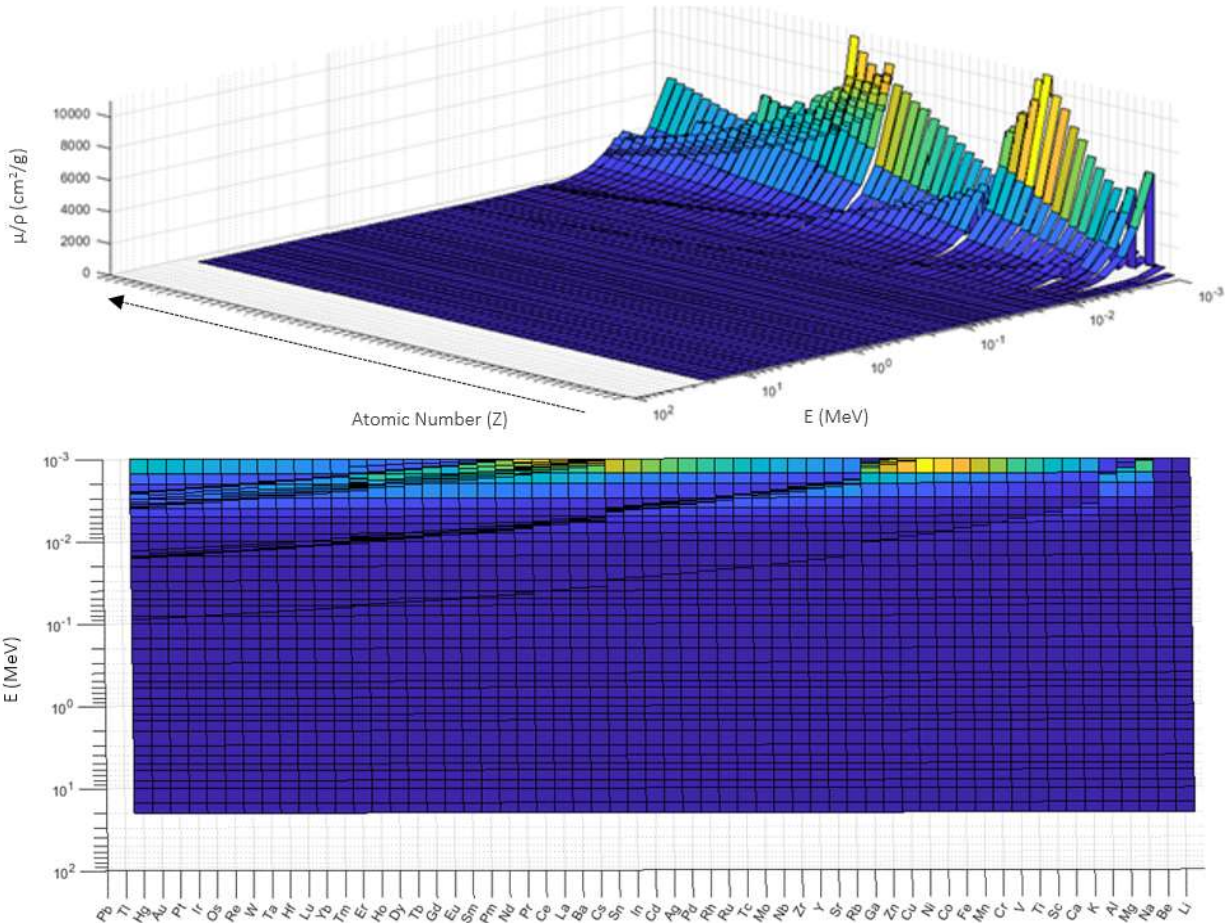


Figure 1.3 - Chart of mass attenuation coefficient by energy and metal elements with increasing atomic number. Maximum occurs at low energies, with ridges corresponding to the inner electron shell resonances (shell-edges). Shell edges occur at higher energies as atomic number increases.

Emission of a photoelectron leaves a vacancy in a lower shell, leaving the atom in an excited state. Subsequently, through atomic relaxation an excited atom will potentially emit Auger electrons. Auger electrons in close proximity to DNA cause damage in a manner comparable with high linear energy transfer (LET) particles [11, 50]. LET is important in determining the effectiveness of radiation to cause biological damage, or relative biological

effectiveness (RBE). RBE is defined as the inverse ratio of test radiation dose necessary to cause the same biological effect as a reference radiation, generally 250 kV photons [194]:

$$RBE = \frac{\text{Dose of 250 kV xrays to produce effect } X}{\text{Dose of test radiation to produce effect } X} \quad (1.9)$$

LET (L_{Δ}), is related to the restricted stopping power, the average energy lost by collisions up to a cutoff energy Δ in traversing a distance dl less the kinetic energy of the particles released with energy in excess of Δ [193].

$$L_{\Delta} = dE_{\Delta}/dl \quad (1.10)$$

Collision mass stopping power accounts for δ -rays that may travel a significant distance with sufficient kinetic energy ($> \Delta$). At low energy, and in water density material, however, the collision mass stopping power is a good approximation for LET. The mass collision stopping power of electrons is inversely proportional to electron energy in low energy range (below 1 MeV) as shown in Figure (1.4) [113].

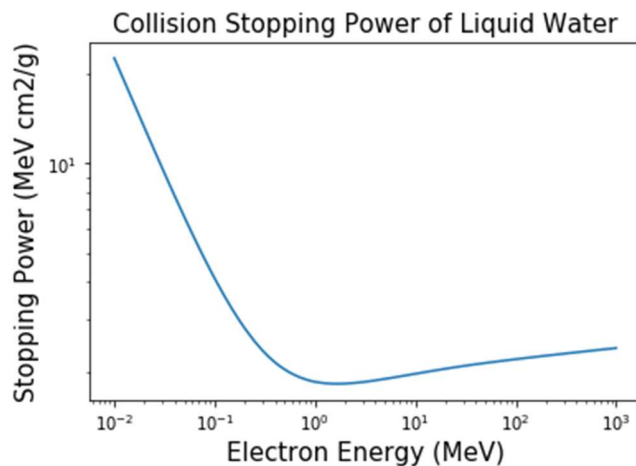


Figure 1.4 Collision mass stopping power for electrons as a function of electron energy in liquid water. At low energies (< 1 MeV) the value of stopping power increases with decreasing energy.

When low energy electrons (LEE) are released within close proximity to DNA they release substantial energy causing damage. Multiple clustered damages to the genetic material results in higher probability of mitotic death [50-54]. Auger electrons are a fundamental component to causing high-LET damage in radiosensitization models, as low-energy electrons have been shown to cause molecular damage more densely through resonant dissociative electron attachment [11, 43-45]. High-LET radiation DNA damage is considerably less repairable by the cell as the energy deposition is densely populated along the path of the particle [49-50]. Increased electron production from radiosensitizers also increases the amount of ROS species created by radiolysis of water; the mechanisms for increased DNA damage from metal radiosensitizers is summarized in Figure (1.5).

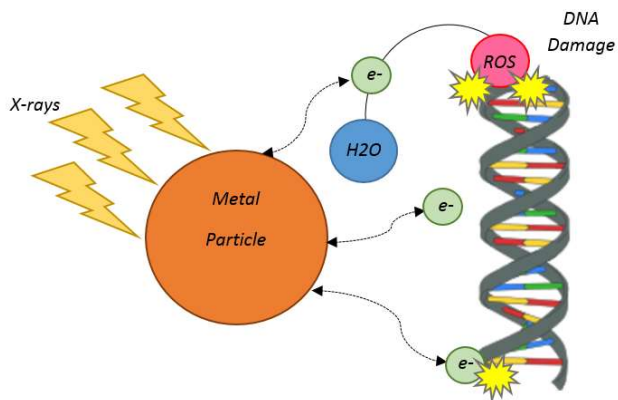


Figure 1.5 - Summary of the theoretical framework by which metal particles act to enhance DNA damage with external radiation. Metal particles when irradiated emit electrons via photoelectric effect and Auger cascade atomic relaxations. Electrons can be directly damaging to DNA or can increase ROS production through radiolysis to damage DNA indirectly.

An important treatment caveat to consider is that in order to overlap the energy with the K-edge energy for most non-toxic heavy metals the photon energy must be lowered, which

reduces photon penetration depth, although some studies have revealed dose enhancement with higher energy beams possibly related to the physiochemical interactions of metals with oxygen radicals [55-56, 67].

Furthermore, there is a tradeoff wherein the probability for photoelectric interaction increases with increasing atomic number (Z), but the probability for Auger cascade (in competition with fluorescent x-ray emission in atomic relaxation) is higher in lower Z materials [105] (Figure 1.6).

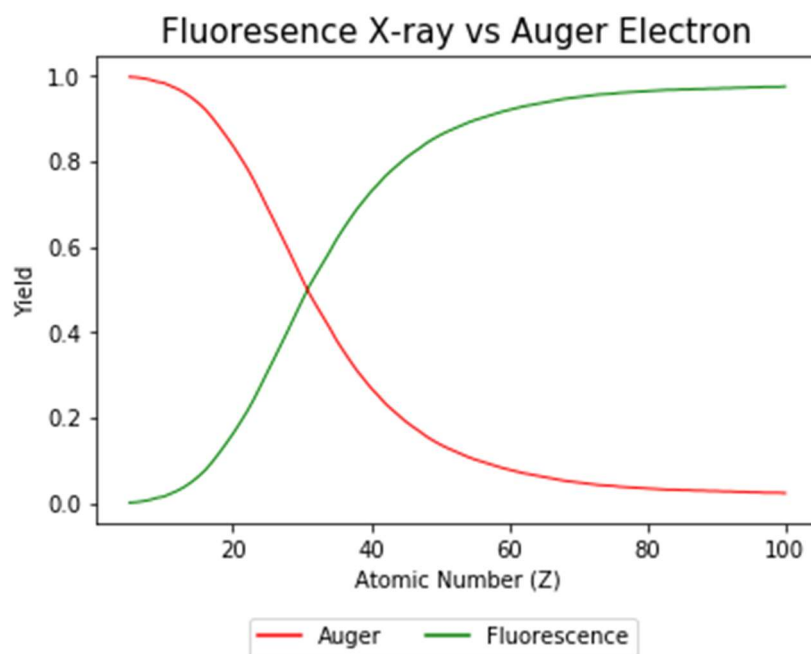


Figure 1.6 - Fluorescence X-ray vs. Auger electron yield in K-shell by atomic number. Atomic relaxation results in the emission of either Auger electrons or fluorescent x-rays.

Numerous metal salts and complexes have been found to have radiosensitizing ability, including salts with copper [11, 26, 37, 50, 57, 111]. In cases where copper was reduced to Cu(I) under anoxic conditions, it was found to have greater radiosensitizing effects than in normoxic conditions where the copper was able to return to the second oxidation state and exit the cells

through normal copper metabolism [26, 88, 111]. Copper holds specific interest because it is present as a trace cofactor in intracellular machinery such as cytochrome-c oxidase [27].

Additionally, copper may act as an indirect enhancer of radiation by increasing the rate of production of hydroxyl radicals from hydrogen peroxide by a Fenton-like reaction.

1.5 – Fenton-like reaction of Copper in Reactive Oxygen Species Production

Biological metabolism naturally leads to the creation of reactive oxygen species (ROS) from the biologically essential molecule oxygen [173]. External factors also affect the generation of ROS. For example ionizing radiation alters the transcription of certain genes via the epidermal growth factor receptor (EGFR-ras) leading to ROS overproduction in irradiated tissue [177]. Examples of ROS include superoxide, superoxide dismutase, and hydrogen peroxide which results in hydroxyl radicals [178].

Iron is an essential element in biological organisms, found primarily in hemoglobin in erythrocytes and myoglobin in muscle cells, it plays a role in oxygen mediation from lung to tissues [182]. It is also a component of proteins and enzymes, and plays a role in metabolism, immune function, and synthesis of structural proteins. Iron undergoes cyclic oxidation and reduction in mediating these functions, and this redox activity plays a role in the generation of ROS and other strongly oxidizing species capable of causing biological injury [181]. Radical creation from iron mediated reaction of superoxide and hydrogen peroxide was one of the earliest known causes of biological damage and is known as the Haber-Weiss reaction [183]:



The Haber-Weiss reaction is a specific step of the Fenton reaction that acts to recycle Fe^{2+} from Fe^{3+} to make the iron act catalytically in further steps of the Fenton reaction.

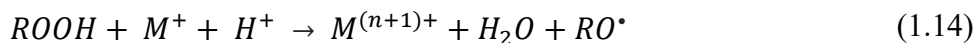
The Fenton reaction is a process that converts hydrogen peroxide with metallic ion present to highly toxic hydroxyl free radical [173]. It was first developed by Fenton in the 1890's in the oxidation of tartaric acid with iron to produce color reactions. Several metals have oxygen transfer capabilities that facilitate the generation of hydroxyl radicals [179-180]. Fenton reaction refers specifically to iron mediated hydrogen peroxide dissociation that has several possible mechanisms for action, the simplest of which [180-181]:



The reaction is capable of reacting with several substrates and causing biological damage by amplifying the amount of ROS created [181]. ROS are often referred to interchangeably with free radicals, and although the two chemical classes are similar, they are not entirely synonymous [175]. Overproduction of ROS can lead to oxidative stress, a disruption in the balance between the populations of ROS and antioxidant molecules, by overwhelming the antioxidant defense mechanisms [174]. Oxidative stress plays a role in DNA damage, gene expression and cell apoptosis [140-141, 173]. In cancer, oxidative stress is linked to amplified expression of hypoxia inducible factors (HIF) and a more aggressive, and invasive cancer phenotype [96, 110].

Other transition metal ions and complexes have been found to have oxidative features similar to the Fenton reaction, and the combination of these compounds with hydrogen peroxide are referred to as "Fenton-like" reagents [184]. In many cases these metals do not undergo the same reactions with hydrogen peroxide, and the production of hydroxyl radicals depends on the rate of decomposition reactions of metal-peroxide complexes and subsequent reaction with

organic substrates. A more general form of the Fenton reaction where M can generalize metal ion and organic peroxides $ROOH$ can generalize hydrogen peroxide yields alkoxy radicals:



Hydroxyl radical formation yields differ with different reagents, as well as the oxidizing species that result. Copper as a part of the natural cell metabolism is normally bound in proteins within cells, however, when released it is capable of catalyzing the formation of hydroxyl radicals [188]. Copper ions and complexes in the presence of a reducing agent and hydrogen peroxide are potent oxidants to biomolecules [186-187]. The first oxide state of copper, $Cu^+(aq)$ was found to not result directly in the formation of hydroxyl radicals in reaction with hydrogen peroxide as the initial step in the reaction formed a low valent peroxide complex of the form [185]:



Hydroxyl radicals subsequently result from the decomposition of the peroxide complex [185].

1.6 – Nanoparticles as a Mechanism for Dose Enhancement

Nanoparticles have become a major focus of research into efficient sensitizers as advances in nanochemistry have enabled a great variety of structures [92]. An important consideration for the application of a metal radiosensitizer is the toxicity of the injected material in the patient; toxicity can cause adverse effects and therefore limit the concentration of the metal deposited to sub-radiosensitizing levels. The development of sensitizers with low or no toxicity have gained attention after research into some chemical solutions were limited by cytotoxicity to normal cells [57]. Gold nanoparticles (GNP) have been at the forefront of development because of their low toxicity, high photoelectric cross-section, and ability to be manipulated allowing hydrophilic coatings and attachment of antibodies which can increase

cellular uptake [58-62, 91, 133, 138]. Cellular uptake and distribution has been a deficiency in the development of nanoparticles for radiosensitization given the importance of short-range decay particles in dose deposition models.

Targeted delivery of drugs, including radiosensitizers to tumors depends on the mechanism of enhanced permeability and retention [63-64]. Vessels synthesized within the tumor are leaky compared to those formed throughout normal tissue, allowing more diffusion of particles into the cells they supply [65-66, 153]. Additionally, the disorderly nature of vasculature construction, and the lack of accompanying lymphatic drainage causes positive pressure from vessels further causing additional deposition and retention. Nanoparticles (and other drugs) rely on this mechanism for preferential deposition into tumor areas. There have been mixed outcomes in investigating the level of uptake within hypoxic cells, a critical requirement for increasing the dose within large tumors. The best supported model indicates that GNP uptake decreases in hypoxic environments as those cells have less energy with which to uptake external particles, although this may only be in acute hypoxic conditions [68-70, 106]. Furthermore, GNP are large particles with limited diffusivity in fluid motion at the tumor level [94, 107]. GNP have limited motility in tumors distant from vasculature, decreasing in concentration as a function of distance from the vasculature. Cell layers also act to successively block the progression of GNP travelling through the tissue, because GNP need to be energetically endocytosed, this limits the concentration of GNP more than a few cell layers from vasculature [108]. GNP have been shown to move further in tissue with highly porous extracellular matrix (ECM), but they are also more likely to be trapped in unstructured ECM [109]. Nevertheless, nanoparticles have resulted in radiosensitivity and dose escalation in cells, mice, and human utilizations [71-74]. GNP have also been shown to radioenhance with MV radiation [56, 67]. It has been proposed that damage

to critical organelles may contribute to the dose enhancement from GNP [75]. Alternatively, other models have suggested the potential for GNP to damage the endothelial linings of vessels supplying tumor cells, and to starve them of their potential metabolism [76]. Although, this mechanism is controversial as it could also lead to unintended metastatic potential through reoxygenation of previously hypoxic tissue inducing cycling hypoxia [65-66, 77].

1.7 – The Role of CuATSM as a Hypoxic Tracer

The detriment of hypoxia to radiation outcomes has stimulated research and development for hypoxic tracers for prognostic indication [83]. The ideal hypoxia tracer would have the characteristics indicated in Table 1 [98]:

Table 1.1 - Characteristics of an ideal hypoxic tracer from Fleming et al. 2015.

Hypoxia-specific retained in regions with low partial oxygen pressure (mmHg) levels, but not by normoxic or necrotic cells.
Mechanism of cellular retention should be well defined and cell type independent.
Sufficiently lipophilic to enter cells and allow uniform tissue distribution, but also sufficiently hydrophilic to avoid membrane sequestration, and have faster clearance from systemic circulation and normoxic tissue.
Pharmacokinetic profile and tissue distribution should exhibit little dependence on parameters that may co-vary with hypoxia, such as blood flow or pH.
High stability against non-hypoxia specific metabolism in vivo.
Tissue kinetics should be suitable to imaging within a timeframe permitted in the clinical
Should be easy to synthesize and readily available.
Amenable dosimetry profile.
Be repeatable to allow both detection of hypoxia and return to normoxia.
Should be effective in multiple tumor types.

Radioactive CuATSM (diacetyl-bis N4-methylthiosemicarbazone), was developed to have characteristics useful in hypoxia tracing and although it does not meet all characteristics to be ideal, it has been shown to have efficacy, and is an FDA approved PET imaging agent [82, 88, 98]. PET is an imaging modality that uses radioactive isotopes incorporated into metabolically relevant compounds. The decay of the isotope produces a positron, the antimatter analog of an electron. When positrons interact with electrons, the charged particles are converted into photons by the annihilation process. The resulting discharge is similar to gamma ray emission, except that in general two photons are emitted at almost exactly 180° from each other. A ring of detectors surrounds a patient being imaged, and the collection of simultaneous photon events can be used to back project the location of the annihilation event. Electrons are quite abundant in tissue, making the annihilation event occur rapidly upon production and providing a millimeter resolution when used in diagnostic imaging [194].

ATSM is the biologically relevant component of the CuATSM ligand. The ATSM chelate has been shown to deposit its metal ion (copper or zinc) preferentially in reduced tissues which is an indirect correspondent for hypoxia in several cell types [78-80, 87-88]. Tissue reduction is correlated with the conditions in many hypoxic tumor regions because the stalled electron transport chain in hypoxic cells feature electrons attached to nicotinamide adenine dinucleotide (NAD) coenzymes [86-88].

CuATSM is a lipophilic molecule with high membrane permeability. It has low redox potential allowing for passive and facilitated diffusion transport into and out of most normoxic cells. The mechanism of cell trapping is still not entirely understood, however, the best indication is that CuATSM is retained in hypoxic cells by two mechanisms in sequence [88]. First, CuATSM is permeable to cell membranes and is able to pass freely into cells. Upon

entrance into a normoxic cell, the molecule is able to pass back through the cell membrane out of the cell. In hypoxic cells however, decreased metabolism causes the creation of reduced biomolecules associated with the electron transport chain. Bioreductive electron donating enzymes such as NADH and NADPH present in the microsomes or cytosol act to reduce the copper in CuATSM from Cu(II) to Cu(I) oxidation state which is less permeable to cell membranes. The CuATSM forms a wide array of charged configurations, only some of which have been identified by x-ray diffraction. These molecules host a negative charge that restricts permeability out of the cell [66, 99]. Cellular trapping at this stage is reversible in the presence of oxygen that may occur through reoxygenation of cycling hypoxic tissue [88, 100, 103]. Reoxidizing the reduced species reconfigures the molecules allowing for the reestablishment of permeability to the cell membrane and the ability of the Cu(II)ATSM to leave the cell. It is for this reason that some researchers have made suggestions that CuATSM should be used as a reduced tissue tracer [78, 88, 100, 103]. Alternatively, if the hypoxic conditions persist then the charged Cu(I)ATSM configurations can interact with copper chaperone proteins or ROS to release the copper ion from the ATSM chelate [88, 103] (Figure 1.7).

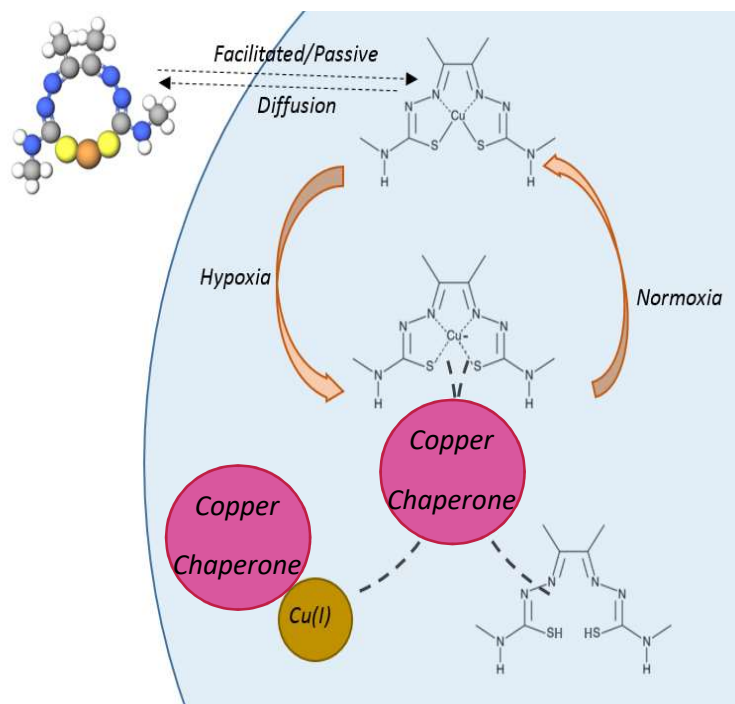


Figure 1.7 - Proposed mechanism for hypoxic cellular trapping of copper as deposited by CuATSM. CuATSM is lipophilic allowing it to enter and exit cell membranes uninhibited. In hypoxic cells, the reduction of the copper atom results in cellular trapping by copper chaperone proteins.

Therefore, as a free ion, Cu(I) will remain trapped within hypoxic cells, however, if oxygen returns then the copper will oxidize to Cu(II) and will follow copper metabolic pathways dependent on diffusion gradients in the same way as copper ions deposited by salts [88].

CuATSM has been benchmarked against Eppendorf oxygen probes, and was found to be in good agreement, although it is difficult to evaluate the functionality of a non-invasive hypoxia tracer with an invasive one [79]. It shows negative correlation with oxygen indicative non-invasive imaging techniques such as microscopic diffusion capacity weighted MRI [46]. It shows inconsistent results against the immunohistochemical stain pimonidazole, time based autoradiography has indicated that there is weak correlation, however, the strongest signal regions have been shown to have the best correlation [100]. This is attributed at least in part to

the different uptake mechanisms of pimonidazole and CuATSM. Pimonidazole is an integral accumulator in hypoxic tissue; below a certain oxygen level it remains in the cell and does not have a mechanism to leave as has been shown in CuATSM [88]. This could indicate that CuATSM has potential as a cycling hypoxia tracer, although no experiments have been made to evaluate this potential. It has also shown inconsistent correlation with other hypoxic PET tracers such as F18-FMISO and F18-FAZA, although to date, a perfect PET hypoxic tracer has not been developed. CuATSM is particularly poorly suited for prostate and liver [98, 101-102]. The uptake has been shown to have very high uptake in the liver from first pass pharmacokinetics [101]. In prostate, CuATSM has been shown to uptake into regions non-specific for hypoxia, but more likely associated with fatty-acid synthesis [102]. CuATSM has also been used as a cancer stem cell tracer [244]. CuATSM is the recommended option for hypoxia imaging in brain, renal, and bladder cancers; it is useful in lung, colorectal, and cervical cancers [98].

1.8 – CuATSM in Radiation Therapy

Hypoxia imaging-guided intensity-modulated radiation therapy (HIG-IMRT) or dose painting has been investigated using radioactive CuATSM as a method to identify hypoxic regions and overcome tumor radioresistance by improved targeting and escalating dose within a hypoxic region [103, 154, 246]. Additionally, radiotheranostic treatment has been suggested by employing $^{64}\text{CuATSM}$ that targets the hypoxic tumor tissue and could enhance tumor kill by microscopic emission of Auger electrons in proximity to the DNA [43-44, 52, 79, 126, 152]. If sufficient tumor to normal tissue ratios of the $^{64}\text{Cu-ATSM}$ can be achieved, increasing the dose could preferentially kill the tumor [52].

CuATSM can enter cells through diffusion and is able to travel through tumor volume from vessels into the hypoxic regions. Additionally, the deposition in hypoxic regions is verifiable through imaging with the PET scans, which can be used as functional imaging. A downfall of using ^{64}Cu -ATSM as a theranostic agent is that it has been shown to accumulate in other low oxygen areas in the intestines and liver [88-90, 101, 126]. Therapeutic enhancement to the tumor at the expense of cytotoxicity within normal tissues is antithetical to the goals of radiotherapy.

Auger electron emissions used in ^{64}Cu therapy could alternatively be initiated in nonradioactive copper metal (^{63}Cu) with external beam photons, reducing the radioactive burden to normal tissue as well as radiation safety protocols. In many ways increasing dose to hypoxic regions has served as the impetus the development of external beam radiosensitizers.

This work will assess nonradioactive CuATSM as a radiosensitizer of external beam photon radiation. GNP have been the primary focus of radiosensitization because of their favorable physical attributes, however, they have biokinetic constraints that limit their application [40, 50, 75-76, 111, 137]. The investigation of CuATSM, alternatively, is initiated primarily from the biokinetic potential it has as a hypoxic tracer [43-44, 52, 79, 103, 126, 152, 154, 246]. CuATSM has potential to improve radiation therapy in hypoxic tumors.

CHAPTER 2

MONTE CARLO EVALUATION OF METAL DOSE ENHANCEMENT WITH EXTERNAL BEAM SPECTRA

2.1 – Introduction

Radiosensitizer in radiation therapy broadly refers to any method or material that when combined with radiation increases the tumor inactivation beyond what would have been expected from the additive effect of each modality [196]. This may refer to the concurrent application of external chemicals in chemotherapy, anti-angiogenic therapy, or anti-growth factor receptor targeted therapies that act chemically on biological mechanisms to reduce DNA repair [197]. Alternatively, hyperthermia can be considered a radiosensitizer as through improved vascular flow rate it acts to improve the results of treatment over radiation alone [198].

Generally, when metals are used for radiation therapy, radiosensitization is attributed to physical principles that act to increase the number and effectiveness of radiation particles in proximity to vulnerable targets in the tumor. The absorption of energy from radiation is accounted for with dose; therefore, metals acting to increase energy absorption in a medium can also be considered dose enhancers. Interaction of photon radiation with matter is heavily dependent on the energy of radiation. In particular, the photoelectric interaction is probabilistically related to the energy of the radiation source and the material being irradiated. In the usage of metals as radiosensitizers for external beam photon radiation therapy it is crucial to optimize beam energy to maximize dose enhancement. As numerous photon sources exist in the clinical landscape, a common primary step in evaluating radiosensitizers, in either simulations or

natural experiments, has been with Gaussian distributed monoenergetic photon beams [135, 199]. Monoenergetic x-ray beams can be produced as synchrotron radiation in the storage rings or undulators of synchrotrons; or monoenergetic γ -rays can be the result of radioactive decay processes [53, 200]. Experiments utilizing monoenergetic beams have the advantage of simplicity, devices that are used commonly for radiation treatment generally have spectral distributions and electron contamination that may confound findings. It also has the advantage of a dosimetric response that has a direct linear relationship with the chemical and biological results, which may not be possible when comparing spectra from different sources.

Radiation treatments utilizing radioactive γ -ray sources exist and treatments using synchrotron radiation are in development, providing a clinically realizable application of the fundamental physics employed. The majority of radiation treatments, however, utilize x-ray beam spectra with megavoltage peaks (MV) from compact linear accelerators. Research has indicated that radiosensitizers result in improved tumor control probability using megavoltage x-ray spectra [55-56]. Therefore, standard megavoltage radiation will be considered, as well as two additional radiation spectra with peaks in the low megavoltage and orthovoltage range. The difference between monoenergetic photon irradiation and photon spectra irradiation can be seen in Figure (2.1). The maximum dose enhancement occurs just above the K-edge (8.97 keV) for copper (30 keV) as expected in the monoenergetic case, but with a spectrum, the maximum may occur at a higher voltage peak, because of low energy spectral components.

Copper Dose Enhancement by Monoenergetic or Spectral X-ray

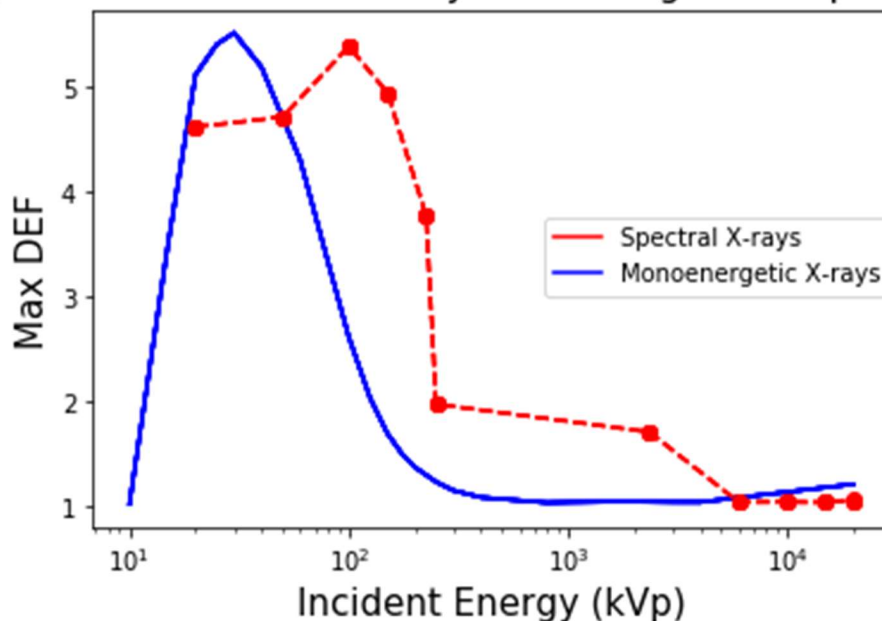


Figure 2.1 - Monte Carlo simulation of copper dose enhancement with monoenergetic photon beams compared to spectral photons. Maximum dose enhancement factor (DEF) is plotted against peak incident energy. Monoenergetic X-rays behave as expected with highest DEF just above the K-edge. Spectral x-rays have substantial contributions to their distributions from photon energies below the peak, causing a shift in maximum DEF.

The aim of this work, is to characterize the dose enhancement of several potential radiosensitizing metals when the irradiating source has a spectrum rather than a monoenergetic beam to provide improved clarity for how commonly available treatment devices could be used in researching potential radiosensitizers.

CuATSM is the primary analyte of this research, therefore, the dose enhancement of copper will be evaluated [143]. It is well known that gold nanoparticles (GNP) act as radioenhancers, and therefore the dose enhancement of gold will be considered as a positive control [42]. From the photoelectric cross-section, (Equation 1.8) it would be anticipated that gold with a higher atomic number ($Z = 79$), would have a higher dose enhancement than copper ($Z = 29$), with any photon radiation spectrum. With only two examples, a difference may be

demonstrated, but to show the trend between dose enhancement and atomic number, two other metals will be investigated following the methods of Paro, et al., silver ($Z = 47$) and gadolinium ($Z = 64$) [135]. Silver and gadolinium are practical examples, as the inner electron shell energies are intermediate between copper and gold [113] (Figure 2.2). Furthermore, investigations have been made into using silver and gadolinium nanoparticles for use in external beam radiosensitization [202-205].

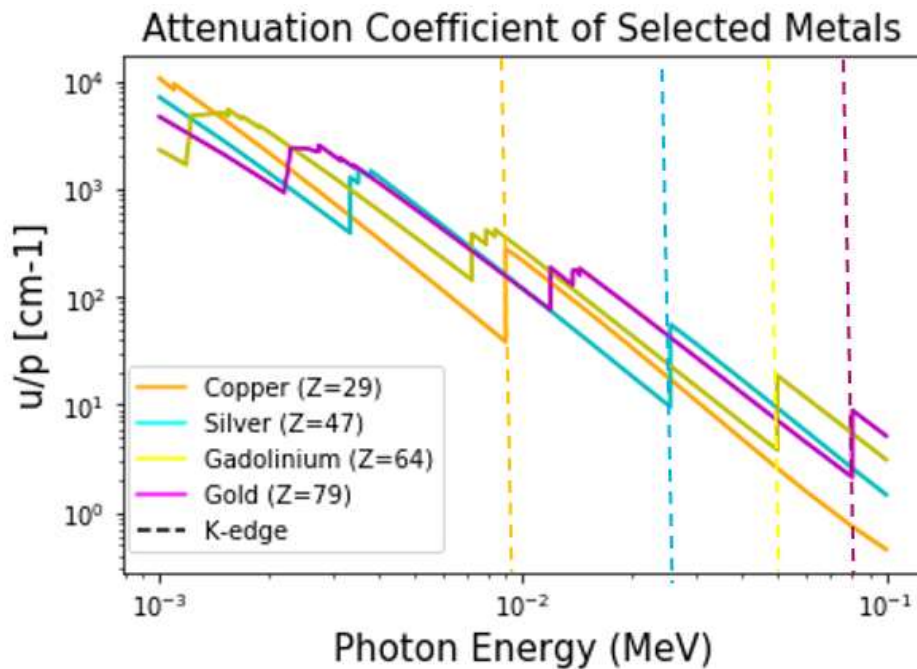


Figure 2.2 – Mass attenuation coefficients of selected metals. Linear attenuation coefficient μ/ρ [cm^{-1}] is plotted as a function of photon energy (MeV). Copper (orange) was plotted previously as Figure (1.2). Silver (cyan), gadolinium (yellow), and gold (magenta) were also plotted to demonstrate the higher linear attenuation coefficient for these metals at higher energy when compared to copper. K-edges of each metal are plotted as vertical dotted lines, and indicate the same trend: the energy resonance of gold’s inner electron shell is higher in energy than copper, with silver and gadolinium at intermediate values.

This chapter will outline the use of EGSnrc Monte Carlo software for simulating and benchmarking external radiation sources. These radiation sources will be subsequently used to model dose enhancement and electron fluence by metals at various concentrations in solution

with water. The central question of this investigation is: *Can CuATSM be used as a radiosensitizer of external beam radiation.* The results of this section are intended to answer a subset of the central question: *Can copper (a component of CuATSM) be used to enhance dose (a method of radiosensitization)?* These results will serve as a necessary first step for further analysis of CuATSM as a radiosensitizer.

2.2 –Analytical Attenuation and Energy Absorption of Metal Solutions

Recall from Section (1.1) that the probability of interaction for photons in a given material per unit distance, is the linear attenuation coefficient μ . This value is commonly tabulated in radiation physics resources for elements and several mixtures and compounds [191]. For materials without tabulated values, an effective linear attenuation coefficient can be calculated generally by:

$$\mu_{eff} = \sum_i w_i \mu_i \quad (2.1)$$

With w_i as the weight fraction of the i^{th} element. Effective linear attenuation coefficients are calculated on an elemental basis, for example the effective linear attenuation of the compound water should sum the relative molecular weight and coefficient of hydrogen and oxygen.

Consider a simple example of a copper solution in water. It will be assumed that water molecules act elementally, and that the addition of copper creates a mixture between copper ions and water, but that hydrogen and oxygen gases are not created. Chemically, this assumption is reasonable given that any gases created from the addition of copper to the solution would eventually, given adequate time to come to equilibrium, evaporate from the solution, leaving a homogeneous water composition. Thermodynamically, the assumption does not take into

account the changes that adding copper to water would have on the density of the resulting water.

Copper as a fraction of the molecular weight of the mixture will be evaluated, but the alteration to the separation of water molecules from each other will not be accounted for, and water will be assumed to maintain a density of 1 g/cm^3 and copper will be assumed to have density 8.96 g/cm^3 . The linear attenuation for a solution containing a 10^{-1} copper concentration in water at 0.05 MeV can be determined by:

$$\mu_{eff} = \mu_{H_2O} w_{H_2O} + \mu_{Cu} w_{Cu} = 2.54 \text{ cm}^{-1} \quad (2.2)$$

With $\mu_{H_2O} = 0.225 \text{ cm}^{-1}$ and $\mu_{Cu} = 23.39 \text{ cm}^{-1}$. Recall also that collision kerma K_c is a fundamental dosimetric quantity related to dose. It accounts for the energy absorbed in matter locally and can be evaluated by:

$$K_c = \psi \left(\frac{\mu_{en}}{\rho} \right) \quad (2.3)$$

Where ψ , is the energy fluence of the photon radiation and μ_{en}/ρ , is the mass energy absorption coefficient, the probability of the source radiation and secondary electrons to deposit energy locally less the energy that goes to photon creation (ex. Bremsstrahlung). Usefully, materials without tabulated mass energy absorption values can be calculated similar to Equation (2.1):

$$\mu_{en,eff} = \sum_i w_i (\mu_{en})_i \quad (2.4)$$

From this, the energy absorbed in an absorber of thickness L , under simple exponential attenuation can be determined:

$$\frac{E_{transmitted}}{E_{incident}} = e^{-\mu_{en}L} \quad (2.5)$$

$$E_{absorbed} = E_{incident} - E_{transmitted} \quad (2.6)$$

Using this framework, the energy absorbed was calculated for trace copper solutions with mass fraction of copper from 10^{-4} to 10^{-1} in water at incident energies ranging from 0.05 MeV to 10 MeV . The energy absorption in copper solutions was then normalized to pure water to evaluate the energy enhancement (Figure 2.3).

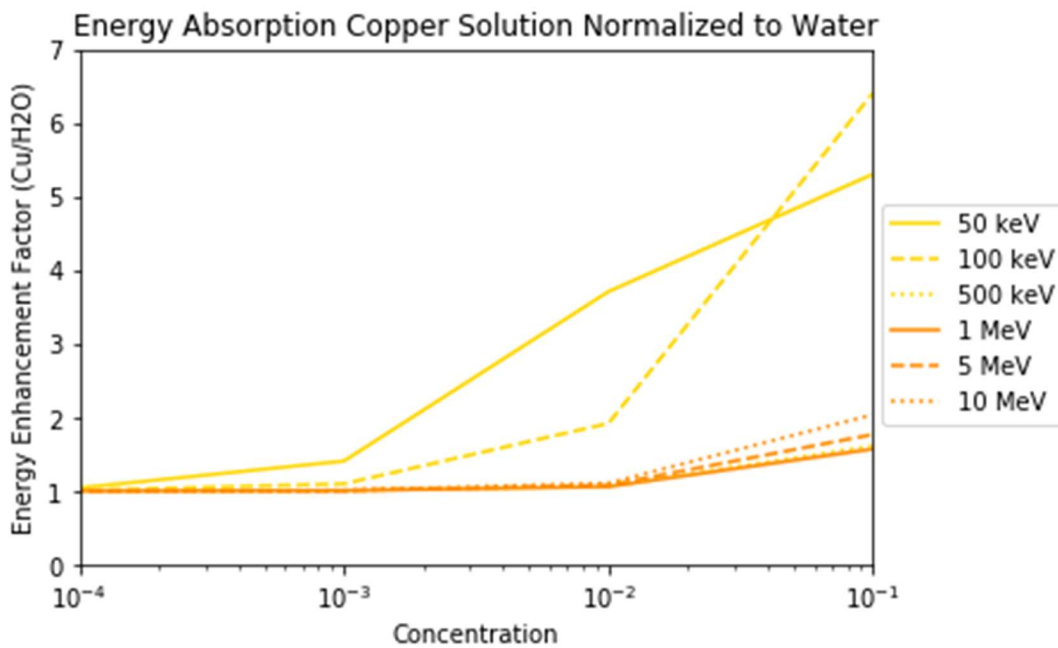


Figure 2.3 - Energy absorption in metal solution phantom for copper solutions normalized to water. Copper concentrations ranged from 10^{-4} to 10^{-1} for selected incident energies from 0.05 MeV to 10 MeV . Energy enhancement is highest in the two lowest photon energies measured (50 keV and 100 keV). A decrease in EEF is observed at 500 keV , and increases with each subsequent energy measured. Concentration of metal below 10^{-4} in solution was below 1% in all cases.

Energy enhancement is related to dose enhancement (Equation 1.6), but is differentiated here to emphasize that the quantity being investigated is absorbed energy. The energy enhancement factor (EEF) would be evaluated by:

$$EEF = \frac{\text{Absorbed Energy in Metal Solution}}{\text{Absorbed Energy in Water}} \quad (2.7)$$

Absorbed energy increases with incident energy in both copper solution and pure water. Energy enhancement, alternatively, was highest in the two lowest incident photon energies 50 keV & 100 keV with EEF of 5.3 and 6.4 respectively (10^{-1} copper concentration). Incident photons above 100 keV resulted in decreased energy enhancement, with lowest EEF at 500 keV (1.06) increasing with energy to 10 MeV (2.04). The results within the analytical model indicate that there is some feasibility in copper acting as an enhancer of absorbed energy, to further evaluate this potential, Monte Carlo methods will be used as a more accurate prediction of dose enhancement.

2.3 – Monte Carlo as a Tool for Dose Prediction

Monte Carlo (MC) methods are statistical techniques that use the process of repeated random sampling to make numerical estimations to solve for unknown parameters in deterministic problems. The use of MC has increased recently; increases in computational power have enabled the flexible application of MC simulations for rapid experimentation. The uses of MC are broad and have been employed in the fields of physics, biology, economics, and finance [206]. Although earlier variations of MC techniques exist, the development of modern MC is generally credited to Stanislaw Ulam, while working on nuclear weapons at Los Alamos in the 1940's [207-208].

Monte Carlo simulations rely on random numbers in order to evaluate mathematical expressions relating to physical decisions along the trajectory of the particle [212]. The decisions made about the particle generally fall into one of several categories: where the particle is born, initial particle energy, initial particle direction, distance to next collision, type of collision, and outcome of scattering collision (new energy and direction). At any point along the trajectory of a particle physical parameters of interest can be measured by the observer to determine total

outcomes such as dose [212]. The summation of each of these probabilistic events calculated through the transport of the particle is the history of the particle. Ultimately, each particle history is combined and averaged with many additional histories using different random number seeds leading to a condensed history solution [201].

The generation of a pure random number is a computationally intensive process, therefore pseudo-random numbers that have been pre-calculated are used in a look-up table method by the software in order to approximate pure random numbers. Each simulation begins with a starting random number generator seed that can be supplied by the user. This defines the sequence of numbers to be used along the trajectory of the particle. At each new interaction point the transport code refers to the next number in its sequence as the input for the next calculation [213]. This method allows for repeatability with exact replication of starting parameters, while also allowing a wide array of unique solutions utilizing the same random numbers as inputs for different physical interactions.

2.4 – Electron Gamma Shower (EGSnrc) Monte Carlo Codes

As in many other areas of radiation, the Monte Carlo method is the most accurate method for the simulation of radiotherapy equipment such as linear accelerators [201]. Radiation transport in the real world can be substantially more complicated than hypothetical processes, and accurate modeling requires large collaborations between scientists to create reliable software and libraries for simulations. The electron gamma shower (EGSnrc) codes are a project of the National Research Council of Canada (NRC) expanded and improved from original EGS4 collaboration of NRC and Stanford Linear Accelerator Center (SLAC) [201]. EGSnrc is a flexible code used in numerous areas of radiation transport calculation, and widely regarded as

the most accurate computer program for the simulation of photon and electron transport. It has widespread usage in research and therefore has been tested and evaluated repeatedly in peer-review, leading to a robust and well benchmarked simulation code. EGSnrc was used in this research because it is particularly well suited for medical physics applications such as the simulation and development of radiation devices. It also utilizes modular design and utilities with graphical user interfaces for many applications, making it easily accessible for medical physicists without advanced programming backgrounds.

MC calculations of radiation transport require substantial computation power and can be time-consuming to achieve accurate predictions of radiation dose. In a typical MC simulation, significant computation time may be allocated to tracking non-important events [218]. To reduce computational allocation to these events, variance reduction techniques are commonly implemented to reduce the statistical variance. EGSnrc has an extensive suite of variance reduction tools available; in the following methods some techniques were used and will be noted in the procedure.

BEAMnrc

The BEAMnrc software component, specializing in radiotherapy beam modeling of complex material components, is currently included in the EGSnrc package [209]. It was originally developed by the OMEGA collaboration between NRC and the University of Wisconsin-Madison. BEAMnrc simplifies beam modeling through the inclusion of modifiable 3-D geometrical volumes, termed component modules (CM). Component modules include basic geometrical shapes as well as medical radiotherapy unit specific geometries such as MLCs.

Materials composing the CMs are provided externally through PEGS4, although particle energy cutoffs and interaction profiles can be changed in system. Particles can be simulated with a variety of possible initial geometries and directions and transported through each CM generating new particles. Each CM can be succeeded by planes perpendicular to the central axis with the entire collection of particles stored as phase space files for further downstream analysis and implementation. The phase space file contains information about: charge, energy, position, and momentum of each particle. Phase space files can be analyzed or combined with a separate utility, BEAMdp, on a particle-by-particle basis or more generally for spectral data.

DOSXYZnrc

The phase space file created in BEAMnrc can then be used as an input for downstream application in voxelized dosimetric phantoms. DOSXYZnrc, another project of the OMEGA collaboration, can be used to calculate dose in a rectilinear phantom [210]. The phantom is composed of user defined voxels, with each voxel potentially containing different volume, media and density. This geometry is a common feature of medical physics measurements, often dose calculated in a rectilinear water phantom is used to characterize the output and profiles of a linear accelerator. A companion program, ctcreate, can be used to import the Hounsfield unit data from a CT image dataset for patient specific simulations.

FLURZnrc

The EGSnrc software additionally comes bundled with a toolkit originally developed to model ionization chambers called NRC user codes [211]. This toolkit utilizes cylindrical and spherical coordinate geometries to analyze radiological and dosimetric quantities. The codes in this package includes tools for generalized dose scoring in cylindrical geometries (DOSRZnrc),

ion chamber dose scoring (CAVRZnrc/CAVSPHnrc), stopping-power ratio calculation (SPRRZnrc), energy deposition kernels (EDKnrc), and cylindrical fluence scoring (FLURZnrc). For the purposes of this investigation, the FLURZnrc toolkit was used for calculation of electron fluence.

2.5 – External Radiation Beam Models

All simulations were run on the Rocky Mountain Advanced Computing Consortium (RMAcc) Summit supercomputer, running Red Hat Enterprise Linux Server 7.3 with access to up to 904 Intel Xeon E5-2680 v3 processors 12 cores X 2.5 GHz [115].

Each external beam radiation source model was created using EGSnrc, a Monte Carlo software toolkit for the passage of electrons and photons through matter [134]. The BEAMnrc code, specializing in simulating radiation beams from radiotherapy units, was used to create three beam sources with differing photon spectra [114]. In each case a phase space file of at least 10^9 particles was created with each particle's positional information upon exiting the beam source model. Several runs of 10^9 initial histories with different random number generator seeds were combined utilizing the *addphsp* utility to create the phase space file, and spectral distributions were calculated using BEAMdp. In all cases, EGSnrc physics parameters were modified to allow for electron impact ionization, Rayleigh scattering, atomic relaxations, and photoelectric angular sampling to enhance low energy tracking. Beam sources were composed of International Commission on Radiation Units and Measurements (ICRU) materials edited with PEGS4 to have lowest possible energy cutoffs of 512 keV for electrons and 1 keV for photons (Appendix A.1). EGSnrc physics libraries and values were chosen to have the most accurate

results at low energies and best computational performance, for additional information the reader is referred to the BEAMnrc User's Manual [209] (Table 2.1).

Table 2.1 – EGSnrc parameters for all simulations.

<i>PARAMETER</i>	<i>LIBRARY/VALUE</i>
<i>Maximum Step Size (cm)</i>	<i>1e10</i>
<i>Maximum Fractional Energy Loss/Step</i>	<i>0.1</i>
<i>Maximum Step Size</i>	<i>0.5</i>
<i>Boundary Crossing Algorithm (BCA)</i>	<i>EXACT</i>
<i>Skin Depth for BCA</i>	<i>0.0001</i>
<i>Electron-Step Algorithm</i>	<i>PRESTA-II</i>
<i>Bremstrahlung Angular Scattering</i>	<i>Koch-Motz</i>
<i>Bremstrahlung Cross Section</i>	<i>NIST</i>
<i>Bound Compton Scattering</i>	<i>Norej</i>
<i>Compton Cross Sections</i>	<i>Default</i>
<i>Pair Angular Sampling</i>	<i>Koch-Motz</i>
<i>Pair Cross-Sections</i>	<i>NRC</i>
<i>Photon Cross-Sections</i>	<i>Storm-Israel</i>

Phase space files were subsequently used as a planar input source for a rectilinear voxelized dosimetric phantom in DOSXYZnrc. The phantom was created with dimensions of 30 cm x 30 cm perpendicular (x/y) to the beam direction with 5 mm voxel resolution, and 8 cm in the direction of the beam (z) with 0.5 mm resolution. All voxels were assigned water material with density 1 g/cm³ and the lowest material energy cutoffs definable in PEGS4. The resulting dose grid was analyzed with MATLAB (MathWorks, Inc.), to determine the percentage depth dose (PDD), and profile dose data.

Varian Clinac Linear Accelerator

An approximate model for the Varian Trilogy linear accelerator head (Varian Medical Systems, Inc.), was created using the High-Energy Clinac schematics available by way of a non-

disclosure agreement. An isotropically emitting point source of electrons, with energy 6 MeV was simulated directly preceding the CMs modeling the linear accelerator head. A diagram created within the BEAMnrc framework and a 3-D model created with code in MATLAB is shown in Figure (2.4).

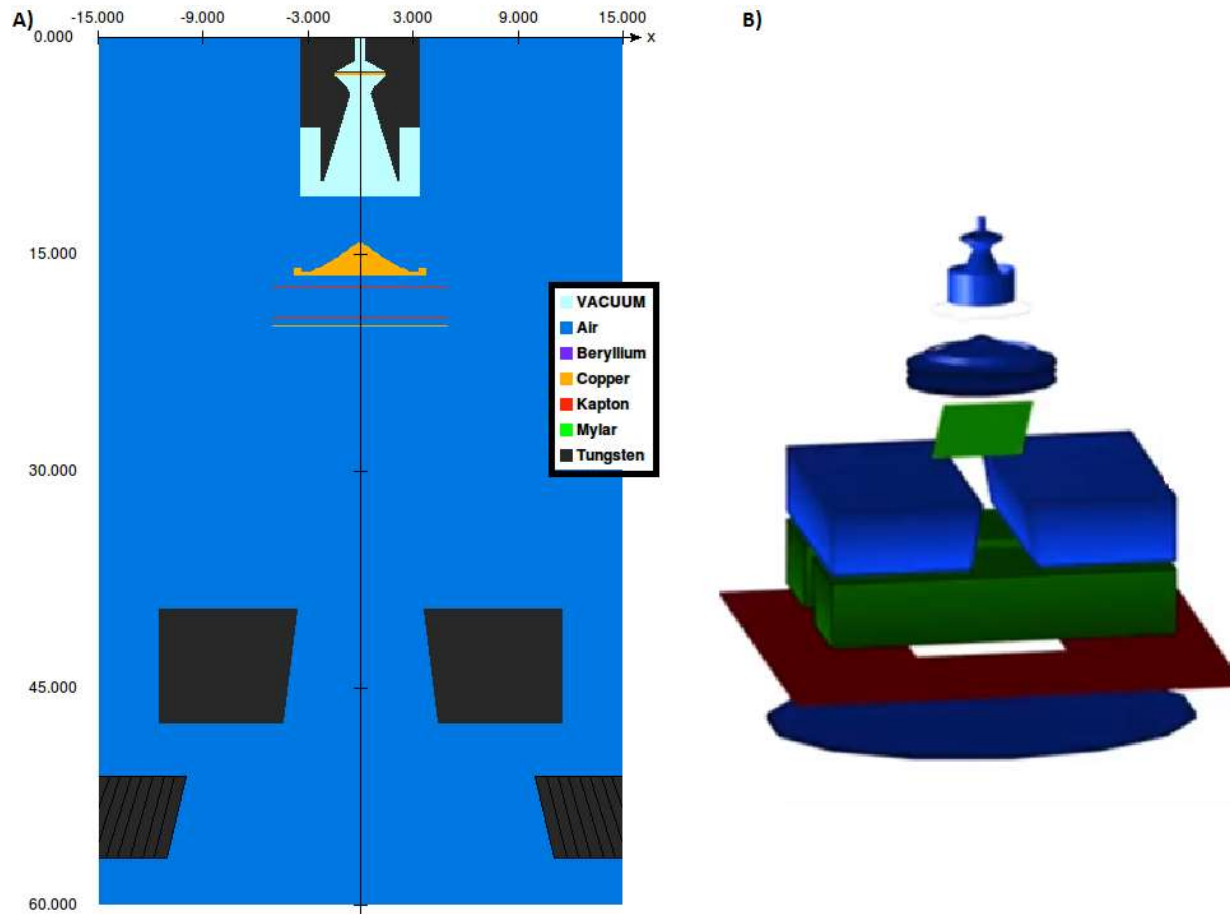


Figure 2.4 – Varian Trilogy linac head model with scale in centimeters. Components include primary collimator and target, flattening filter, and secondary collimation. (A) Exit window is located at 60.6 cm from the electron source. In this case the secondary collimator (jaws) is aligned to define a 20 cm x 20 cm field at 100 cm SSD. (B) A three-dimensional model corresponding to the same geometry as (A).

The standard beamline for photon therapy starts with a beam of electrons that strikes a target generally composed of subsequent layers of tungsten for bremsstrahlung production and copper

for heat dissipation. The bremsstrahlung x-rays are defined in field size by the primary collimator composed of tungsten. Downstream, the photons are filtered through an energy dependent beam flattener. This component is generally made of tungsten that is thicker at the center than the outer edges to produce a radiation field of uniform intensity at a selected depth (generally 10 cm). Subsequently, photons travel through a transmission monitor ion chamber, composed of several equidistant parallel electrodes that minimally affect beam output and act to internally measure exposure. A mirror in the beamline acts in combination with a light source to project an image congruent with the radiation field for external patient setup. Secondary collimator jaws, composed of tungsten, define the treatment field size by moving independently in the (X) and (Y) axes. Multi-leaf collimators (MLC), also composed of tungsten follow secondary collimation and define treatment specific fluence. Unless additional field shaping devices (wedge) are needed, the photons pass through a Mylar window to exit the linac for use in treatment. The most important factors which affect the exiting beam spectra are the incident beam energy, target, and flattening filter. A summary of the component modules used to create this model is presented in Table (2.2):

Table 2.2 – Summary of components used to define the Trilogy model.

<i>LINAC COMPONENT</i>	<i>EGSNRC COMPONENT</i>	<i>MATERIALS</i>
<i>Primary Collimator/Target</i>	<i>FLATFILT</i>	<i>Tungsten, Copper, Vacuum, Beryllium</i>
<i>Flattening Filter</i>	<i>FLATFILT</i>	<i>Copper, Air</i>
<i>Ionization Chamber</i>	<i>SLABS</i>	<i>Copper, Kapton, Air</i>
<i>Mirror</i>	<i>MIRROR</i>	<i>Mylar, Air</i>
<i>Jaws</i>	<i>JAWS</i>	<i>Tungsten, Air</i>
<i>Multi-Leaf Collimator (MLC)</i>	<i>MLC</i>	<i>Tungsten, Air</i>
<i>Exit Window</i>	<i>SLABS</i>	<i>Mylar, Air</i>

Variance reduction included directional bremsstrahlung splitting with splitting number 29 and a splitting field radius of 20 cm at a source to surface distance (SSD) of 100 cm. Energy cutoffs for photons (PCUT) and electrons (ECUT) were set to 1 keV and 20 keV, respectively, with higher cutoff values (ECUTIN) for electrons within the primary collimator, the flattening filter, the jaws, and the MLC based on the electron range in those materials. An example run file is included in Appendix (A.2).

Megavoltage Imaging Spectra

A lower-energy flattening filter free (FFF) linac with maximum energy 2.35 MV was created by altering the Clinac design with a low-Z target composed of graphite and removal of the flattening filter [116, 215]. This design is borrowed with permission from researchers at Dalhousie University (Figure 2.5).

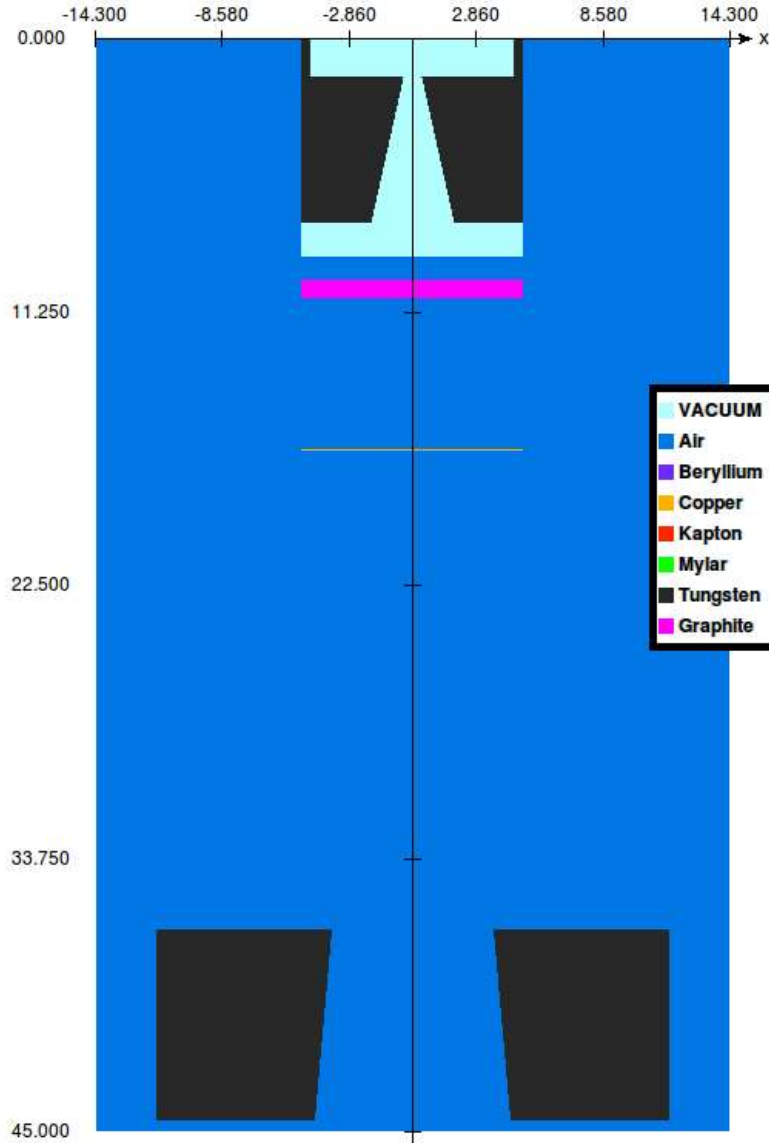


Figure 2.5 – Megavoltage imaging beam spectra model with scale in centimeters. Components include primary collimator, graphite target in place of flattening filter, and secondary collimation. MLC were not included in this model to be consistent with Dalhousie University model.

The implementation of the imaging beam requires the removal of the standard target from the primary collimator and addition of a cylindrical graphite target in place of the flattening filter. The conception behind this design is to allow for cone beam CT (CBCT) in the low MV range with a beam-eye-view imaging consistent with treatment geometry. The low MV energy

enables better tissue contrast than treatment beams, while additionally providing MLC defined volume-of-interest imaging [216]. In addition to imaging, the Imaging beam has also been considered for radiotherapy treatments involving GNP [76]. The component modules used for this beam design are in Table (2.3):

Table 2.3 – Summary of components used to define the Imaging model.

<i>LINAC COMPONENT</i>	<i>EGSNRC COMPONENT</i>	<i>MATERIALS</i>
<i>Primary Collimator</i>	<i>FLATFILT</i>	<i>Tungsten, Vacuum, Beryllium</i>
<i>Low-Z Target</i>	<i>FLATFILT</i>	<i>Graphite, Air</i>
<i>Ionization Chamber</i>	<i>SLABS</i>	<i>Copper, Kapton, Air</i>
<i>Mirror</i>	<i>MIRROR</i>	<i>Mylar, Air</i>
<i>Jaws</i>	<i>JAWS</i>	<i>Tungsten, Air</i>
<i>Exit Window</i>	<i>SLABS</i>	<i>Mylar, Air</i>

Uniform bremsstrahlung splitting with splitting number 29 was used with 20 keV ECUT and 1 keV PCUT as before. An example run file is included in Appendix (A.3).

Small Animal Orthovoltage Spectra

Finally, a low energy beam (225 kVp) was created to model the small animal radiotherapy research platform (SARRP) from schematics and models provided by Xstrahl for a 5 mm x 5 mm nozzle (Xstrahl Medical & Life Sciences, Inc.) [118] (Figure 2.6).

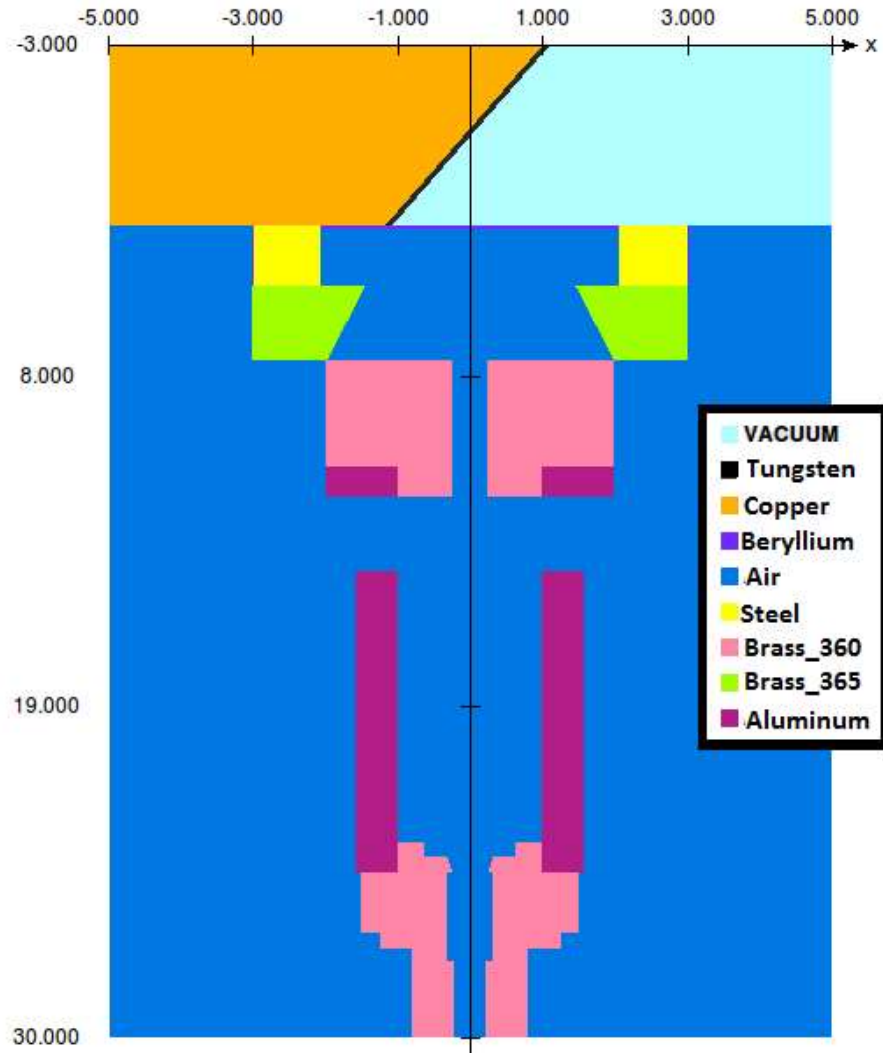


Figure 2.6 - An orthovoltage energy source (225 kVp) with scale in centimeters. Model of the small animal research platform (SARRP) modeled with 5 mm applicator.

The primary difference between the SARRP model and the Trilogy and Imaging models is that it is not based on a linear accelerator design. The source of x-rays in this case comes from a COMET x-ray tube (COMET Group, Inc.). The electron source is projected horizontally (right to left) to interact with the tungsten target positioned diagonally. The Bremsstrahlung photons that result are oriented downward through a collimator and applicator specific to the design of

the irradiator. Xstrahl has several applicator sizes available, the one chosen for this model has a circular aperture of 5 mm diameter.

Table 2.4 – Summary of components used to define the SARRP model.

<i>IRRADIATOR COMPONENT</i>	<i>EGSNRC COMPONENT</i>	<i>MATERIALS</i>
<i>X-ray Tube</i>	<i>XTUBE</i>	<i>Tungsten, Vacuum, Copper</i>
<i>Housing</i>	<i>CONESTAK</i>	<i>Beryllium, Steel, Air</i>
<i>Primary Collimator</i>	<i>PYRAMIDS</i> <i>CONESTAK</i> <i>CONESTAK</i>	<i>Air, Brass_365, Brass_360,</i> <i>Copper, Aluminum</i>
<i>Support</i>	<i>CONESTAK</i> <i>CONESTAK</i>	<i>Air, Brass_360, Aluminum</i>
<i>Applicator</i>	<i>FLATFILT</i> <i>PYRAMIDS</i>	<i>Tungsten, Air</i>

Uniform bremsstrahlung splitting with splitting number 300 was used in this case with electron range rejection of 10 MeV. An example run file is included in Appendix (A.4).

External Beam Spectra

Monoenergetic photons can be used in radiation treatments utilizing radioactive sources or synchrotron accelerators. More commonly, clinical radiation sources including diagnostic and therapeutic x-ray tubes and linear accelerators output photon spectra composed of a range of energies with the maximum being the peak voltage applied in acceleration. Recall from Section (2.1) that the distribution of photon energies in a spectrum can result in different dose properties from monoenergetic photons. BEAMnrc was used to create models of external beam radiation sources; monoenergetic electrons were injected into the models and the output of interactions were collected after the final component module in the model as a phase space file.

The phase space file is a summary of information about the particles that are present at the collection plane. As the models were intended to serve as external beam photon sources the phase space files created from these beam models consisted of at least 10^9 photons. This large collection of data resulted in files that require 40-50 GB of hard disk space. The EGSnrc utility BEAMdp was used to evaluate the spectra of each outputted phase space file. The entire energy spectrum for each beam model is plotted in Figure (2.7A). The spectra are normalized to the maximum photon fluence energy window in each case. The results are consistent with findings in literature [216, 219-220]. The spike in the Trilogy data at 0.511 MeV can be attributed to annihilation photons, and those in the SARRP data are the characteristic photon emissions of the x-ray target material, tungsten.

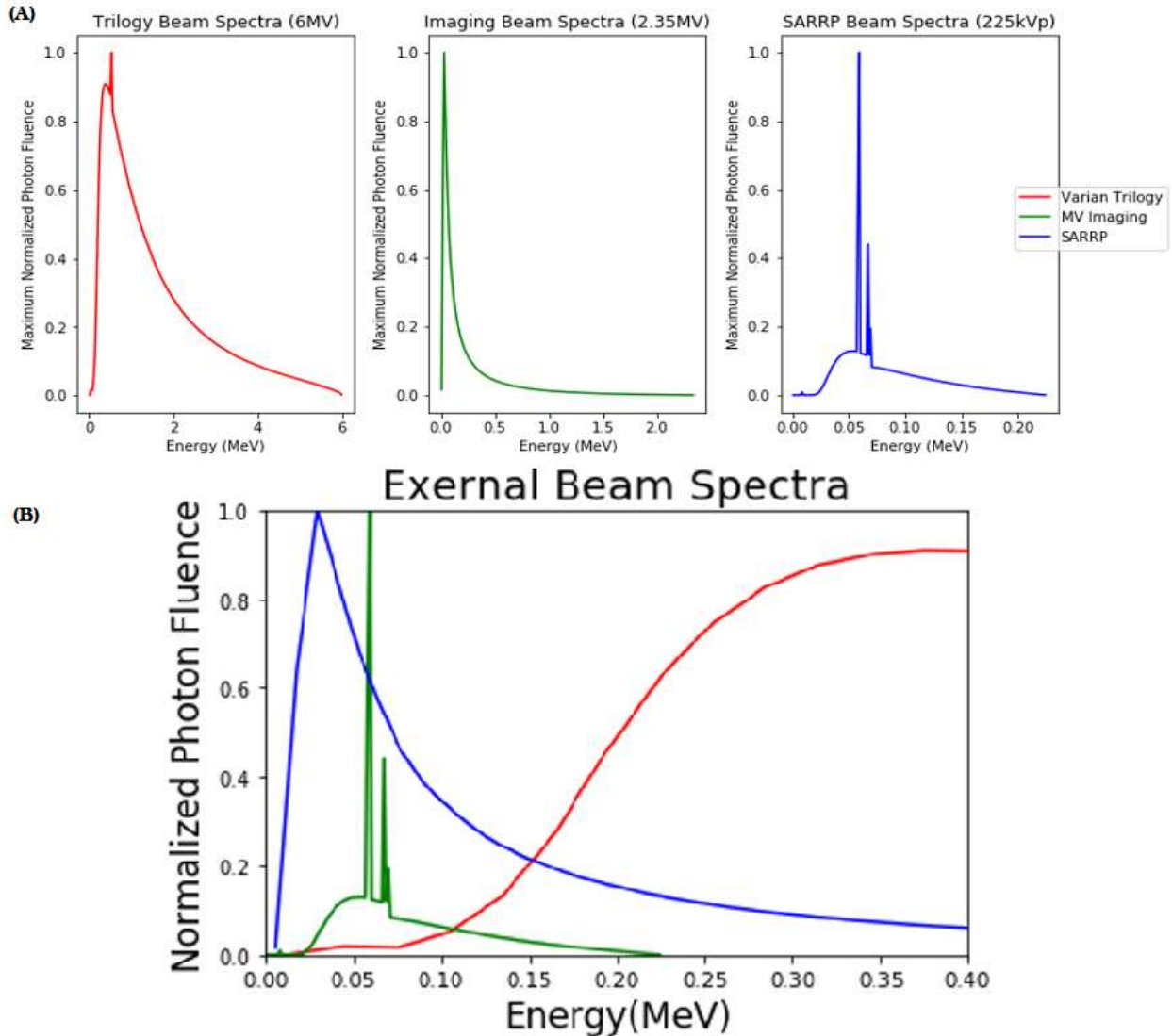


Figure 2.7 – Photon energy spectra for beam models. Spectrum is an important consideration in dose enhancement with metal particles because low energy photons have higher probability of resulting in photoelectric emissions. (A) Independent beam spectra, and (B) overlapping spectra, showcase that the spectra have different energies of maximum fluence.

Figure (2.7B), portrays the overlapping spectra below 400 keV; the beam designs were chosen to have substantial non-overlapping energy windows in order to maximize the differences observed in subsequent dose enhancement investigations.

Percentage Depth Dose

A common method for characterizing a radiation beams is to measure the dose distribution within a phantom. Generally this measurement is done at the central axis of the beam field, and each dose value at depth (D_{depth}) is normalized to the maximum value (D_{max}):

$$PDD = \frac{D_{\text{depth}}}{D_{\text{max}}} * 100 \quad (2.8)$$

The value of PDD at depth below maximum dose, increases with beam energy. As mentioned previously, this characteristic has made megavoltage treatments primary in modern radiation therapy. Higher-energy beams are more penetrating and result in a higher PDD at depth [93].

The EGSnrc package DOSXYZnrc was used to create a rectilinear phantom with dimensions 30 cm (X) x 30 cm (Y) x 8 cm (Z) with identical voxels with resolution 5 mm (X) x 5 mm (Y) x 0.5 mm (Z). The phantom was assigned liquid water material for all voxels, and the phase space file of each external beam model was used to irradiate the phantom, and the dose in each voxel was recorded to characterize the PDD of each beam. The dose at each depth along the central axis was averaged with two adjacent voxels in each direction of X/Y (total 25 voxels) to improve the signal-to-noise ratio (Figure 2.8).

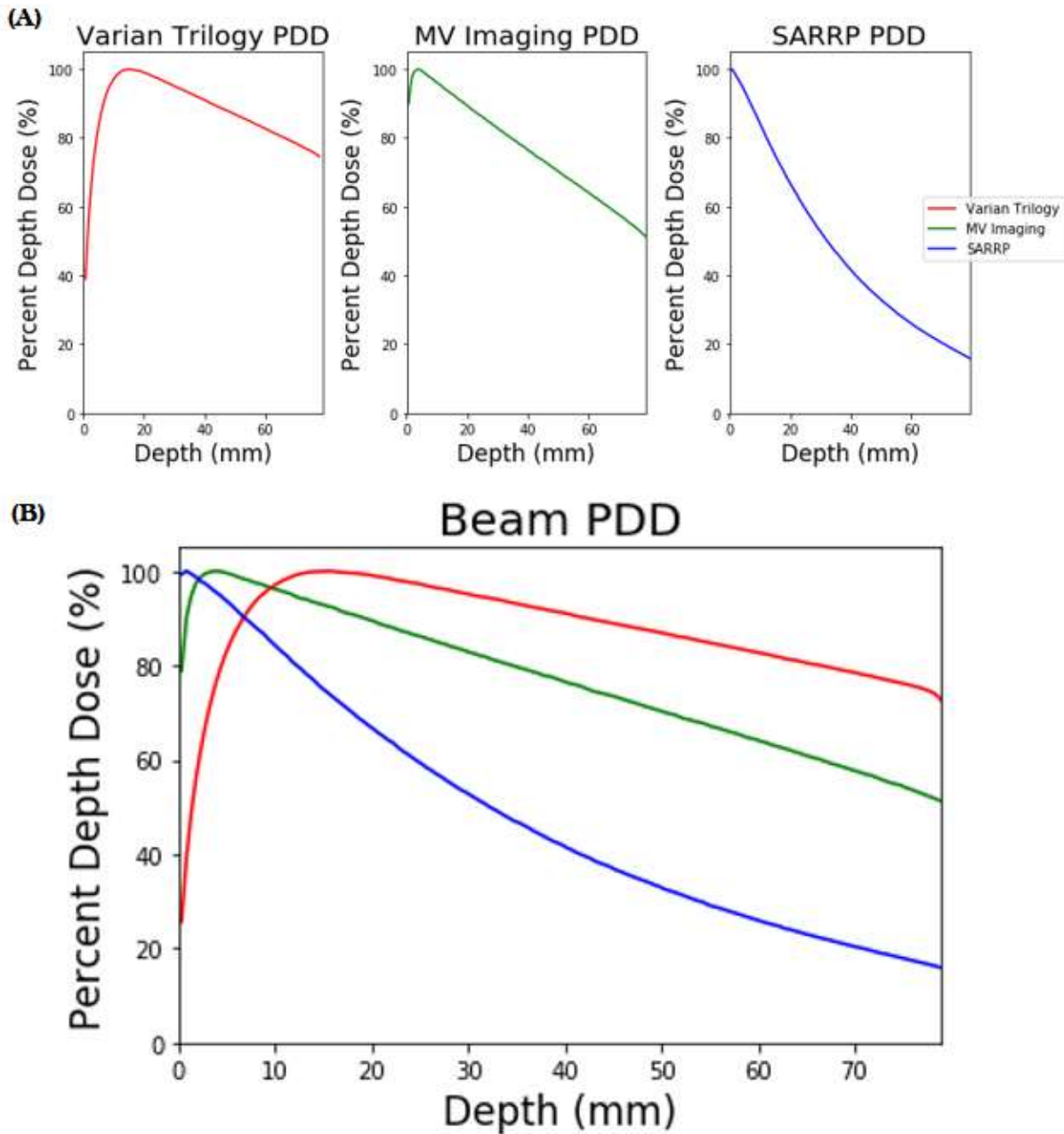


Figure 2.8 – Percentage depth dose for beam models. PDD is a common metric used to evaluate the behavior of dose deposition at depths within a patient or phantom. (A) Independent PDD of each beam and (B) overlapping PDD show the differences of D_{max} and dose behavior at depth for the three beam spectra.

As predicted, the PDD for the highest energy model (Trilogy) had the highest dose levels at depth, with a D_{max} of 1.4 cm. The SARRP has the lowest dose levels at depth with a D_{max} at

the surface, and the Imaging model had intermediate behavior between the other beam models at depth and had a Dmax of 0.4 cm.

Field Size and Shape

Another common metric used to evaluate or compare different beams are the geometric parameters unique to the output field of a treatment machine. The field size and shape are defined within the treatment head of the radiation device at the collimating sources (see Tables 2.2, 2.3, 2.4). Commonly, the parameters are summarized by measurements of the dose along the non-depth dimensions (X/Y), normalized to the value of dose at the central axis. The dose profile along the X-axis is commonly called the crossplane profile, and along the Y-axis it is called an inplane profile [93].

To characterize the field shapes and sizes of each of the beam models, the same phantom geometry was used with the change that the high resolution voxel length (0.5 mm) was used in the planar dimensions and 5 mm was used in the Z dimension. The output was collected at 5 cm depth (Z) at the midline of the radiation field along either the X or Y dimension, and similarly averaged over two adjacent voxels in the two non-analyzed dimensions. For these measurements there was very little difference between the crossplane profile and the inplane profile, therefore only crossplane will be presented (Figure 2.9).

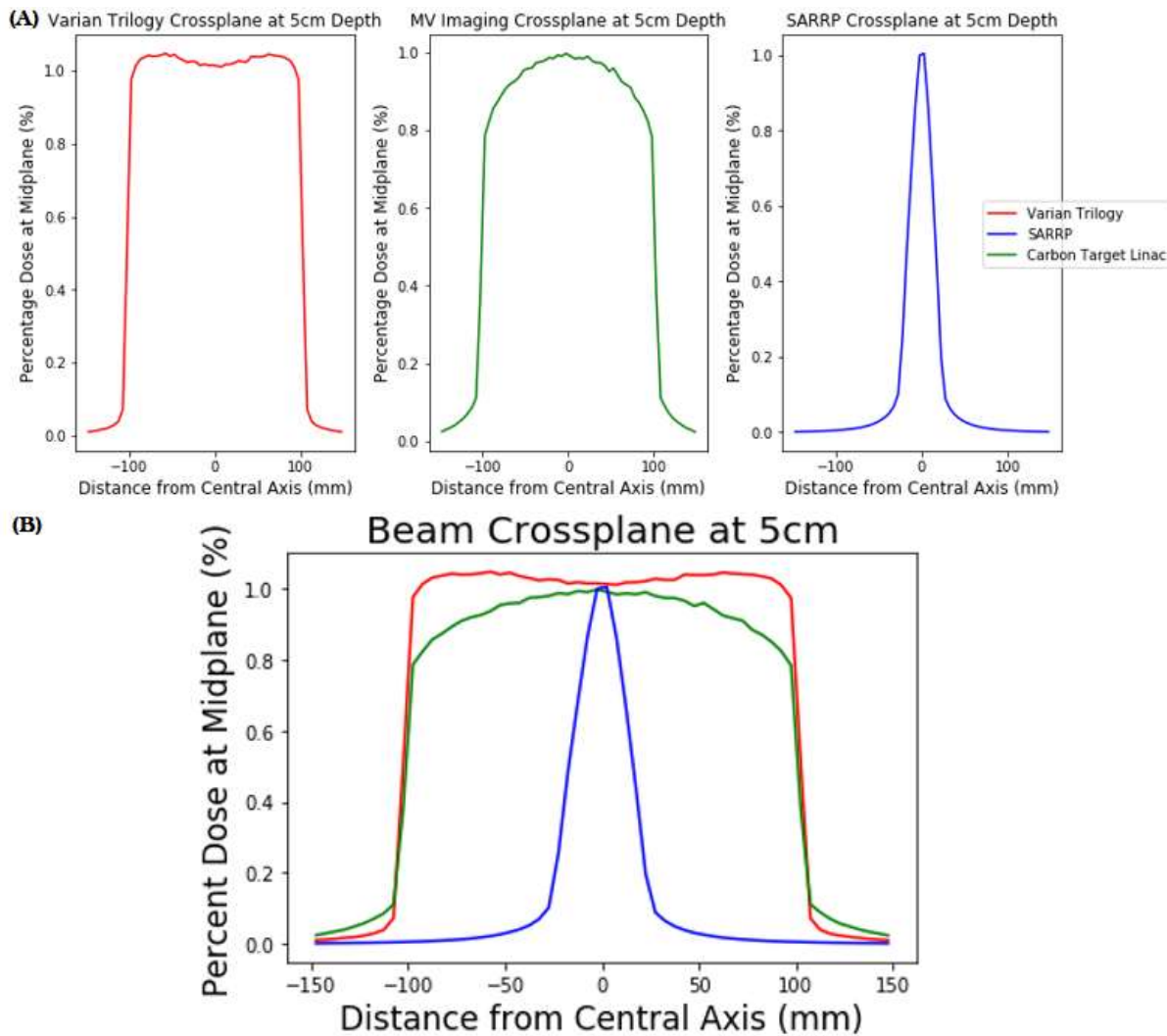


Figure 2.9 – Crossplane profile for beam models. Profiles are a common metric to evaluate the geometric parameters of a beam. (A) Independent crossplane and (B) overlapping crossplane showcase the size and shape of the beam profiles.

The size differences of the beam profiles are attributable to the field shaping collimators. The SARRP beam profile is smaller in dimension than the other beam profiles, and centrally peaked. The Imaging beam profile matches the spatial extent of the Trilogy beam (defined by identical secondary collimation) it differs by having a central peak defined by the target alone. The Trilogy beam had an additional filter in its beam path which acts to flatten the profile at 10

cm. The crossplane here at 5 cm shows higher dose features at the peripheral edges of the beam profile from the reduced filtering of the photons traveling through those areas.

Benchmarking Trilogy Model to Varian Trilogy

This research was conducted at Colorado State University, Veterinary Teaching Hospital (VTH), which employs a Varian Trilogy. The model was benchmarked against the clinical data collected with ionization chamber, for 6 MV photons using a 20 cm x 20 cm field with both PDD and crossline profile (Figure 2.10).

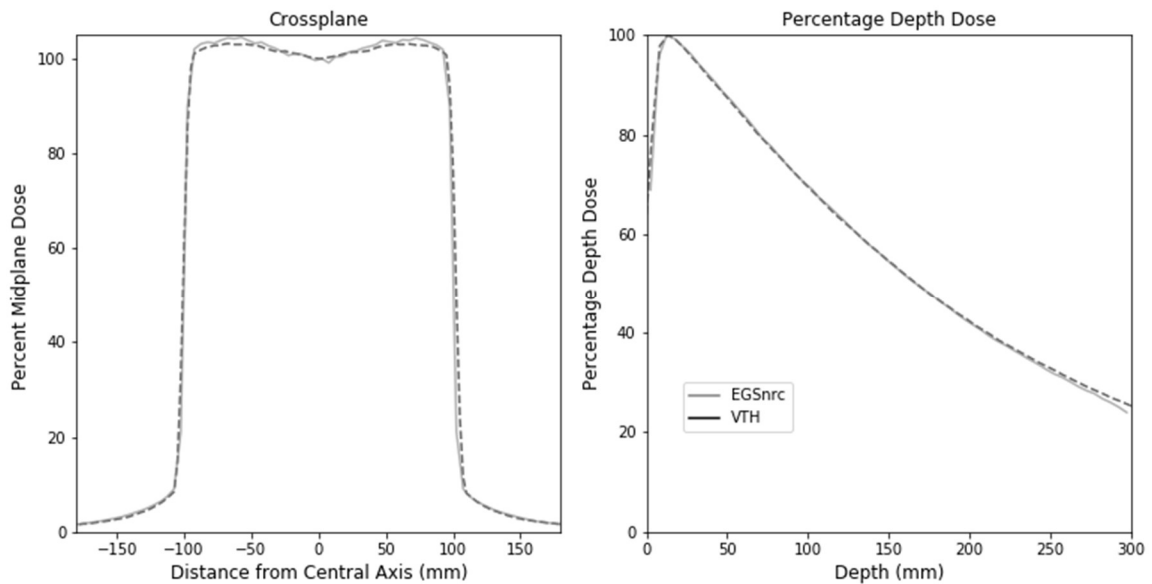


Figure 2.10 – Benchmarking of Trilogy MC Model to VTH Varian Trilogy linac. There is good agreement between model and linac with PDD and beam profile measurements.

2.6 – Dose Enhancement in Various Metals

Dose enhancement was measured with solutions of the metals mentioned in Section (2.1): copper, gold, silver, and gadolinium. For each metal, solutions in water were created with metal composing between 10^{-4} (0.1 g/kg) and 10^{-1} (100 g/kg) of the solution by mass (Appendix A.5).

Phase space files, from the previous section (2.5), were used as the inputs to measure dose in voxelized phantoms. DOSXYZnrc phantoms were created with the same spatial dimensions and resolutions as described in the previous section (2.5), an example run file is included in Appendix (A.6). In addition to water material, a metal solution layer of 1 cm thickness was added at a depth of 3 cm (Figure 2.11). EGSnrc physics parameters and libraries were the same used previously as described in Table (2.1), and all simulations for this section were again run on Summit.

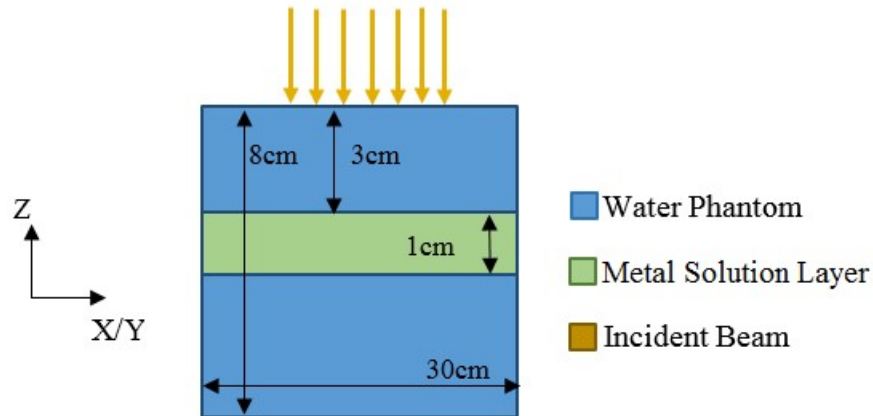


Figure 2.11 – Geometry for simulation of dose in voxelized phantom, not to scale. Multi-layer phantom with 1 cm metal solution layer at 3 cm depth extending the dimensions of the phantom in X/Y.

Dose was evaluated throughout the depth of the phantom at the central axis. A total of twenty-five voxels were averaged together from the two adjacent voxels in X/Y at each depth. Dose enhancement is determined from Equation (1.6), by the ratio of dose in each analyzed region to the dose in a region of equal volume filled with water material. At this point a clarification is needed for the term dose enhancement that will become a critical distinction in Chapter 5. Consider that the dimensions of the voxels defined in in this experiment are small (5 mm x 5 mm x 0.5 mm), but compared to the scale of electron energy depositions the scale is

large. Were we to consider these voxels as collections of smaller nanometer sized voxels, we can then define a macroscopic dose enhancement factor as [221]:

$$DEF_{macro}(\vec{x}) = \frac{\int_{V(\vec{x})} Dose_{radiosensitizer}(\vec{x}) d^3x}{\int_{V(\vec{x})} Dose_{water}(\vec{x}) d^3x} \quad (2.9)$$

The macroscopic DEF (DEF_{macro}), is the ratio of integrals of regions of interest either containing radiosensitizers or water. It is distinct from the ratio of the individual regions of interest, or microscopic DEF (DEF_{micro}):

$$DEF_{micro}(\vec{x}) = \frac{D_{radiosensitizer}(\vec{x})}{D_{water}(\vec{x})} \quad (2.10)$$

For the remainder of this section, the term dose enhancement will refer to the macroscopic DEF.

Dose Enhancement with Concentration of Metal Solution

Irradiation with external beam phase space files of at least 10^9 histories was modeled in water phantoms containing copper solution layers and dose enhancement was calculated. The data are plotted with concentrations of copper ranging from 0.1 g/kg to 100 g/kg (Figure 2.12).

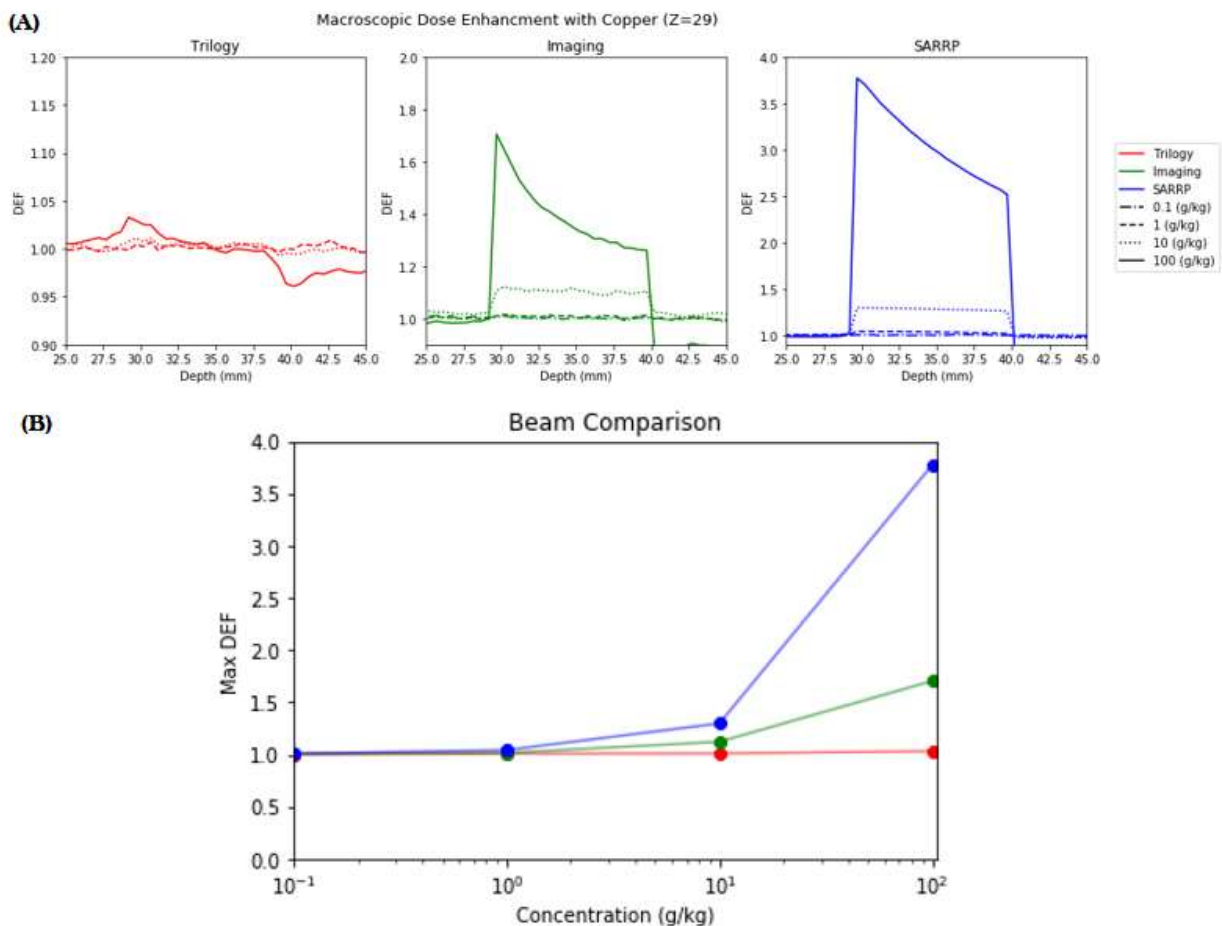


Figure 2.12 – Dose enhancement evaluation of copper ($Z = 29$) by concentration. The dose enhancement factor as a function of depth is shown in (A) for each of the beam model irradiations. Concentrations below 0.1 g/kg resulted in below 1% dose enhancement in all cases. A summary of the maximum DEF by log concentration is shown in (B), with comparisons of the beam models.

The data indicate that copper can be used as dose enhancer with each radiation source. SARRP beam irradiation resulted in the highest DEF with substantial values ($> 10\%$) for concentrations down to 10 g/kg, a maximum DEF of 3.8 at 100 g/kg, and discernible ($> 1\%$) DEF down to 0.1 g/kg. Trilogy irradiations resulted in a maximum DEF of 1.03 with 100 g/kg, and no discernible dose enhancement below 10 g/kg. The Imaging beam resulted in intermediate DEF between the SARRP and Trilogy models. The DEF was substantial for concentration down

to 10 g/kg, discernible down to 0.1 g/kg, and a maximum DEF of 1.7 for 100 g/kg. DEF was calculated for gold using the same techniques (Figure 2.13).

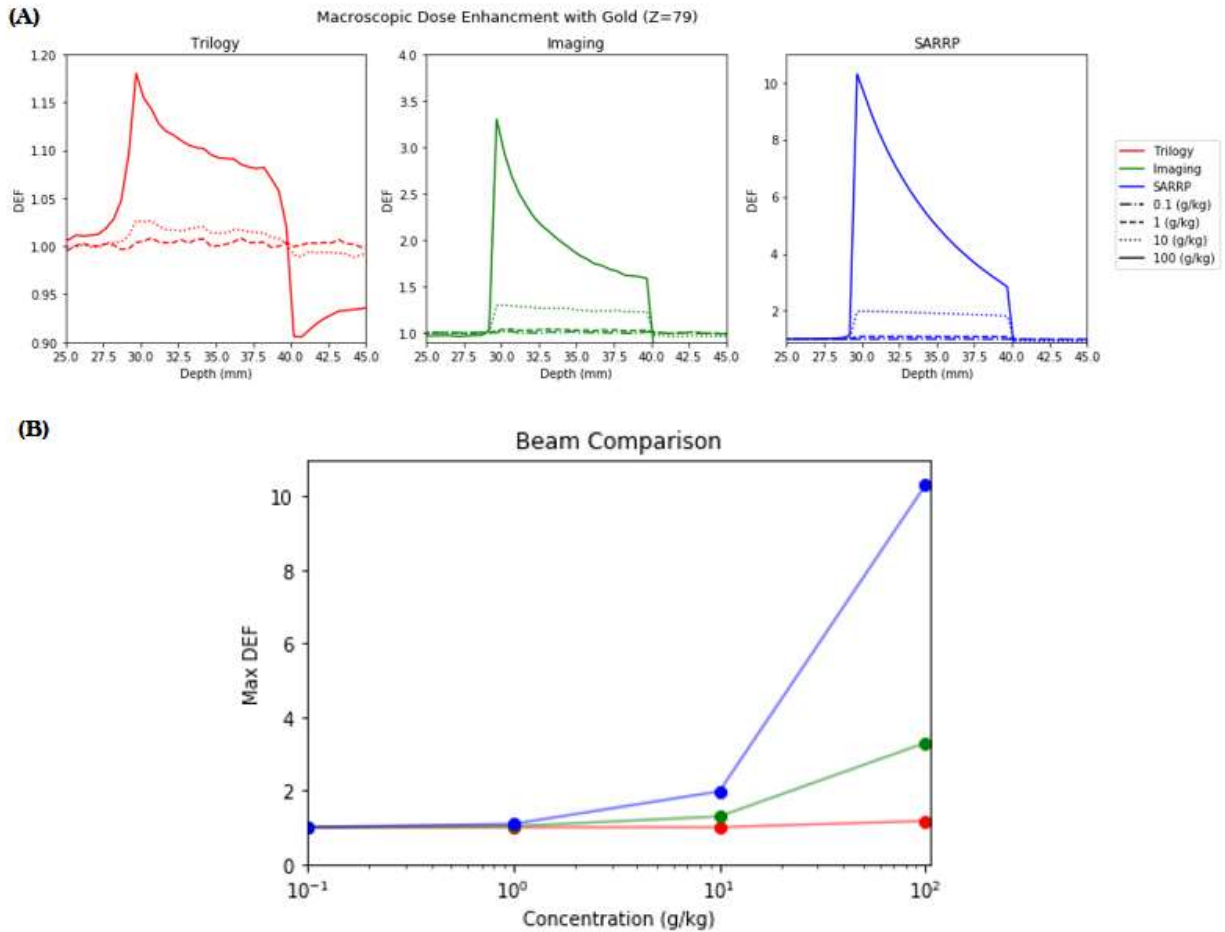


Figure 2.13 – Dose enhancement evaluation of gold ($Z = 79$) by concentration. The dose enhancement factor as a function of depth is shown in (A) for each of the beam model irradiations. Concentrations below 0.1 g/kg resulted in below 1% dose enhancement in only the Trilogly case, but lower concentrations are not presented to be consistent with copper. A summary of the maximum DEF by log concentration is shown in (B), with comparisons of the beam models.

Gold is a well-known radiosensitizer and resulted in dose enhancement for each radiation source. Irradiation with the SARRP beam resulted in the highest DEF with substantial values for

concentrations down to 1 g/kg, a maximum DEF of 10.4 at 100 g/kg, and discernible DEF below 0.1 g/kg.

Trilogy irradiations resulted in a maximum DEF of 1.18 with 100 g/kg, and discernible dose enhancement down to 0.1 g/kg. Irradiation with the Imaging beam resulted in intermediate DEF between the SARRP and Trilogy models. The DEF was substantial for concentration down to 10 g/kg, discernible DEF down to 0.1 g/kg, and a maximum DEF of 3.3 with concentration of 100 g/kg.

Maximum DEF values are found at the front side of the slab with a decrease in dose deposition deeper within the slab. The DEF is below unity within the water phantom beyond the slab due to photon depletion. In all cases, the dose enhancement is greater in gold than in copper for equal concentrations. The SARRP beam resulted in the largest differences by concentration, and the Trilogy resulted in the smallest differences. DEF were additionally calculated for silver and gadolinium and reported in Appendix (A.7). Maximum DEF evaluations of these metals indicate a relationship between atomic number and dose enhancement (Figure 2.14). The maximum DEF was also evaluated for the same metals with the Imaging beam (Appendix A.8).

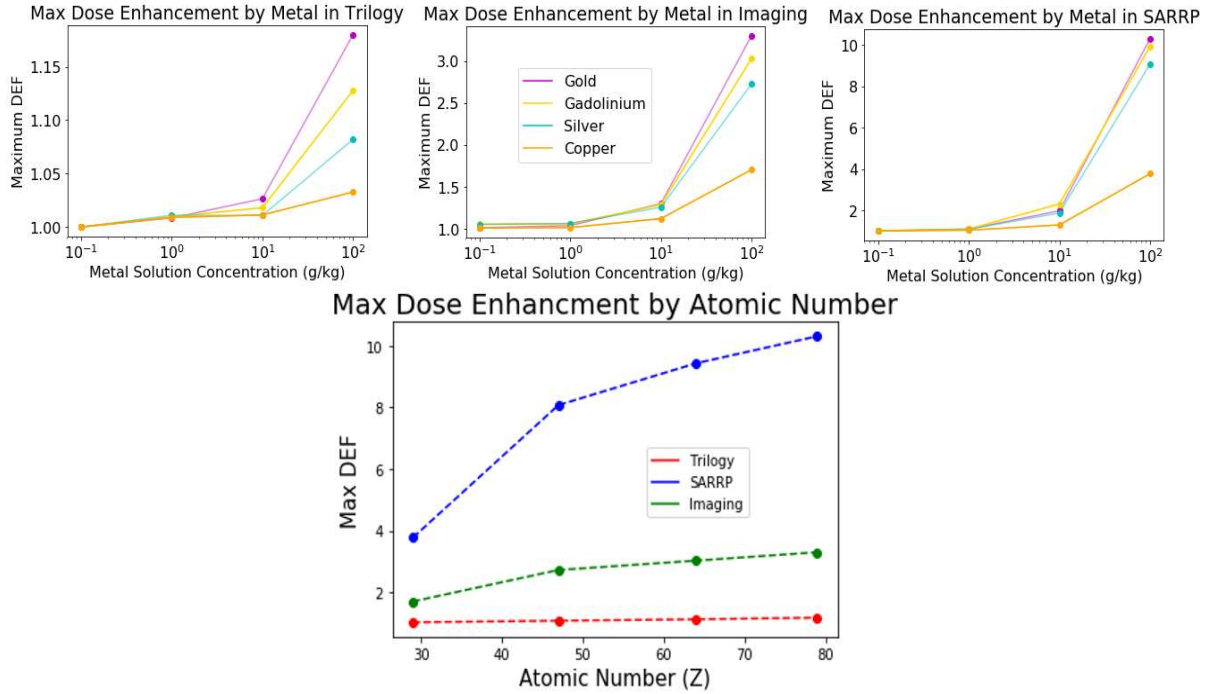


Figure 2.14 – Maximum dose enhancement comparison of four metals (copper, silver, gadolinium, and gold). (A) Concentration range from 0.1 to 100 g/kg. (B) Maximum DEF as a function of atomic number (Z) indicates for each beam model that DEF increases with Z.

Dose Enhancement with Depth in Phantom

As noted in Section (2.5), dose in a phantom decreases with depth relative to the maximum. This decrease is primarily the result of photon attenuation in the phantom, and low energy photons are attenuated more than high energy photons because of the photoelectric effect (Equation 1.8). This phenomenon is known as beam hardening, and is a common source of artifacts in diagnostic imaging [194]. Dose enhancement with metals is the result of metal particles interacting with primarily low energy photons, and at increasing depths in a phantom, there will be fewer low energy photons. In order to evaluate the effects of beam hardening on dose enhancement, the metal solution layer from the previous phantom (Figure 2.11) was moved

to different depths within the phantom and irradiation modeled with beam phase space files of at least 10^9 histories (Figure 2.15).

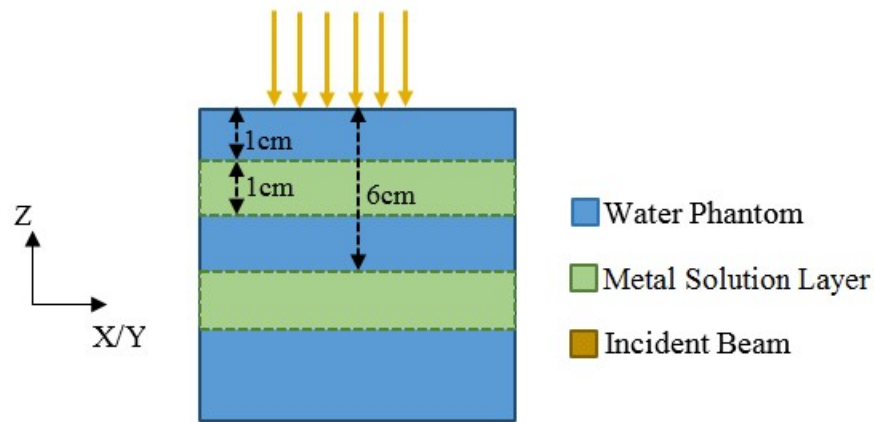


Figure 2.15 – Geometry for dose simulation with metal solution layer at increasing depths (not to scale). Metal solution layer is 1 cm thick in Z and extends the range of the phantom in X/Y.

A copper metal solution layer with concentration 100 g/kg was moved from 1 cm to 6 cm from the beam face of the phantom. Results are presented in Figure (2.16), with water Dmax normalized PDD, to show the effect of depth on dose. For the Trilogy model, the dose from metal solution layers at depths from 2 cm to 6 cm are shown, because the 1 cm depth overlapped Dmax.

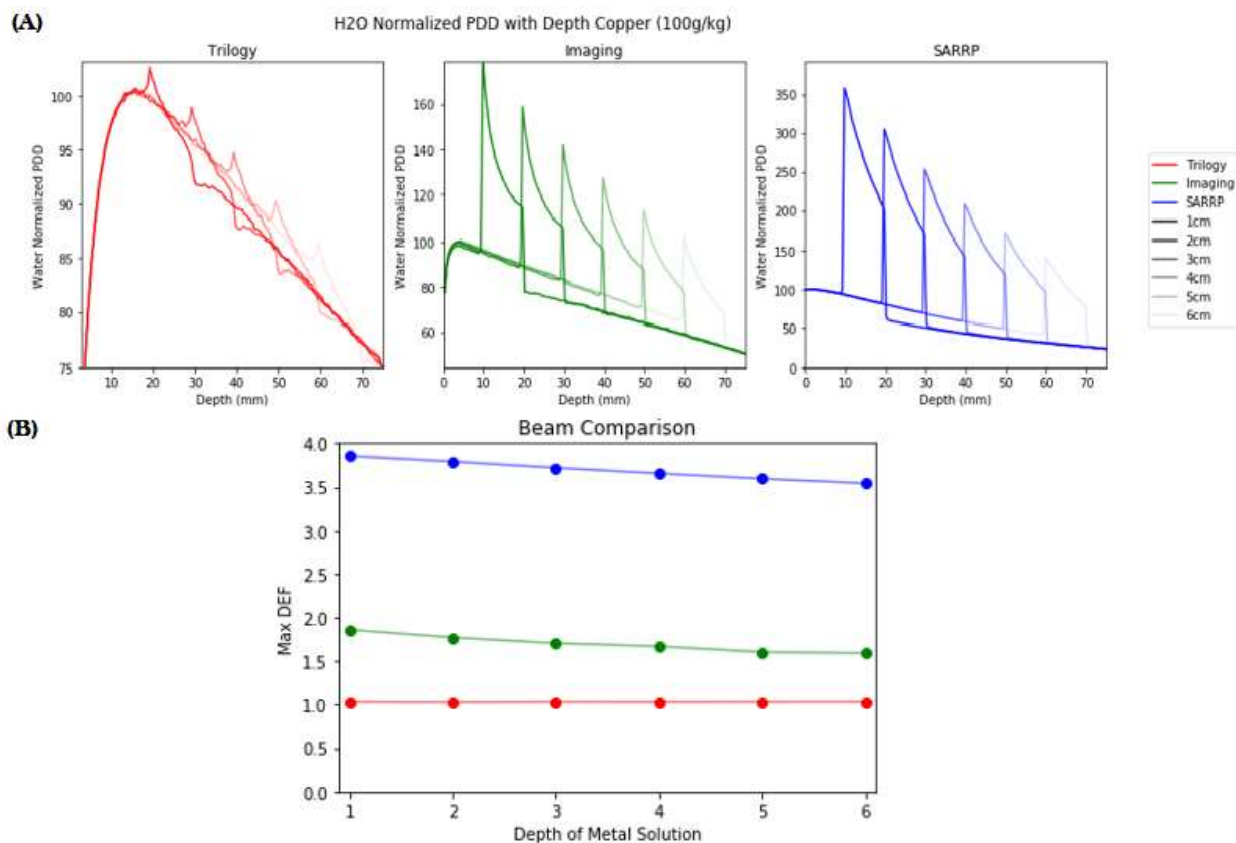


Figure 2.16 – Evaluation of maximum DEF for a copper solution layer (concentration 100 g/kg) at increasing depths within a water phantom. (A) Water Dmax normalized PDD for each depth. (B) Maximum DEF for each beam model as a function of depth.

Dose enhancement with copper was reduced with increasing depth in the phantom. The SARRP beam resulted in the largest reduction in dose enhancement of 31% between the depths of 1 cm and 6 cm. The Trilogy beam resulted in the smallest change; 0.5% reduction in maximum DEF between 2 cm and 6 cm depths. The Imaging beam had intermediate reduction to the other beams, with a decrease of 11% from 1 cm to 6 cm depths. The effect of depth when using gold was also analyzed (Figure 2.17).

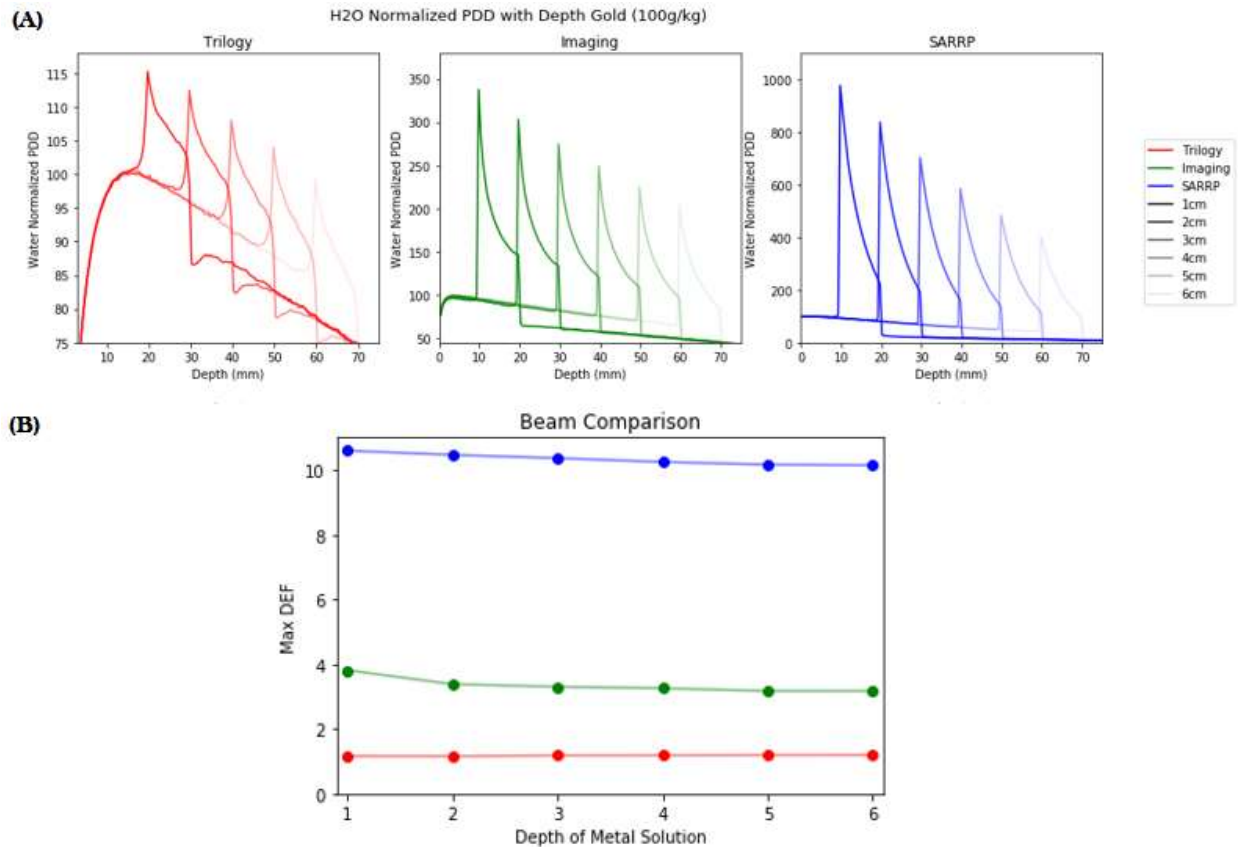


Figure 2.17 – Evaluation of maximum DEF for a gold solution layer (concentration 100 g/kg) at increasing depths within a water phantom. (A) Water Dmax normalized PDD for each depth. (B) Maximum DEF for each beam model as a function of depth.

There was a reduction in the maximum DEF with gold with each beam energy. The largest decrease was found with the SARRP beam; a decrease of 35% was observed. The Trilogy beam was reduced the least, with a 1% decrease in maximum DEF. An intermediate effect was observed for the Imaging Beam with a 23% decrease. Silver and gadolinium metal solution layers were evaluated at the same range of depths, and the data are provided in Appendix (A.9).

The results of reduced dose enhancement with increasing depth correspond to the spectral data in Figure (2.7). Recall, that the Trilogy beam is the spectrum with the highest energy range, and a maximum photon energy of 6 MeV. The small reductions in DEF observed in the Trilogy

beam can therefore be attributed to the relatively minor reduction in photon fluence, that also makes this beam type suitable for treatments of deep tumors. The Imaging beam resulted in decreases in maximum DEF with depth that were intermediate in value between the Trilogy beam and the SARRP beam. The spectrum of the Imaging beam peaked at an energy below the peak of the SARRP beam; the range of energies, however, was greater than the SARRP spectra and extended to 2.35 MeV. The SARRP beam was the spectrum with the lowest energy range and a maximum photon energy of 225 keV.

It is therefore predictable that the SARRP beam would have the largest reduction of photons with depth and therefore the largest reduction in DEF with depth. The value of maximum dose enhancement, however, was larger than those of the Imaging or Trilogy beams, even at depths of 6 cm. The reduction of dose with depth in the SARRP beam will considerably reduce the tumors that could be treated by this modality, despite its ability to amplify dose. This concept will be evaluated more fully in Chapter 3.

2.7 – Electron Spectra Enhancement with Metal

Recall from Section (1.1), that photon radiation deposits dose in media indirectly; by creating electrons which interact directly with the atoms in media. Dose enhancement is intricately tied to the increase in electron yield by metal particles interacting with photons through the photoelectric effect. The previous section explored the dose enhancement resulting from photon beams interacting with metal solutions. The MC code calculated the creation of secondary electrons as photons interacted within media, then calculated the energy depositions in the media to output dose. The DOSXYZnrc base code however, does not output information about the electrons that were created.

FLURZnrc, is an EGSnrc toolkit for calculation of fluence of different particles in cylindrical geometry. The toolkit was used to evaluate the increase in electron yield resulting from a metal solution layer. The simulations use the same EGSnrc physics and libraries as were used with BEAMnrc and DOSXYZnrc. The simulations enumerate the secondary electrons created from the photon beams created in Section (2.5). Secondary electrons in this simulation did not include the knock-on electrons from Moller events and any secondary particles that these electrons may set in motion. Example is provided in Appendix (A.10).

A cylindrical phantom with radius 15 cm divided into consecutive cells of 5 cm and total height of 8 cm was created with three concentric regions consisting of water and metal radiosensitizer solution each with resolution of 0.5 mm in the depth (Z) direction. The phantom was composed of water material for 2 cm proximal to the beam side, followed by a 1 cm slab of metal solution with 100 g/kg concentration, and finally a 5cm water slab completed the phantom. The model is equivalent to that used in the dose enhancement simulations (Figure 2.11). The spatial extent in both X/Y dimensions (30 cm diameter) is greater than the diagonal of the largest beam field (~28.3 cm) used for simulations, and the depth (8 cm) is the same as that used in the dose enhancement model.

Electron fluence was measured as a function of depth within the phantom for each beam phase space file using at least 10^9 histories. Values of electron fluence with copper and gold metal solution layers are normalized to the maximum value in water (Figure 2.18).

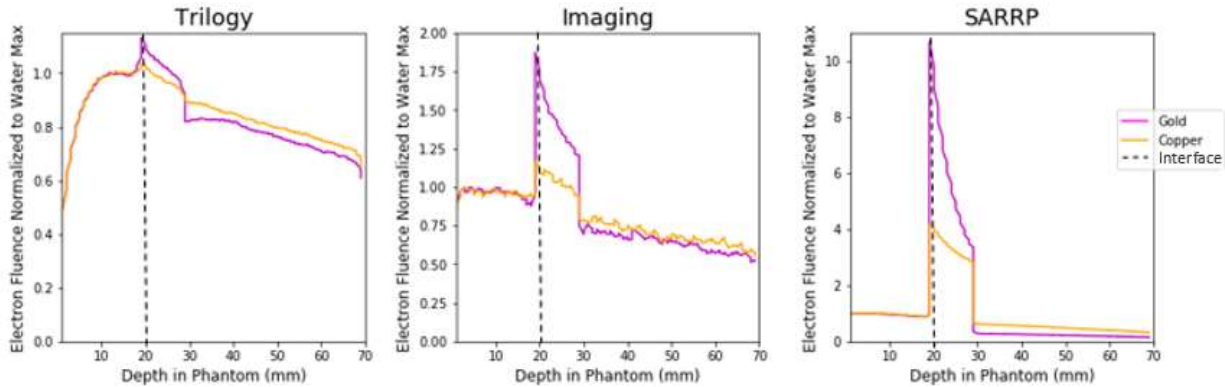


Figure 2.18 – Electron fluence as a function of depth in phantom with metal solution layer at between 20 mm and 30 mm. Three photon beams are evaluated for amplification of electron yield. Dotted lines denote the evaluation at 20.5 mm; the interface between metal solution and water.

The electron fluence yield with a metal solution phantom closely mirrors that of dose deposition (Figures 2.12-2.13), indicating a high level of correlation between electron fluence and dose.

The electron spectra provide insight into the electron energies that are created from the interaction of photons with the metal solution. The spectra are measured at 20.5 mm deep within the phantom; the interface between the first water layer and the metal solution layer where the amplification of electron yield in metal solution is highest (Figure 2.18). The electron yield is measured and binned into 200 equally spaced energy windows up to the maximum for each beam. Each value is normalized to the energy window with maximum yield in water (Figure 2.19A). Yield is also collected for low energy electrons up to 30 keV. Data are presented in 1 keV energy bins and normalized to the fluence yield in water for the same beam energy (Figure 2.19B).

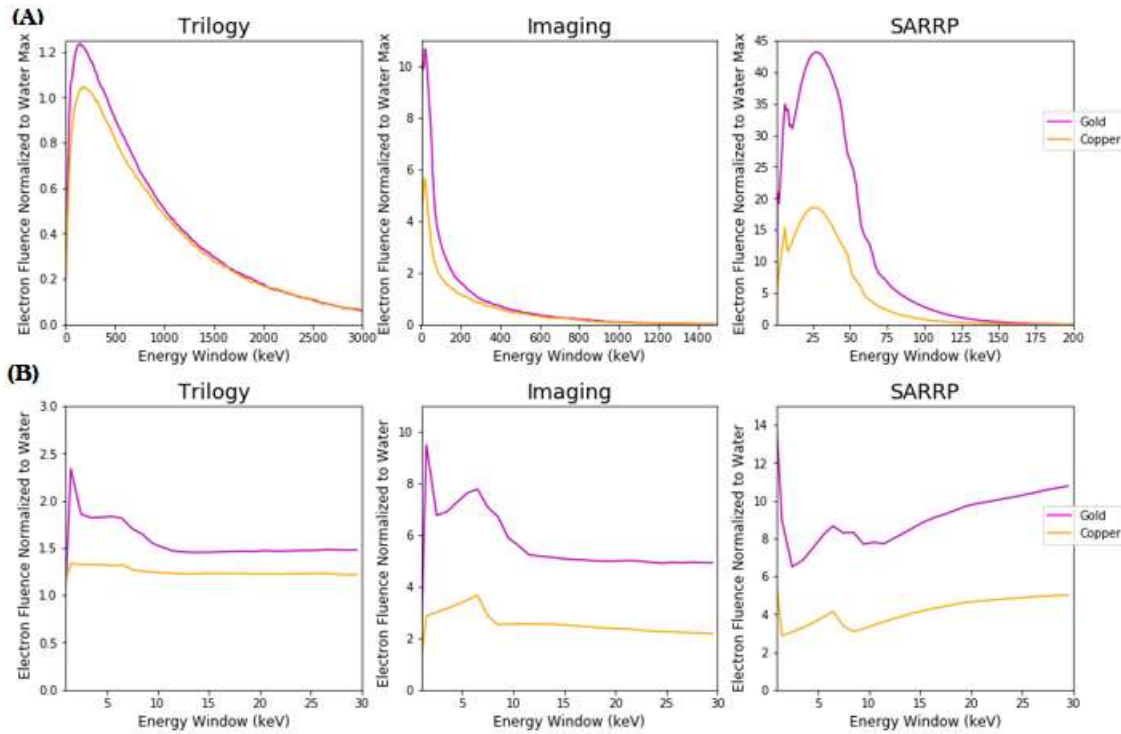


Figure 2.19 –Three photon beam models are used as the input to evaluate electron yield amplification in metal solution layer. (A) Electron yield binned into 200 equally spaced energy windows to maximum energy. Fluence is normalized to the highest yield energy window in water. (B) Yield for low energy electrons up to 30 keV binned in 1keV energy windows. Fluence in metal solution is normalized to water in each energy bin.

Copper and gold metal solution layers both resulted in increased electron yield when irradiated, thus validating the notion that dose amplification is connected to a similar amplification in electron yield. Low energy electrons are the most frequently created with all beam types and metals.

Recall that the photoelectric effect is the mechanism responsible for increasing electron yield with metals, and that the effect is most probable at low photon energies (Equation 1.8).

$$\frac{\tau}{\rho} \propto \left(\frac{Z}{h\nu}\right)^3 \quad (cm^2/g) \quad (1.8)$$

Electrons created through the photoelectric effect cannot have greater energy than the photon that created them, and therefore, the amplification of low energy electrons more than high energy electrons with metal solutions is expected. The electron yield was also calculated for silver and gadolinium; those results are presented in Appendix (A.11). The methods developed here will be of critical importance when transitioning to a microscopic model in Chapter 5.

Photoelectrons and Emission of Auger Electron/Fluorescent Photon upon Atomic Relaxation

The FLURZnrc toolkit allows the user to enumerate the electrons created in an area of interest, which can be useful in evaluating the energy spectra of electrons. The code however, does not intrinsically report the origin of the electrons that were created. Recall from Section (1.4), that Auger electrons play a pivotal role in explaining the efficacy of metals as radiosensitizers.

Auger electrons have been shown to cause highly damaging high-LET injury to DNA. Auger electrons are the result of atomic relaxation of an excited atom. An atom may become excited by radioactive decay, or by emitting one of the electrons from an inner electron shell by photoelectric interaction. The emission of an inner-shell electron results in a vacancy that is filled by an electron from an outer-shell and releasing energy in the processes. Often the energy is released as a fluorescent photon, but it can also be transferred to another outer-shell electron resulting in the ejection of that electron (Auger) from the atom. The outer-shell that was vacated for the electron to enter the inner-shell will subsequently be filled by an electron at a higher energy, resulting in a cascade of relaxations and emissions.

The probability for an Auger electron emission compared to a fluorescent photon is higher with lower ($Z < 33$) atomic number elements (Figure 1.6). To investigate the yield of

Auger electrons from metal, the MORTRAN code of the DOSXYZnrc toolkit was altered to tag origin of electrons and photons that are produced in a simulation. While it is possible to tag numerous physical phenomenon in a simulation, in this case the code was designed to tag photoelectric events, Auger electron creation, and fluorescent photon creation. A uniform phantom containing metal solution (100 g/kg) was created with the same dimensions as the previous examples. Irradiation by the beam sources (10^6 histories) from Section (2.5) were modeled in the phantom, and electrons or photons with specified characteristics are tagged and recorded. The energy and origin of electrons are enumerated and plotted in histograms to compare the number of low energy electrons created in each metal. The results for copper metal are shown in Figure (2.20).

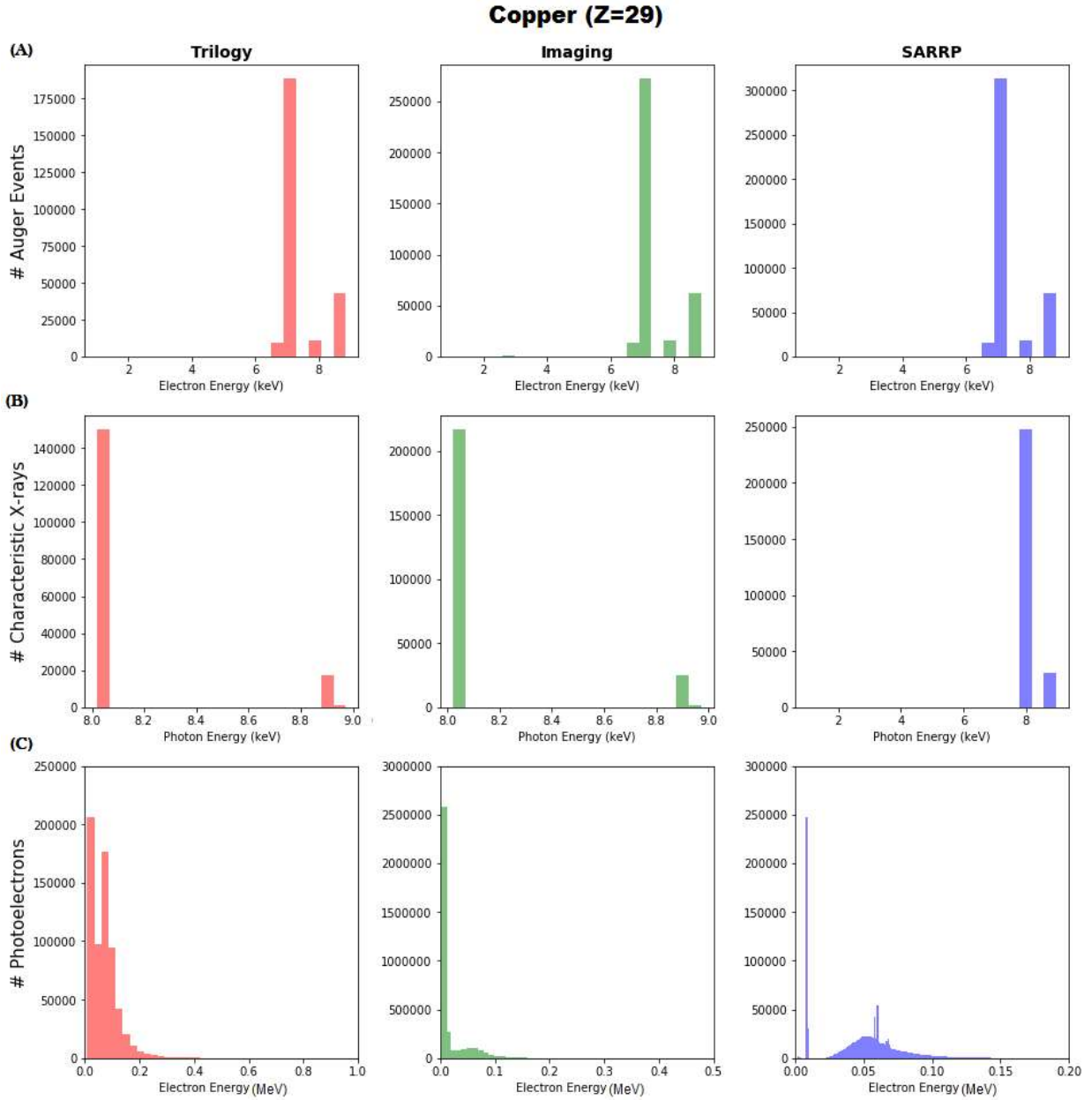


Figure 2.20 – Electron and photon origin tracking with modified DOSXYZnrc code 10^6 histories. (A) Number of Auger electrons enumerated by energy in copper solution phantom. (B) Fluorescent photons with the same simulation parameters as (A). (C) The energy spectrum of electrons produced from photoelectric interactions. Auger electrons and fluorescent photons are likely the result of photoelectric events.

The resulting energies of photoelectrons were plotted in a histogram with 200 equally spaced energy bins. The energies span depends on the beam input, with the Trilogy beam the energy

ranged from 1 keV to 1 MeV, while in the Imaging and SARRP the energy ranged to 500 keV, and 200 keV respectively. The SARRP beam also resulted in the highest yield of photoelectrons with Imaging and Trilogy having decreased yield. Auger electron and fluorescent photon emission occur in discrete energy units associated with the energy difference between electron shells. The energy of electrons was plotted in a histogram with 20 equally spaced energy bins. The energy windows for electron and photon emissions were the same for all three beams. With both Auger electrons and fluorescent photons, the yield was highest with the SARRP beam and decreased in the Imaging and Trilogy beams. The data for silver, gadolinium, and gold were calculated and are presented in Appendix (A.12). It is informative to compare the Auger emission yield of copper to gold. Gold ($Z = 79$), will interact more with photons of higher energy in photoelectric events causing more excited atoms, however, recall from Section (1.4) that when gold atoms relax to a lower energy state, they are more likely to result in the emission of fluorescent x-rays than Auger electrons. Copper ($Z = 29$), is less likely to interact by photoelectric interactions, but excited electrons in copper are more likely to result in the emission of Auger electrons upon relaxation (Figure 1.6). Although there is a relatively modest yield of Auger electrons from the K-shell (~ 80.7 keV) of gold, subsequent electron relaxations from higher energy shells can also result in Auger electron emissions at lower energy (Figure 2.21).

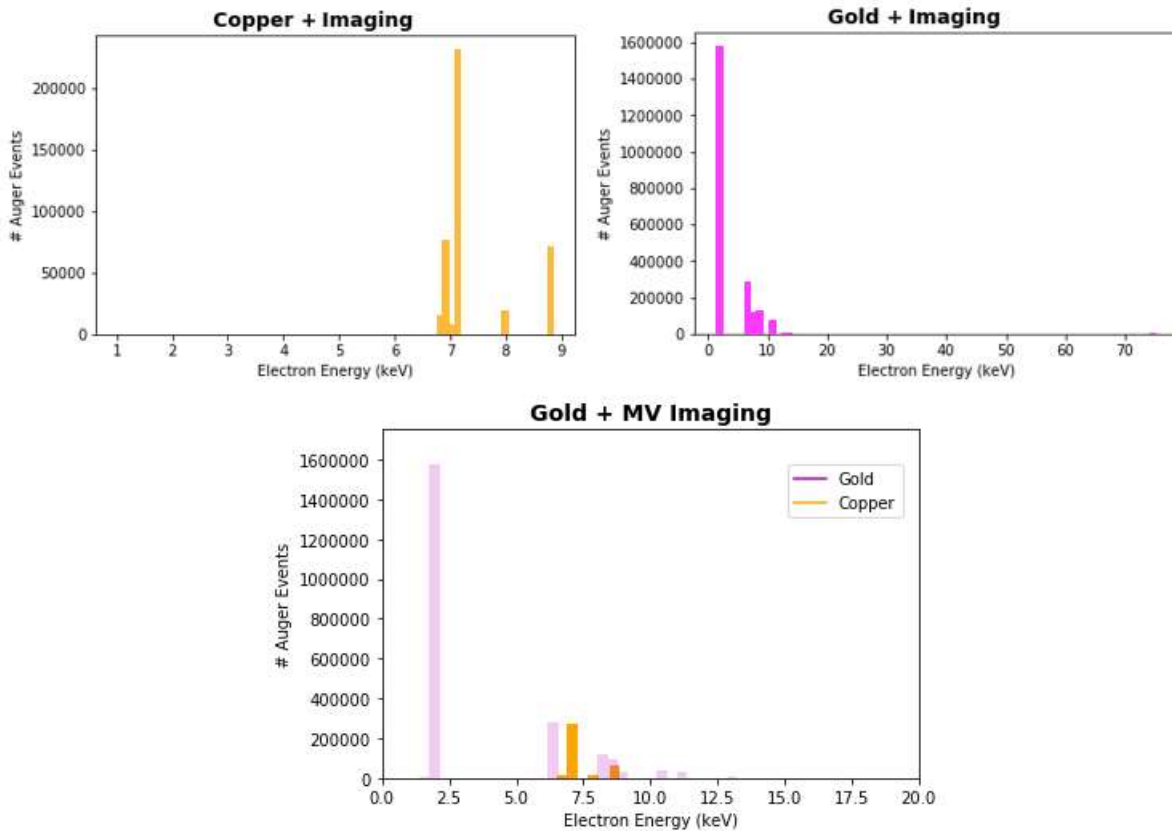


Figure 2.21 – Comparison of Auger emission from gold and copper. Gold results in higher energy Auger electrons, a greater range of emissions, and a greater total yield above 1 keV.

The comparisons were made with the Imaging beam, although the results are consistent with each beam. The results indicate that the total yield of Auger electrons in gold is higher than that of copper. Gold also results in a larger range of Auger electrons energies and contains emissions of both lower and higher energy Auger electrons than copper. The probability for K-shell Auger emissions is significantly higher for lower atomic number elements (Figure 1.6). Outer shells (L, M, N, etc.), also have higher probability of Auger emissions for lower Z, however, the probability for Auger emission is more uniform for higher atomic number elements (Figure 2.22).

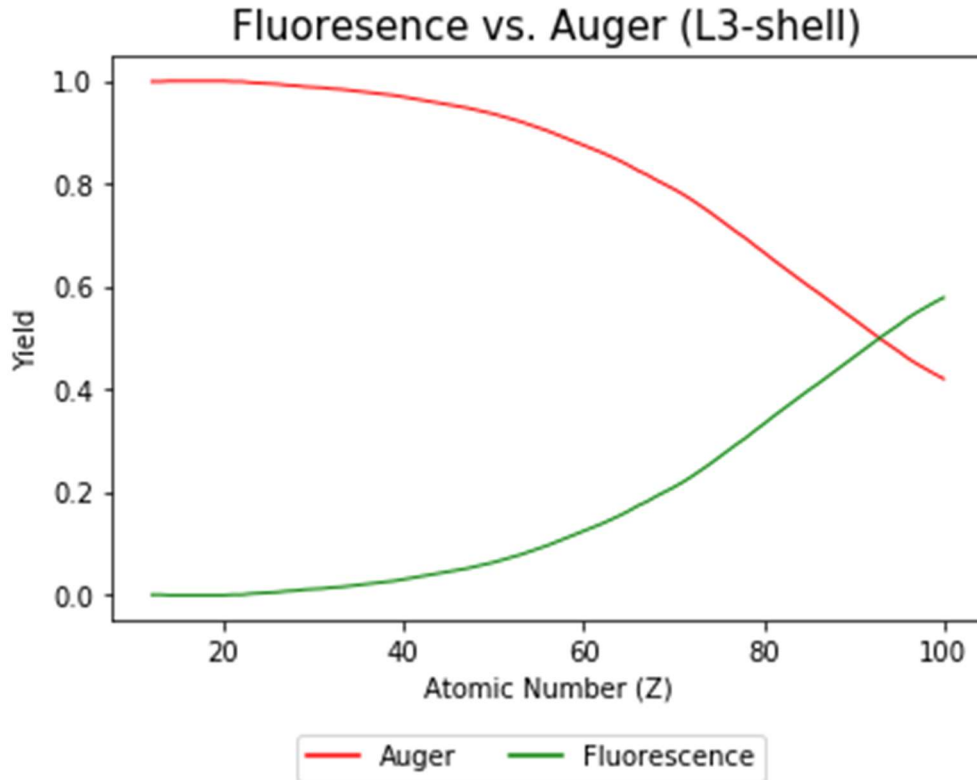


Figure 2.22 – Fluorescence vs Auger electron yield from the L3-shell. Contrast with Figure (1.6), in K-shell the probability of Auger emission is much greater for low-Z than high-Z elements. In the L3-shell and other outer shells the probability of Auger emission is more consistent across Z.

The greater number of excited atoms combined with the greater number of electrons in higher energy shells results in greater Auger electron yield for gold. Additionally, EGSnrc only tracks electrons down to 1 keV; and copper has substantial yield from the sub keV threshold that cannot be accounted for with this MC package. The limitations that a 1 keV threshold sets on dose enhancement calculations will be explored more fully in Chapter 5.

2.8 – Discussion

Dose enhancement is a valuable metric for analyzing the radiosensitization potential of high-Z materials. While radiosensitization can be achieved through several mechanisms, with

metals an important facet to their efficacy is to physically increase dose. The aim of this chapter was to answer the question: *Can copper be used to enhance dose*. From the analysis it is clear that the answer is yes, and further: that it is concentration dependent, that it is affected by depth of irradiation, and that it is the result of an increase in electron yield. The models in this chapter serve to establish a foundation that may better inform clinicians and the scientists about the potential of copper in enhancing radiation therapy. However, throughout the course of these investigations, additional questions about the use of CuATSM as a radiosensitizer presented themselves. It will be the goal of the remainder of this dissertation to more clearly evaluate the potential of CuATSM as a radiosensitizer.

Primarily, the results indicated that for substantial dose enhancement to occur with copper solutions, the concentration would need to be at least 0.1 g/kg, and may necessitate the use of orthovoltage, a modality that is ill-suited for large tumors. Thus the subsequent investigation, initiated by these observations, will evaluate the following: *Can CuATSM be used to deposit copper at a sufficient concentration to result in dose enhancement?* and *Can orthovoltage x-rays, when combined with copper as a dose enhancer, be used to treat hypoxic regions in large tumors?*

Special thanks to Dr. Thilakshan Kaneshalingam and the Research and Development team at Xstrahl for providing EGSnrc models and schematics for the Small Animal Radiation Research Platform and Dr. Dave Parsons and Dr. James Robar, for models of the MV imaging carbon graphite target linear accelerator modification.

CHAPTER 3

CuATSM DOSE ENHANCEMENT IN HYPOXIC TUMOR MODEL WITH ORTHOVOLTAGE TREATMENT

3.1 – Introduction

Hypoxia is a prominent feature of solid tumors, resulting from the decrease in oxygen due to rapid consumption by tumor cells and vasculature deficiencies. The efficacy of radiotherapy utilizing x-rays to treat tumors, is decreased when hypoxia is present (Figure 3.1).

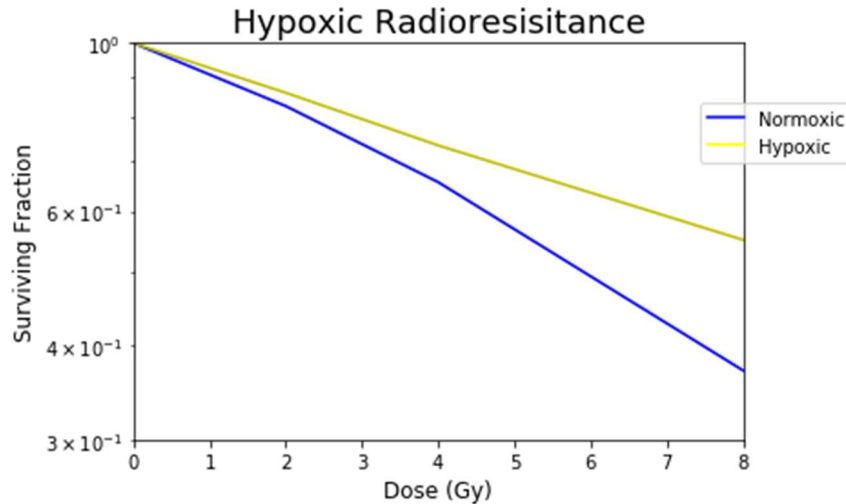


Figure 3.1 – Hypoxic cell survival with irradiation. Hypoxic conditions increase the number of surviving cells compared to normoxia.

In fact, hypoxia is one of the most important causes for x-ray therapy failure [222-224].

Although hypoxia can act as a major impediment to radiation therapy, it is an identifiable physiological difference between tumor and normal tissue and can be an attractive treatment target [156]. Knowledge of the hypoxia state of the tumor allows for prediction of outcome and patient selection for hypoxia modifying treatment [119].

Dose enhancement to hypoxic tissue is a goal of radiosensitization using metals. The prominent research using metal radiosensitizers has focused on nanoparticles, and although they have shown efficacy in improving radiotherapy outcomes in hypoxic tumors, they are limited in targeting hypoxic tissues by their size [107, 225]. Copper has previously been shown to act as a radiosensitizer of hypoxic cells [135]. In Chapter 2, it was confirmed that copper can act as a dose enhancer with high concentrations (> 0.1 g/kg). Dose escalation using metal radiosensitizers has been shown to result in the largest enhancement when treatment is combined with low energy photon beams, due to the increased probability for photoelectric interaction at low energy [67, 135]. As a confirmation, models of the SARRP and a MV Imaging beams, with lower photon energy spectra, were shown to have higher dose escalation when paired with metals than conventional 6 MV treatment (Chapter 2).

The practicality of using a low energy external beam is generally limited to shallow treatments; deeper treatment would require higher MV energies [67, 137]. The phantom models in Chapter 2, identified decreased dose enhancement related to depth. The decrease in maximum dose enhancement was more substantial for low energy spectra because of substantial low energy photon fluence reduction at depth caused by beam hardening. Large tumors, which often have significant regions of hypoxia, would generally be untreatable with low energy spectra, as substantial dose would be deposited in surface tissue.

The aim of this chapter, therefore, is to evaluate the following questions posed from the outcome of the investigation in Chapter 2: *Can CuATSM be used to deposit copper at a sufficient concentration to result in dose enhancement?* and *Can orthovoltage x-rays, when combined with copper as a dose enhancer, be used to treat hypoxic regions in large tumors?*

To investigate those questions, a simple hypoxic tumor model will be created with EGSnrc, and values from literature will be used to create materials corresponding to the uptake of metals in hypoxic and normoxic tissues. The copper deposited by CuATSM will be compared to gold deposition by GNP.

Orthovoltage Arcs

Arc therapy has been used to improve MV radiotherapy treatment [226]. Arc therapy works by irradiating a patient from multiple angles that combine to form a continuous arc around the patient. This technique increases the conformality of high dose on target areas, and decreases maximum dose to delicate non-target areas by dispersing the dose throughout the body. This technique will be evaluated with orthovoltage arcs over small surface areas to decrease the surface dose and escalate dose in target areas within large tumors.

Recall from Section (1.8), that radioactive CuATSM has been used as a target for dose painting. Areas identified as hypoxic by PET received a boosted dose, as a supplement to the dose covering the bulk of the tumor. Following this strategy, orthovoltage arcs will be used as a supplemental hypoxic boost to a standard (6MV) treatment. The photon energy used for this fluence amplification will also result in dose enhancement with metal, and therefore, this technique can be called energy painting.

An evaluation of this concept will be tested with a simulated treatment plan of a canine osteosarcoma tumor (OSA). Tumors of this origin can become large, and are likely to have a substantial volume of tissue under hypoxic conditions. These tumors often arise in extremities and therefore, there is a decreased risk of irradiating most critical organs in the torso. A group of dogs with osteosarcomas were previously imaged with $^{64}\text{CuATSM}$ at the Colorado State

University Veterinary Teaching Hospital (VTH). The image dataset was imported into two treatment planning systems: Varian Medical Systems Eclipse v11 (Eclipse) and Precision X-ray Irradiation (PXi) Small Animal Radiation Therapy (SmART) Advanced Treatment Planning (ATP) System (SmART-ATP). Eclipse was used to predict dose from an irradiation to the bulk tumor with 6 MV radiation, and SmART-ATP was used to predict the boost dose with orthovoltage. The two treatment planning systems differ by their method of dose calculation. Eclipse uses a 3D pencil beam convolution-superposition algorithm called Analytical Anisotropic Algorithm (AAA) for dose calculation [227]. SmART-ATP uses a Monte Carlo (MC) solution to predict dose based on the EGSnrc software.

3.2 - Monte Carlo Dose Prediction Compared to Analytical Models

All treatment planning algorithms make approximations in order to account for the intrinsic lack of information in estimating resultant dose. Prior to computer assisted treatment planning, dose calculations were done using hand-calculations based on measurements of coefficients from beam data [229]. Later, computers enabled the use of pencil beam scattering kernels to improve the predictive dose, but still required approximations of the media within an electron-density adjusted matrix corresponding to the anatomy of the patient [228, 231]. Currently, most modern clinical dose prediction software uses convolution-superposition techniques to calculate dose within a uniform water phantom, and approximations are made to account for inhomogeneities [232]. Numerical techniques have emerged as valuable alternatives to analytical dose calculations. The Boltzmann transport equation is the exact description of the macroscopic behavior of radiation particles interacting with matter, but is generally unsolvable analytically [330]. Linear Boltzmann algorithms iteratively solve a simplified version of the equation by discretization of physical parameters [331]. Linear Boltzmann algorithms offer the

most accurate dose prediction aside from Monte Carlo, which is considered too time consuming at the current state of computational performance.

Monte Carlo simulation is a numerical method that is unique from analytical algorithms in that it simulates the way nature transports radiation through matter on a particle-by-particle basis [228]. MC calculations are built on fundamental physical interactions, probability distributions, scattering processes, and energy loss [210]. Each MC particle approximates a real radiation particle by sampling values from probability density functions representing physical processes. Modeling numerous particles allows for the averaging of several trajectories to accurately estimate stochastic values such as absorbed dose [201].

Accurate dose information is necessary in radiation therapy as relatively small dose errors of 5% can lead to significant tumor control probability (TCP) changes of 10-20% and even higher normal tissue complication probability (NTCP) changes [240]. Improving the quality of the dose calculation will reduce the overall uncertainty in the delivered dose [233]. MC is the most accurate dose modeling method available, but is still subject to statistical noise. In addition, approximations of geometrical and material properties in beam components and phantoms are sources of error with varying degrees of significance. Uncertainties in absorption probabilities, statistical noise from history number, and computed tomography (CT) data conversion to material composition can also result in systematic errors [242].

Any treatment simulation is composed of a geometrical representation of the patient and surroundings, and the radiation beam incident for treatment. MC has virtually unparalleled versatility in geometry and source definitions [235-236]. Geometrical definitions with MC are generally not limited to treatment scenarios, and complex architectures can be constructed with

CAD or ray tracing software [235]. Furthermore, particles available for simulation include most ionizing and non-ionizing radiation with massive libraries of energy dependent interactions, decay schemes, and fragmentation profiles [236].

In contrast, analytical algorithms are much less flexible, and typically only function with a simple voxelized patient geometry, pre-calculated radiation dose kernel, and pre-calculated or assumed photon fluence and spectra. These simplifications are a requirement because the geometry and radiation need to be represented analytically. Analytical algorithms also have limited capability in calculating non-water interactions with radiation. It is assumed that differences in convolution occur on a voxel by voxel basis based on the changes of electron density corresponding to the Hounsfield unit (HU) value of that voxel, where:

$$HU = 1000 * \frac{\mu - \mu_{water}}{\mu_{water} - \mu_{air}} \quad (3.1)$$

Analytical algorithms compare adequately with MC for homogeneous water calculations, but are significantly affected by different density materials and sharp transitions in density [237].

Furthermore, HU values vary between CT scanners, meaning that dose calculations can be affected by the conversion scale applied to the images [238].

MC simulations in contrast, calculate dose in voxels with atomic composition, providing a more accurate result, however, CT number conversion tables typically do not account for atomic number [242]. In many cases using a MC simulation is preferable to real-world measurements because of the difficulty of making measurements in certain situations, such as small field irradiation [239]. Implementation of the MC method could improve confidence in

dose distributions and lead the field of radiation oncology to deliver higher doses, leading to improved outcomes [243].

Despite the fact that Monte Carlo is the most accurate and versatile method of technique for dose calculation, its wide implementation is limited because of computational time constraints. Ultimately, the required accuracy in treatment planning is determined by the treatment for which it is applied. Analytical algorithms maintain relevance as clinically viable approximations in 3D treatment planning and secondary MU checks [229].

3.3 – Hypoxic Tumor Model

Tumors can have complex geometries and oxygen distributions, however for simplicity, geometric approximations were used in this model. The tumor was approximated by three concentric cuboids, with normal tissue forming the exterior body. The tumor encompassed by the body was composed of normoxic and hypoxic regions. Although tumors are composed of tissue, water is often used as a surrogate for soft tissue because they have similar interactions with photons at low energy [93].

The similar behavior with photons can be attributed to water and soft tissue having approximately the same effective atomic number (~ 7.4), which can be determined from [189]:

$$Z_{eff} = \sqrt[3.5]{a_1 Z_1^{3.5} + a_2 Z_2^{3.5} + \dots} \quad (3.2)$$

Where $a_1 = (f_1 Z_1 / A_1) / \sum_i (f_i Z_i / A_i)$, is the fraction of electrons present in the mixture that belong to atoms with atomic number Z_1 , and f_1 is the fractional weight of that element. The dose was calculated within tissues at various concentrations with different effective atomic numbers (Appendix B.1).

Simple geometrical representations have previously served as tumor models, as they provide a basis for extension to more complex features [76, 120-122]. A cuboidal phantom with dimensions 5cm x 5cm x 5cm (0.5mm resolution), with pure water as base material was used to simulate a simple 125 mm³ tumor with an 8 mm³ hypoxic core with different uptake of metal by oxygen concentration [68, 80, 101, 123] (Figure 3.2).

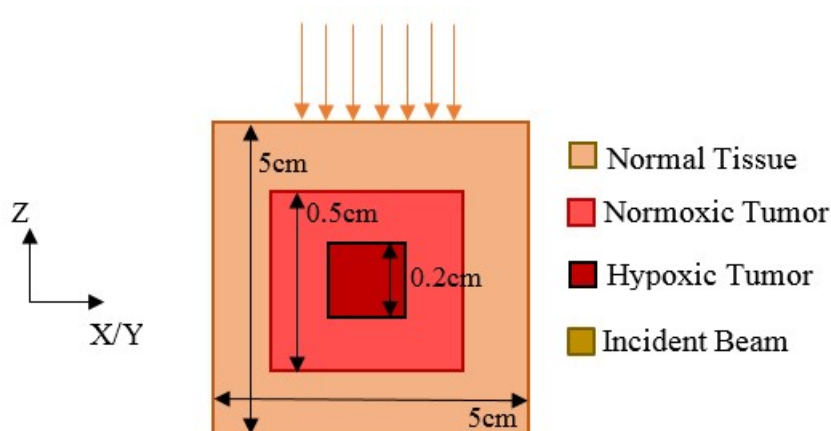


Figure 3.2 – Hypoxic tumor model geometry with phantom representing section of body containing a tumor with normoxic and hypoxic regions.

In all cases, normal tissue, surrounding the simulated tumor was assumed to have zero uptake of radiosensitizing metal. Within the tumor, uptake of gold or copper was determined for normoxic and hypoxic tissue uptake of gold nanoparticle (GNP) and CuATSM, respectively.

For GNP simulations, concentrations were informed by a previous mouse study where 1.35 g/kg (GNP/bodyweight) were injected intravenously and deposited from the circulation into the tumor [125]. In vitro, it was found that GNP uptake into cells was decreased by a factor of approximately 3.4 in anoxic compared to normoxic conditions [67]. In addition, the degree of GNP uptake decreases in volumetric tumors distant from the vasculature due to the low diffusion of GNP in tissue [107, 109, 121]. Under these assumptions, the dose enhancement factor (DEF)

was calculated for a concentration of 1.35 g/kg assuming direct injection into the tumor. Uptake for GNP in the hypoxic region was then evaluated at a decreased concentration (Reduced) for decreased uptake due to anoxic conditions alone, and zero concentration of GNP uptake (Zero) for considerations of cell layer blocking diffusion (Table 3.1).

Table 3.1 – Concentrations of gold (GNP) with initial injection concentration of 1.35 g/kg in normoxic and anoxic tissue.

<i>Hypoxic Uptake</i>	<i>Injection Concentration GNP [g/kg]</i>	<i>Gold Concentration Normoxic [g/kg] (factor)</i>	<i>Gold Concentration Anoxic [g/kg] (factor)</i>
<i>Reduced</i>	<i>1.35</i>	<i>1.35 (1)</i>	<i>0.397 (1/3.4)</i>
<i>Zero</i>	<i>1.35</i>	<i>1.35 (1)</i>	<i>0 (0)</i>

Previous studies using mice with induced tumors found that ⁶⁴CuATSM has a high deposition in over-reduced hypoxic regions of tumor tissue [244]. Additionally, cell models have indicated that uptake of CuATSM is about 9 times greater in anoxic regions than in normoxic conditions for certain cell lines [122]. Studies using non-radioactive CuATSM systemic injections for treatment of motor neuron disease have limited concentration levels at approximately 0.1 g/kg due to the concerns of the toxicity of the CuATSM solvent dimethyl sulfoxide (DMSO) [129 -130]. Copper was assumed to comprise 19.7% by mass of the CuATSM chelate in these simulations [128, 144-145].

Therefore, assuming a direct tumor injection, having the highest potential concentrations, at (0.1 g/kg) concentration of CuATSM (*Low*) yielded a pure copper concentration of 0.18 g/kg

within the hypoxic tumor region, this is taking into account the atomic composition (0.197) and uptake factor (9). It has been found that the lethal dose (LD₅₀) for DMSO is 25 g/kg in subcutaneous injections in mice [131]. With the solubility of CuATSM in DMSO of 15 mg/ml and assuming a density of DMSO of 1.1 g/ml the maximum concentration of CuATSM at this lethal dose would be 0.34 g/kg (*Medium*) [129].

Additionally, initial CuATSM injections of the same concentration (1.35 g/kg) as the GNP model were used (*High*), as well as a very high concentration (*Very-High*) of 6.85 g/kg CuATSM (1.35 g/kg pure copper) to gain insight into how copper would act to enhance dose with the same injection concentration of gold. However, it should be noted that this is a theoretical target concentration, requiring a large volume of DMSO and would require another lower toxicity solvent to achieve this concentration [139] (Table 3.2).

Table 3.2 – Concentrations of copper as deposited by CuATSM with a range of initial injected concentrations, and their simulated uptake in normoxic and anoxic tissues.

<i>Concentration</i>	<i>Injection Concentration CuATSM [g/kg]</i>	<i>Copper Concentration Normoxic [g/kg] (factor)</i>	<i>Copper Concentration Anoxic [g/kg]</i>
<i>Low</i>	<i>0.1</i>	<i>0.0197 (0.197)</i>	<i>0.177 (9)</i>
<i>Medium</i>	<i>0.34</i>	<i>0.0672 (0.197)</i>	<i>0.605 (9)</i>
<i>High (Theoretical)</i>	<i>1.35</i>	<i>0.27 (0.197)</i>	<i>2.39 (9)</i>
<i>Very High (Theoretical)</i>	<i>6.85</i>	<i>1.35 (0.197)</i>	<i>12.1 (9)</i>

The concentrations outlined in Tables (3.1-3.2), were used to create metal solutions in water. The summary of PEGS4 materials is provided in Appendix (B.2).

3.4 – Dose Enhancement with CuATSM or GNP in Hypoxic Tumor

The photon beam SARRP from Section (2.5), was used to irradiate the hypoxic tumor model, as it resulted in the largest amplification of dose when irradiating metal solutions in

Section (2.6). An example input file is provided in Appendix (B.3). The dose enhancement resulting from GNP deposited in hypoxic tumor is provided in Figure (3.3).

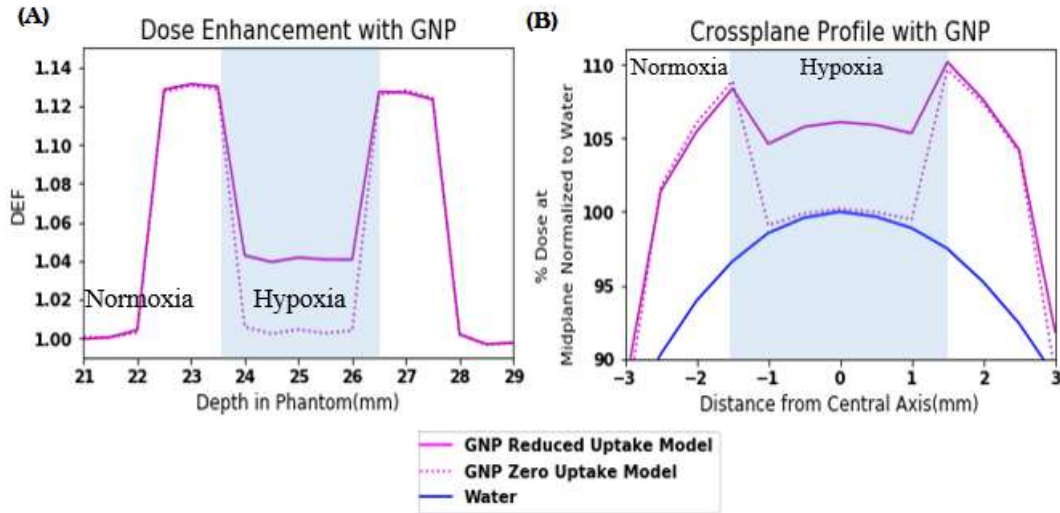


Figure 3.3 – Dose enhancement factor in hypoxic tumor model with GNP. (A) DEF plotted against depth in phantom. (B) Crossplane profile with percent dose normalized to dose at midplane of water.

Both GNP simulations exhibit a DEF of approximately 1.13 within the proximal normoxic tumor region and 1.12 distally, due to photon depletion in the metal solution layer. Within the hypoxic core region, the DEF decreases from normoxic levels for both GNP cases, and is near unity for the zero concentration GNP case. The GNP model with reduced hypoxic uptake has a DEF within the hypoxic region of 1.04. DEF was also evaluated with the CuATSM concentration in Table (3.2), the data are presented in Figure (3.4).

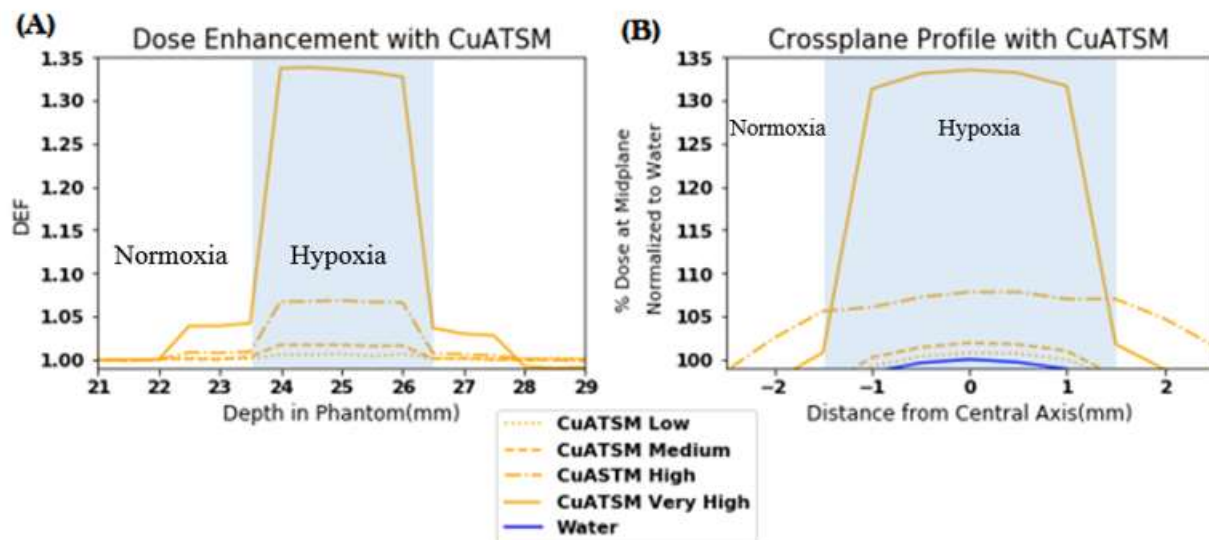


Figure 3.4 – Dose enhancement factor in hypoxic tumor model with CuATSM. (A) DEF plotted against depth in phantom. (B) Crossplane profile with percent dose normalized to dose at midplane of water.

Nearly all the CuATSM simulations show entry and exit DEFs close to unity within the normoxic tumor region, with the exception of the *Very High* concentration case which has a DEF of about 1.04 in the normoxic regions. Within the hypoxic core region, the DEF increases linearly with concentration from about 1.007 in the *Low* concentration case to 1.34 in the *Very High* concentration case.

CuATSM and GNP behave differently in normoxic and hypoxic environments; GNP leads to high DEF in normoxic tissue, but decreased DEF in hypoxia, and CuATSM follows the reverse behavior. Therefore, a combination of the two radiosensitizers will be evaluated as a mechanism for uniformly enhancing dose in tumors. The concentration of copper for which the dose enhancement in hypoxic tissue is equal to the level dose in normoxic tissue using GNP was determined from interpolating DEF values (Table 3.3).

Table 3.3 – Concentrations of copper and gold from a hybrid scenario combining GNP and CuATSM. Copper concentration in anoxia was chosen to match dose with gold in normoxia.

<i>Radiosensitizer</i>		<i>Injection Concentration [g/kg]</i>	<i>Concentration Normoxic [g/kg] (factor)</i>	<i>Concentration Anoxic [g/kg] (factor)</i>
<i>Mix (Theoretical)</i>	<i>CuATSM</i>	2.6	0	4.68
	<i>GNP</i>	1.35	1.35	0

The hybrid scenario, using a combination of GNP (1.35 g/kg) in normoxic tissue, with CuATSM (2.6 g/kg) in hypoxic regions was also evaluated to generate a uniform dose enhancement across the total tumor (Mix) (Figure 3.5).

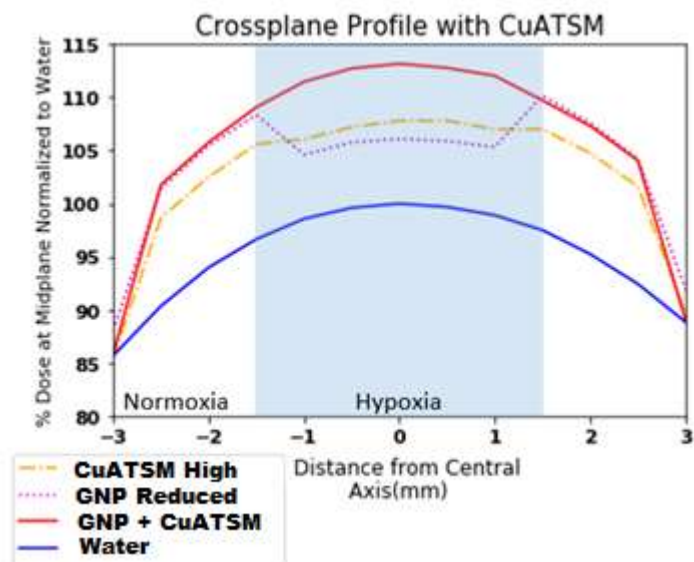


Figure 3.5 – Mixture of GNP in normoxic tissue with CuATSM in hypoxic tissue to create a uniform dose distribution.

An altered version of the Imaging beam with reduced field size by multi-leaf collimator (MLC), was evaluated for dose enhancement using the concentrations of gold and copper outlined in Tables (3.1-3.2); the results are provided in the Appendix (B.4). The Trilogy beam was not considered in these dose enhancement predictions, since Section (2.6) indicated there would be an indiscernible (<1%) enhancement below 10 g/kg. Therefore, dose enhancement with SARRP, at kV energies, in different tissues was solely considered for the CuATSM *High* concentration (Appendix B.5)

3.5 – Orthovoltage Arcs

SARRP is the photon beam spectrum that resulted in the highest dose enhancement for all metals (Section 2.6). The maximum energy of the SARRP beam is 225 keV which is in the orthovoltage range. Recall from Section (3.1) that orthovoltage energies do not penetrate deeply, limiting their application to shallow treatments. Regions of hypoxia often develop within the core of large tumors where vasculature is unable to penetrate.

To evaluate if SARRP could be used to treat small areas of hypoxia deep within tumors, a variation on the tumor model (Figure 3.2) was created and irradiation modeled with different techniques. For this example, the *High* CuATSM injection concentration was considered (Table 3.2). The phantom consists of a cuboidal tumor volume with dimensions 8 cm x 8 cm x 8 cm with normoxic CuATSM uptake. Within the tumor there is a hypoxic core with hypoxic CuATSM uptake and dimensions 6 mm x 6 mm x 6 mm. Water material was added as a 3 mm region to the exterior surfaces of the tumor volume to act as a skin layer (Figure 3.6).

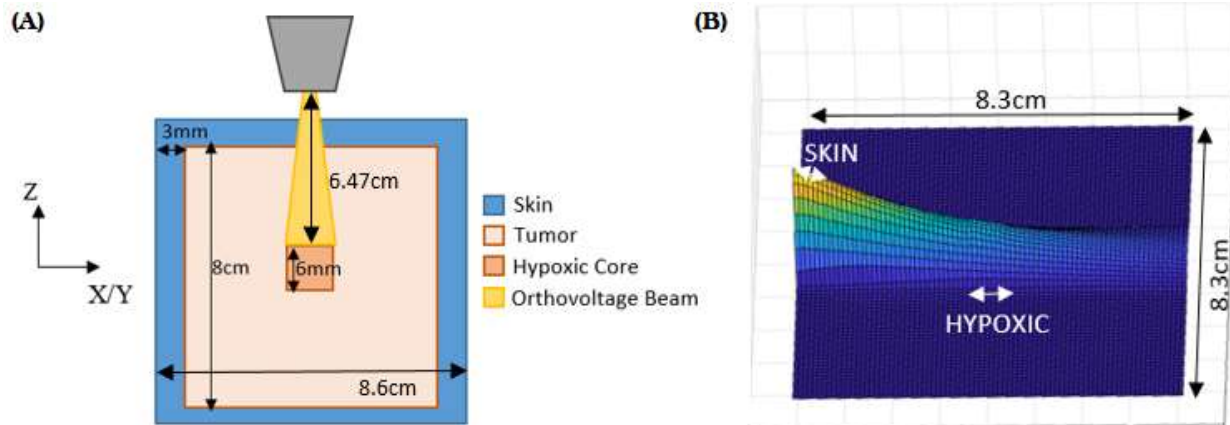


Figure 3.6 – Large tumor model with hypoxic core and skin layer. (A) Dimensions were chosen to represent a large tumor. (B) The dose distribution from a single beam has maximum dose at surface and falls off rapidly in the phantom.

The SARRP beam was used to model irradiation at a single angle as well as in arcs. With a single beam angle the maximum dose occurs at the surface that would correspond to a large skin dose for treatments prescribed to a depth. The SARRP beam was also used to model irradiation the phantom at discrete angles of 4.5 degrees in three non-overlapping orthogonal arcs (Figure 3.7).

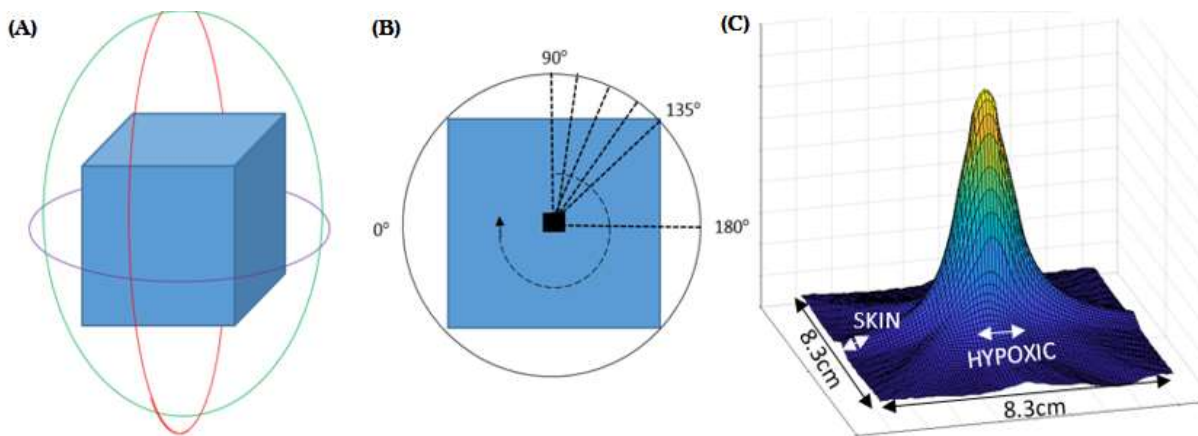


Figure 3.7 – Dose deposition within large hypoxic tumor with orthovoltage arcs. (A) Irradiation scheme with non-overlapping orthogonal arcs. (B) Discrete angles of irradiation along each arc. (C) Using arcs results in the maximum dose in the hypoxic region.

The combination of arcs causes the surface dose at any one place to be substantially less than the targeted center region. This technique may be used to treat deep hypoxic regions as well as amplify dose with CuATSM.

3.6 – Hypoxic Boost

Section (3.5) established that orthovoltage arcs can be used to reduce skin dose and escalate dose at a depth. This concept will be extended by simulating the treatment of a canine osteosarcoma tumor with an orthovoltage dose boost. Recall from Section (3.1), that a group of dogs were previously imaged with $^{64}\text{CuATSM}$. The patient with the largest tumor was chosen to evaluate the feasibility of an orthovoltage boost. The presence and spread of hypoxic conditions differ between tumors necessitating a patient specific analysis and treatment based on their tumor metabolic profile, therefore the evaluation within this particular tumor is intended to be a demonstration, rather than a generality.

This patient, a Labrador retriever with right humoral OSA, was imaged at six years old with 4.81 mCi ^{64}Cu , with left hind limb injection for a total body PET/CT scan. The DICOM images for this case were downloaded from Phillips Intellispace PACS Radiology software. SmART-ATP is designed for small animals; because the canine image set exceeded the dimensions for which the software was designed, some alterations to the image set was required. The image set was larger than the SmART-ATP software could accommodate. Therefore, the CT image set was restricted to 33 slices (Z) of 0.5 cm slices centered on the tumor with IBM Watson Health eFilm Workstation. The SmART-ATP software also has a limited range in an individual slice (X/Y) that can be accessed by the user, and as a result the PET/CT scan was centered on the liver and in some cases the extremities extended beyond that 10 cm range. This issue was

resolved by using MATLAB to adjust the *ImagePositionPatient* DICOM header tag to shift the image set to center on the tumor.

The PET/CT was evaluated by a veterinary radiologist to ensure a proper image registration in Eclipse. Eclipse was then used to define critical areas of interest by contouring. The Body Search tool was used to define the body region, and skin was created with the Margin for Structure tool to define a 3mm extension from the body region. The gross tumor volume (GTV), is a term that refers to the extent of the primary tumor that can be seen, palpated, or imaged [245]. The GTV was created from a clinical evaluation of the extent of disease within the CT scan, and extended to include the extent of PET uptake in the tumor. These contours were evaluated and approved by a veterinary oncology resident. Finally, a contour corresponding to the regions of hypoxia was created by windowing the highest intensity values of the ^{64}Cu PET within the tumor (Figure 3.8).

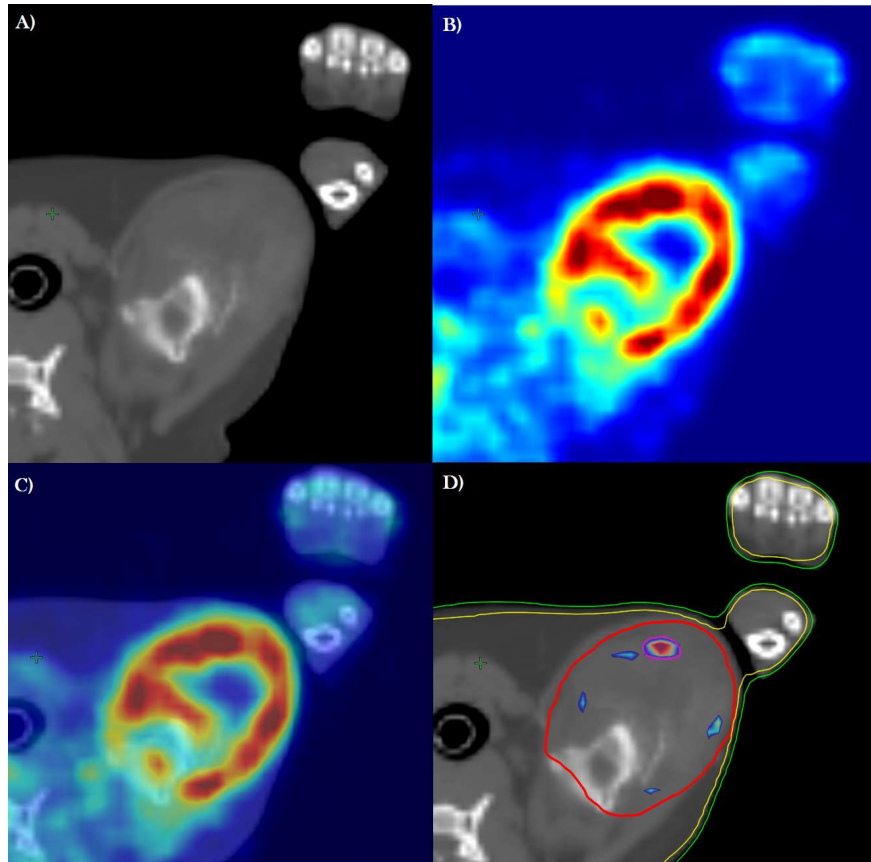


Figure 3.8 – Image dataset used to evaluate the hypoxic region that will receive a dose boost. (A) CT scan. (B) PET scan. (C) CT/PET fusion. (D) Contours defined. Body (green) and skin (yellow) are delineated with image processing tools. The GTV contour (red line) is defined clinically by the extent of disease with CT and PET. The hypoxic regions (magenta line) are defined by the highest intensity values within the PET image.

Techniques have been devised by researchers to best define hypoxic areas for dose boosts using $^{64}\text{CuATSM}$ [154, 246]. Those techniques were not employed in this case, because they were not optimized for dose enhancement.

A 3-D conformal radiation therapy plan was created with Eclipse to treat the bulk of the tumor. The GTV was the target of four 6 MV radiation fields at different angles with a total prescribed dose of 10 Gy (VTH). The image and structure set were then imported into SMART-ATP where an additional 10 Gy was prescribed to the hypoxic region. The hypoxia region was

segmented into three-centimeter scale volumes within the GTV volume. Each of these segments was assigned a unique isocenter to adequately cover the volume without overdosing non-target tissue. The XRAD SmART irradiator has several collimators used to define the field size and shape, and SmART-ATP has beam data associated with each collimator. Each isocenter was assigned the smallest collimator capable of covering the hypoxic segment (Figure 3.9).

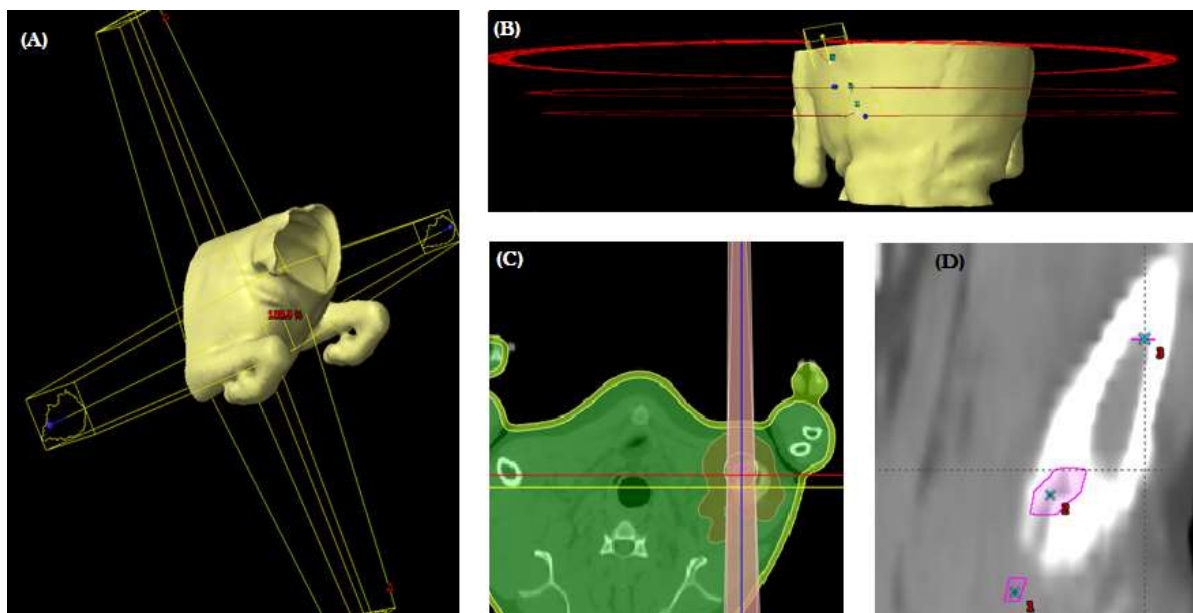


Figure 3.9 – Treatment fields for bulk irradiation and boost. (A) Four-field VTH irradiation for treatment of bulk of tumor. (B) 6MV boost treatment to hypoxic region utilizing arcs. (C) Orthovoltage boost treatment of hypoxic region. (D) Hypoxic segments (magenta) and isocenters (cyan crosses).

For dose calculation, media defined in PEGS4 corresponding to soft tissue, air, and bone were assigned to the CT by HU value. The hypoxic region was assigned *High* concentration of CuATSM (Table 3.2) for the dose enhancing case (KVC), and zero concentration of copper for the soft tissue for the orthovoltage only case (KVX). The resultant dose distributions from the MC calculations were exported from SmART-ATP then imported and combined with the original dose in Eclipse where a plan sum could be evaluated (Figure 3.10).

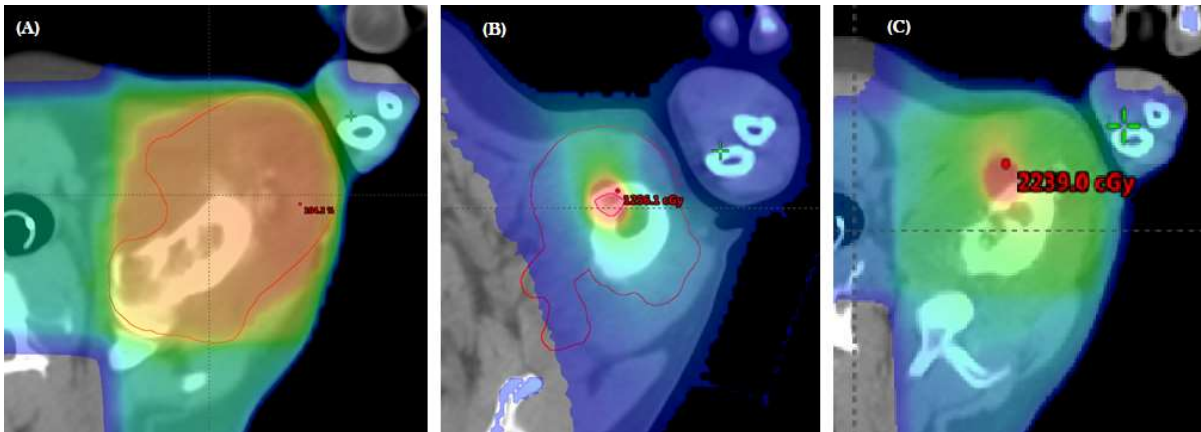


Figure 3.10 – Calculated dose for bulk treatment and boost displayed with color wash. (A) The original 4-field MV treatment prescribed to 10Gy to the GTV. (B) Copper dose enhanced orthovoltage boost. (C) Plan sum of the original plan with a *High* concentration of copper.

A 6MV treatment boost was also considered; three isocenters were assigned in order to maintain the very small field size restriction of the small animal irradiator to each segment of the hypoxic tissue contour within Eclipse, and three corresponding arcs were used to irradiate the volume to a 10 Gy prescription dose (MV). Accordingly, the small field sizes used by the SmART ATP were matched by MLC of the MC linear accelerator to compare equal field sizes. Isodose comparisons between the MV boost and the KVC and K VX boosts for an axial plane are provided in Appendix (B.6).

A common metric for evaluating the quantitative information in a treatment plan is the dose volume histogram (DVH). The DVH summarizes the dose distribution into a single curve for each anatomical structure of interest, which is valuable for evaluating and comparing plans [93]. In this case the integral cumulative form of the DVH is used, which plots the volume (y-axis) of the structure receiving a dose at least as high as what is specified on the x-axis. Dose calculation algorithms implement the input prescribed dose (10 Gy) and adjust the beam-on time parameter to achieve the desired dose.

Treatment planning requires careful consideration by the planner and comparisons between different resultant plans may need to be considered. For example, when comparing within a TPS such as SmART-ATP different beams (KVC/KVX) can be compared easily by equaling the beam-on time for each arc. However, when comparing between different TPS other normalization procedures may be necessary, such as the dose calculated by Eclipse for the 10 Gy boost to the hypoxic region did not adequately cover the hypoxic region with the prescribed dose. Here Eclipse uses weighting factors to achieve the desired dose, whereas the SmART-ATP simply uses a beam on time parameter, and the raw results from each TPS would not fairly compare the MV boost plan to the KV plans. Therefore, the dose calculated within the MV case was normalized to match the dose in 60% volume of the KVC case in the hypoxic region. The MV with copper boost was not considered because Eclipse does not have a mechanism for implementing metal solutions, and as noted in Section (2.6). Moreover, a 6 MV beam would result in an indiscernible (<1%) dose enhancement at concentrations below 10 g/kg (Figure 3.11).

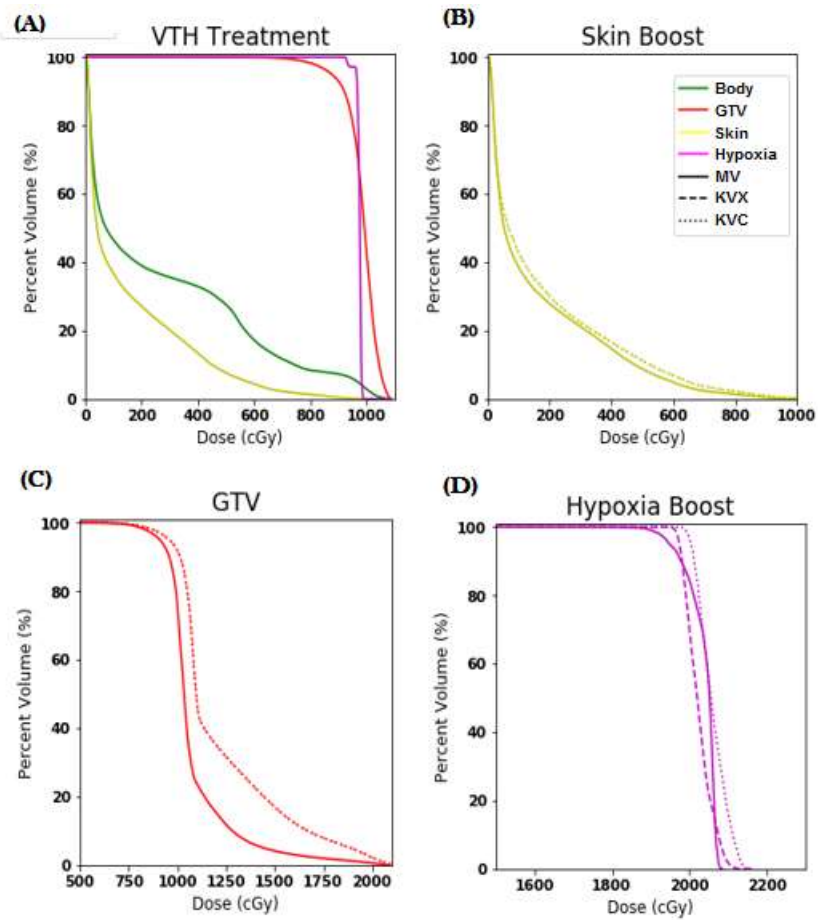


Figure 3.11 – Dose volume histograms used to evaluate the efficacy of copper boosted orthovoltage (KVC). (A) DVH for the original 6 MV treatment. (B) Results of boost dose in skin volume indicates that even with arcs orthovoltage still results in higher skin dose than 6 MV. (C) Boost dose to GTV. For (B-C) the KVC and KVC are overlapping. (D) Boost dose to hypoxic region. Dose in MV normalized to KVC at 60% volume.

Data are also presented in tabular form for quantitative assessment (Table 3.4).

Table 3.4 – Dose metrics for three boost techniques: MV, KVC (dose enhanced) orthovoltage, K VX (non-enhanced) orthovoltage. All boosts have been summed with VTH.

<i>Anatomical Region (Contour)</i>	<i>Dose Metric</i>	<i>MV (Gy)</i>	<i>KVC (Gy)</i>	<i>KVX(Gy)</i>
<i>Hypoxic Region</i>	<i>Min</i>	17.9	19.6	19.5
	<i>Max</i>	20.9	21.6	21.3
	<i>Mean</i>	20.4	20.6	20.2
<i>GTV</i>	<i>Min</i>	2.6	3.1	3.1
	<i>Max</i>	20.9	21.7	21.6
	<i>Mean</i>	10.8	12.3	12.3
<i>Body</i>	<i>Min</i>	0.02	0.02	0.009
	<i>Max</i>	10.3	21.7	21.6
	<i>Mean</i>	1.6	3.3	3.3
<i>Skin</i>	<i>Min</i>	0.02	0.009	0.009
	<i>Max</i>	10.3	11.9	11.9
	<i>Mean</i>	1.6	1.8	1.8

The results indicate that KVC and K VX share very similar dose behavior throughout the body, with the exception that there is a small boost in the hypoxic region. The comparison of KVC with MV indicates that orthovoltage treatment using arcs still results in a higher max and mean dose in skin compared to megavoltage treatments. The dose to hypoxic region is more nuanced. While the mean and max doses are close in value, the minimum dose in KVC is 10% higher.

3.7 – Discussion

Hypoxia is an undermining factor in the efficacy of radiation therapy with photons, however, because it is a physiologically distinct trait, it can be targeted molecularly. CuATSM has been found to have increased uptake in hypoxic cells and has been utilized to identify hypoxic regions for improved targeting for radiation therapy treatments. Recall from Chapter 2, that copper does act as a dose enhancer, however, clarifications were needed to evaluate whether

CuATSM could be used to practically deposit sufficient copper concentrations for dose enhancement. The aim of this chapter, therefore, was to address the questions from Chapter 2: *Can CuATSM be used to deposit copper at a sufficient concentration to result in therapeutically viable dose enhancement?* and *Can orthovoltage x-rays, when combined with copper as a dose enhancer, be used to treat hypoxic regions in large tumors without excessive normal tissue damage?*

The first question was addressed in Sections (3.3 - 3.4); within a simulated hypoxic tumor, CuATSM concentration values from literature were used to evaluate dose enhancement by copper. The results indicated that at diagnostic levels of CuATSM (100 mg/kg) there is modest dose enhancement in hypoxic regions (~1%) with orthovoltage radiation. Increasing the concentration to the LD₅₀ for DMSO (340 mg/kg) in subcutaneous mouse injections resulted in a DEF of 1.02 in the hypoxic core. Above this concentration, systemic injections would result in lethal DMSO toxicity and therefore only a direct injection into the tumor would be possible. Increasing CuATSM injection concentrations to 1.35 g/kg and 6.85 g/kg were then also considered and resulted in DEF of 1.07 and 1.33 respectively in the hypoxic core. These chosen concentration values are related directly to the GNP injection by Hainfeld et al., with matching concentrations for CuATSM and pure copper respectively. Comparative dose enhancement by GNP was considered under two conditions: a reduced uptake in the hypoxic core resulting in a DEF of 1.04 in the hypoxic region; and a complete elimination of uptake in hypoxia resulting in a DEF of unity in the hypoxic region. Finally, CuATSM was combined with GNP to evaluate the possibility of uniform dose enhancement across the entire tumor region – both hypoxic and normoxic. With an initial injection concentration of 2.6 g/kg CuATSM and 1.35 g/kg GNP, dose was escalated uniformly across the normoxic and hypoxic regions of the tumor.

The second question was addressed in Sections (3.5 - 3.6); orthovoltage arcs were used to model irradiation in the hypoxic region of a large tumor in both cuboidal form, and in a CT image set. The results indicated that when used in arcs, orthovoltage can amplify dose to hypoxic regions in tumors with a relatively small dose increase to skin. In comparison with an MV boost, however, the orthovoltage (KVC/KVX) irradiated skin to both a higher max and mean dose. The dose deposited in the hypoxic region was matched at dose to 60% volume; in this case the KVC irradiated to a slightly higher mean and max dose. KVC also resulted in 10% larger minimum dose compared to MV, which resulted in a dose profile with a steeper fall-off. There could be advantages to such a profile for therapeutic applications with sensitive non-target tissue proximal to a boosted hypoxic region.

The results of this chapter indicate that CuATSM may have efficacy for radiosensitization through dose enhancement; radiosensitization however, has not been demonstrated. Clinical radiosensitization occurs when an external chemical acts to improve biological outcome (cell death, tumor-size reduction) beyond what would be accomplished by radiation alone. It is also critical that the action of that chemical is improved by radiation. CuATSM may lead to dose enhancement, but if CuATSM causes increased cell death without radiation, then its action may be more attributable to toxicity than radiosensitization. The next step will be to evaluate radiosensitization directly in living tissue, in order to more directly answer the central thesis of this work. Chapter 4, will evaluate the following query: *Can CuATSM radiosensitize external beam radiation without toxicity?*

CHAPTER 4

LABORATORY EVALUATION OF THE RADIOSENSITIZATION OF COPPER (CuATSM) IN DNA AND MAMMALIAN CELLS

4.1 – Introduction

The goal of radiation therapy is to improve biological outcomes, and therefore, analysis of the radiosensitization potential of CuATSM would be incomplete without experimental measurements in biological systems. The relationship between biological survival and radiation exposure has been explored since the discovery of radiation. Biological outcomes have been foundationally connected to the use of radiation in medicine. Radiology was one of the earliest beneficial uses of radiation, however, it also established that radiation could result in side effects, cancer or death [247-248]. Modern uses of radiation in medicine require substantial regulations for protection of patients and the public, and biological outcomes remain integral considerations in radiation applications and research. Radiation has also been critical in understanding fundamental biological concepts. Experiments irradiating cells served as the foundation for knowledge of DNA repair, cell cycle checkpoints, the bystander effect, and genomic instability [249].

Radiation causes damage to cells, but some cells are more sensitive to radiation than others. It was known as early as 1903 that rapidly growing cells are more radiosensitive [250]. Growing cells progress through the cell cycle rapidly, and during the mitosis phase, the cell's DNA is not tightly bundled with proteins and is more susceptible to radiation damage [251]. Many tumor cells are highly metabolic and fast growing, making them more radiosensitive than

normal tissues [252]. This feature of tumors is what brings efficacy to radiation therapy, and as early as 1915 radiosensitivity was a factor in treatment recommendations by tumor type [253]. The most common use of radiotherapy relies on a division of the total treatment dose into several smaller doses delivered over a duration of time, known as fractionation. Fractionation in radiotherapy is an approach that improves outcomes, in part by allowing tumor cells to progress through the cell cycle to become more radiosensitive than normal cells [254].

The previous experimental discussion (Chapter 2-3) focused on macroscopic tumor radiosensitivity as a function of dose enhancement, but recall from Section (2.1), that radiosensitivity is a complex phenomenon attributable to many factors. CuATSM has been shown to have potential as a dose enhancer, however, if it does not increase biological outcomes, it would not be considered a clinical radiosensitizer.

The results of this chapter are expected to confirm the results of the previous chapters with laboratory experiments *in vitro* with viral DNA and by measuring cell survival with CuATSM. Recall, that the central thesis of this dissertation is *Can CuATSM be used as a radiosensitizer of external beam radiation?*

The laboratory techniques employed in this chapter differ from the simulations used in the majority of this work. Simulations, or models, act as representations of existing or proposed systems, and are often valuable tools. They allow researchers to understand factors that control a system, and allow for predictions of future behavior of the system. Simulations were used extensively in this research, because they provide a way to evaluate different designs without having to do experimentation on a real system, which might be prohibitively costly, dangerous, time-consuming, and impractical [263]. Radiation modeling requires input of data from

experimentation to benchmark outputs and improve correspondence with reality. The results of these biological experiments are intended to inform improvements to the modeling of radiosensitization.

4.2 – Background

Tumors vary by origin and individual, resulting in unpredictable outcomes to radiation treatment. Tumor cells can have distinct morphological and phenotypic profiles, including gene expression, metabolism, proliferation, and metastatic potential [255]. These differences occur both between tumors and within tumors and arise from both genetic and non-genetic factors. Ideally, research would be conducted with tissue that is identical to the tumor being treated, however, it is often not possible to perfectly replicate a tumor, and therefore, tumor models are employed as analogs.

Tumor models are often employed to serve as an analog for a tumor under investigation without risk to the patient [278]. Human xenograft models utilize growing tumor tissue removed through biopsy and transplanted to a rodent host. This method has the advantage of featuring the same complexity of genetic and epigenetic abnormalities from the original tumor population [279].

One of the most pressing shortcomings of the human xenograft model is that rodent immune response is often different or suppressed for implantation [257]. In some cases, this has led to poor predictability in clinical human patients [256]. Companion animal models are an attractive alternative to xenograft. In this model, potential treatments are evaluated in spontaneous natural disease in animals. Advantages of this model include, an intact host immune system and a closer size and genetic profile to humans.

Cell Culture

Tumor-derived cell lines are one of the most prominent methods of tumor modeling [258]. They allow for rapid analysis of underlying biological processes, as well as analyzing the efficacy of novel anticancer therapies. In some cases, cells can be grown as spheroids in three-dimensional culture; this method offers the advantages of cellular contact with other cells and extracellular matrix, and is more representative of the *in vivo* environment than two-dimensional culture [259]. Neuroblast cells were first cultured in 1907, and by 1955 cultured mammalian cells were used by Puck and Marcus for radiation survival experiments [260-261].

One of the most prominent cell-lines used in medical research is Chinese hamster ovary (CHO) cells (Figure 4.1). CHO cells were one of the earliest stable mammalian cell lines, and have been cultured since 1956 [262]. With a long history in research, much is known about CHO cell genetics and growth characteristics. CHO cells are derived from ovarian epithelium; based on their origin, they are considered a non-cancer model for most studies. They display some features typical for tumorigenic cells, including abnormal p53 function, as a consequence of their immortalization [264].

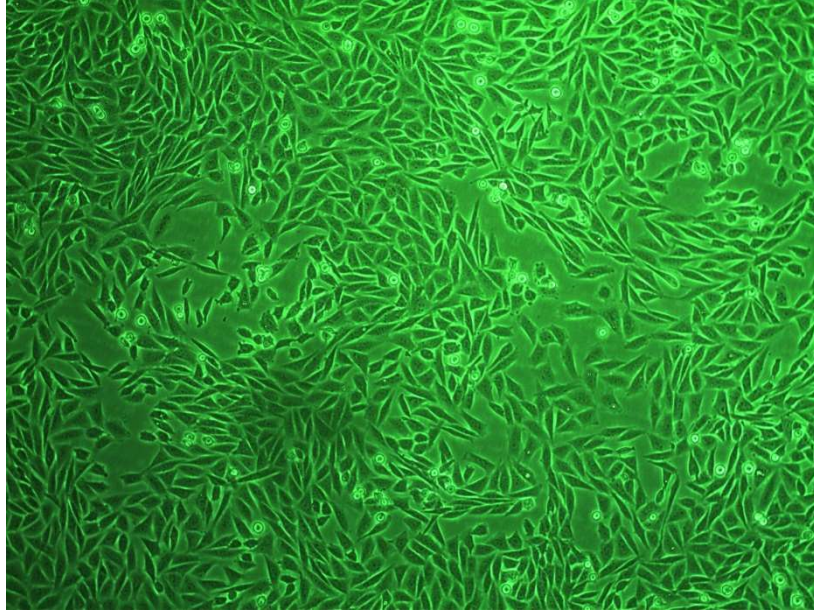


Figure 4.1 – Chinese hamster ovary cells in cell culture.

CHO cells are commonly used in radiation studies because of their rapid growth and small number of chromosomes, enabling facile experiments with radiation cytogenetics [265]. Many studies use CHO-wild type cells in the role of control to analyze baseline effects before adding complicating factors [52].

Cell Survival Curves

Cell survival curves are a statistical representation of the likelihood of cells to remain replicative after irradiation, and are the most common way of presenting the outcomes in radiation studies with cells [268]. They describe the relationship between absorbed dose of radiation and proportion of cells that survive and are able to grow into a colony [266]. Survival was first utilized in radiation experiments and remains a critical tool in radiation research, although it has become a more general tool in cellular analysis [261].

Radiation damage to DNA in a cell can either be repaired or lead to the death of the cell. There are several mechanisms of death that occur within cells. For the purposes of survival analysis, a cell that has lost its ability to reproduce indefinitely would be considered to have undergone mitotic or reproductive death. This categorization includes cells that have undergone necrosis, apoptosis, autophagy, or senescence. This definition of death includes cells that remain sufficiently intact after treatment to produce proteins, replicate DNA, and even undergo up to two cell divisions [267].

The standard established way of measuring cell survival is with a clonogenic assay. When a cell survives and has the capacity to grow into a colony, it is referred to as clonogenic. The method is initiated with plating a known number of cells exposed to the target condition, incubating for weeks and counting the macroscopically visible colonies that can be fixed and stained [267]. The definition of colony varies throughout the literature, but is generally considered to be when the origin cell has reproduced sufficiently to result in a cluster of at least fifty cells [269]. Not every seeded cell will form a colony, even in the absence of external manipulation, resulting in fewer colonies than plated cells. The plating efficiency (PE) accounts for this deficiency and is defined as:

$$PE = \frac{\# \text{ Colonies Formed}}{\# \text{ Cells Plated}} \quad (4.1)$$

Parallel dishes are plated that have been exposed to radiation, and the surviving fraction (SF) of those treatment cells is therefore:

$$SF = \frac{\# \text{ Colonies Formed}}{\# \text{ Cells Plated} \times PE} \quad (4.2)$$

The results are then plotted logarithmically with increasing dose.

4.3 – DNA Strand Break Assay

A preliminary investigation was conducted to both confirm the findings of metal dose enhancement within an *in vitro* system, and optimize the parameters of cell experiments. Single-stranded viral DNA isolated from M13mp18 virus (New England Biolabs, Inc.) was used to analyze radiosensitizing ability of copper. Viral DNA is a useful tool that can be used to evaluate single-stranded nucleotide breaks (SSB) occurring from radiation [271]. This method was selected because it offers manageable biological data with insight into cellular mechanisms.

MC simulations were previously used (Chapters 2-3) to evaluate the dose enhancement resulting from radiation in metal solutions. Dose enhancement is often a primary mechanism of radiosensitization with metals, but radiosensitization can occur from different mechanisms. Recall from Section (1.5), that copper can act to enhance reactive oxygen species (ROS), which are known to cause DNA breaks, and are regarded to account for the majority of damage to DNA with photon radiation [270]. The macroscopic MC models used previously did not account for increases in ROS that would occur from metals within the tumor region. Strand breaks in viral DNA will occur from interactions with secondary electrons and additionally ROS, thereby exhibiting all mechanisms of radiosensitization.

In a preliminary investigation, copper was analyzed as a radiosensitizer compared to other metals. A 10 μ L DNA solution was created for each sample that consisted of 0.11 μ L DNA (250 μ g/mL); 0.1 μ L Tris (hydroxymethyl) aminomethane (THAM) hydrochloride (Tris-HCL) as an electrophoresis buffer; 8.72 μ L water; and 1 μ L of 2 mM metal salt solution (resulting in a 200 μ M final concentration). Each sample was exposed to 10 Gy gamma-rays from a Cs-137 source, and then run through gel electrophoresis (1% agarose gel in 1X TAE buffer and 0.05%

ethidium bromide), after adding 2 μL of 6X DNA loading dye (15% Ficoll (w/v), 10% glycerol (v/v), 0.25% bromophenol blue (w/v), and 0.25% xylene cyanol FF (w/v) in distilled water) [271].

Electrophoresis is a technique used to separate DNA molecules by size. Voltage is supplied across the gel and negatively charged DNA migrates to the positive terminal. The gel contains small pores that the DNA fragments can travel through, with large fragments traveling more slowly than small fragments. After sufficient time the DNA will be separated into bands corresponding to the length of fragments [272]. Electrophoresis was run at 100 V for 1 hour; the gels were then submerged in buffer and stored at 4 °C for 24 hours before imaging. Gel images were obtained with Molecular Imager Gel Doc XR (Bio-Rad Laboratories, Inc.) (Figure 4.2).

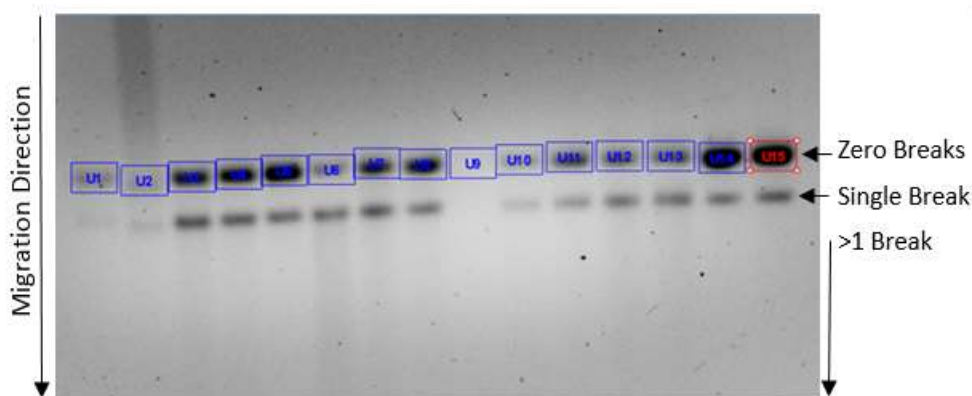


Figure 4.2 – Gel image for viral DNA single-strand break assay. Gel electrophoresis causes migration of DNA along the gel, separating DNA fragments by size. Unbroken fragments are high intensity bands denoted with analysis regions [U1-U15]. Single breaks are the high intensity bands just below the unbroken analysis bands, and smaller fragments present as a streak below this band represent more than 1 break.

The gel images are analyzed by optical density using Image Lab (Bio-Rad Laboratories, Inc.).

The M13mp18 viral single-stranded DNA is circular; unbroken strands are large and migrate the

least distance with gel electrophoresis, resulting in a high intensity band. A single break in DNA results in a topoisomer DNA fragment the same length as the circular, but capable of migrating more quickly through pores. These DNA fragments migrate slightly further along the gel, resulting in an additional high intensity band below the first. Any additional breaks to a strand, results in smaller fragments that migrate farther in a continuous smear.

Copper, in the form of CuCl_2 , was analyzed as a radiosensitizer against several other metal salts : Iron (FeSO_4), Aluminum (AlKSO_4), Silver (AgNO_3), Nickel (NiSO_4), and Cobalt (CoCl_2). Intact DNA for each metal salt was defined as the optical density (OD) in the intact analysis bands, normalized to water without irradiation. Radiosensitivity was determined from the ratio of unirradiated OD to irradiated OD for the same metal salt to demonstrate the greatest difference between toxicity and radiation response (Figure 4.3):

$$\text{Radiosensitivity} = \frac{\text{Unbroken Unirradiated DNA}}{\text{Unbroken Irradiated DNA}} \quad (4.3)$$

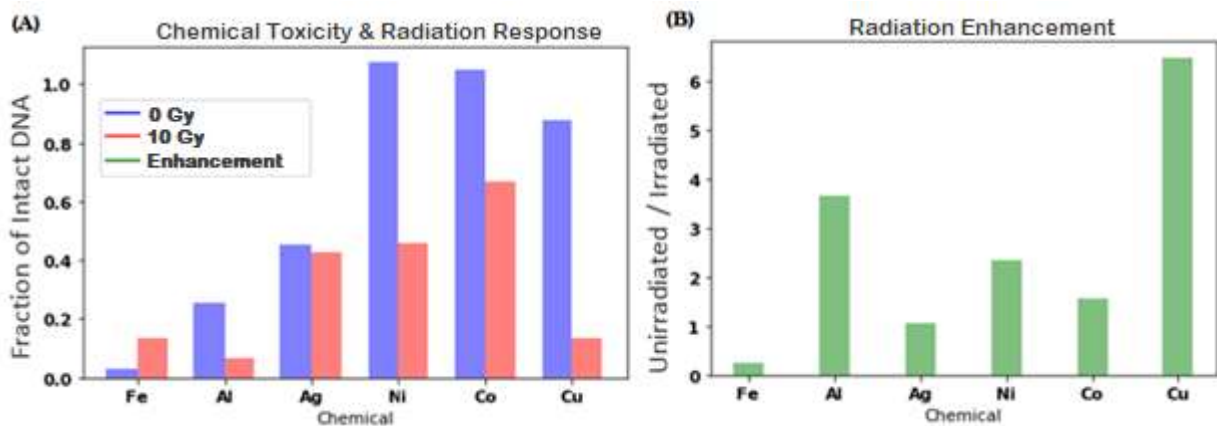


Figure 4.3 – Six metal salts analyzed for radiosensitization: (Fe, Al, Ag, Ni, Co, and Cu). (A) Each sample was normalized to unirradiated water. Metal salt alone (blue), gives an indication of the implicit toxicity of the metal salt leading to DNA breaks ($N = 1$). Irradiated samples (red), combine DNA damage from toxicity and radiation. (B) Ratio of unirradiated sample to irradiated sample was used to evaluate radiosensitization.

Of the metal salts analyzed, several caused DNA fragmentation with their presence in solution; only cobalt and nickel salts did not have a toxic effect on DNA. With radiation, DNA was fragmented with all metal salts. FeSO₄ resulted in more DNA damage in the unirradiated case, indicating that the molecule acts as a radioprotector. A single measurement was used for this experiment to demonstrate initial evidence that copper can feasibly act as a radiosensitizer.

Copper resulted in the largest value of radiosensitization among the metals studied, prompting additional analysis. Three CuCl₂ final concentrations (50 μM, 200 μM, 800 μM) were investigated to evaluate radiosensitization dependence on metal salt concentration. Each concentration was irradiated with 5 Gy from two external beam radiation sources: 6 MV Trilogy (Varian Medical Systems, Inc.) (VTH), and 225 kVp PXI XRAD SmART (Precision X-ray, Inc.) (PXI), to evaluate DNA survival from different energy spectra. Intact DNA was evaluated as the OD for each concentration normalized to unirradiated water (0 μM CuCl₂) (Figure 4.4).

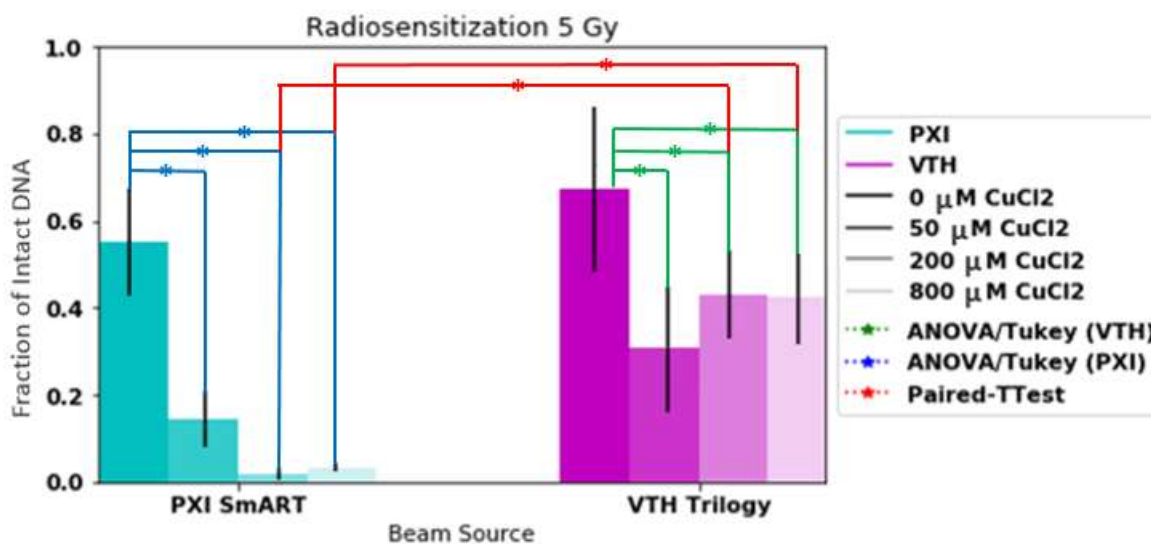


Figure 4.4 – Radiosensitization with copper at various concentrations for kV (PXI SmART) and MV (VTH Trilogy) beam energies. Two beam sources were evaluated PXI (cyan) and VTH (magenta). Values for fraction of intact DNA compared to unirradiated 0 μM CuCl₂ are plotted for each concentration. Statistical tests evaluated radiosensitization at each concentration (green + blue), and comparisons of beam energy (red).

CuCl₂ acts as a radiosensitizer with both beam spectra. Each CuCl₂ concentration was significantly reduced compared to the control (0 μM) case (Analysis of Variance (ANOVA) 2-tailed, with post hoc Tukey Honestly Significant Difference (HSD) ($\alpha = 0.05$) $n = 3$) [273]. Higher concentrations resulted in decreased intact DNA, but the results were not significant. The difference between each concentration and the control case was calculated; the mean difference between the two beam energies was evaluated to determine difference in radiosensitization from energy.

The amount of intact DNA was decreased for all CuCl₂ concentrations in the PXI irradiations compared to the Trilogy. PXI resulted in significantly different radiosensitization values from VTH at 200 μM and 800 μM concentrations (Paired 2-tailed T-test ($\alpha = 0.05$)); a lower value of intact DNA was observed in the 50 μM case, but the results were not significant. The data indicate that radiosensitization can occur for low concentrations. For example, 50 μM CuCl₂ (134.45 g/mol) corresponds to 1.32 mg/kg copper concentration (copper composes 47% of CuCl₂ by mass fraction); this value is two orders magnitude lower than the concentration necessary for dose enhancement in the MC models of Chapters (2-3). Additionally, the data indicate that there is more radiosensitization when using the PXI beam, as predicted from the results of Chapters (2-3).

4.4 – CuATSM Toxicity

Radiosensitization is only efficacious if the analyte under consideration is sufficiently non-toxic to allow for application. Recall from Section (4.3) that CuCl₂ resulted in damage to DNA without radiation, and from Section (3.3) that the solvent for CuATSM, dimethylsulfoxide (DMSO), is known to be toxic. Growth inhibition with CHO cells was assessed for DMSO and

CuATSM solution (10 mg/ml in DMSO; 31 mM) to determine toxic thresholds. Cell culturing is generally conducted under favorable cell growth conditions to facilitate rapid proliferation. Alterations to the growth environment, however, can significantly affect cellular growth. Growth inhibition is a relative measure of the altered environment to normal growth conditions to evaluate the effects of the alterations [274]. Growth inhibition values can be calculated with:

$$GIV = \frac{\text{Treated Cell \#}}{\text{Control Cell \#}} \quad (4.4)$$

CHO cells were cultured in 1X Alpha Modified (L-Glutamine/ribonucleosides/deoxyribonucleosides) Minimum Essential Medium (α -MEM) (HyClone Laboratories), with 10% (v/v) Fetal Bovine Serum (FBS), and 1% 100X Gibco Antibiotic-Antimycotic (Anti-Anti) (ThermoFisher Scientific, Inc.). Cells from actively growing stock were harvested from culture by phosphate buffered saline (PBS) wash, and 1X 0.25% Trypsin- ethylenediaminetetraacetic acid (EDTA) detachment (trypsinization). Trypsin acts to hydrolyze proteins and EDTA is a chelate that removes calcium-ions, important in cell anchoring, from solution. Cells were counted electronically with Coulter Counter (Beckman Coulter, Inc.), and 5,000 were plated in dishes.

For the DMSO toxicity analysis, DMSO was added to compose 0%, 5%, 10%, and 20% (v/v) of culture media for one hour; then washed and replaced with fresh media. Samples were incubated in a Thermo Forma 3110 CO₂ Water Jacketed Incubator (ThermoFisher Scientific, Inc.) at standard conditions (37 °C with 5% CO₂) for 2 and 4 days, when samples were recounted. Doubling time was assessed from the exponentially growing phase using:

$$2N(0) = N(0)e^{nt} \quad (4.5)$$

$$t_{double} = \frac{\ln(2)}{n} \quad (4.6)$$

Where n , is the growth rate, defined as the slope of the growth points in logarithmic scale.

Doubling time for untreated CHO cell samples was found to be approximately 14.5 hours.

Growth inhibition values (GIV) were calculated from day 6 samples (Figure 4.5).

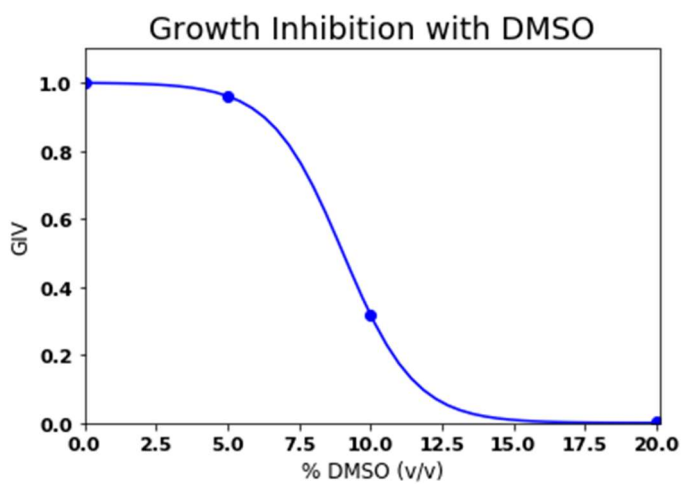


Figure 4.5 – Growth inhibition with DMSO. Sigmoid function fit to data points. (N = 1)

A single experiment was conducted to determine maximum concentration of DMSO and CuATSM that could be added to the growth medium before overbearing toxicity, defined as 0.5 GIV. The results of growth inhibition with DMSO indicated that beyond 5% (v/v) of solution, DMSO resulted in a rapid decrease in cell viability.

Toxicity of CuATSM (Cayman Chemical, Inc.) was also assessed, using the same cell-line and techniques described above; however, the procedure differed in some respects. A qualitative assessment of CuATSM was made with microscopy. Cells were plated (100,000) and CuATSM was added to the culture medium to final concentration of 31.1 μ M. Microscopy

images were collected over time with Micrometrics 519CU and SE Premium (Accu-Scope, Inc.) (Figure 4.6).

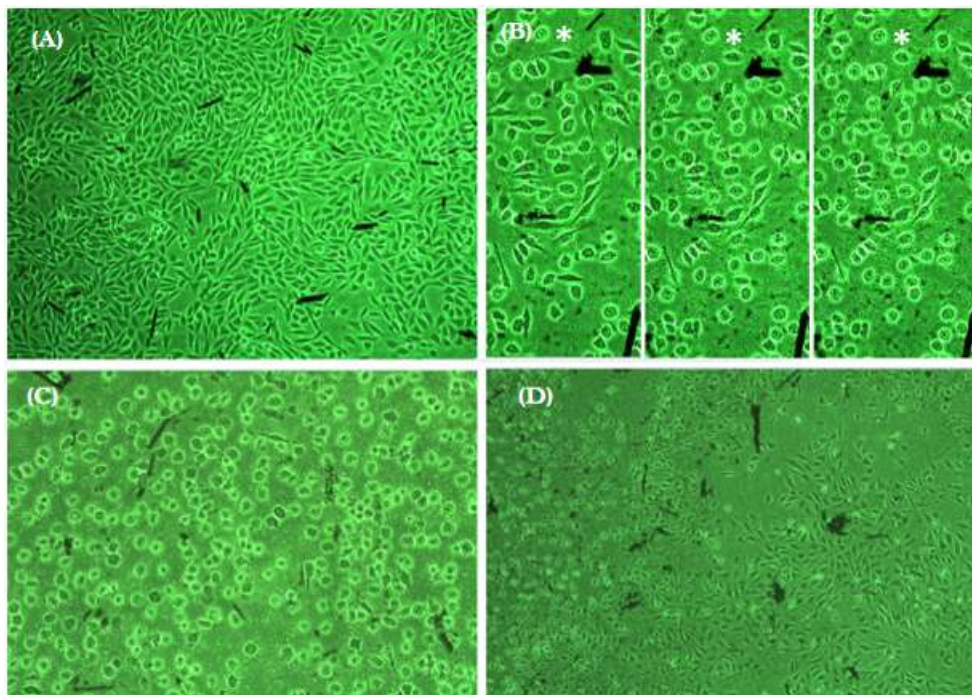


Figure 4.6 – CHO cell alterations from CuATSM. (A) Initial shape of CHO cells upon application. (B) Cell shapes at three time points (15 min; 30 min; 45 min) within the first hour after application. Star (white) identifies single cell undergoing shape change. (C) Cell shape 24 hours after application. Cells shown are still attached even with vigorous agitation. (D) Mixture of altered shapes and cells with normal phenotype.

CuATSM was found to cause alterations to cells at 31.1 μM concentration. Within the first hour of application, CuATSM caused cells to change shape; often decreasing the apparent attachment area of the cell with the surface (Figure 4.6B). In some cases these cells detached from the dish surface, but in other cases the cells were not detached even with vigorous agitation. After 24 hours, there was substantial detachment, but other regions were attached with shape changes (Figure 4.6C), or had returned to their normal phenotype (Figure 4.6D).

The protocol used here for CuATSM incubation was developed based on data from Burgman, et al., which indicate maximum uptake of CuATSM occurred at approximately 1 hour [123]. In order to maximize cellular concentration of copper without toxicity from DMSO, a high concentration would be administered over a short duration (1 hr). Subsequently, the CuATSM solutions were removed and replaced with fresh media. The qualitative assessment indicated that high concentration of CuATSM for short duration might lead to confounding results from cell detachment. This finding was used to alter the procedure of growth inhibition with CuATSM. In this case 100,000 cells were plated in each dish and lower concentrations of CuATSM were added to the media permanently rather than for 1 hour as in the DMSO case (Figure 4.7).

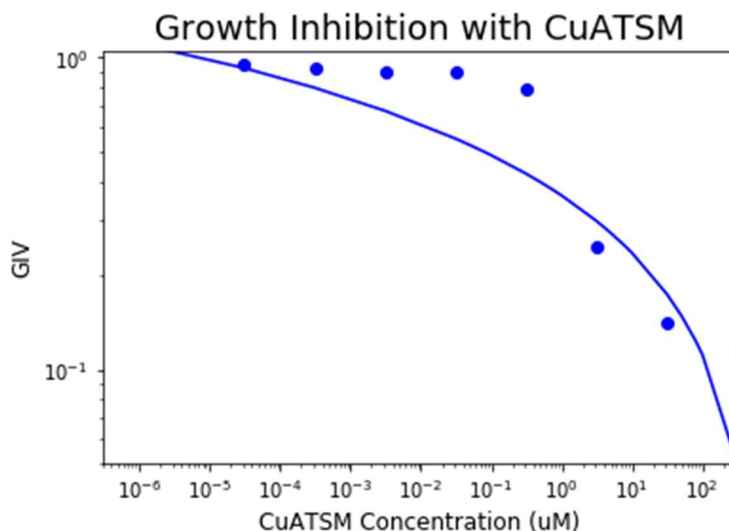


Figure 4.7 – Growth inhibition with CuATSM. Logarithmic function to fit data points.

Evaluation of growth inhibition indicated that CuATSM solution was a limiting factor in CHO cell growth. A single experiment was conducted to determine the maximum concentration of CuATSM that could be added before overbearing toxicity ($GIV = 0.5$). With concentrations above $0.311 \mu\text{M}$, CuATSM results in a GIV below 0.5, therefore, $0.311 \mu\text{M}$ was used as the final concentration of CuATSM solution for radiosensitization analysis. Recall from Section (2.6),

that macroscopic Monte Carlo models resulted in discernable dose enhancement only when the copper concentration was at least 100 mg/kg of the total solution. The CuATSM concentration determined in this section to be non-toxic to cells (0.311 μM), would result in elemental copper composing 18 $\mu\text{g}/\text{kg}$ of the total solution, a much lower concentration than the dose enhancing concentration.

4.5 – Radiosensitization of CHO cells with CuATSM

With radiation treatment of cells, it is clarifying to understand the parameters of radiosensitization. Dose enhancement (Chapters 2-3), features heavily as a proposed mechanisms for improved outcomes with metal radiosensitizers. *In vitro* analysis of DNA breaks provides insight into the combinatory action of ROS and dose to result in a fundamental mechanism for cell death. DNA breaks can result in mitotic death, and are crucially correlated to cell survival, however, they are not the only mechanism for cell death. For therapy applications with the intent to reduce the number of tumor cells, the primary concern is cell death, by any mechanism.

Survival curves were generated for cells exposed to CuATSM and radiation with increasing dose. Cells were cultured with the procedure outlined in Section (4.4), and 100,000 cells were plated for each sample. Recall from Section (1.8), that CuATSM was developed as a tracer for hypoxia, and the evaluation of its efficacy as an external beam radiosensitizer has focused on the increased therapeutic advantage it would have in hypoxic tissues (Section 3.3). Therefore, samples were exposed to hypoxic environment within a hypoxia chamber (Coy Lab Products, Inc.)

A hypoxia chamber creates and maintains a stable low-oxygen environment (< 10 ppm) for cell culture experiments. Atmosphere is removed from the chamber by vacuum pump and

replaced with a nitrogen/hydrogen gas mixture (95% N₂ + 5% H₂) that removes residual oxygen from the environment by formation of water molecules with a palladium catalyst. After removal of atmosphere, oxygen concentration was measured to be stable (± 3 ppm) over a two hour period as measured by Coy Anaerobic Monitor (CAM-12). An external validation of low oxygen conditions was evaluated by YSI 5000/5010 dissolved oxygen instruments (YSI, Inc.). Media (10 ml) were exposed to the hypoxic environment in the chamber for two hours, and transported using an air-tight container (Mitsubishi Gas Chemical Company, Inc.) sealed with anaerobic vinyl tape (Coy Lab Products, Inc.). The results indicated that the oxygen concentration in media were well below the stated oxygen in the chamber (< 10 ppm), and approached the limits of resolution of the monitor (10 ppb).

Cells were adapted to the low oxygen environment for two hours, and CuATSM (0.001% v/v) was added for one hour. Samples were transported and irradiated using the PXI X-RAD SmART irradiator with 40 mm x 40 mm cone to cover each dish uniformly. Radiation doses of 0, 2, 4, and 8 Gy were applied. Gafchromic EBT2 dosimetric film (Ashland, Inc.), was used to ensure proper alignment and coverage (Figure 4.8).

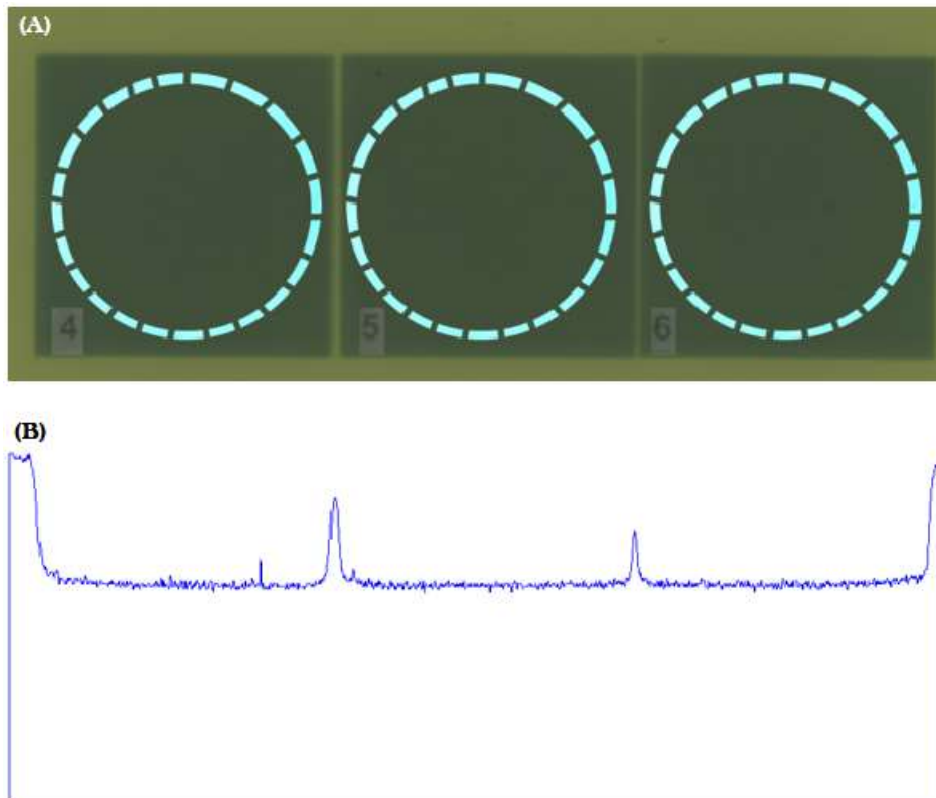


Figure 4.8 – Film analysis for 6-well plate irradiation. (A) Film with 2 Gy irradiation fields; 6-well plate overlaid with dimensions (cyan) to demonstrate coverage. (B) Image profile across center of film indicates uniformity within irradiated field.

Samples were then returned to incubator at standard conditions for two days allowing for two CHO cell divisions to occur [264]. The analysis of cell survival differed from the standard clonogenic assay. Recall from Section (4.2), that the clonogenic assay requires the plating of a known number of cells, but that CuATSM caused shape changes and detachment of cells (Section 4.4). Therefore, an alternative method was used to ensure that all cells present in the plate would be counted. Alternative methods of cell survival analysis have been utilized in the past and found to be successful in ranking the cell lines in order of radiosensitivity [275-277]. In this case, the samples were harvested with trypsin and recounted with Coulter Counter after incubation. This method conservatively accounts for the phenotypically altered cells described in

Section (4.4) by accounting for dead and dying cells in addition to clonogenic cells. Therefore the definitions of plating efficiency and survival fraction are changed from the definitions in Section (4.2):

$$PE = \frac{\# \text{ Cells Counted}}{\# \text{ Cells Plated}} \quad (4.7)$$

$$SF = \frac{\# \text{ Cells Counted}}{\# \text{ Cells Plated} \times PE} \quad (4.8)$$

Four conditions were considered: normoxic cells without CuATSM (NXC); normoxic cells with CuATSM (N+C); hypoxic cells without CuATSM (HXC); and hypoxic cells with CuATSM (H+C). Five trials were conducted for each condition and results were plotted logarithmically against dose (Figure 4.9).

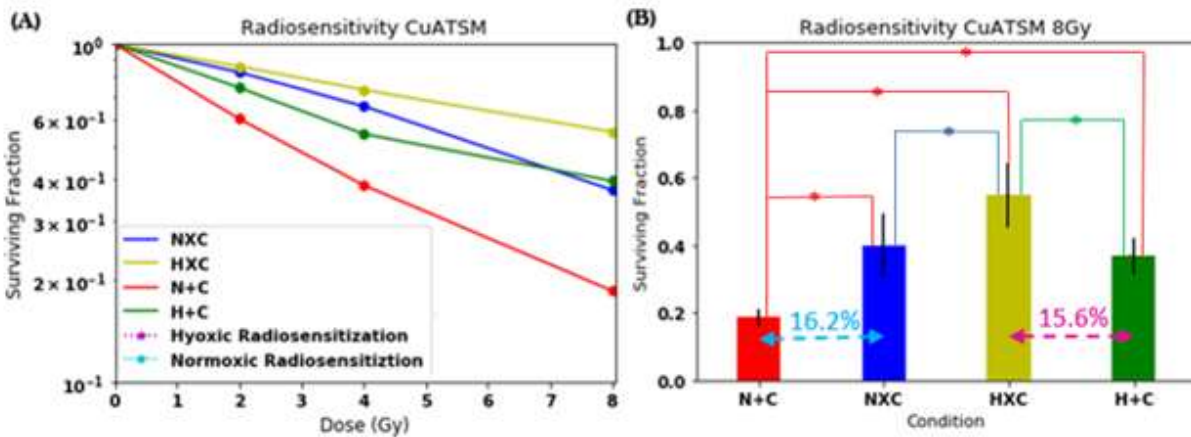


Figure 4.9 – Cell survival with CHO exposed to CuATSM and PXI orthovoltage radiation. Four conditions were considered: normoxic cells without CuATSM (blue); hypoxic cells without CuATSM (yellow); normoxic cells with CuATSM (red); hypoxic cells with CuATSM (green). (A) Surviving fraction from 0 to 8Gy. (B) Bar graph for each condition at 8 Gy. Hypoxic radiosensitization (magenta), and normoxic radiosensitization (cyan) are calculated from the differences in each oxic condition between +CuATSM and XCuATSM.

CuATSM acted to radiosensitize cells to external beam orthovoltage radiation. Each condition was compared (ANOVA (2-tailed) + Tukey HSD ($\alpha = 0.05$) $n = 5$), and significant difference

was found in each case, with the exception that no significant difference was found between NXC and H+C conditions. Radiosensitization was assessed by the difference between presence of CuATSM and absence of CuATSM. The two oxic conditions, hypoxic and normoxic, were compared by linear combination of population means (contrast) with the following null and alternative hypotheses:

$$H_o: \mu_{nxc} - \mu_{n+c} = \mu_{hxc} - \mu_{h+c} \quad (4.9)$$

$$H_a: \mu_{nxc} - \mu_{n+c} \neq \mu_{hxc} - \mu_{h+c} \quad (4.10)$$

The contrast estimate was then tested (T-test (1-tailed) ($\alpha = 0.01$) $n = 5$); there was no significant difference between the oxic conditions. Radiosensitization occurred for a very low concentration of copper in this case; approximately 18 $\mu\text{g}/\text{kg}$ copper concentration in solution. CuATSM was 0.311 μM concentration in medium; CuATSM is dissolved in DMSO (10 mg/ml); and copper is approximately 20% (mass fraction) of CuATSM.

4.6 – Discussion

Measurements in biological systems are critical to assessing radiosensitization. Previously, dose enhancement was assessed with simulations of copper (Chapter 2) and CuATSM (Chapter 3). The results of those simulations indicated that in order to produce an enhancement to treatment utilizing CuATSM the following conditions would need to be met: a high concentration would need to be injected; hypoxic tissues would be needed to concentrate copper deposition; and low energy (orthovoltage) irradiation would be needed to enhance the photoelectric effect. Dose enhancement is a mechanism for radiosensitization, but radiosensitization does not occur uniquely from dose enhancement. Clinical radiosensitization occurs when the outcomes of radiation (cell death, tumor-size reduction) are enhanced by the

action of an external additive. It is also critical that the outcomes of the additive are enhanced by radiation, otherwise its action could be attributable to toxicity. The purpose of this chapter therefore, is intended to address the question: *Can CuATSM radiosensitize external beam radiation without toxicity?* The query is addressed with biological measurements in cells and DNA.

Although the analysis was not exhaustive, the results indicated that CuATSM can be used as a radiosensitizer, but differed in some respects from the implications of dose enhancement (Section 4.1). Section (4.3), indicated that copper, in the form of CuCl_2 could be used to amplify single-strand breaks in viral DNA. Although orthovoltage (PXI), was found to result in more DNA breaks, megavoltage (VTH) was also shown to act as a radiosensitizer. Furthermore, the data indicate that radiosensitization occurred with both megavoltage and orthovoltage, below concentrations necessary for MC predictions of physical dose enhancement at the macroscopic level. Recall from Section (2.6) that macroscopic dose enhancement occurred with the SARRP (orthovoltage) beam at a minimum copper concentration of 100 mg/kg. Radiosensitization in DNA experiments occurred at copper (CuCl_2) concentrations as low as 1.32 mg/kg; two orders of magnitude lower than macroscopic MC.

As a precursor for assessment of radiosensitization in cells, an assessment of toxicity was made with CuATSM and its solvent, DMSO (Section 4.4). DMSO is toxic to cells, however with limited incubation time, cells can recover from exposure. Burgman, et al., indicated that maximum uptake of CuATSM occurred at approximately 1 hour after application. A protocol utilizing high concentrations of CuATSM (31.1 μM) for short durations (1 hour) in medium was intended to achieve increased copper concentrations without toxicity. Qualitative microscopy analysis precluded such a methodology, as replacement of medium following short duration

incubation of CuATSM would permanently remove cells from culture that might reattach without stressors present. Permanent incubation of CuATSM was evaluated for toxicity at several concentrations in media and 0.311 μM was determined to be the maximum concentration without overbearing ($\text{GIV} < 0.5$) toxicity.

The goal of this research is to investigate whether CuATSM can be developed into a radiosensitizer to improve tumor cell kill in radiotherapy applications. CHO cells were selected for this study because of their prominent role as a baseline in radiation cytogenetics research. Recall from Section (2.2), that CHO cells are considered to be non-cancerous and therefore, survival outcomes in this study will not directly apply to expected outcomes in cancer cells. The methods described in this chapter should be extended to a number of cancer cell lines to fully evaluate the mechanisms of radiosensitization with CuATSM. Nevertheless, the demonstration of radiosensitization in CHO cells should serve as an indicator that radiosensitization would likely occur in cancer cells, which are often more radiosensitive [252-253].

Coulter counting was used to evaluate the total number of cells remaining after treatment in this study. This differs from the typical clonogenic survival assay because in addition to replicative cells, dead or dying cells will be counted. Research has indicated that alternative counting methods can serve as estimations of cell survival in radiation research at low doses [275-277]. The methods used here are a conservative approach that accounts for the phenotypically morphed cells noted in Section (4.4) that could later reattach and proliferate after adaptation to environmental stress. Previous research has indicated that an advantage of estimating survival fraction with Coulter counting is that it avoids underestimation of the total cell number that can lead to ratios greater than 100% [276]. Dead and dying cells should be a

relatively small fraction of the total cell number after two days of incubation, allowing for at least 2 cell divisions of CHO cells [267].

The maximum concentration of CuATSM without toxicity (0.311 μM) was used to analyze radiosensitivity in cell culture (Section 4.5). CuATSM did act as a radiosensitizer at concentrations that were four orders of magnitude below what was determined necessary for dose enhancement using macroscopic MC. The results of this chapter indicated that radiosensitization with CuATSM occurred at a lower concentration of elemental copper (18 $\mu\text{g}/\text{kg}$) than with CuCl_2 in viral DNA (1.32 mg/kg) or in bacterial cells (1.74 mg/kg); however, it should be noted that low copper concentration sensitivity was not thoroughly evaluated with either analyte [111]. Furthermore, radiosensitization occurred in both hypoxic and normoxic conditions, although there was no significant difference in the level of radiosensitization between the two conditions. Equal radiosensitization with either hypoxic or normoxic conditions, corresponds with the findings of McMillan, that $^{64}\text{CuATSM}$ was uptaken at the same rates in hypoxic and normoxic CHO cells [117]. These results suggest, therefore, that cellular uptake is the primary regulator of radiosensitivity.

The results of this chapter answer the central postulate of this dissertation in the affirmative: CuATSM can be used as a radiosensitizer. The low concentration of copper for radiosensitization, entails a follow-up question: *Why does CuATSM cause radiosensitization in laboratory experiments (DNA/mammalian cells) at lower copper concentrations than MC macroscopic dose predictions?* This question will be addressed in the following chapter.

CHAPTER 5

NANOSCALE MONTE CARLO ASSESSMENT OF DOSIMETRY AND RADIOCHEMICAL YIELD IN CELLULAR MODEL

5.1 – Introduction

Dose analysis is generally conducted at a macroscopic scale of millimeters and above.

Macroscopic dosimetry is the technique where the average values of stochastic quantities are used to define values such as absorbed dose [233, 241]. Macroscopic dose analyses are standard for radiotherapy applications; providing a quantitative correlational metric to predict deterministic treatment outcomes. As radiotherapy advances, however, sub-millimeter dose resolution may provide valuable insights into stochastic radiotherapy outcomes. When a problem is evaluated at increasingly smaller scales, a microdosimetric consideration may be warranted [241].

Microdosimetry considers dose at the scale of micrometers, and differs from macroscopic dosimetry in that the entire stochastic energy deposition process is studied [146, 241]. For studies within cells, radiation interaction with nanostructures such as DNA are critical. Often, nanoscale considerations of dose analysis are referred to as nanodosimetry, however, because the methodology does not change from microscale considerations, microdosimetry is used in this chapter to refer to dosimetric analysis below millimeter scales [233, 241]. To evaluate the outcomes of radiotherapy as a function of cell damage, it will be essential to better understand the fundamental mechanism involved in biological damage by radiation [281]. In biology, this will require an improved understanding of the biological processes within and between cells. In

physics, it will necessitate an improved theoretical determination of radiation track structure through biological material.

Evaluating radiation damage to DNA and other small cellular components requires a shift in measurement to the nanoscale [155, 280]. Recall from Section (1.2) that damage to DNA from photon therapy is done primarily indirectly; through secondary electrons and reactive chemical species [288]. Additionally, low-energy electrons (LEE) are critical considerations in biological damage and are integral to radiosensitization (Section 1.4) [289-290, 295]. Electrons with electron volt (eV) level energies have ranges on the nanometer scale. This can be important to determine the ensemble of particle histories and thereby to determine the path of secondary electrons down to the excitation threshold of a media (7-10 eV for water) [155, 282, 287] (Figure 5.1).

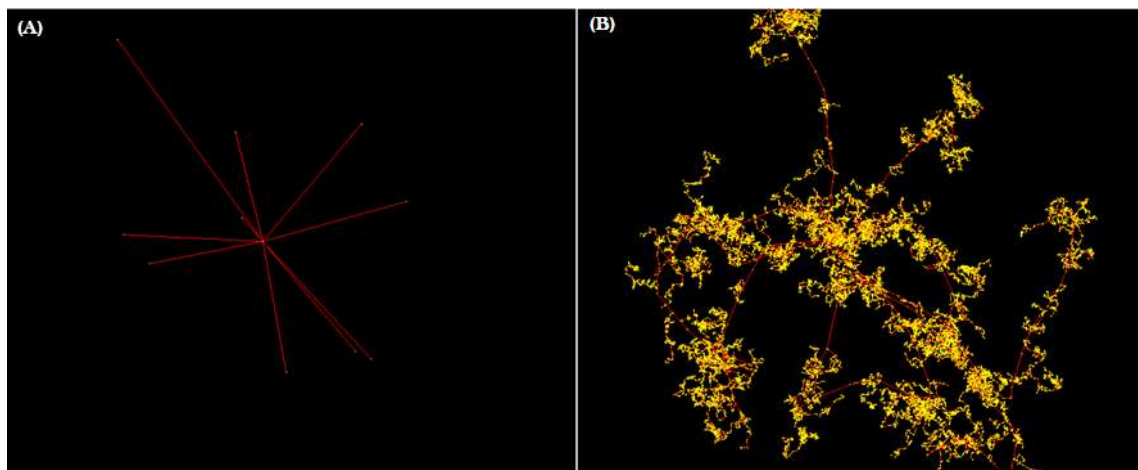


Figure 5.1 – Differences in electron track structure resulting from differences in energy cutoff. (A) With energy cutoff at 1 keV (standard for general purpose MC codes) the electron tracks (red) deposit energy at the end of their range. (B) With energy cutoff at 8.22 eV the electrons are capable of traveling farther and creating secondary electrons (yellow) that deposit energy throughout the path of the electron.

The Monte Carlo (MC) approach, is critical for simulation of radiobiology. The research in biological MC has been largely motivated by the need for improved planning tools for heavy-ion therapy, but radiosensitization studies have also featured prominently [124, 132, 136, 155, 221, 283-286]. The MC techniques used here differ in some respects from those presented in Chapters (2-3). At the microscale, predictions will need to account for physical interactions to lower energies, as well as physiochemical, and chemical processes.

Recall from Section (2.3) that many general purpose radiation transport MC codes rely on the averaging of many individual histories at certain energy or geometrical thresholds resulting in a condensed history (CHMC) [280-281]. This approximation is implemented for large-scale simulations to make the process computationally feasible [280]. The CHMC approach uses multiple scattering theories and stopping power data to be applicable to many materials; they can be used for a variety of applications usually from the keV up to the GeV-TeV energy range, spanning from high-energy physics, to medical physics and space radiation applications [155]. CHMC is however, intrinsically unsuitable for analysis of particles at the nanometer scale [280]. An alternative MC approach is referred to as track structure (TSMC) modeling, where each particle is tracked independently, event-by-event [287] (Figure 5.2).

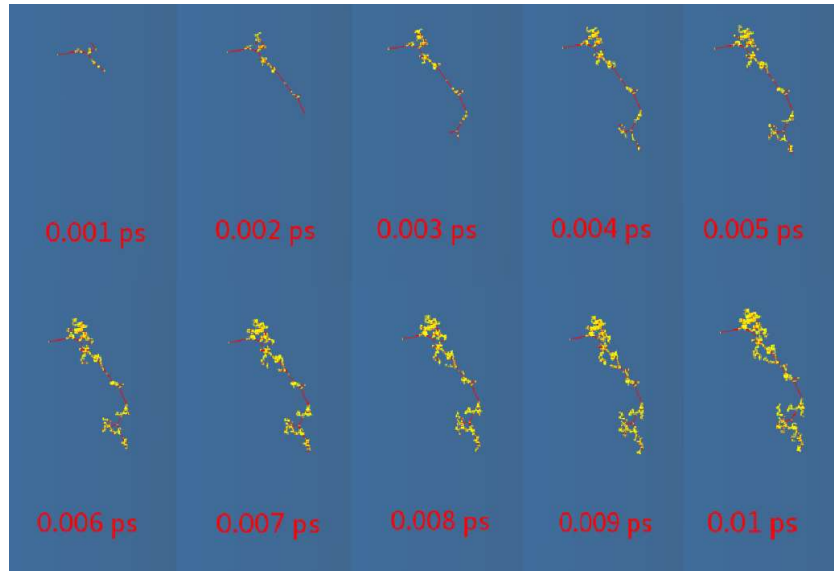


Figure 5.2 – Track structure evolution of an individual electron and the resultant secondary electron creation is shown over the timespan of 0.001 ps to 0.01 ps. TSMC does not combine the histories of a number of particles as does CHMC, allowing for time based dosimetric analysis.

MC simulation accuracy is limited by the realism of their physics models. With TSMC codes, this limitation results from the experimental difficulties of measuring LEE [295]. Biological media are often approximated by liquid water. For LEE, the dominant processes in liquid water are ionization, electronic excitation, and elastic scattering [291]. Unfortunately, measurements in liquid water are difficult, and often approximations are made by theoretical and semi-empirical models using data from water vapor [291, 298-302]. Additionally, the approximation of biological material as water can be limiting for certain applications, although substantial experimentation and theoretical progress has been made to provide data for LEE interaction with structural components of DNA [287, 292-293].

For the macroscopic MC simulations used previously (Chapters 2-3), the calculations of dose enhancement with high-Z elements, were completed by mixing water with metals in heterogeneous compositions. For TSMC models, this methodology falls short on two accounts:

physics interaction cross-sections are often unavailable for high-Z elements; and resulting distributions of secondary radiation from metal particles are anisotropic on the nanoscale [124, 132, 136, 221, 286]. Numerous techniques have been developed to adapt to those limitations, including the use of macroscopic electron spectra. High energy electrons (> 1 keV) are generated using CHMC tools in a macroscopic representation of the system including the metal under investigation. These electrons are then input into a microscopic representation and tracked to low energies (<10 eV) within the water-only geometry [127, 200]. Cross-sectional data for water are used to evaluate the scattering, excitation, and ionization processes that each electron undergoes as it deposits energy down to the cutoff energy.

This chapter will introduce the TSMC code Geant4-DNA, and use macroscopic electron spectra data from copper containing cells to estimate dosimetric quantities on the nanoscale. Chapter 5 is also intended to unite concepts from each of the preceding chapters to fulfill the initial thesis of this dissertation and make the most accurate estimate of the radiosensitization potential of CuATSM. Recall the central postulate of this work: *Can CuATSM be used as a radiosensitizer of external beam radiation?* Chapter 2 attempted to solve this question by macroscopic analysis of copper; Chapter 5 will extend this investigation into the nanoscale. Chapter 3 attempted to clarify lingering clinical considerations of CuATSM in a tumor model; Chapter 5 will appropriate CuATSM uptake data from Section (3.3) to consider effects in a cellular model. Chapter 4 made direct biological measurements of radiosensitization in DNA and mammalian cells confirming the central thesis directly. The concentration of copper necessary for that radiosensitization however, was substantially lower than what was needed for macroscopic dose enhancement, prompting a follow-up question: *How does CuATSM cause radiosensitization at lower concentrations than macroscopic dose evaluation would predict?*

Chapter 5 will attempt to address this discrepancy by analyzing enhancements to microdosimetry, DNA strand breaks, and chemical species creation.

5.2 – *Geant4-DNA*

The implementation of TSMC computational tools to simulate radiation in biological matter has been advancing rapidly. Arguably, the most state-of-the-art examples are the PARTRAC and KURBUC codes which are able to simulate direct and indirect damage to DNA, as well as biological repair [155, 303-306]. Unfortunately, these codes are not openly available to users, preventing large-scale usability and adaptability to various needs [306].

The Geant4-DNA (G4DNA) project is an open access, experimentally validated, software framework for simulating early radiobiological damage on the nanoscale [155, 280-282, 285, 306]. The G4DNA project was initiated in 2001 at the European Space Agency for estimations of biological effects from space missions. Currently, the project is managed by the G4DNA collaboration; a multidisciplinary group with experts in theoretical elementary particle physics, radiochemistry, and microdosimetry [308]. G4D is an extension of the general-purpose Geant4 Monte Carlo simulation toolkit, a state-of-the-art code that was originally developed at the European Organization for Nuclear Research (CERN) for high energy physics at the Large Hadron Collider [307]. G4DNA is made possible because Geant4 software is built with C++; an object oriented programming language that provides flexibility and extensibility [306]. Geant4 is updated frequently, the release that was used for this work is: *geant4.10.04.p01*. G4DNA has been extensively benchmarked against experimental data and other MC codes [306, 309-311].

The open nature of Geant4 has resulted in numerous physics models and processes that can be implemented by the user depending on their needs. This is facilitated with pre-built C++

physics constructor classes; which contain the list of particles, processes, and models available for applications [281, 306]. The default physics constructor for LEE processes in water is called *G4EmDNAPhysics*; it employs the G4DNA extension (Table 5.1), as well as low energy models for photon interactions based on the Livermore library of the low energy electromagnetic physics processes and standard energy models for positrons [281, 306].

Table 5.1 – List of G4DNA physics processes for DNA extension.

<i>Process</i>	<i>Model</i>	<i>Low Energy Limit</i>	<i>High Energy Limit</i>
<i>Elastic Scattering</i>	<i>Screened Rutherford</i>	<i>8.23 eV</i>	<i>10 MeV</i>
	<i>Campion (alternative)</i>	<i>8.23 eV</i>	<i>10 MeV</i>
<i>Excitation</i>	<i>Emfietzoglou</i>	<i>8.23 eV</i>	<i>10 MeV</i>
<i>Ionization</i>	<i>Born</i>	<i>12.61 eV</i>	<i>30 keV</i>

Developments are ongoing for the project and after publication, the developments are made available as examples for open access with released versions of the Geant4 toolkit. For this investigation, two examples were adapted to evaluate microdosimetry and radiochemical yield within a CuATSM loaded cell. All simulations were developed and tested with the Geant4 Virtual Machine, developed by the Centre d’Etudes Nucléaires de Bordeaux-Gradignan. Simulations were subsequently run for production using the Rocky Mountain Advanced Computing Consortium (RMACC) Summit supercomputer running Red Hat Enterprise Linux Server 7.3 with access to up to 904 Intel Xeon E5-2680 v3 processors 12 cores X 2.5 GHz [115].

Pdb4dna

For accurate estimates of DNA damage, realistic cellular geometries should be considered [293-294]. The *pdb4dna* example is used to simulate energy deposition in a target volume with a geometry that can be defined from a protein databank (PDB) model [295, 306, 308, 312-313]. Additionally, using time and positional information collected in a DNA geometry, strand breaks can be estimated. In this case a compact tetranucleosome was used as the structure. This DNA/protein structure was derived from *Xenopus laevis* (African clawed frog), and resolved with x-ray diffraction to 9 Å resolution [312-313] (Figure 5.3).

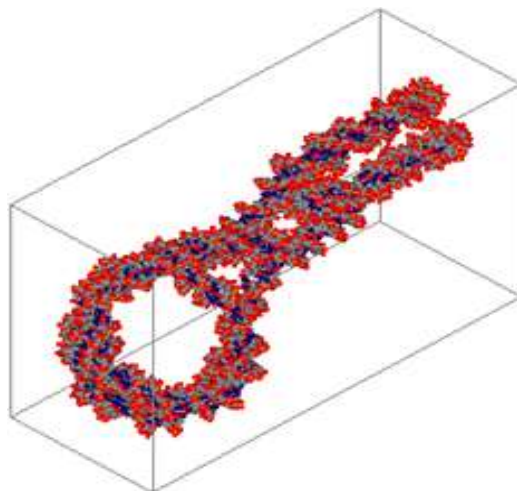
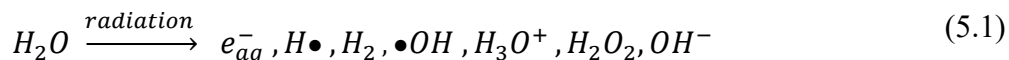


Figure 5.3 – Geometrical model of compact tetranucleosome implemented for *pdb4dna* simulation of energy deposition and strand breaks. The source of the geometry is the protein databank (PDB). CPK color model used for representation; carbon (gray), oxygen (red), nitrogen (blue), sulfur (yellow), phosphorus (orange).

Chem4

DNA damage in a living cell by ionizing radiation is about one-third direct and two-thirds indirect [230]. Indirect damage results from radiation induced reactive species in the medium surrounding the DNA. Water composes up to 90% of living mater, therefore water radiolysis is

closely related to the biological damage to biological tissue. Excitation and ionization of water molecules interacting with radiation produce a number of chemical species within the nanoseconds following irradiation:



These molecules have lifetimes of nanoseconds and are considered the primary yield of radiolysis; among them, the hydroxyl radicals ($\bullet OH$) are the most critical for DNA damage. Interaction of hydroxyl radicals with DNA can cause strand breaks that may be repaired on the microsecond scale [230, 234]. Hydroxyl radicals also react with other hydrogenated molecules (XH) to result in secondary radicals ($X\bullet$):



These molecules have lifetimes of microseconds and can cause irreparable damage to biologically important molecules (BIM):



The implementation of chemistry tracking in G4DNA, requires the activation of an additional physics constructor. Physics constructors can either be: complementary, making available a different non-overlapping set of particles, models, and processes that do not interfere with other constructors within a specified energy range; or alternative, overriding models and processes [306]. For low energy physics modeling, there is a complementary chemistry physics constructor: *G4EmDNAChemistry* which introduces several products of radiolysis [281, 314].

With *G4EmDNAChemistry*, the physical interactions resulting in energy deposition from *G4EmDNAPhysics* are followed by physicochemical and chemical stages [281, 314]. The former

occurs within picoseconds of energy deposition, and includes ionized and excited water molecules through dissociative attachment processes. Following, the nanosecond scale chemical stage, allows for the creation of new chemical species that can be tracked through diffusion and mutual interaction in liquid water and deposit energy in a target volume (Figure 5.4).

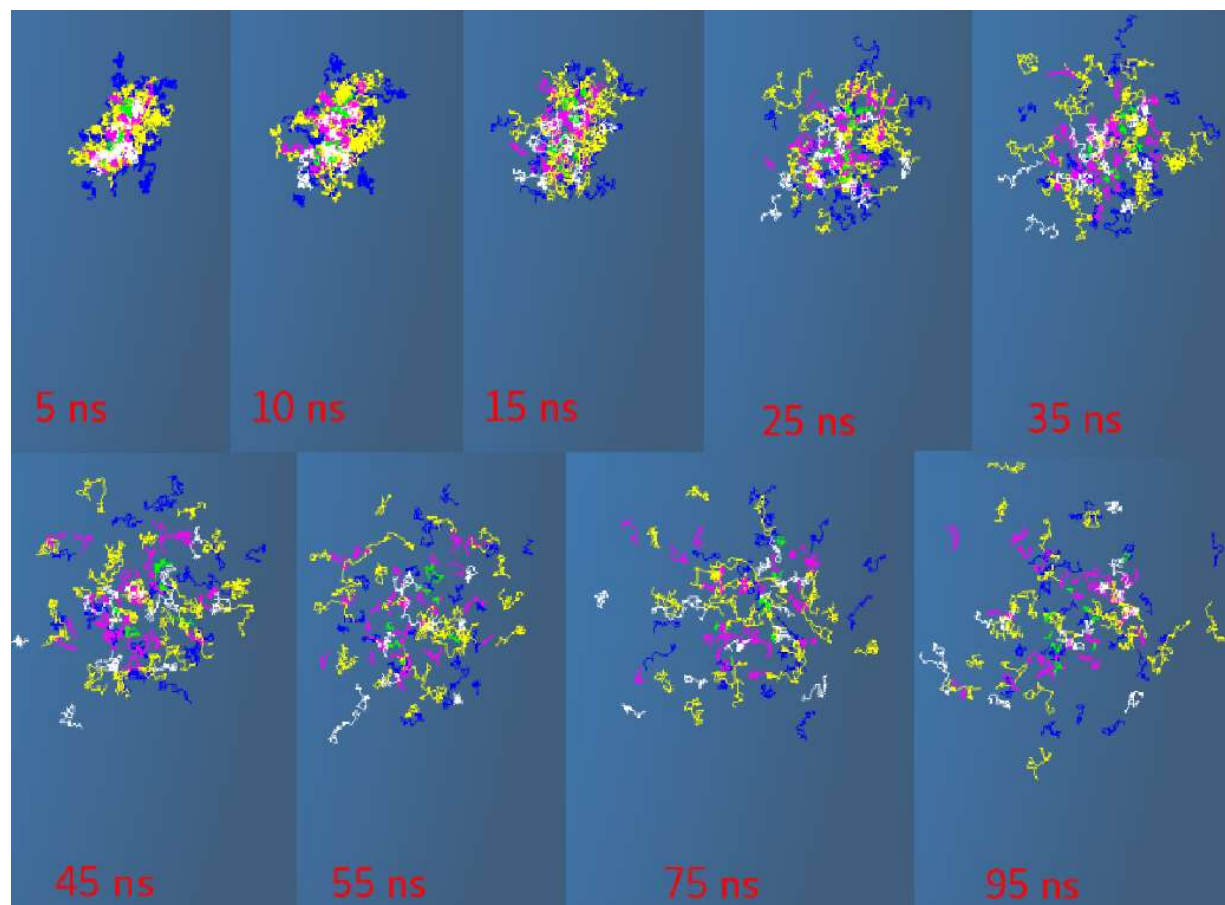


Figure 5.4 – Chemical species generation, diffusion, and mutual interaction to create different species. Interactions occur on a nanosecond time scale. Chemical species represented here: aqueous electrons (purple), hydronium (red), hydroxide (blue), hydroxide ion (pink), molecular hydrogen (cyan), atomic hydrogen (lime green), and hydrogen peroxide (forest green).

The *chem4* example is designed to track and score the total radiochemical yield of the following chemical species: aqueous electrons (e_{aq}^-), hydronium (H_3O^+), hydroxide ($\bullet OH$), hydroxide ion

(OH⁻), molecular hydrogen (H₂), atomic hydrogen (H•), and hydrogen peroxide (H₂O₂).

Radiochemical yield (*G*) is defined as:

$$G(t) = \frac{N(t)}{E_{dep}} = \frac{\text{Number of chemical species } X \text{ at time } t}{\text{deposited energy scaled to 100 eV}} \quad (5.4)$$

The molecules can also mutually interact to form different species by the reactions in Table (5.2) [314-317].

Table 5.2 – Intermolecular reactions and reaction rates within the G4DNA chemical model.

<i>Reaction</i>	<i>Reaction Rate (10⁷ m³ mol⁻¹ s⁻¹)</i>
$H_3O^+ + OH^{-1} \rightarrow 2 H_2O$	14.3
$\bullet OH + e_{aq}^- \rightarrow OH^{-}$	2.95
$H\bullet + e_{aq}^- + H_2O \rightarrow OH^{-} + H_2$	2.65
$H_3O^+ + e_{aq}^- \rightarrow H\bullet + H_2O$	2.11
$H\bullet + \bullet OH \rightarrow H_2O$	1.44
$H_2O_2 + e_{aq}^- \rightarrow OH^{-} + \bullet OH$	1.41
$H\bullet + H\bullet \rightarrow H_2$	1.20
$e_{aq}^- + e_{aq}^- + 2H_2O \rightarrow 2 OH^{-} + H_2$	0.50
$\bullet OH + \bullet OH \rightarrow H_2O_2$	0.44

5.3 – Simulation Design

This study implements designs based on the *pdb4dna* example for microdosimetric evaluations and the *chem4* example for radiochemical yield. The unique aspects of these simulations are discussed in the subsequent sections. The geometry used to define the cell, and the electron spectra tracked to low energies are consistent between the two simulations. Benchmarking data are provided in Appendix (C.1).

Mammalian Cell Geometry

Mammalian cells have substantial range in size, from 10 to 100 μm in diameter [151]. Additionally, the average diameter of the cell nucleus is approximately 6 μm , which occupies about 10% of the cell volume. Furthermore, cell sizes can change because of their external environment and nutritional supply [318]. Although tools are available with G4DNA to create realistic cellular phantoms based on confocal microscopy imaging, a more abstract method was implemented here to generalize the cell geometry [319].

Cell nucleus and cell body were each represented by spheres; the diameters of these spheres will fall within the ranges for mammalian cells, and be selected based on the parameters of the electron radiation. Recall from Section (2.7), electron spectra data and Auger electron emissions were calculated within a copper solution phantom. The maximum energy window for electron spectrum (26.5 keV) in the SARRP case was used to determine the cell body dimension, and the maximum Auger electron energy (8.972 keV) was used to determine the cell nucleus dimension. The ranges of those electrons were determined from tabulated data of continuous-slowing-down approximation range (NIST-CSDA) above 10 keV, and MC simulations below 10 keV (G4DNA-*TestEm12*) [113, 308] (Figure 5.5).

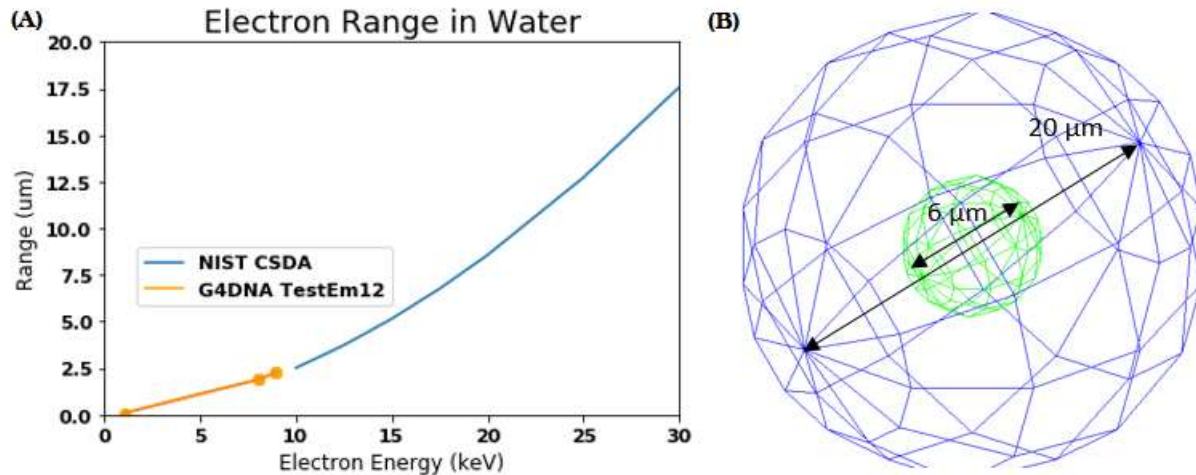


Figure 5.5 – Cell dimensions rationale. (A) Electron ranges in water. NIST CSDA range data are unavailable below 10 keV; The G4DNA extension to the *TestEm12* example was used to calculate the electron ranges of the Auger electrons (<10 keV). (B) Geant4 cell geometry parameters.

Electron Spectra

Recall from Section (3.3), that several tumor uptakes of CuATSM were considered based on application method and toxicity of DMSO. CuATSM injected at a concentration of 1.35 g/kg (*High*), was utilized as the starting concentration for electron spectra determinations. This concentration was then partitioned between the cell nucleus and cell cytoplasm compartments.

Obata, et al., evaluated the uptake of CuATSM into subcellular compartments [80]. They found that within hypoxic Ehrlich ascites tumor cells approximately 30% of the ATSM was deposited in the nucleus of the cell, however, accounting for normal brain cells and tumor cells with different oxygen concentrations, the compartment uptake was highly variable (5% - 35%). Burgman, et al., found dynamic uptake of CuATSM in cells that varied with time, oxygen concentration, and by cell type [123]. Attempts were made to investigate the subcellular uptake in canine osteosarcoma cells with trace element mass spectroscopy analysis of copper. The

results of the experiments were erroneous, however, the copper concentration indicated substantial variation in cellular compartment uptake. These considerations motivated the implementation of a span of copper concentrations between compartments (nucleus – 0-85%). FLURZnrc (Section 2.4), was used to evaluate the electron spectra from copper solutions in the cell nucleus and cytoplasm with a span of concentrations. SARRP (Section 2.5), was used as the external beam input. The base material for nucleus was from ICRU, and for cytoplasm was soft tissue (ICRP) [149-150] (Figure 5.6).

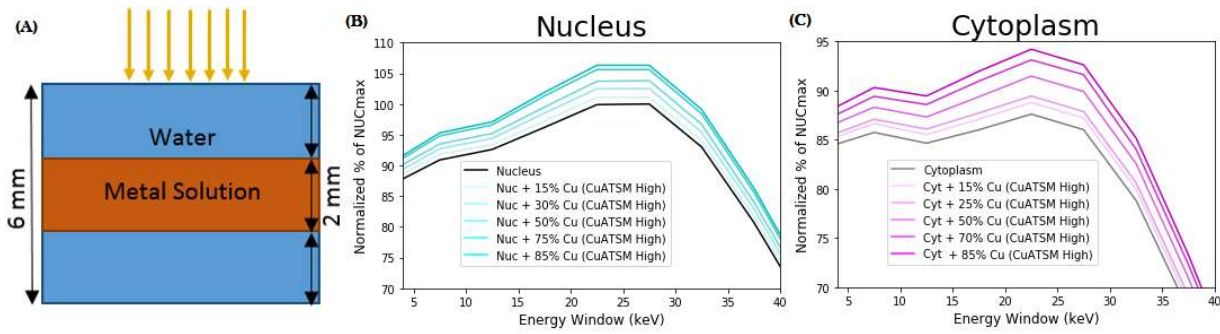


Figure 5.6 – The electron spectra used for input to the microdosimetric models were generated with FLURZnrc in a cylindrical phantom. (A) Phantom geometry used to create the electron spectra; see Section (2.7) for details on geometry within FLURZnrc. (B) Electron spectra for nucleus. Copper concentration in compartment ranges from 0-85% of the initial 1.35 g/kg CuATSM injection. Spectra normalized to maximum value of the electron spectrum for the nucleus without copper case. (C) Spectra for cytoplasm. Copper concentration ranges from 0-85% with values complimentary to those found in the nucleus. Cell nucleus material (ICRU) has a higher effective atomic number than soft tissue (ICRP), resulting in more electron production.

The material files used to calculate the electron spectra will be available in Appendix (C.2). A plot of the rationale for compartment distribution is provided in Appendix (C.3).

5.4 – Microdosimetric Model

The *pdb4dna* example was used as the starting point for evaluating dosimetry and DNA strand breaks from the copper spectra. The target was the DNA segment from Figure (5.3); the atomistic representation is built into the functionality of the example with each atom filled with *G4_WATER* material. The segment is bounded by a rectangular prism containing *G4_Galactic* material. The geometry was extended with a single sphere representing the cell body with a diameter of 20 μm filled with *G4_WATER* material. The nucleus and cytoplasm electron spectra were used as the particle source input.

The starting point of the radiation source for the microscopic modeling was derived from the macroscopic modeling that determined the electron spectra. These spectra were not entire phase space files, and therefore the direction of electron emissions required some approximations. The proximal angular dispersion of electron ejections from the photon irradiation of an atom or particle depends on photon source direction, but is inherently a nanoscale consideration because of the probabilistic processes inherent in the creation of an electron [136, 221]. The materials representing the nucleus and cytoplasm in the macroscopic model were mixtures of copper and tissue that do not account for the individual atomic interactions with photons that would result in those electrons. Therefore, the initial electron direction was approximated as isotropic emissions.

Furthermore, the high pressure liquid chromatography (HPLC) data used to approximate the copper distribution within the cells (Obata, et al.) was only able to resolve whether the CuATSM was in the nucleus or the cytoplasm. The distribution of copper within each subcellular compartment would be difficult to elucidate with current technology. We could reasonably expect that copper, as a small ion, would distribute throughout the enclosing subcellular

compartments dynamically by diffusion. The emission of electrons from interaction with copper within a subcellular compartment, therefore, could be approximated as uniform.

For a small DNA segment, the originating direction of an impinging electron would be inconsequential for determining energy deposition, but the distance between the electron source and the DNA target would determine whether or not the electron would have the energy to travel far enough for an interaction to occur between the electron and the DNA. Therefore, the electron source starting points were uniform randomly distributed along a single direction from 0.01 nm to 3 μm in the case of the nucleus, and 3 μm to 10 μm for the cytoplasm.

Finally, the probability of an isotropically emitting electron source interacting with a nanoscale volume such as the DNA segment can be estimated by the solid angle (Ω) that the area (A) of the DNA segment subtends, from a given distance in the cell (r) [198]:

$$\Omega = \frac{A}{r^2} [sr] \quad (5.5)$$

The probability of an isotropically emitted particle interacting with a small target is very low. Consider, for example, the geometry of the *pdb4dna* example. The largest dimension of that geometry is 19.6 μm , and assuming a square target, the total target area would be 384.3 μm^2 . For an electron a distance of 10 μm from this target, the total target area would subtend a solid angle of 3.8(10^{-14}) sr. Therefore, if 10^6 particles were necessary for a simulation, an isotropically emitting source would necessitate 3.3(10^{14}) histories to achieve the same level of precision and statistical noise over the area of interest. As a computational consideration, the initial starting direction was set to point toward the DNA segment and not be isotropically emitting. Electron spectra from the nucleus and cytoplasm were run independently with different source positions linearly distant from the DNA and the results were summed together.

This approximation would result in a substantial overestimation of electron fluence from the cytoplasm over the nucleus emitting locations because of the small solid angles are further subtended at greater distances from the target. To adjust the relative fluence ratios, an approximation of the difference in electron interaction probability between nucleus and cytoplasm was determined. Solid angles were calculated at several distances from the DNA target corresponding to distances within the nucleus and cytoplasm. A power equation was fit to the points in the nucleus, and an exponential equation to those in the cytoplasm (Figure 5.7):

$$\Omega = 4 * 10^{-12} r^{-2} \text{ (nucleus function)} \quad (5.6)$$

$$\Omega = 9 * 10^{-13} e^{-0.336r} \text{ (cytoplasm function)} \quad (5.7)$$

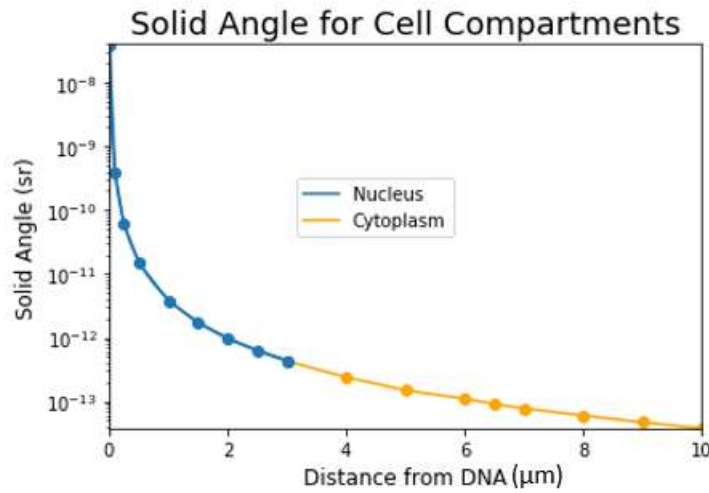


Figure 5.7 – Solid angle at various distances within the nucleus and cytoplasm to the DNA segment. Functions were fit to the data and the ratio of the areas under the curves was used as an estimate for reduced electron fluence from the cytoplasm.

The fluence in the cytoplasm was reduced by the ratio of the area under the curves of the cytoplasm function to the nucleus function, as an approximation of the probability ratios. A representation of the source within geometry is provided in Figure (5.8).

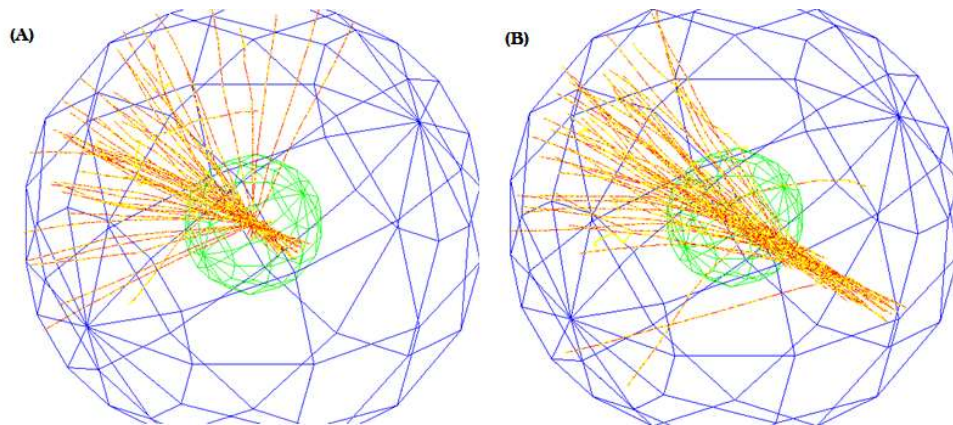


Figure 5.8 – Representation of microdosimetry irradiation scheme within geometry. Simulations for nucleus and cytoplasm were run independently and subsequently summed. (A) The spectra emitting within the nucleus are directed toward the target DNA; the initial starting position is randomly assigned along a single axis from 10 nm to 3 μm from the center. (B) The spectra emitting within the cytoplasm; random starting position from 3 μm to 10 μm from the center, fluence was reduced from the nucleus case by the ratio of probabilities of interaction.

Using this methodology, the energy deposited in the DNA target was determined from the nucleus and cytoplasm electron spectra for the case with equal distribution of CuATSM between the two compartments. The predicted spectrum for the nucleus without copper case (NXC) from the macro MC simulations as detailed in Section (5.3), was used as the basis for generating the electron fluence to be used in the microdosimetry in each case. The total number of electrons in the NXC case was $5(10^7)$ and distributed in discrete 5 keV energy windows from 3.5 keV to 222.5 keV with the relative number of electrons for each energy window corresponding to the relative fluence in the spectral distribution (Figure 5.6).

The NXC case was combined with a cytoplasm without copper case (CXC) to compose the without copper case (XC). The number of electrons for each energy window from 3.5 keV to 222.5 keV for the CXC case was determined from the relative electron fluence from that simulation (Section 5.3) normalized to $5(10^7)$ total particles in the NXC case. It is clear from

Figure (5.6) that this normalization would result in a lower number of electrons in each energy window for the CXC case compared to the NXC case.

Each of the other electron spectra that were compared to the XC case contained copper as deposited by *High* CuATSM (Section 3.4), with distribution of copper shared between nucleus and cytoplasm from a low of 15% copper in the nucleus (85% cytoplasm) to a high of 85% of copper in the nucleus (15% cytoplasm). The number of electrons in the energy windows for each of these spectra were similarly determined by normalizing to the relative spectrum within the NXC case. From examination of Figure (5.6) it is clear that for each nucleus containing copper case the number of electrons is higher in each energy window compared to the NXC case and increases with concentration deposited in the nucleus from 15% to 85%. Similarly each cytoplasm copper case has a higher number of electrons in each energy window than the CXC case with an increase with concentration in the cytoplasm from 15% to 85%. Finally, each combination of cytoplasm and nucleus with copper has a higher number of electrons in each energy window than the XC case.

The spectra for the micro MC model were then input into the system as discrete monoenergetic electrons spanning the energy range of the spectra in 5 keV intervals. An abbreviated example input file is included in Appendix (C.4). The number of interactions with the target were tallied for each simulation and plotted in 1 eV energy windows from 1 to 1000 eV. The cytoplasm contribution to energy deposition is minimal. Initial simulations indicated nearly zero deposition, therefore an amplification of electron fluence (x1000) from that compartment was simulated to demonstrate the scale of discrepancy between the two compartments. (Figure 5.9).

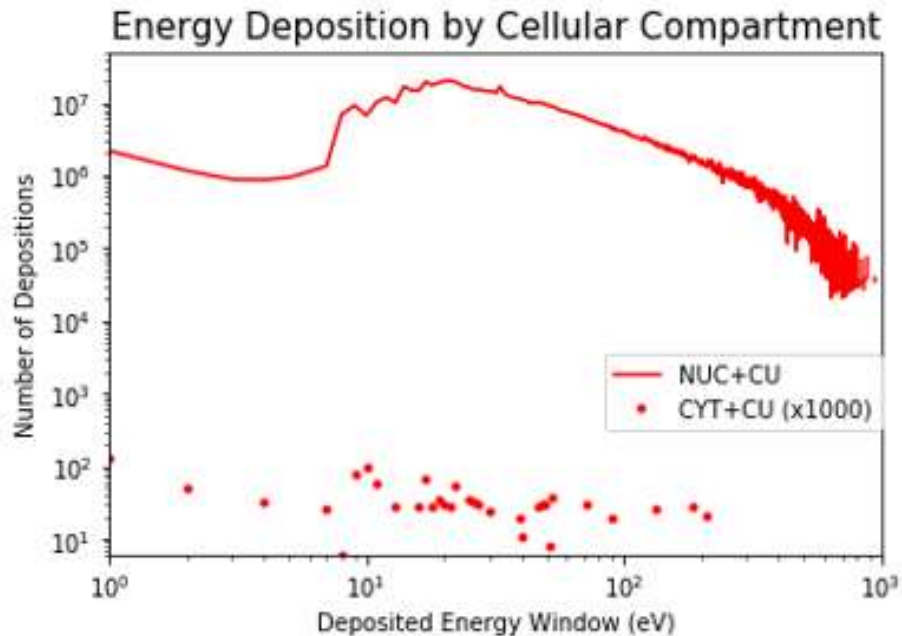


Figure 5.9 – Energy deposition by energy window (1-1000 eV) from nucleus and cytoplasm with equal distribution of CuATSM in each cellular compartment. The number of interactions from the cytoplasm compartment with the DNA is considerably lower than that from the nucleus compartment even with an amplification of fluence by three orders of magnitude.

For the values reported in the subsequent results, the nuclear and cytoplasm energy depositions are summed, however, in all cases the cytoplasm contribution is inconsequential.

Energy deposition was tallied in energy bins comparing the copper (+C) case with equal distribution of CuATSM between nucleus and cytoplasm, and the no copper (XC) case. Energy enhancement factors (EEF) (Section 2.2) were calculated with Equation (2.7) using the ratio of the +C case to the XC case (Figure 5.10).

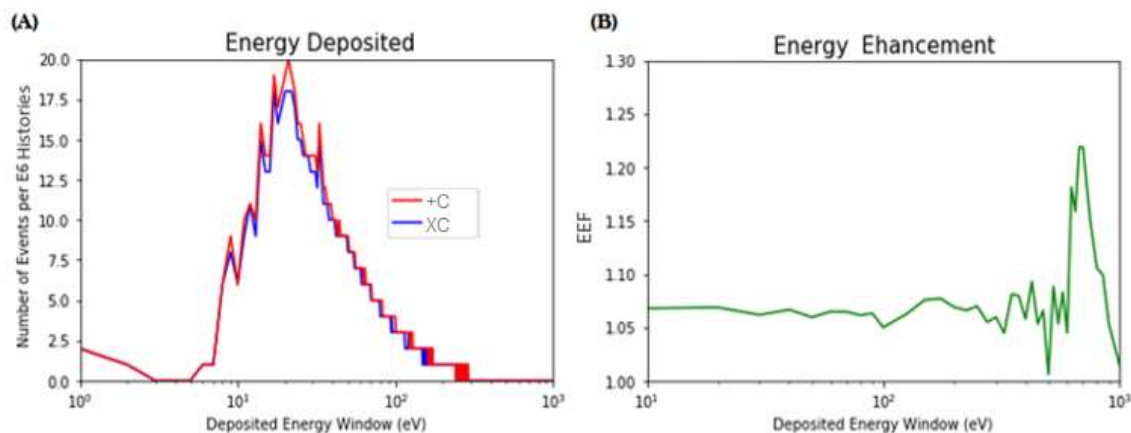


Figure 5.10 – Comparison between the +C case and the XC case, with $5(10^7)$ histories normalized to NXC. (A) Energy deposited, number of depositions per E6 histories for energy windows (1-1000 eV). (B) Energy enhancement for +C case for energy range 1-1000 eV. EEF is averaged for pools of energy bins to reduce fluctuations: 10 eV pools are used from 0-100eV; 25 eV pools for 100-500 eV; and 50 eV pools from 500 eV to 1000 eV. Energy enhancement is consistent (1.07) up to 300 eV; the small number of depositions above the 300 eV window result in noisy evaluation of EEF, a common feature of energy deposition simulations caused by the low probability of a large energy deposition in a small volume (Figure C.3) [241].

Copper spectrum resulted in modest increase in energy deposition in all 1 eV energy windows up to 300 eV. Particle yield decreased from 1 eV to 8 eV; a large increase in yield occurred from 8 eV corresponding to the excitation and ionization cross sections for water and DNA nucleotide materials. Particle yield peaked at about 20 eV with a gradual decline from 20 eV to 300 eV. Above 300 eV the low probability of large energy depositions within a small volume resulted in random fluctuations in yield without clear amplification from copper spectrum. EEF values indicated an enhancement in energy deposition from copper spectrum of about 7% for energy windows up to 300 eV. Above 300 eV few depositions results in noisy evaluations of EEF.

The *pdb4dna* code also allows for estimations of DNA strand breaks within the nucleotide geometry. The default definition for DNA strand breaks were used in the simulation;

a single stranded break (SSB) was determined to occur if 8.22 eV was deposited in a nucleotide; and a double stranded break (DSB) was tabulated when two SSB occurred on complimentary strands within 10 base pairs (bp). Complex breaks were tabulated when an SSB occurred within 10 bp of another SSB on the same strand (Figure 5.11).

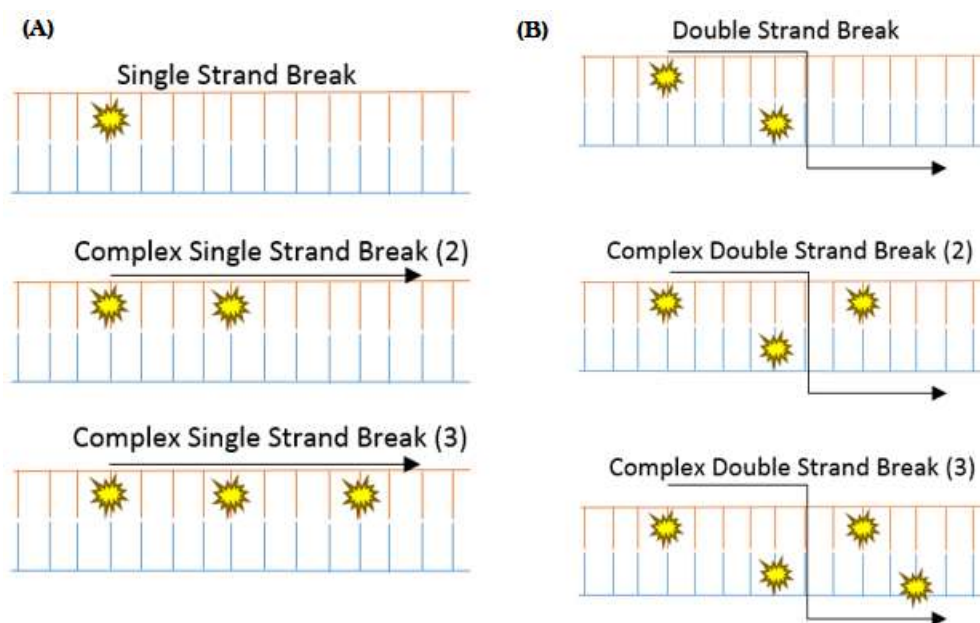


Figure 5.11 – DNA strand break definition. (A) SSB occurs when 8.22 eV of energy are deposited in nucleotide. Complex SSB is tabulated when additional SSB occurs within 10 bp. (B) DSB occurs when two SSB occur within 10 bp of each other on complimentary strands (blue/red). Complex breaks occur when an additional SSB occurs within 10 bp of the DSB.

The SSB and DSB were compared between the +C case, and the XC case (Figure 5.12).

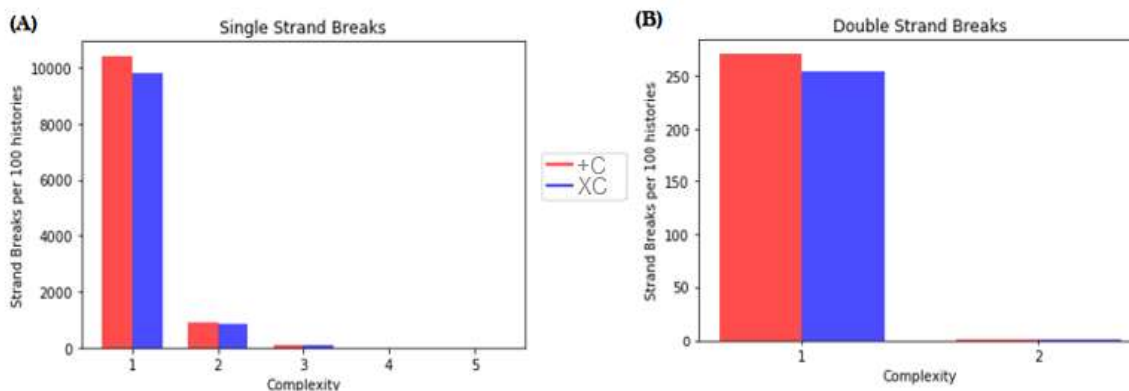


Figure 5.12 – DNA strand break comparison between +C copper spectrum and XC spectrum with $5(10^7)$ histories normalized to NXC. Number of breaks per 100 histories. (A) Single strand breaks are more prominent in the +C case. Complex breaks are also tabulated and occur at a frequency of about 1/10 that of non-complex. (B) Double strand breaks occur less frequently (1/40) than SSB.

The goal of this section is to determine the microscopic dose enhancement (mDEF) within a nanoscale target (Section 2.6). As noted earlier, the *pdb4dna* example allows for calculation of deposited energy within the target volume. Recall from Section (1.2), that dose and energy are closely related, and equivalent under certain conditions; unfortunately, those conditions are not present at the nanoscale. Dose quantities are based on averaging procedures that make the concept of dose at microscopic scales untenable [146-148, 214, 217]. This is because ionizing radiation interacts randomly with matter, with substantial fluctuations for smaller volumes, smaller doses and for more densely ionizing radiations [331]. Absorbed dose is a statistical average that disregards the importance of the statistical fluctuations that occur in small volumes and is therefore inadequate to describe the energy deposited in cellular and sub-cellular structures. Although dose no longer correlates perfectly with energy at this scale, energy per mass is still a valid measurement in an analysis volume [330]. The target region for these microdosimetric simulations have identical volume and mass, therefore, dose enhancement is still a valid measurement [221].

Microscopic DEF was calculated (Equation 2.10) for each copper distribution as the total energy deposited compared to the XC case. Single strand break enhancement (SSBEF), and double strand break enhancement (DSBEF) are evaluated similarly:

$$SSBEF = \frac{SSB_{+copper}}{SSB_{xcopper}} \quad (5.6)$$

$$DSBEF = \frac{DSB_{+copper}}{DSB_{xcopper}} \quad (5.7)$$

Results by concentration of copper in the nucleus are plotted in Figure (5.13).

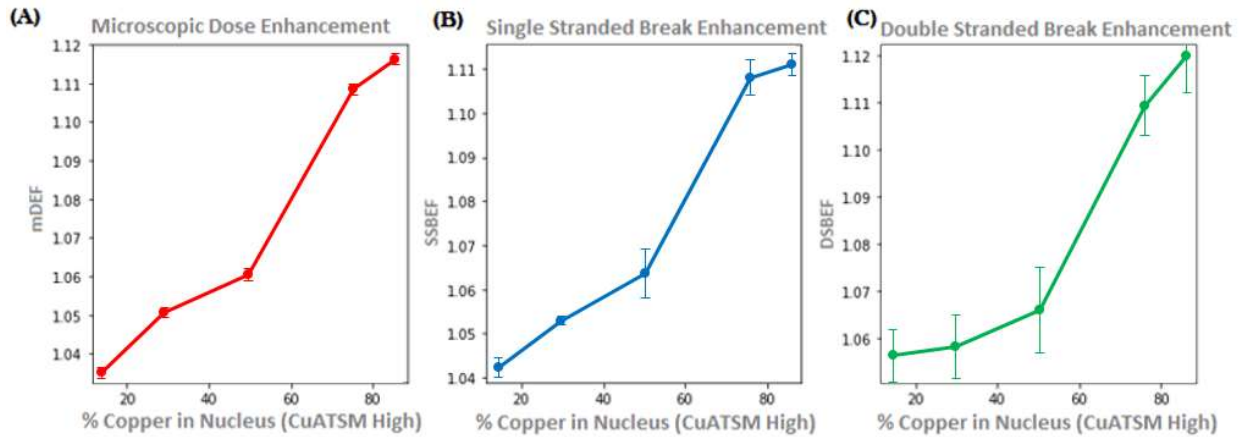


Figure 5.13 – Enhancement factors for copper spectra. (A) Microscopic DEF. (B) Single-strand break enhancement. (C) Double-strand break enhancement. All factors increase with concentration. (Error bars are standard deviation with N = 5)

Values of energy deposited, SSB, and double strand breaks were summed for the nucleus and cytoplasm compartments, however, as previously elucidated (Figure 5.9), the cytoplasm contribution to tally was minimal. Therefore, each enhancement factor increased with concentration of copper in the nucleus. Each measurement resulted in a maximum enhancement

factor of about 1.12. Although total yield of energy, SSB and DSB are different in scale, the enhancement factor trends are similar.

5.5 – Radiochemical Yield Model

The *chem4* example from the G4DNA package was used as a foundation for evaluating the radiochemical yield enhancement for copper spectra. The geometry was altered to create two concentric spheres with diameters 6 μm and 20 μm , corresponding to the nucleus and cell body respectively. In this case, the target volume for enumerating chemical species was the entire nucleus, rather than a DNA segment.

The electron spectra were simulated from two compartments, nucleus and cytoplasm. The starting position of the source was uniformly random along a single axis from the center of the sphere: 0 μm to 3 μm for the nucleus; and 3 μm to 10 μm for the cytoplasm. The nucleus was a large enough target in this case, that an isotropic emission would have a reasonable probability of interacting from the cytoplasm. Therefore, a uniformly random direction was chosen from the starting position (Figure 5.14).

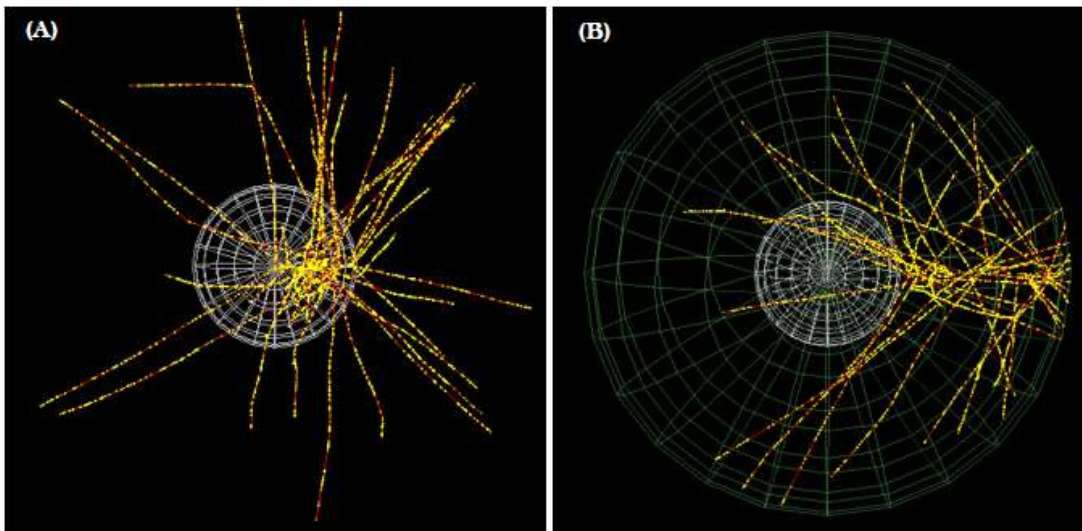


Figure 5.14 - Representation of radiochemical radiation scheme within geometry. Simulations for nucleus and cytoplasm were run independently and subsequently summed. (A) The spectrum for the nucleus has a random starting position from 0 μm to 3 μm . (B) The spectrum for the cytoplasm has a random starting position from 3 μm to 10 μm . The initial direction for both cases is randomly isotropic from the starting position.

The chemical yield from the cytoplasm was collected in two phases: the electron spectra were simulated and the energy deposited in the nucleus was scored; the corresponding energy was then simulated in the nucleus to determine chemical yield. The resulting chemical yields for the cytoplasm and nucleus compartments were summed. The calculation of chemical yield is computationally intensive, and parallel computing methods were not applied for this process as interactions between chemical species histories could affect yield outcome. The radiochemical yield, or G-values (Equation 5.4), are computed using the *chem4* program for a range of deposited energy (1 keV – 20 keV) [320].

Each chemical species can be individually scored at several time points on a relevant scale for the lifetimes of the particles. The case with equal concentration of CuATSM in each compartment is shown in Figure (5.15).

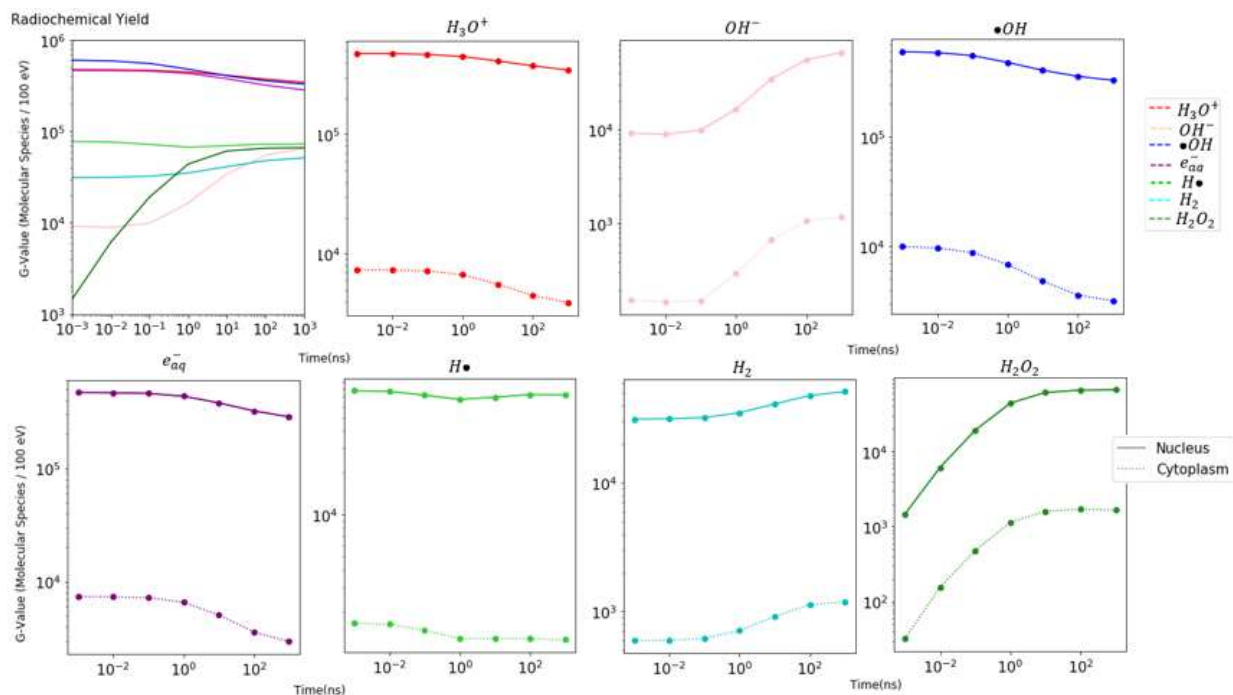


Figure 5.15 – Time based evaluation of radiochemical species yield with equal concentration of copper in nucleus and cytoplasm. Top left displays logarithmic comparison of all species, colors match output of Figure (5.4). Hydronium (red), hydroxide (blue), and aqueous electrons (purple) dominate the radiochemical output, each tabulation decreases with time from 1 ps to 1 μ s. Atomic hydrogen (lime green) decreases to a minimum at 1 ns before increasing. Hydroxide ion (pink), molecular hydrogen (cyan), and hydrogen peroxide (forest green), all increase with time. Nucleus and cytoplasm contribution to the total radiochemical yield are plotted for each species. Events occurring in the cytoplasm contribute approximately 2 orders of magnitude lower to the production of radical chemical species in all cases compared to when they occur in the nucleus.

The radiochemical yield is directly related to total energy deposited by electrons within the target volume, but independent of the energy of the incident electron. Each chemical species has its own characteristic behavior in time, as governed by the equations in Table (5.2) dependent only on energy deposited. Hydroxyl radicals, which were previously denoted as critical for DNA damage (Section 5.2), are among the most prominent molecules created from radiolysis along with aqueous electrons and hydronium. Each of these chemical species have

maximum yield at 1 ps and decrease logarithmically in time up to 1 μ s as they are each primarily consumed upon interacting via the processes in Table (5.2). Atomic hydrogen follows as the fourth most numerous chemical species; the yield of this chemical decreases logarithmically from 1 ps to a minimum at 1 ns then increases logarithmically from 1 ns to 1 μ s. Hydroxide ions, molecular hydrogen, and hydrogen peroxide all increase logarithmically in time from 1 ps to 1 μ s, as they are created from other species via the processes in Table (5.2). The total radiochemical yield is dominated by the nucleus, which has a yield approximately two orders of magnitude larger than the cytoplasm in the target volume. The forthcoming data comparing copper distribution within the cell considers the sum of the two compartments, however, the cytoplasm contribution is negligible.

The maximum total chemical yield occurs at the initial time point of 1 ps. Comparing total chemical yield for the copper cases to the case with no copper (XC), we can define the total chemical enhancement factor (TCEF) as:

$$TCEF = \frac{\text{Total \# of Radiochemicals at 1 ps + copper}}{\text{Total \# of Radiochemicals at 1 ps Xcopper}} \quad (5.8)$$

Additionally, each individual radiochemical can be compared between the copper condition and no copper to define the chemical enhancement factor (CEF) for each molecule:

$$CEF = \frac{\text{\# of Radiochemical at 1 ps + copper}}{\text{\# of Radiochemical at 1 ps Xcopper}} \quad (5.8)$$

Each copper spectra from Section (5.3), was normalized in fluence to the nucleus without copper (NXC) case with a total of 10^4 particles. The spectra were input into the system as discrete monoenergetic electrons spanning the energy range of the spectra in 5 keV intervals. An abbreviated example run file is provided in Appendix (C.5). Values of TCEF were evaluated for

each electron spectrum with copper concentration shared between cytoplasm and nucleus; values are plotted against the copper concentration in the nucleus. The CEF of each individual chemical species comprising the total was also evaluated by normalizing to the yield of that chemical in the nucleus without copper case. The results are plotted against the concentration in the nucleus (Figure 5.16).

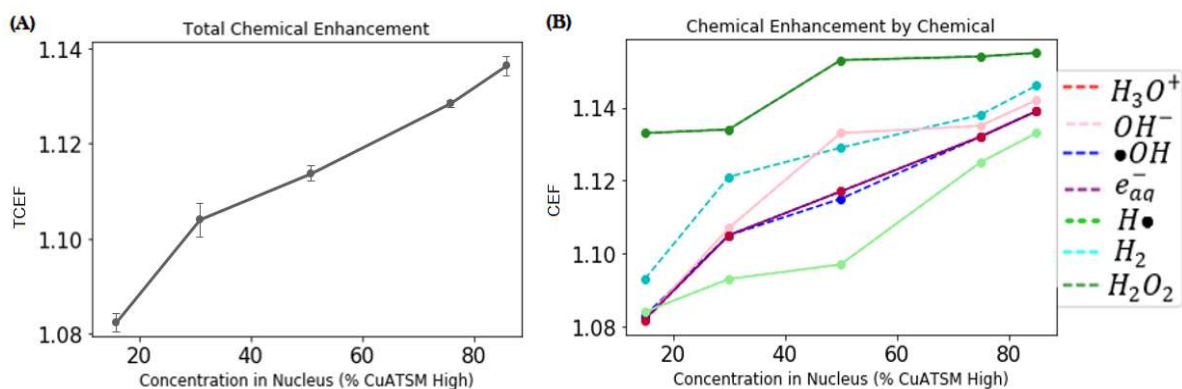


Figure 5.16 – Chemical enhancement measured against percent of copper from CuATSM *High* injection that was deposited in the nucleus. (A) Chemical enhancement factor at 1 ps with total chemical yields compared. (Error bars are standard deviation N = 3) (B) Enhancement for each chemical species at 1 ps. Normalized chemical yields for hydronium (red), and aqueous electrons (purple) are overlapping.

Total chemical enhancement factors increased with concentration of copper in the nucleus. The maximum value of TCEF for these concentrations was approximately 1.14 when 85% of the copper was in the nucleus. Each individual chemical species increased with concentration in the nucleus, however, there were differences between each species. Hydrogen peroxide had the largest CEF (1.155), it also had the least variation in enhancement (0.022) between 15% and 85% copper in the nucleus. Each of the other species behaved similarly starting from a minimum CEF (1.082 – 1.093) at 15% copper concentration in the nucleus and increasing by about 0.05 to a maximum CEF (1.133-1.146) with 85% copper in the nucleus.

5.6 – Discussion

Radiation therapy has long been evaluated by macroscopic changes in tumors caused by absorbed radiation dose. Advancements in radiotherapy will require a more intimate analysis of the changes to the nanoscale cells that compose the tumors. From a physics perspective, analysis at this scale requires a deeper insight into the trajectories and interactions that occur at very low energies. Track structure Monte Carlo (TSMC) is a tool set developed for modeling and predicting outcomes at the nanoscale. Geant4-DNA (G4DNA), an open-source TSMC software package, was used in this investigation to evaluate enhancement of dose, strand-breaks, and chemical species, occurring from CuATSM.

There were several goals for this chapter. As the final experimental content for the dissertation, Chapter 5 was intended to thoroughly conclude the work done in the previous chapters. Chapter 5 completes the analyses conducted in Chapters 2-3; extending the macroscopic dose enhancement studies to the low energy regime, and evaluating dose enhancement within a nanoscale cellular model. The primary motivation for this inquiry, however, was to evaluate an outcome from the biological work done in Chapter 4. The measurements in Chapter 4 indicated that radiosensitization occurred at a substantially lower concentration of CuATSM, than was thought necessary from macroscopic dose enhancement analysis. That finding prompted the inquiry for this chapter: *How does CuATSM cause radiosensitization at lower concentrations than macroscopic dose evaluation would predict?* Efforts to resolve this query focused on the DNA strand break, and chemical species enhancement from CuATSM.

The results of this study were successful in concluding the evaluation of dose enhancement with copper. Microscopic dose enhancement was measured in a nanoscale DNA

structure. The evaluation was made with energy depositions from the 0 eV to 1000 eV energy range; below the cutoff energy for macroscopic codes (1000 eV). Microscopic dosimetry predicts a substantial increase in expected outcome from macroscopic data. The maximum DEF for the hypoxic tumor with CuATSM *High* was 1.069 (Section 3.4), the corresponding mDEF with 85% nucleus uptake of CuATSM was 1.116 (Section 5.4).

The cellular model also clarified the importance of not only cellular uptake of CuATSM, but specifically nucleus uptake. Figures (5.9 & 5.15), demonstrated the minute contributions that electron spectra made to overall dosimetric quantities when they originated in the cytoplasm. With the relatively large target of the nucleus in the radiochemical yield model, the nucleus accounted for approximately two orders of magnitude greater chemical yield than did the cytoplasm. In the microdosimetry model, electrons from the cytoplasm were unlikely to interact with the small DNA segment target. Electrons emanating from the nucleus accounted for approximately 8 orders of magnitude greater contribution to dosimetric quantities in that model.

The deficiency between dose enhancement and radiosensitization using CuATSM was analyzed by enumerating DNA strand breaks and radiochemical yield. Unfortunately, the evaluations of these nanoscale quantities did not resolve the mechanism for radiosensitization. Single-strand breaks with copper resulted in an enhancement factor of 1.112, and double-strand breaks were enhanced by a factor of 1.119, both with the 85% nucleus uptake condition. Furthermore, the enhancement of radiochemical yield was evaluated with copper, and found to result in a maximum factor of 1.139 with 85% nucleus uptake. Although, the enhancement factor values from the microscopic models improve upon the prediction ability from the macroscopic dose enhancement model, neither is able to account for the 4 orders of magnitude concentration difference seen in the biological studies.

The field of TSMC for calculation of microdosimetric quantities is rapidly evolving, and any consideration here may be later proved inadequate by advancements in experimental data or theoretical frameworks. For example, low energy data and models within copper metal will be useful in simulating copper solutions directly, without macroscopic electron spectra.

Additionally, the PARTRAC and KURBUC codes referred to in Section (5.1), enable the tracking of radiochemical species to simulate chemical DNA strand breaks, and cell repair kinetics. Similar functionalities are being developed in the G4DNA codes, but neither resource was available for this research [321]. Future considerations of metal radiochemical reactions, such as the Fenton-like reaction (Section 1.5), will improve radiochemical yield simulations.

Models such as the local effect model and the microdosimetric kinetic model, have been developed that match simulation data to radiobiological experiments. These models may then be utilized to estimate relative biological effectiveness for future developments in treatment planning [281, 322-323]. However, the models require the input of biological data in order to make predictions, and therefore, do not result in the answer to why radiosensitization is discrepant from dose enhancement. To the best knowledge of the author, while much has been learned in this area, the basic question: *How does radiation dose result in cell death?* is still a partially unresolved inquiry, which this dissertation was not able to elucidate.

The work here was intended to evaluate CuATSM as a radiosensitizer. That goal has been accomplished, and extended with additional lines of inquiry. Although questions remain about the mechanism of radiosensitizers for cell death, that work will be left to future researchers.

CHAPTER 6

CONCLUSION

In this dissertation, the hypoxic PET tracer CuATSM was investigated as a potential external beam radiosensitizer for improving radiation therapy. Hypoxia is a negative prognostic factor for radiation therapy; by radiosensitizing hypoxic regions the efficacy of radiation therapy may be improved. Radioactive CuATSM has been implemented in radiation therapy as a hypoxic tracer for dose painting and theranostic treatments. To the knowledge of the author, this is the first evaluation of non-radioactive CuATSM for use in radiation therapy. Gold nanoparticles (GNP) have been extensively studied as a mechanism for radiosensitization, however, their efficacy to radioenhance hypoxic regions is limited by the difficulty of getting gold into the hypoxic regions through typical diffusive and vascular methods. GNP have been considered largely for their physical properties of low toxicity and high atomic number. Alternatively, the investigation of CuATSM was initiated by favorable biokinetic properties; CuATSM has a higher uptake in hypoxic tissue.

Chapter 2 evaluated the macroscopic dose (above 1 keV) enhancing properties of copper with clinical external beam photon sources of different energy spectra. The degree of dose enhancement was compared to other metals, and found to correlate strongly with atomic number. Previous research has investigated several metals including gold, copper, silver, and gadolinium and found each to result in enhanced dose via Monte Carlo dose predictions [42, 135, 143, 202-205]. Generally, simulations have either systematically evaluated the response of metals to monoenergetic (synchrotron) photons; or have investigated the efficacy of a single clinical photon spectrum with a metal nanoparticle as positive control. The intention of the research

presented in Chapter 2 is to generalize the findings of these previous investigations by systematically comparing a range of metal radiosensitizers with a range of clinical photon spectra. To the knowledge of the author this work presents the first MC evaluation of the carbon-target Imaging beam for dose enhancement with copper, gadolinium, and silver. Additionally, it is the first evaluation of the SARRP as an external photon beam for dose enhancement with metals. Although the results of this section could be inferred from previous data from literature, they confirm previous research and present a generalization of the findings with useful clinical implications.

Although, copper was found to enhance dose at all energies tested, the greatest dose enhancement occurred with the orthovoltage SARRP spectrum, which was the lowest energy external beam (Section 2.5). A minimum copper metal concentration of 0.1 g/kg was found to be necessary to achieve a dose enhancement factor (DEF) greater than 1% with SARRP. The DEF value of 1.01 was chosen as the minimum cutoff value for discernible dose enhancement to contrast with statistical noise inherent to Monte Carlo simulations. The 0.1 g/kg CuATSM concentration is the highest value considered for systemic injection for PET or motor neuron studies (Section 3.3) because of concerns with toxicity. The relatively high concentration of copper necessary to achieve the 1% benchmark from a macroscopic dose prediction standpoint casts doubt on the feasibility of CuATSM to be used as a radiosensitizer.

The metal solution layer was tested at various depths within the phantom and a 31% decrease in DEF was found to occur between 1 and 6 cm with SARRP, for a 100 g/kg copper solution. This decrease indicates that for low energy photon spectra, beam hardening (Section 2.6) caused a reduction of photon fluence that in turn reduces dose enhancement at depth. The

decrease in DEF with orthovoltage x-rays further introduced hurdles to the application of CuATSM as a dose enhancer of external beam radiation.

Electron production, including photoelectrons and Auger electrons, was investigated in metal solutions and found to correlate strongly with dose enhancement. To the knowledge of the author, this was the first attempt to analyze the spectral electron output and Auger electron output of the SARRP and Imaging beams with metal radiosensitizers. The results of this chapter serve as the basis for methods and parameters that the subsequent chapters relied upon to more deeply investigate the feasibility of CuATSM as a radiosensitizer.

Chapter 3 investigated the feasibility of using CuATSM to deposit sufficient copper for dose enhancement within hypoxic regions. Previous research has attempted to evaluate the dose enhancement within tumors and cells with varying degrees of complexity. A decrease in dose enhancement with GNP has been assumed to occur within hypoxic tissue, however, the degree of decrease is difficult to predict because of tumor heterogeneity in oxygen levels and extracellular membrane density. The results of Chapter 3 do not offer new fundamental insights into GNP dynamics; however, they reaffirm previous findings, call attention to potential failures of GNP aided radiotherapy in hypoxic tumors, and suggest the need for GNP uptake mapping for dose enhancement prediction. Furthermore, the failure of GNP in hypoxic tissue adds to the rationale for the development of a particle directly suited for hypoxic tissue radiosensitization, namely CuATSM.

Dose enhancement factors were evaluated for realistic concentrations of CuATSM and GNP from literature within a hypoxic tumor model. CuATSM within the tumor region was found to result in detectable levels of dose enhancement. For an initial injected CuATSM concentration of 1.35 g/kg (*High*), matching a GNP concentration value from Hainfeld, et al., copper was

found to result in a DEF of 1.069 within hypoxic tissue [125]. This result is novel and intriguing, and to the knowledge of the author, Chapter 3 offers the first Monte Carlo evaluation of macroscopic dose enhancement with CuATSM. Furthermore, because radioactive CuATSM can be initially employed as a PET imaging agent prior to application of non-radioactive CuATSM as a radiosensitizer, the distribution can be mapped prior to radiation and high uptake regions corresponding to hypoxia can be targeted specifically.

Dose painting with CuATSM improves radiation therapy even at concentrations insufficient for radiosensitization. The research here proposes a novel addendum to the already useful hypoxic targeting of dose painting radiation therapy by combining it with high-Z tissue augmentation to enhance dose. An area that was not addressed with this research, but should be investigated by future researchers is an evaluation of CuATSM as a cycling hypoxia tracer. In Section (1.7), the biokinetic theory behind CuATSM as a hypoxic tissue tracer was outlined. CuATSM differs from other PET hypoxic tracers in that, with the reintroduction of oxygen, it can change conformation and exit previously hypoxic cells. Currently, there is no standard PET cycling hypoxia tracer. The author proposes that $^{64}\text{CuATSM}$ should be compared to dynamic contrast enhanced MRI in small animals to evaluate its efficacy as a cycling hypoxia tracer. A cycling PET hypoxia tracer could have potential application in PET-Linac radiation therapy. An active monitoring and targeting of cycling hypoxia in a tumor could improve treatment outcomes.

Chapter 3 also investigated the feasibility of using orthovoltage radiation to treat deep regions of hypoxia. Orthovoltage is generally unsuitable for radiation therapy at depth because of undesirable skin dose. However, delivering the external beam over an arc was considered as a mechanism for improving dose deposition within hypoxic cores while decreasing dose to the

surface. The results indicated that CuATSM radiosensitized orthovoltage was comparable to megavoltage (MV) treatment; MV resulted in decreased skin dose, while CuATSM radiosensitized orthovoltage resulted in a 10% higher minimum dose to hypoxic regions. The results of this section indicate that CuATSM and its affinity to hypoxic tissue can be used to enhance dose in hypoxic tumors by amplifying the concentration of copper in a hypoxic core.

The physics of high-Z radiosensitization is simple and elegant, which may promote an overconfidence with practitioners to undervalue the complexity that occurs within real biological systems. A lack of information may undermine a seemingly perfect physics plan and result in incomplete dosing of tumor or the development of metastatic potential from hypoxic regions. GNP in particular have been the central focus of radiosensitization research for more than a decade [125].

Occasionally in science, substantial progress with one method can encourage a myopia when considering alternative ideas. Nanotechnology in general has been successful in so many areas of science that it has taken on an almost mythical role in the minds of some scientists and laypeople, who believe that all problems can be solved with its application. Perhaps the most important narrative from this research is that innovative thinking is critical to broadening the knowledge of science. That narrative was most acutely employed in Chapter 3; CuATSM may not be a perfect solution to radiosensitization, but these findings have highlighted some areas of need in radiosensitization research.

Radiosensitization therapy should be tailored to the environment of the tumor; the uptake map of any radiosensitizer should be known for external beam targeting and regions of low uptake (hypoxic) should be targeted with companion radiosensitizers. Furthermore, the results of this chapter encourage the reevaluation of technologies that have gone dormant. Orthovoltage

has a rich history in radiation therapy, which, for some with a rigid historical bias, preempts the consideration of its use in modern applications. The success of CuATSM enhanced orthovoltage to produce a plan comparable to, and in some ways exceeding megavoltage arc therapy, can serve as an inspiration that with proper application, antiquated technologies may prove useful in new ways.

Chapter 4 measured radiosensitization with various concentrations of copper by measuring the amount of DNA breaks and cell survival in two different experiments. The addition of CuCl_2 resulted in increased viral DNA single-strand breaks (SSB) that were non-significantly correlated with concentration between $50 \mu\text{M}$ and $800 \mu\text{M}$, but did find increase in SSB with any concentration of copper. In addition, significant differences were found between megavoltage and orthovoltage copper enhanced radiosensitization. The results of this section indicate that CuCl_2 can increase DNA SSB *in vitro*.

DMSO and CuATSM were evaluated for toxicity with CHO cells: DMSO resulted in a growth inhibition value below 0.5 at a concentration of 5% (v/v); CuATSM resulted in a growth inhibition value below 0.5 at a concentration of $3.11 \mu\text{M}$. CuATSM when added to culture medium at $0.311 \mu\text{M}$ concentration was found to be a significant radiosensitizer of CHO cells. Radiosensitization occurred in both normoxic and hypoxic conditions without significant difference between the radiosensitization of the two oxic conditions. The radiosensitization occurred for concentrations of copper ($18 \mu\text{g}/\text{kg}$) that were much lower than those found to cause macroscopic dose enhancement with MC ($> 100 \text{ mg}/\text{kg}$).

Previous research from Hesslewood, et al. has established that copper (CuCl_2) can act as a radiosensitizer of hypoxic mammalian cells [111]. The goal of this chapter was to build on this evidence to evaluate similar radiosensitization properties of CuATSM. Preliminary research with

CuCl₂ and viral DNA was conducted to evaluate the parameters of radiosensitization that theoretically could be generalized to CuATSM. Although the scope of those investigations were modest, they reaffirmed previous research and models by showing that copper can act as a radiosensitizer. Additionally, increased concentration of copper at lower energy photon spectrum resulted in greater radiosensitization, reaffirming the observations of Chapter 2.

Radiosensitization with CuATSM was not a forgone conclusion, and in fact the toxicity studies lowered achievable concentrations to levels two orders of magnitude below the required concentrations predicted in Chapter 2. Interestingly, CuATSM did result in radiosensitization at these low concentrations of copper. To the knowledge of the author, this section presented a substantial contribution to science: serving as the first evaluation of CuATSM as a radiosensitizer in any biological system. Specifically, the results presented here indicated that CuATSM was a radiosensitizer of CHO cells under normoxia or hypoxia when irradiated with orthovoltage (PXI SmART) photons. Unfortunately, the narrow boundaries of these results highlights the limits of the research and encourages the expansion of this research to examine parameters and other biological systems.

Additionally, CuATSM should be evaluated as a radiosensitizer with other beam qualities including: megavoltage photons; electrons; protons and carbon-ions, using similar experimental procedures. Metal radiosensitization has been demonstrated to occur with heavy-ion therapy and the mechanism for that action likely relies on the augmentation to reactive oxygen species (ROS) production. Recall from Section (1.5), that copper interacts with hydrogen peroxide, a product of radiolysis, to facilitate the production of hydroxyl radicals which are quite damaging to DNA. ROS need to be in close proximity to DNA in order to cause damage resulting in mitotic death, therefore a vehicle for increasing ROS production within cells and specifically within the

nucleus, may have substantial value for heavy-ion therapy radiosensitization. Heavy-ion radiotherapy already has increased efficacy over photon therapy in hypoxic tissue, and with the addition of CuATSM that advantage may be increased.

Furthermore, a single cell-line was evaluated in this section; this methodology should be extended to a variety of cells to evaluate the efficacy of CuATSM as a radiosensitizer in general. Specifically, utilizing the data from McMillan, cell-lines with greater differential uptake of CuATSM by oxic condition should be evaluated for radiosensitization under normoxic and hypoxic condition [117]. A summary of cell types with substantial hypoxic radiosensitization would be a useful tool for determining suitable tumors for CuATSM treatment. The results of this section, as well as the treatment potential outlined in Chapter 3, indicate that CuATSM should also be evaluated as a radiosensitizer in small animal tumors. Survival studies and tumor reduction assays should be conducted in tumors of sufficient size to sustain chronic hypoxic regions to evaluate whether CuATSM results in radiosensitization. Following the concepts of Section (3.6), $^{64}\text{CuATSM}$ PET should be used in a small animal tumor to map hypoxia and dose enhancing orthovoltage boosts should be evaluated within high uptake regions.

Finally, radioactive $^{64}\text{CuATSM}$ has been evaluated as a radiotheranostic capable of imaging and treating hypoxic regions of tumors (Section 1.8). Although the findings of Chapters 2 & 3 indicated that nonradioactive copper would not have sufficient efficacy as an external beam dose enhancer for diagnostic concentrations of CuATSM (< 100 mg/kg), the results of Chapter 4 indicated that clinical radiosensitization could be achieved at sub-diagnostic concentrations of copper. Combining external beam radiation with $^{64}\text{CuATSM}$ may amplify radiosensitization above either modality used alone. Researchers should evaluate small animal tumor reduction using $^{64}\text{CuATSM}$ as a radiotheranostic followed by external beam radiation.

Chapter 5 investigated microdosimetric MC predictions that would be produced from CuATSM enhanced electron spectra within a cellular model. The electron spectra initiated in the microdosimetry predictions within the cell used the CuATSM *High* concentration from the macroscopic dose enhancement evaluation from Chapter 2. SARRP external beam photon spectrum was modeled in a water phantom and electron spectra were determined for different concentrations of copper solutions. A range of complementary cellular compartment values between nucleus (0-85%) and cytoplasm (0-85%) were considered to evaluate cellular distribution on microscopic dose enhancement. Microscopic dose enhancement factors (mDEF) were evaluated in a small volume enclosing a DNA segment and found to correlate with nucleus uptake, with a maximum mDEF of 1.116 when 85% of copper was in the nucleus. SSB and double-stranded breaks (DSB) were also scored in the same geometry and concentrations. CuATSM electron spectrum was found to result in enhancements of 1.112 and 1.119 for SSB and DSB respectively, with 85% copper in the nucleus. Chemical species enhancement was evaluated in a cellular model. Enhancement of total chemical yield was 1.139 with 85% of copper in the nucleus. These evaluations were not able to resolve the reason for low concentration radioenhancement observed in Chapter 4. The results of this section indicated that the enhanced electron emission due to CuATSM within the tissue cause enhancements to dose according to microscopic MC predictions, as well as SSB, DSB and radiochemical species yield.

Microdosimetry and track structure Monte Carlo (TSMC) are burgeoning fields investigating the interaction of radiation with matter at low energies and small resolutions. TSMC codes for evaluating microdosimetric quantities with metal particles have been developed, utilizing approximations for the trajectories of radiation within metal. As the field

matures, low energy predictions of ionizations and excitations in metals will improve the understanding of radiation enhancement.

To the knowledge of the author, this section presented the first evaluation of CuATSM as a dose enhancer at the microscopic level, a DNA strand break enhancer, and a radiochemical enhancer. Additionally, the results indicate that electrons originating in the cytoplasm contribute minimally to microdosimetric quantities evaluated in the nucleus. Therefore, when considering radiosensitizers for targeting DNA, uptake into the cell nucleus should be the primary consideration for improving biokinetics. These results were modest and did not fully bridge the gap between modeled macroscopic dose enhancements (Chapters 2 & 3) with observed cellular radiosensitization (Chapter 4).

In order to improve the modeling efficacy of CuATSM at the microdosimetric level, several improvements need to be pursued within the field. Models and cross-sections for copper metals needs to be evaluated at low energies so that copper can be implemented as metal solutions directly within TSMC codes. Additionally, metal-radiochemical reactions (Section 1.5) should be implemented for copper metal in chemical TSMC codes such as those used in Chapter 5 to more accurately model the chemical species creation.

While there are ways that the microdosimetric models could be improved, the question of how radiation results in cell death is critically dependent on deepening the understanding of the underlying radiobiology principles. Progress has been made with TSMC codes to evaluate DNA damage and repair kinetics. A deeper conception of cellular response to damage of non-DNA cellular targets (organelles, cell membranes, etc.) may improve the understanding of radiation induced cell death. Furthermore, when considering cell culture or tumors, considerations of cellular signaling between irradiated and unirradiated cells may improve cell death models.

The results of this dissertation successfully resolved the central query: *Can CuATSM be used as a radiosensitizer of external beam radiation?* in the affirmative. The work presented here should be expanded upon by the scientific community to improve the understanding of the potential of CuATSM in that role.

REFERENCES

[1]"Cancer Fact sheet N°297". World Health Organization. November 2017. Archived from the original on 29 December 2010. Retrieved 28 November 2017.

[2]"Defining Cancer". National Cancer Institute. Archived from the original on 25 June 2014. Retrieved 10 June 2014.

[3]"Targeted Cancer Therapies". NCI. 25 April 2014. Archived from the original on 28 May 2014. Retrieved 11 June 2014.

[4]Gardner H L, Fenger JM, London CA. Dogs as a Model for Cancer. Annual Review of Animal Biosciences. 2016; 4 (1): 199–222. Doi: 10.1146/annurev-animal-022114-110911.

[5] Ballas LK, Elkin EB, Schrag D, Minsky BD, Bach PB. Radiation therapy facilities in the United States. Int J Radiat Oncol Biol Phys. 2006; 66:1204–1211.

[6] "Radiation Therapy for Cancer", National Cancer Institute. November 2017. Reviewed: June 30, 2010, Retrieved 28 November 2017.

[7] Baumann M, Petersen C. TCP and NTCP: a basic introduction, Rays, 30 2005; pp. 99-104.

[8] Taylor ML, Kron T. Consideration of the radiation dose delivered away from the treatment field to patients in radiotherapy J. Med. Phys. 2011; 36 59–71.

[9] Podgorsak EB. External photon beams-physical aspects Radiation Oncology Physics: Handbook for Teachers and Students (Vienna: IAEA) 2005; pp: 161-216.

- [10] "The mechanism of action of radiosensitization of conventional chemotherapeutic agents". *Seminars in Radiation Oncology*. 13 (1): 13–21.
- [11] Kobayashi K, Usami N, Porcel E, Lacombe S, Le Sech C. Enhancement of radiation effect by heavy elements *Mutat. Res.* 2010; 704 123–32.
- [12] Cho SH. Estimation of tumour dose enhancement due to gold nanoparticles during typical radiation treatments: a preliminary Monte Carlo study. *Phys Med Biol* 2005; 50:N163–73.
- [13] Ianzini F, Mackey MA. *Mitotic Catastrophe: Apoptosis, Senescence, and Cancer*. Humana Press. pp. 73–91. ISBN 978-1-58829-527-9; 2007.
- [14] Hall EJ. *Radiobiology for the Radiologist*. 5th ed. Philadelphia, Baltimore, New York: Lippincott Williams & Wilkins; 2000.
- [15] Bond VP, Fliedner TM, Archambeau JO. *Mammalian Radiation Lethality: A Disturbance in Cellular Kinetics*. New York: Academic Press; 1966.
- [16] Moulder JE, Rockwell S. Tumor hypoxia: its impact on cancer therapy. *Cancer Metastasis Rev* 1987; 5:313–41.
- [17] Hockel, M, Vaupel, P. Tumor hypoxia: definitions and current clinical, biologic, and molecular aspects. *J. Natl Cancer Inst.* 2001; 93, 266–276.
- [18] Bartkowiak K, Riethdorf S, Pantel K. The interrelating dynamics of hypoxic tumor microenvironments and cancer cell phenotypes in cancer metastasis. *Cancer Microenvironment*, 2011; 5, 59–72.

- [19] Carlson DJ, Yenice KM, Orton CG. Tumor hypoxia is an important mechanism of radioresistance in hypofractionated radiotherapy and must be considered in the treatment planning process. *MedPhys* 2011; 38(12):6347–6350.
- [20] Harada, H. How can we overcome tumor hypoxia in radiation therapy? *J. Radiat. Res.* 2011; 52, 545–556.
- [21] Barker HE, Paget JT, Khan AA, Harrington KJ. The tumour microenvironment after radiotherapy: mechanisms of resistance and recurrence. *Nat. Rev. Cancer* 2015; 15, 409–425.
- [22] Thomlinson RH, Gray LH. The histological structure of some human lung cancers and the possible implications for radiotherapy. *Br J Cancer* 1955; 9: 539–549.
- [23] Rahal A, Kumar A, Singh V, Yadav B, Tiwari R, Chakraborty S, Dhama K. Oxidative stress, prooxidants, and antioxidants: the interplay. *Biomed Res Int* 2014; 761264.
- [24] Li L, Tan J, Miao Y, Lei P, Zhang Q. ROS and autophagy: interactions and molecular regulatory mechanisms. *Cell. Mol. Neurobiol.* 2015; 35, 615–621.
- [25] Bristol IJ, Woodward WA, Strom EA et al. Locoregional treatment outcomes after multimodality management of inflammatory breast cancer. *Int J Radiat Oncol Biol Phys* 2008; 72:474 – 484.
- [26] Farrell N. Metal complexes as radiosensitizers. *Prog Clin Biol Med.* 1989; 10: 90–109.
- [27] Horn D, Barrientos A. Mitochondrial copper metabolism and delivery to cytochrome c oxidase. *IUBMB life.* 2008.

- [28] Gorrini C., Harris IS, Mak TW. Modulation of oxidative stress as an anticancer strategy. *Nat. Rev. Drug Discov.*, 2014; 12, pp. 931-947.
- [29] Peiris-Pages M, Martinez-Outschoorn UE, Sotgia F, Lisanti MP. Metastasis and oxidative stress: are antioxidants a metabolic driver of progression? *Cell Metab.* 2015; 22, 956–958.
- [30] Gill JG, Piskounova E, Morrison SJ. Cancer, oxidative stress, and metastasis. In: *Cold Spring Harb Symp Quant Biol.* Cold Spring Harbor: Cold Spring Harbor Laboratory Press; 2016.
- [31] Malicki J. The importance of accurate treatment planning, delivery and dose verification. *Rep Pract Oncol Radiother* 2012; 17: 63-5.
- [32] Carlson DJ, Keall PJ, Loo Jr BW, Chen ZJ, Brown JM. Hypofractionation results in reduced tumor cell kill compared to conventional fractionation for tumors with regions of hypoxia *Int J Radiat Oncol Biol Phys*, 2011; 79, pp. 1188-1195.
- [33] Hong BJ, Kim J, Jeong H, Bok S, Kim YE, Ahn GO. Tumor hypoxia and reoxygenation: the yin and yang for radiotherapy. *Radiat Oncol J* 2016; 34: 239–249.
- [34] Steel GG, McMillan TJ, Peacock JH. The 5Rs of radiobiology. *Int J Radiat Biol* 1989; 56: 1045 –8.
- [35] Barlow ML, Battaglia N, Gerber SA, Lord EM. Hypofractionated radiotherapy treatment preserves immune function and improves tumor control vs. hyperfractionated treatment. *J Immunol* May 1, 2016; 196 (1 Supplement) 213.13;
- [36] El-Sayed MI, Abdel-Wanis ME. Comparison of Hypofractionated and Conventional Radiotherapy Protocols in Breast Cancer Patients: A Retrospective Study. *J Cancer Sci Ther.* 2012; 4: 158-163.

- [37] Raviraj J, Bokkasam VK, Kumar VS, Reddy US, Suman V. Radiosensitizers, radioprotectors, and radiation mitigators *Ind. J. Dent. Res.* 2014; 25, pp. 83-90.
- [38] Malik A, Sultana M, Qazi A, Qazi MH, Parveen G, Waquar S, Ashraf AB, Rasool M. Role of natural radiosensitizers and cancer cell radioresistance: an update. *Anal Cell Pathol (Amst)* 2016; 2016:6146595. Doi: 10.1155/2016/6146595.
- [39] Xiang-Yu S, Pei-Dang L, Hao W, Ning G. Enhancement of radiosensitization by metal-based nanoparticles in cancer radiation therapy *Cancer Biol Med.* 2014; Jun; 11(2): 86–91.
- [40] Rosa S, Connolly C, Schettino G, Butterworth KT, Prise KM. Biological mechanisms of gold nanoparticle radiosensitization *Cancer Nanotech. Basic Transl. Clin. Res.* 2017; 8, p. 2.
- [41] McQuaid HN, et al. Imaging and radiation effects of gold nanoparticles in tumour cells. *Sci. Rep.* 2016; 6, 19442.
- [42] Dorsey JF, Sun L, Joh DY, Witztum A, Zaki AA, Kao GD, Alonso-Basanta M, Avery S, Tsourkas A, Hahn SM. Gold Nanoparticles in Radiation Research: Potential Applications for Imaging and Radiosensitization. *Transl. Cancer Res.* 2013; 2, 280–291.
- [43] Laster BH, Shani G, Kahl SB, Warkentien L. The biological effects of Auger electrons compared to α -particles and Li ions. *Acta Oncol.* 1996; 35: 917–923.
- [44] Aghevliana S, Boylea AJ, Reilly, RM. Advanced Radioimmunotherapy of cancer with high linear energy transfer (LET) radiation delivered by radionuclides emitting α -particles or Auger electrons *Drug Delivery Reviews* Volume 109, 15 January 2017; Pages 102-118.
- [45] Laporta V, Celiberto R, Tennyson J. Dissociative electron attachment and electron-impact resonant dissociation of vibrationally excited O₂ molecules *Phys. Rev.* 2015; A 91 012701.

- [46] Hino-Shishikura A, Tateishi U, Shibata H, Yoneyama T, Nishii T, Torii I. Tumor hypoxia and microscopic diffusion capacity in brain tumors: a comparison of (62)Cu-Diacetyl-Bis (N4-Methylthiosemicarbazone) PET/CT and diffusion-weighted MR imaging. *Eur J Nucl Med Mol Imaging*. 2014.07; 41 (7): 1419-1427.
- [47] Das IJ, Kase KR. Higher energy: is it necessary, is it worth the cost for radiation oncology? *Medical Physics*, vol. 19, no. 4, pp. 917–925, 1992.
- [48] Moding EJ, Mowery YM, Kirsch DG. Opportunities for Radiosensitization in the Stereotactic Body Radiation Therapy (SBRT) Era. *Cancer J*. 2016; Jul-Aug; 22(4):267-73.
- [49] Hayes DP. Non-problematic risks from low-dose radiation-induced DNA damage clusters. *Dose-Response* 2008; 6 (1), 30-52.
- [50] Asaithamby A, et al. Mechanism of cluster DNA damage repair in response to high-atomic number and energy particles radiation. *Mutat. Res*. 2010; vol. 711 (pg. 87-99).
- [51] Reissig F, Mamat C, Steinbach J, Pietzsch HJ, Freudenberg R, Navarro-Retamal C, Caballero J, Kotzerke J, Wunderlich G. Direct and Auger Electron-Induced, Single- and Double-Strand Breaks on Plasmid DNA Caused by 99mTc-Labeled Pyrene Derivatives and the Effect of Bonding Distance. *PLoS One* 2016; 11, e0161973.
- [52] McMillan DD, Maeda J, Bell JJ, Genet MD, Phooswadi G, Mann KA, Kraft SL, Kitamura H, Fujimori A and Yoshii Y: Validation of 64Cu-ATSM damaging DNA via high-LET Auger electron emission. *J Radiat Res*. 56:784–791. 2015.

- [53] Kobayashi K, Bruttini E, Balerna A. Radiobiology using synchrotron radiation. Proceedings of the International School of Physics ‘Enrico Fermi’, vol. Course CXXVIII, IOS Press, Amsterdam 1996; pp. 333-352.
- [54] Kobayashi K, Mozumder A, Hatano Y. Photon-induced biological consequences Charged Particle and Photon Interactions with Matter, MerceL Dekker Inc. 2003; pp. 471-489.
- [55] Ka M. Studying effects of gold nanoparticle on dose enhancement in megavoltage radiation. J Biomed Phys Eng. 2015; 5:185–90.
- [56] Saberi A, Shahbazi-Gahrouei D, Abbasian M, Fesharaki M Baharlouei A, Arab-Bafrani Z. Gold nanoparticles in combination with megavoltage radiation energy increased radiosensitization and apoptosis in colon cancer HT-29 cells. International Journal of Radiation Biology. 2017; 93(3):315-323.
- [57] “III. Other halogenated pyrimidines”. Acta Radiologica: Diagnosis 1971; 11:sup311, 31-33.
- [58] Yao XB, Huang CN, Chen XP, Zheng Y, Sanche L. Chemical radiosensitivity of DNA induced by gold nanoparticles, J. Biomed. Nanotechnol. 2015; 11, 478–485.
- [59] Zhang ZY, Van Steendam K, Maji S, Balcaen L, Anoshkina Y, Zhang QL, Vanluchene G, De Rycke R, Van Haecke F, Deforce D, et al. Tailoring cellular uptake of gold nanoparticles via the hydrophilic-to-hydrophobic ratio of their (co)polymer coating. Adv Funct Mater. 2015; 25:3433–9.
- [60] Liang M, et al. Cellular uptake of highly packed polymer coated gold nanoparticles. ACS Nano 2010; 4, 403–413.

- [61] Jazayeri MH, Amani H, Pourfatollah AA, Pazoki-Toroudi H, Sedighimoghaddam B. various methods of gold nanoparticles (GNPs) conjugation to antibodies. *Sens. Biosensing Res* 2016; 9, 17–22.
- [62] Moser F, Hildenbrand G, Müller P, Al Saroori A, Biswas A, Bach M, et al. Cellular uptake of gold nanoparticles and their behavior as labels for localization microscopy. *Biophys J.* 2016; 110:947–53.
- [63] Torrice M. Does nanomedicine have a delivery problem? *ACS Cent. Sci.* 2016; 2, 434–437.
- [64] Bae YH, Park K. Targeted drug delivery to tumors: Myths, reality and possibility *J. Control. Release*, 2011; 153, pp. 198-205.
- [65] McDonald DM, Baluk P. Significance of blood vessel leakiness in cancer. *Cancer Res.* 2002; 62, 5381–5385.
- [66] Nagy JA, Chang SH, Dvorak AM, Dvorak HF. Why are tumour blood vessels abnormal and why is it important to know? *Br J Cancer* 2009; 100: 865– 869.
- [67] Jain S, Coulter JA, Hounsell AR, Butterworth KT, McMahon SJ, Hyland WB. Et al. Cell-specific radiosensitization by gold nanoparticles at megavoltage radiation energies. *Int J Radiat Oncol Biol Phys.* 2011; Feb 1; 79(2):531-9.
- [68] Jain S, Coulter JA, Butterworth KT, Hounsell AR, McMahon SJ, Hyland WB. Et al. Gold nanoparticle cellular uptake, toxicity and radiosensitisation in hypoxic conditions. *Radiother Oncol.* 2014; 110:342–7.
- [69] Oh N, Park JH. Endocytosis and exocytosis of nanoparticles in mammalian cells *Int. J. Nanomed.* 2014; 9, pp. 51-63.

- [70] Boyoglu C, He Q, Willing G, et al. Microscopic studies of various sizes of gold nanoparticles and their cellular localizations. *ISRN Nanotechnol.* 2013; 10.1155/2013/123838.
- [71] Brun E, Sanche L, Sicard-Roselli C. Parameters governing gold nanoparticle X-ray radiosensitization of DNA in solution *Colloids Surf B: Biointerfaces*, 2009; 72, pp. 128-134.
- [72] Zhang X, Xing JZ, Chen J, Ko L, Amanie J, Gulavita S, et al. Enhanced radiation sensitivity in prostate cancer by gold-nanoparticles *Clin Invest Med*, 2008; 31, pp. E160-E167.
- [73] Kong T, Zeng J, Wang X, Yang X, Yang J, McQuarrie S, et al. Enhancement of radiation cytotoxicity in breast-cancer cells by localized attachment of gold nanoparticles. *Small*, 2008; 4, pp. 1537-1543.
- [74] Mesbahi, A. A review on gold nanoparticles radiosensitization effect in radiation therapy of cancer *Rep. Prac. Oncol. Radiother.* 2010; 15, 176.
- [75] Kodiha M, Wang YM, Hutter E, Maysinger D, Stochaj U. Off to the organelles—Killing cancer cells with targeted gold nanoparticles. *Theranostics* 2015; 5:357–370.
- [76] Berbeco RI, Detappe A, Tsiamas P, Parsons D, Yewondwossen M, Robar J. Low Z target switching to increase tumor endothelial cell dose enhancement during gold nanoparticle-aided radiation therapy *Med. Phys.* 2016; 43(1), 436–442.
- [77] Reuter S, Gupta SC, Chaturvedi MM, Aggarwal BB. Oxidative stress, inflammation, and cancer: How are they linked? *Free Radic. Biol. Med.* 2010; 49, 1603.
- [78] Donnelly PS, Liddell JR, Lim S, Paterson BM, Cater MA, Savva MS, et al. An impaired mitochondrial electron transport chain increases retention of the hypoxia imaging agent

diacetyl-bis (4-methylthiosemicarbazonato) copperII. Proc Natl Acad Sci U S A. 2012; 109:47–52.

[79] Lewis JS, Laforest R, Buettner TL, et al. Copper-64-diacetyl-bis (N4-methylthiosemicarbazone): an agent for radiotherapy. Proc Natl Acad Sci USA 2001; 98:1206–1211.

[80] Obata A, Yoshimi E, Waki A, Lewis JS, Oyama N, Welch MJ, Saji H, Yonekura Y, Fujibayashi Y. Retention mechanism of hypoxia selective nuclear imaging/radiotherapeutic agent Cu-diacetyl-bis(N4-methylthiosemicarbazone) (Cu-ATSM) in tumor cells. Ann Nucl Med 2001; 15:499–504.

[81] Wadas TJ, Wong EH, Weisman GR, Anderson CJ. Coordinating radiometals of copper, gallium, indium, yttrium, and zirconium for PET and SPECT imaging of disease. Chem Rev 2010; 110:2858–902.

[82] Anderson CJ, Ferdani R. Copper-64 radiopharmaceuticals for PET imaging of cancer: advances in preclinical and clinical research. Cancer Biother Radiopharm 2009; 24: 379-93.

[83] Walsh JC, Lebedev A, Aten E, Madsen K, Marciano L, Kolb HC. The clinical importance of assessing tumor hypoxia: relationship of tumor hypoxia to prognosis and therapeutic opportunities. Antioxid Redox Signal. 2014; 21(10):1516–54.

[84] Muz B, de la Puente P, Azab F, Azab AK. The role of hypoxia in cancer progression, angiogenesis, metastasis, and resistance to therapy. Hypoxia (Auckl) 2015; 3:83–92.

[85] Wu D, Yotnda P. Induction and testing of hypoxia in cell culture J. Vis. Exp. 2011; Aug 12; (54). 2899.

- [86] Vaupel P, Harrison L. Tumor hypoxia: causative factors, compensatory mechanisms, and cellular response. *Oncologist* 2004; 9 (Suppl. 5), 4–9.
- [87] Lapi SE, Lewis JS, Dehdashti F. Evaluation of hypoxia with copper-labeled diacetyl-bis (N-methylthiosemicarbazone) *Semin Nucl Med.* 2015; 45 (2), pp. 177-185.
- [88] Colombie M, Gouard S, Frindel M, Vidal A, Cherel M, Kraeber-Bodere F, et al. Focus on the controversial aspects of (64)Cu-ATSM in tumoral hypoxia mapping by PET imaging *Front Med.* 2015; 2, p. 58.
- [89] Yoshii Y, Furukawa T, Kiyono Y, Watanabe R, Mori T, Yoshii H, et al. Internal radiotherapy with copper-64-diacetyl-bis (N4-methylthiosemicarbazone) reduces CD133+ highly tumorigenic cells and metastatic ability of mouse colon carcinoma. *Nucl Med Biol.* 2011; 38:151–7.10.1016.
- [90] Tokuda E, Furukawa Y. Copper homeostasis as a therapeutic target in amyotrophic lateral sclerosis with SOD1 mutations. *Int. J. Mol. Sci.* 2016; 17.
- [91] Ngwa W, et al. Targeted radiotherapy with gold nanoparticles: current status and future perspectives *Nanomedicine.* 2014; 9, pp. 1063-1082.
- [92] Retif P, Pinel S, Toussaint M, Frochot C, Chouikrat R, Bastogne T, Barberi-Heyob M. Nanoparticles for radiation therapy enhancement: the key parameters. *Theranostics.* 2015; 5:1030–44.
- [93] Khan FM. *The Physics of Radiation Therapy.* Baltimore, MD, Williams and Wilkins, 1984, pp 39-41.

- [94] Forster JC, Harriss-Phillips WM, Douglass MJ, Bezak E. A review of the development of tumor vasculature and its effects on the tumor microenvironment. *Hypoxia*. 2017; 5:21-32.
- [95] Matsumoto S, Yasui H, Mitchell JB, Krishna MC. Imaging Cycling Tumor Hypoxia. *Cancer research*. 2010; 70(24):10019-10023.
- [96] Dewhirst MW, Cao Y, Moeller B. Cycling hypoxia and free radicals regulate angiogenesis and radiotherapy response *Nat Rev Cancer*. Author manuscript; available in PMC 2014 Mar 5. Published in final edited form as: *Nat Rev Cancer*. 2008; Jun, 8(6): 425–437.
- [97] Dhermain F, Barani IJ. Complications from radiotherapy, *Handb Clin Neurol*. 2016 134, pp. 219-234.
- [98] Fleming IN, Manavaki R, Blower PJ, West C, Williams KJ, Harris AL, Domarkas J, Lord S, Baldry C, Gilbert FJ. Imaging Tumour Hypoxia with Positron Emission Tomography. *Br. J. Cancer*. 2015; 112, 238–250.
- [99] Cowley AR, Dilworth JR, Donnelly PS, Labisbal E, Sousa A. An Unusual Dimeric Structure of a Cu(I) Bis(thiosemicarbazone) Complex: Implications for the Mechanism of Hypoxic Selectivity of the Cu(II) Derivatives *Journal of the American Chemical Society*. 2002; 124 (19), 5270-5271.
- [100] Hansen AE, Kristensen AT, Jørgensen JT, et al. ^{64}Cu -ATSM and ^{18}F FDG PET uptake and ^{64}Cu -ATSM autoradiography in spontaneous canine tumors: comparison with pimonidazole hypoxia immunohistochemistry. *Radiat Oncol*. 2012; 7:89.
- [101] Yoshii Y, Matsumoto H, Yoshimoto M, Furukawa T, Morokoshi Y, Sogawa C, et al. Controlled Administration of Penicillamine Reduces Radiation Exposure in Critical Organs

during ^{64}Cu -ATSM Internal Radiotherapy: A Novel Strategy for Liver Protection. PLoS ONE 2014; 9(1): e86996.

[102] Vavere AL, Lewis JS. Cu-ATSM: a radiopharmaceutical for the PET imaging of hypoxia. Dalton Trans. 2007; 43:4893–4902.

[103] Tsujikawa T, Asahi S, Oh M, Sato Y, Narita N, Makino A, et al. Assessment of the Tumor Redox Status in Head and Neck Cancer by ^{62}Cu -ATSM PET. PLoS ONE 2016; 11(5): e0155635.

[104] Hirayama H. “Lecture note on photon interactions and cross sections.” [PDF Document] Retrieved from Lecture Notes: Internal 2000-10, KEK High Energy Accelerator Research Organization, Oho, Tsukuba, Ibaraki, Japan, November 2000. Accessed 4/24/2019.

[105] Krause MO. Atomic radiative and radiationless yields for K and L shells. J. Phys. Chem. Ref. Data. 1979; 8, 307–328.

[106] Neshatian M, Chung S, Yohan D, Yang C, Chithrani DB. Uptake of gold nanoparticles in breathless (hypoxic) cancer cells. J Biomed Nanotechnol. 2015; 11(7):1162–72.

[107] Dewhirst MW, Secomb TW. Transport of Drugs from Blood Vessels to Tumour Tissue. Nat. Rev. Cancer 2017; 17, 738.

[108] Barua S, Mitragotri S. Challenges associated with Penetration of Nanoparticles across Cell and Tissue Barriers: A Review of Current Status and Future Prospects. Nano today. 2014; 9(2):223-243.

[109] Yohan D, Cruje C, Lu X, Chithrani DB. Size dependent gold nanoparticle interaction at nano-micro interface using both monolayer and multilayer (tissue-like) cell models. Nano-Micro Lett. 2016; 8 (1), pp. 44-53.

- [110] Lee CT, Boss MK, Dewhirst MW. Imaging tumor hypoxia to advance radiation oncology. *Antioxid Redox Signal* 2014; 21:313–337.
- [111] Hesslewood IP, Cramp WA, McBrien DC, Williamson P, Lott AK. Copper as a hypoxic cell sensitizer of mammalian cells. *Br J Cancer Suppl.* 1978; 3:95–97.
- [112] Hubbell JH, Seltzer SM. Tables of X-Ray Mass Attenuation Coefficients and Mass Energy-Absorption Coefficients (version 1.4). [Online] 2014; National Institute of Standards and Technology, Gaithersburg, MD. Available: <http://physics.nist.gov> Accessed 7/6/2018.
- [113] Berger MJ, Coursey JS, Zucker MA, Chang J. ESTAR, PSTAR, and ASTAR: Computer Programs for Calculating Stopping-Power and Range Tables for Electrons, Protons, and Helium Ions (version 1.2.3). [Online] 2004; National Institute of Standards and Technology, Gaithersburg, MD. Available: <http://physics.nist.gov/Star> Accessed 7/6/2018.
- [114] Rogers DWO, Faddegon BA, Ding GX, Ma C-M, Wei J, Mackie TR. BEAM: a Monte Carlo code to simulate radiotherapy treatment units *Med. Phys.* 1995; 22 503-24.
- [115] Anderson J, Burns PJ, Milroy D, Ruprecht P, Hauser T, Siegel HJ. Deploying RMACC Summit: An HPC Resource for the Rocky Mountain Region. In Proceedings of PEARC17, New Orleans, LA, USA, July 09-13, 2017, 7 pages.
- [116] Parsons D, Robar JL, Sawkey D. A Monte Carlo investigation of low-Z target image quality generated in a linear accelerator using Varian’s VirtuaLinac. *Med Phys.* 2014;41(2):021719.
- [117] McMillan, D. Evaluation of Cu-64-ATSM in Cell Culture for Potential Use as a Radiotherapy Agent, Colorado State University Thesis, 2014.

- [118] Tryggestad E, Armour M, Iordachita I, Verhaegen F and Wong J W 2009 A comprehensive system for dosimetric commissioning and Monte Carlo validation for the small animal radiation research platform *Phys. Med. Biol.* 54 5341-57.
- [119] Challapalli A, Carroll L, Aboagye EO. Molecular mechanisms of hypoxia in cancer. *Clin Transl Imaging.* 2017; 5(3):225–253.
- [120] Malmir S, Mowlavi AA, Mohammadi S. Evaluation of Dose Enhancement in Radiosensitizer Aided Tumor: A Study on Influential Factors, *Rep Radiother Oncol.* 2015; 2(4):e11076.
- [121] Zabihzadeh M, Moshirian T. A Monte Carlo Study on Dose Enhancement by Homogeneous and Inhomogeneous Distributions of Gold Nanoparticles in Radiotherapy with Low Energy X-rays. *J Biomed Phys Eng.* 2018; Mar 1; 8(1):13-28.
- [122] Ranjbar H, Shamsaei M, Ghasemi MR. Investigation of the dose enhancement factor of high intensity low mono-energetic X-ray radiation with labelled tissues by gold nanoparticles. *Nukleonika.* 2010; 55(3):307–312.
- [123] Burgman P, O'Donoghue JA, Lewis JS, Welch MJ, Humm JL, Ling CC. Cell line-dependent differences in uptake and retention of the hypoxia-selective nuclear imaging agent Cu-ATSM. *Nucl Med Biol.* 2005; 32:623–630.
- [124] Sakata D, et al. An implementation of discrete electron transport models for gold in the Geant4 simulation toolkit. *J. Appl. Phys.* 2016; 120, 244901.
- [125] Hainfeld JF, Slatkin DN, Smilowitz HN. The use of gold nanoparticles to enhance radiotherapy in mice. *Phys. Med. Biol.* 2014; 49:N309–N315.

- [126] Bell J. Internal dosimetric evaluation of cu-64-atm in canine cancer bearing patients, Colorado State University Thesis, 2015.
- [127] Chow JCL, Leung M, Fahey S, Chithrani D, Jaffray AD. Monte Carlo simulation on low-energy electrons from gold nanoparticle in radiotherapy. *Journal of Physics: Conference Series*. 2012; 341. 012012.
- [128] “Molar Mass Calculator”, <https://www.webqc.org>, Accessed 04/27/2018.
- [129] Williams JR, Trias E, Beilby PR, Lopez NI, Labut EM, Bradford CS, Roberts BR, McAllum EJ, Crouch PJ, Rhoads TW, et al. Copper delivery to the CNS by CuATSM effectively treats motor neuron disease in SOD(G93A) mice co-expressing the Copper-Chaperone-for-SOD. *Neurobiol. Dis.* 2016; 89, 1–9.
- [130] Noel PR, Barnett KC, Davies RE, Jolly DW, Leahy JS, Mawdesley-Thomas LE, Shillam KW, Squires PF, Street AE, Tucker WC, Worden AN. The toxicity of dimethyl sulphoxide (DMSO) for the dog, pig, rat and rabbit *Toxicology*. 1975; 3, pp. 143-169.
- [131] Willhite CC, Katz PI. Toxicology update: dimethyl sulfoxide *J. Appl. Toxicol.* 1984; 4, 155– 160.
- [132] Yuting L, Stephen JM, Matthew S, Harald P, Jan S. Comparing gold nano-particle enhanced radiotherapy with protons, megavoltage photons and kilovoltage photons: a Monte Carlo simulation. *Phys Med Biol.* 2014; 59, pp. 7675-7689.
- [133] Jain S, Hirst DG, O’Sullivan JM. Gold nanoparticles as novel agents for cancer therapy. *Br J Radiol.* 2012 85: 101–113.

- [134] Kawrakow I, Mainegra-Hing E, Rogers DWO, Tessier F, Walters BRB. The EGSnrc Code System: Monte Carlo simulation of electron and photon transport. Technical Report PIRS-701, National Research Council Canada 2017.
- [135] Paro AD, Hossain M, Webster TJ, Su M. Monte Carlo and analytic simulations in nanoparticle-enhanced radiation therapy. *Int J Nanomedicine*. 2016; 11: 4735-41.
- [136] Incerti S, Suerfu B, Xu J, Ivantchenko V, et al. Simulation of Auger electron emission from nanometer-size gold targets using the Geant4 Monte Carlo simulation toolkit *Nucl. Instr. Meth. B*. 2016; 372, pp. 91-101.
- [137] Rahman WN, Bishara N, Ackerly T, et al. Enhancement of radiation effects by gold nanoparticles for superficial radiation therapy. *Nanomedicine*. 2009; 5(2):136–142.
- [138] Alkilany AM, Murphy CJ. Toxicity and cellular uptake of gold nanoparticles: what we have learned so far? *J. Nanopart. Res.* 2010; 12, pp. 2313-2333.
- [139] Buncic G, Hickey JL, Schieber C, White JM, Crouch PJ, White AR, Xiao Z, Wedd AG, Donnelly PS. Water-soluble Bis(thiosemicarbazonato)copper(II) Complexes *Aust. J. Chem.* 2011, 64, 244–252.
- [140] De Ieso PB, Schick U, Rosenfelder N, Mohammed K, Ross GM. Breast cancer brain metastases: a 12 year review of treatment outcomes. *Breast* 2015; 24(4):426–433.
- [141] Piskounova E, Agathocleous M, Murphy MM, Hu Z, Huddlestun SE, Zhao Z, Leitch AM, Johnson TM, DeBerardinis RJ, Morrison SJ. Oxidative stress inhibits distant metastasis by human melanoma cells. *Nature*. 2015; Nov 12; 527(7577):186-91.

- [142] Chao KS, et al. A novel approach to overcome hypoxic tumor resistance: Cu-ATSM-guided intensity-modulated radiation therapy. *Int. J. Radiat. Oncol. Biol. Phys.* 2001; 49, 1171–1182.
- [143] Ali H, van Lier JE. Metal Complexes as Photo- and Radiosensitizers. *Chemical Reviews* 1999; 99 (9), 2379-2450.
- [144] “Toxicological profile for copper” U.S. Department of Health and Human Services: Public Health Service Agency for Toxic Substances and Disease Registry, September 2004.
- [145] Stern BR. Essentiality and toxicity in copper health risk assessment: overview, update and regulatory considerations. *Toxicol Environ Health* 2010; A 73:114–127.
- [146] ICRU. Report 36: Microdosimetry. *Journal of the ICRU.* 1983.
- [147] “IARC Working Group on the Evaluation of Carcinogenic Risk to Humans. Ionizing Radiation, Part 1: X- and Gamma (γ)-Radiation, and Neutrons.” Lyon (FR): International Agency for Research on Cancer; 2000; (IARC Monographs on the Evaluation of Carcinogenic Risks to Humans, No. 75.
- [148] “Electromagnetic Radiation”, MIT Nuclear Science Engineering 22.55 Principles of Radiation Interaction (2014) [PDF Document]. Retrieved 2019.
- [149] White DR, et al. Report 44: *Journal of the International Commission on Radiation Units and Measurements* 1989; Volume 23, Issue 1, 15.
- [150] ICRP, 2007. The 2007 Recommendations of the International Commission on Radiological Protection. ICRP Publication 103. *Ann. ICRP* 37 (2-4).
- [151] Alberts, B. *Molecular biology of the cell.* (4th Ed.) Garland Science. 2002; p. 197.

- [152] Obata A, Kasamatsu S, Lewis JS. Basic characterization of ^{64}Cu -ATSM as a radiotherapy agent. *Nucl Med Biol* 2005; 32:21–8.
- [153] Maeda H, Ueda M, Morinaga T, Matsumoto T. Conjugation of poly(styrene-co-maleic acid) derivatives to the antitumor protein-neocarzinostatin: pronounced improvements in pharmacological properties *J. Med. Chem.* 1985; 28, pp. 455-461.
- [154] Clausen MM, Hansen AE, Lundemann M, Hollensen C, Pommer T, Munck A, Rosenschöld P, Kristensen AT, Kjær A, McEvoy FJ, Engelholm SA. Dose Painting Based on Tumor Uptake of ^{64}Cu -ATSM and FDG: A Comparative Study *Radiat. Oncol.* 2014; 9 (1) 228.
- [155] Incerti S, et al. The Geant4-DNA project. *Int. J. Model. Simul. Sci. Comput.* 2010; 1, 157–178.
- [156] Hammond EM, Asselin MC, Forster D, O'Connor JP, Senra JM, Williams KJ. The meaning, measurement and modification of hypoxia in the laboratory and the clinic *Clin. Oncol. (R. Coll. Radiol.)* 2014; 26, pp. 277-288.
- [157] Warburg O. The Classic: The Chemical Constitution of Respiration Ferment. *Science* 1928; 68:437 443.
- [158] LaRue, S. “Tumor Microenvironment”, Lecture 7. [PDF document]. Retrieved from Lecture Notes: Radiation Biology, Spring 2017.
- [159] Liber, H. “Apoptosis and p53: Guardians of the genome”. [PDF document]. Retrieved from Lecture Notes: Cancer Biology, Fall 2016.
- [160] Brown JM. Evidence for acutely hypoxic cells in mouse tumors, and a possible mechanism for reoxygenation. *Br J Radiol* 1979; 52(620):650-656.

- [161] Vaupel P, Mayer A. Hypoxia in tumors: pathogenesis-related classification, characterization of hypoxia subtypes and associated biological and clinical implications. *Adv Exp Med Biol.* 2014; 812:19-24.
- [162] Ellingsen C, Ovrebo KM, Galappathi K, Mathiesen B, Rofstad EK. pO₂(2) fluctuation patterns and cycling hypoxia in human cervical carcinoma and melanoma xenografts. *Int J Radiat Oncol Biol Phys,* 2012; 83(4):1317-1323.
- [163] Goodall CM, Sanders AG, Shubik P. Studies of vascular patterns in living tumors with a transparent chamber inserted in hamster cheek pouch. *J Natl Cancer Inst* 1965; 35: 497–521.
- [164] Chaplin DJ, Olive PL, Durand RE. Intermittent blood flow in a murine tumor: radiobiological effects. *Cancer Res.* 1987; 47:597–601.
- [166] Cardenas-Navia LI, Mace D, Richardson RA, et al. The pervasive presence of fluctuating oxygenation in tumors. *Cancer Res.* 2008; 68:5812–9.
- [167] Crabtree G, et al. The Action of Radium on Cancer Cells. II.--Some Factors Determining the Susceptibility of Cancer Cells to Radium. The Royal Society Publishing. 1933.
- [168] Dewhirst MW, Ong ET, Braun RD, Smith B, Klitzman B, Evans SM, Wilson D. Quantification of longitudinal tissue pO₂ gradients in window chamber tumours: impact on tumour hypoxia. *Br J Cancer.* 1999; 79(11–12):1717–1722.
- [169] Rankin E, Giaccia A. Hypoxic control of metastasis. *Science.* 2016; 352:175-180.
- [170] Chan N, Koritzinsky M, Zhao H, Bindra R, Glazer PM, Powell S, Belmaaza A, Wouters B, Bristow RG. Chronic hypoxia decreases synthesis of homologous recombination proteins to offset chemoresistance and radioresistance. *Cancer Res.* 2008; 68(2):605–614.

- [171] Semenza G, et al. Hypoxia-Inducible Factors in Physiology and Medicine. *Cell*. 2013; 148(3): 399-408.
- [172] Yang M, Wu M, Chiou S, et al. Direct regulation of TWIST by HIF-1alpha promotes metastasis. *Nat. Cell Biol.* 2008; 10, 295–305.
- [173] Kivrak EG, Yurt KK, Kaplan AA, Alkan I, Altun G. Effects of electromagnetic fields exposure on the antioxidant defense system. *Journal of Microscopy and Ultrastructure*. 2017; Volume 5, Issue 4, Pages 167-176.
- [174] Betteridge DJ. What is oxidative stress? *Metabolism*. 2000; 49 pp. 3-8.
- [175] Lushchak VI. Free radicals, reactive oxygen species, oxidative stress and its classification, *Chemico-Biological Interactions*. 2014; Volume 224, Pages 164-175.
- [177] Jajte J, Zmyslony M. The role of melatonin in the molecular mechanism of weak, static and extremely low frequency (50 Hz) magnetic fields (ELF). *Med Pr.* 2000; 51, pp. 51-57.
- [178] Turrens JF. Mitochondrial formation of reactive oxygen species. *The Journal of Physiology*. 2003; 552 (Pt 2): 335–44.
- [179] Fenton HJH. Oxidation of tartaric acid in presence of iron. *J. Chem. Soc.* 1894; *Trans.* 65 (65): 899–911.
- [180] Lenntech BV. “Fenton Reaction”. Distributieweg 3 2645 EG Delfgauw.
<https://www.lenntech.com>. Accessed 8/7/2018.
- [181] Winterbourn CC. Toxicity of iron and hydrogen peroxide: the Fenton reaction *Toxicol. Lett.* 1995; 82/83, pp. 969-974.

- [182] UCSF Medical Center. "Hemoglobin and Functions of Iron." https://www.ucsfhealth.org/education/hemoglobin_and_functions_of_iron/. Accessed 8/7/2018.
- [183] Koppenol WH. The Haber-Weiss cycle – 70 years later. *Redox Report*. 2001; 6 (4): 229–234.
- [184] Goldstein S, Meyerstein D, Czapski G. The Fenton reagents, *Free Radical Biology and Medicine*. 1993; Volume 15, Issue 4, Pages 435-445.
- [185] Masarwa M, Cohen H, Meyerstein D, Hickman DL, Bakac A, Espenson JH. Reactions of low valent transition metal complexes with hydrogen peroxide. Are they "Fentonlike" or not? The case of Cu^{+q} and $Craq^{2+}$. *J. Am. Chem. Soc.* 1988L; 110:4293-4297.
- [186] Gutteridge JMC, Wilkins S. Copper-dependent hydroxyl radical damage to ascorbic acid. *FEBS Lett.* 1982; 137:327-330.
- [187] Rowley DA, Halliwell B. Superoxide-dependent and ascorbate-dependent formation of hydroxyl radical in the presence of copper salts: A physiologically significant reaction. *Arch. Biochem. Biophys.* 1983; 225:279-284.
- [188] Gaetke LM, Chow CK. Copper toxicity, oxidative stress, and antioxidant nutrients, *Toxicology*. 2003; Volume 189, Issues 1–2, Pages 147-163.
- [189] Attix FH. "Introduction to radiological physics and radiation dosimetry" 1986; WILEY-VCH Verlag GmbH & Co. KGaA.
- [190] Turner JE, "Atoms, radiation, and radiation protection (3rd)" 2007; Wiley-VCH Verlag GmbH & Co. KGaA.

- [191] Linstrom PJ, Mallard WG. NIST Chemistry WebBook, NIST Standard Reference Database Number 69. 2018; National Institute of Standards and Technology, Gaithersburg MD, 20899, Accessed 8/7/2018.
- [192] NDT Education Resource Center. Transmitted Intensity and Linear Attenuation Coefficient. <https://www.nde-ed.org/EducationResources/CommunityCollege/Radiography/Physics/attenuationCoef.html>; Accessed 8/5/2018.
- [193] ICRU. Report 85. Journal of the ICRU, 11(1): NP, 2011.
- [194] Bushberg JT, Seibert JA, Leidholdt Jr. EM, Boone JM. The Essential Physics of Medical Imaging. Medical Physics. 1995; 22(8), 1355.
- [195] Shaw R. “Energy Modulated Radiation Therapy.” RMAAPM Spring Meeting. 2018.
- [196] Hoppe R, Phillips T, Roach M. “Leibel and Phillips Textbook of Radiation Oncology (Third Edition)”, 2010; Saunders.
- [197] Revannasiddaiah S, Susheela SP. Chemically enhanced radiotherapy: visions for the future. Ann Transl Med. 2016; 4(3):52.
- [198] Kampinga HH, Dikomey E. Hyperthermic radiosensitization: mode of action and clinical relevance, International Journal of Radiation Biology. 2001; 77:4, 399-408.
- [199] Brown T, Hogstrom K, Alvarez D, Ham K, Matthews K. SU-E-T-101: Dosimetry Intercomparison for a Synchrotron-Produced Monochromatic X-Ray Beam. Med. Phys. 2012; 39: 3726-3726.
- [200] Jones BL. Development of dosimetry and imaging techniques for pre-clinical studies of gold nanoparticle-aided radiation therapy. PhD Thesis Georgia Institute of Technology 2011

- [201] Kawrakow I, Rogers DWO. The EGSnrc Code System: Monte Carlo simulation of electron and photon transport. Technical Report PIRS–701, National Research Council of Canada, Ottawa, Canada, 2000.
- [202] Su XY, Liu PD, Wu H, Gu N. Enhancement of radiosensitization by metal-based nanoparticles in cancer radiation therapy. *Cancer Biol Med.* 2014; 11(2):86–91.
- [203] Franco-Molina MA, Mendoza-Gamboa E, Sierra-Rivera CA, Gómez-Flores RA, Zapata-Benavides P, Castillo-Tello P, et al. Antitumor activity of colloidal silver on MCF-7 human breast cancer cells. *J Exp Clin Cancer Res.* 2010; 29:148.
- [204] Liu P, Huang Z, Chen Z, Xu R, Wu H, Zang F, et al. Silver nanoparticles: a novel radiation sensitizer for glioma? *Nanoscale* 2013; 5:11829-11836
- [205] Dufort S, Le Duc G, Salomé M, et al. The high radiosensitizing efficiency of a trace of gadolinium-based nanoparticles in the tumor. *Sci. Rep.* 2016; 6, 29678.
- [206] Pease, C. An Overview of Monte Carlo Methods. *Towards Data Science.* <https://towardsdatascience.com> 9/18/2018; Accessed 4/15/2019.
- [207] Behrends E, Buescu J. Buffon: Did He Actually Throw Sticks? *European Mathematical Society Newsletter.* 2014; No. 92, pp. 47–49.
- [208] Metropolis N. The beginning of the Monte Carlo method. *Los Alamos Science.* 1987; 15(584): 125–130.
- [209] Rogers DWO, Walters B, Kawrakow I. BEAMnrc User Manual. Technical Report PIRS–509A, National Research Council of Canada, Ottawa, Canada, 2019.

- [210] Walters BRB, Kawrakow I, Rogers DWO. DOSXYZnrc User's Manual. Technical Report PIRS-794B, National Research Council of Canada, Ottawa, Canada, 2005.
- [211] Rogers DWO, Kawrakow I, Seuntjens JP, Walters BRB, Mainegra-Hing E. NRC User Codes for EGSnrc. Technical Report PIRS-702C. National Research Council of Canada, Ottawa, Canada, 20019.
- [212] Cunningham J. Quality assurance in dosimetry and treatment planning. *Int. J. Radiat. Oncol. Biol., Phys.* 1984; 10, 105–1091984.
- [213] Larsen EW, Tolar DR. A “Transport” Condensed History Method. In: Kling A, Barão FJC, Nakagawa M, Távora L, Vaz P. (eds) *Advanced Monte Carlo for Radiation Physics, Particle Transport Simulation and Applications*. 2001; Springer, Berlin, Heidelberg.
- [214] Goodhead D.T. Spatial and temporal distribution of energy. *Health Phys.* 1988; 55:231–240.
- [215] Xiao Y, Kry SF, Popple R, et al. Flattening filter-free accelerators: a report from the AAPM Therapy Emerging Technology Assessment Work Group. *J Appl Clin Med Phys.* 2015; 16:12–29.
- [216] Robar JL, Parsons D, Berman A, Macdonald A. Volume-of-interest cone-beam CT using a 2.35 MV beam generated with a carbon target. *Med. Phys.* 2012; 39(7), 4209–4218.
- [217] Dietze G, Menzel HG. Dose quantities in radiation protection and their limitations. *Radiat Prot Dosimetry.* 2004; 112(4):457—63.
- [218] Shanmugasundaram S, Chandrasekaran S. Optimization of Variance Reduction Techniques used in EGSnrc Monte Carlo Codes. *J Med Phys.* 2018; 43(3):185–194.

- [219] Mesbahi A, Zakariaee SS. Effect of anode angle on photon beam spectra and depth dose characteristics for X-RAD320 orthovoltage unit, Reports of Practical Oncology & Radiotherapy, Volume 18, Issue 3,2013;Pages 148-152.
- [220] Bojorquez MH, Martinez-Davalos A, Rodriguez-Villafuerte M, Larraga JM, Garcia A, Celis MA. Characterization of the photon energy spectrum of a 6 MV Linac, Med. Phys. 2006; 854, pp. 230–232.
- [221] Zygmanski P, Sajo E. Nanoscale radiation transport and clinical beam modeling for gold nanoparticle dose enhanced radiotherapy (GNPT) using X-rays. Br J Radiol. 2016; 89(1059):20150200.
- [222] Gray LH, Conger AD, Ebert M, Hornsey S, Scott OC. The concentration of oxygen dissolved in tissues at the time of irradiation as a factor in radiotherapy. Br. J. Radiol. 1953; 26:638–648.
- [223] Brown JM, Wilson WR. Exploiting tumour hypoxia in cancer treatment. Nat. Rev. Cancer. 2004; 4:437–447.
- [224] Wang H, Jiang H, Van De Gucht M, De Ridder M. Hypoxic Radioresistance: Can ROS Be the Key to Overcome It? Cancers (Basel). 2019; 11(1):112. Published 2019 Jan 18.
- [225] Kim MS, Lee EJ, Kim JW, et al. Gold nanoparticles enhance anti-tumor effect of radiotherapy to hypoxic tumor. Radiat Oncol J. 2016; 34(3):230–238.
- [226] Teoh M, Clark CH, Wood K, Whitaker S, Nisbet A. Volumetric modulated arc therapy: a review of current literature and clinical use in practice. Br J Radiol. 2011; 84(1007):967–996.

- [227] Van Esch A, Tillikainen L, Pyykkonen J, Tenhunen M, Helminen H, Siljamäki S, Alakujala J, Paiusco M, Lori M, Huyskens DP. Testing of the analytical anisotropic algorithm for photon dose calculation.1. Med Phys. 2006; Nov; 33(11):4130-48.
- [228] Robar, J. “Introduction to Monte Carlo modeling” [PDF document]. Retrieved from Lecture Notes: Computational Methods in Medical Physics.
- [229] Orton B, Niemierko U. The role of medical physicists and the AAPM in the development of treatment planning and optimization. Med. Phys. 2008; 35.
- [230] Wang W, Yu Z, Su W. Ion irradiation and biomolecular radiation damage II. Indirect effect. ArXiv. 2010; no. 1, p. 8.
- [231] Xiaochuan S, La Riviere K. Development of x-ray computed tomography: The role of Medical Physics and AAPM from the 1970s to present. Med. Phys. 2008; 35.
- [232] Wen-Zhou C, Ying X, Jun L. Impact of dose calculation algorithm on radiation therapy, World J Radiol. 2014; Nov 28; 6(11): 874–880.
- [233] Chow J. “Chapter 15 - Dose enhancement effect in radiotherapy: adding gold nanoparticles to tumor in cancer treatment,” (eds) Fikai A, Grumezescu AM. Nanostructures for Cancer Therapies, Nanostructures in Therapeutic Medicine Series, 2017.
- [234] Kato, T. “Radiochemistry”, Lecture 1. Survival. [PDF document]. Retrieved from Lecture Notes: Radiation Biology, Spring 2017.
- [235] Asai, M. “Geometry”, [PDF document]. Retrieved from Lecture Notes: 27 June 2018, Geant4 Tutorial at MD Anderson Cancer Center, Houston, TX.

- [236] Asai, M. “Primary Particle”, [PDF document]. Retrieved from Lecture Notes: 27 June 2018, Geant4 Tutorial at MD Anderson Cancer Center, Houston, TX.
- [237] Han T, Mikell JK, Salehpour M, Mourtada F. Dosimetric comparison of Acuros XB deterministic radiation transport method with Monte Carlo and model-based convolution methods in heterogeneous media. *Med. Phys.* 2011; 38, 2651–2664.
- [238] Zurl B, Tiefling R, Winkler P, Kindl P, Kapp KS. Hounsfield Units variations: impact on CT-density based conversion tables and their effects on dose distribution. *Strahlentherapie und Onkologie.* 2014; 190, 88–93.
- [239] Neph R, et al. Distributed Multi-GPU photon beamlet dose calculation for efficient radiation treatment planning, AAPM Meeting 2018.
- [240] Papanikolaou N, Battista J, Boyer A, Kappas C, Klein E, Mackie TR, Sharpe M, Van Dyk J. Tissue inhomogeneity corrections for megavoltage photon beams AAPM Report No 85 Task group No 65 of the Radiation Therapy Committee of the American Association of Physicists in Medicine. 2004.
- [241] Bardies M. Dosimetry and Microdosimetry of Targeted Radiotherapy. *Current Pharmaceutical Design.* 2000; Volume 6, Number 14, pp. 1469-1502.
- [242] Verhaegen F. Evaluation of the EGSnrc Monte Carlo code for interface dosimetry near high-Z media exposed to kilovolt and 60Co photons, *Phys. Med. Biol.* 2002; 47 1691-1705.
- [243] Cygler JE, Daskalov GM, Chan GH, Ding GX. Evaluation of the first commercial Monte Carlo dose calculation engine for electron beam treatment planning. *Med Phys.* 2004; 31 142-153.

- [244] Yoshii Y, Furukawa T, Matsumoto H, et al. ^{64}Cu -ATSM therapy targets regions with activated DNA repair and enrichment of CD133+ cells in an HT-29 tumor model: sensitization with a nucleic acid antimetabolite. *Cancer Lett.* 2016; 376: 74-82.
- [245] Burnet NG, Thomas SJ, Burton KE, Jefferies SJ. Defining the tumour and target volumes for radiotherapy. *Cancer Imaging.* 2004; 4(2):153–161. Published 2004 Oct 21.
- [246] Bentzen SM, Gregoire V. Molecular Imaging-Based Dose Painting: A Novel Paradigm for Radiation Therapy Prescription. *Semin. Radiat. Oncol.* 2011; 21 (2), 101–110.
- [247] Sansare K, Khanna V, Karjodkar F. Early victims of X-rays: a tribute and current perception. *Dentomaxillofac Radiol.* 2011; 40(2):123–125.
- [248] Gleason KM. Hermann Joseph Muller's Study of X-rays as a Mutagen, (1926- 1927). Embryo Project Encyclopedia (2017-03-07). <http://embryo.asu.edu>.
- [249] Bedford JS, Dewey WC. Historical and current highlights in radiation biology: has anything important been learned by irradiating cells? *Radiat. Res.* 2002; 158, pp. 251-291.
- [250] Vogin G, Foray N. The law of Bergonié and Tribondeau: A nice formula for a first approximation. *International journal of radiation biology.* 2012; 89. 10.3109.
- [251] Yashar CM. Chapter 23 - Basic Principles in Gynecologic Radiotherapy, (eds) Di Saia PJ, Creasman WT, *Clinical Gynecologic Oncology (Eighth Edition)*, Mosby, 2012.
- [252] Packard, C. The Relation between Division Rate and the Radiosensitivity of Cells. *The Journal of Cancer Research.* 1930; August 1, (14) (3) 359-369.
- [253] Ewing J. Radiosensitive epidermoid carcinomas. *Am. J. Roentgenol.* 1929; 21:313-321.

- [254] Pajonk F, Vlashi E, McBride WH. Radiation resistance of cancer stem cells: the 4 R's of radiobiology revisited. *Stem Cells*. 2010; 28(4):639–648.
- [255] Tellez-Gabriel M, Ory B, Lamoureux F, Heymann MF, Heymann D. Tumour Heterogeneity: The Key Advantages of Single-Cell Analysis. *Int J Mol Sci*. 2016; 17(12):2142. Published 2016 Dec 20.
- [256] Davis BW, Ostrander EA. Domestic dogs and cancer research: a breed-based genomics approach. *ILAR J*. 2014; 55, 59 – 68.
- [257] June CH. “Chapter 30 – Adoptive Cellular Therapy with Synthetic T Cells as an ‘Instant Vaccine’ for Cancer and Immunity”, (eds) Bloom BR, Lambert PH, *The Vaccine Book (Second Edition)*, Academic Press, 2016.
- [258] Goodspeed A, Heiser LM, Gray JW, Costello JC. Tumor-Derived Cell Lines as Molecular Models of Cancer Pharmacogenomics. *Mol Cancer Res*. 2015; 14(1):3–13.
- [259] Neely C, A Brief History of Spheroids, ThermoFisher Scientific. (08.24.2016)
<https://www.thermofisher.com>. Accessed 4/6/2019.
- [260] Harrison RG. The Outgrowth of the Nerve Fiber as a Mode of Protoplasmic Movement. *Journal of Experimental Zoology*. 1910; 9: 787–846.
- [261] Puck TT, Morkovin D, Marcus PI, Cieciura SJ. Action of x-rays on mammalian cells. II. Survival curves of cells from normal human tissues. *J Exp Med*. 1957; 106(4):485–500.
- [262] Lewis NE, et al. Genomic landscapes of Chinese hamster ovary cell lines as revealed by the *Cricetulus griseus* draft genome. *Nature Biotech*. 2013; 31, 759–765.

- [263] “Simulation Primer: An Introduction to Basic Simulation Concepts”, GoldSim Technology Group, www.goldsim.com 2017. Accessed 4/10/2019.
- [264] Hu T, Miller MC, Ridder GM, Aardema MJ. Characterization of p53 in Chinese hamster cell lines CHO-K1, CHO-WBL, and CHL: Implications for genotoxicity testing. *Mutation research*. 1999; 426. 51-62.
- [265] Tjio JH, Puck TT. Genetics of somatic mammalian cells. II. Chromosomal constitution of cells in tissue culture. *J. Exp. Med.* 1958; 108(2): 259–271.
- [266] Munshi A, Hobbs M, Meyn RE. Clonogenic cell survival assay. *Methods Mol Med* 2005; 110:21–8.
- [267] “Cell Survival Curves”, MIT Nuclear Science Engineering 22.55 Principles of Radiation Interaction (2014) [PDF Document]. Retrieved 2019.
- [268] “Health Risks from Exposure to Low Levels of Ionizing Radiation: BEIR VII Phase 2” Chapter: 2 Molecular and Cellular Responses to Ionizing Radiation, 2006.
- [269] Kato, T. “Cell killing and survival curves”, Lecture 2. Survival. [PDF document]. Retrieved from Lecture Notes: Radiation Biology, Spring 2017.
- [270] Azzam EI, Jay-Gerin JP, Pain D. Ionizing radiation-induced metabolic oxidative stress and prolonged cell injury. *Cancer Lett.* 2011; 327(1-2):48–60.
- [271] Haskins AH, Buglewicz DJ, Hirakawa H, Fujimori A, Aizawa Y, Kato TA. Palmitoyl ascorbic acid 2-glucoside has the potential to protect mammalian cells from high-LET carbon-ion radiation. *Scientific Reports*. 2018; 13822:8:1.

- [272] Klaus V, Uwe J, Medlin L. Nucleic Acid Isolation from Environmental Aqueous Samples, *Methods in Enzymology*, Academic Press, Volume 395, 2005, Pages 15-37.
- [273] Vasavada N. One-way ANOVA (ANalysis Of VAriance) with post-hoc Tukey HSD (Honestly Significant Difference) Test Calculator for comparing multiple treatments, 2016; www.astatsa.com. Accessed 4/12/2019.
- [274] Reines D. Use of RNA Yeast Polymerase II Mutants in Studying Transcription Elongation, *Methods in Enzymology*. 2003; Academic Press, Volume 371, Pages 284-292.
- [275] Slavotinek A, McMillan TJ, Steel CM. Measurement of radiation survival using the MTT assay, *European Journal of Cancer*, 1994; Volume 30, Issue 9, Pages 1376-1382.
- [276] Henningson EW, Lundquist M, Larsson E, Sandstrom G, Forsman M. A comparative study of different methods to determine the total number and the survival ratio of bacteria in aerobiological samplers, *Journal of Aerosol Science*. 1997; 28, pp. 459-469
- [277] Ross DD, Joneckis CC, Ordonez JV, Sick A, Wu R, Hamburger A, Nora R: Estimation of cell survival by flow cytometric quantification of fluorescein diacetate/propidium iodide viable cell number. *Cancer Res*. 1989; 49:3776.
- [278] Jung J. Human tumor xenograft models for preclinical assessment of anticancer drug development. *Toxicol Res*. 2014; 30(1):1–5.
- [279] LaRue, S. “In-Vivo Models”, Lecture 8. [PDF document]. Retrieved from Lecture Notes: Radiation Biology, Spring 2017.
- [280] Incerti S, Douglass M, Penfold S, Guatelli S, Bezak E. Review of Geant4-DNA applications for micro and nanoscale simulations. *Phys. Med*. 2016; 32(10), 1187-1200.

- [281] Bernal MA, et al. Track structure modeling in liquid water: A review of the Geant4-DNA very low energy extension of the Geant4 Monte Carlo simulation toolkit. *Phys. Med.* 2015; 31 861-874.
- [282] Pianetta, P. Low-energy electron ranges in matter. X-Ray Data Booklet Section 3.2; <http://xdb.lbl.gov> Accessed 4/12/2019.
- [283] Zaidi H, Sgouros G. Therapeutic applications of Monte Carlo calculations in nuclear medicine. CRC Press, London 2002.
- [284] McMahon SJ, Hyland WB, Muir MF, Coulter JA, Jain S, Butterworth KT, et al. Biological consequences of nanoscale energy deposition near irradiated heavy atom nanoparticles *Sci Rep.* 2011; 1, p.18.
- [285] Wälzlein C, Scifoni E, Krämer M, Durante M. Simulations of dose enhancement for heavy atom nanoparticles irradiated by protons *Phys Med Biol.* 2014; 59(6):1441-58.
- [286] Sakata D, et al. Geant4-DNA track-structure simulations for gold nanoparticles: the importance of electron discrete models in nanometer volumes *Med. Phys.* 2018; 45 2230–42.
- [287] Verkhovtsev A, Traore A, Muñoz A, Blanco F, García G. Modeling secondary particle tracks generated by intermediate- and low-energy protons in water with the Low-Energy Particle Track Simulation code. *Radiat. Phys. Chem.* 2017; 130 371–8.
- [288] Surdutovich E, Solov'yov AV. Multiscale approach to the physics of radiation damage with ions. *Eur Phys J D.* 2014; 68(11):353.
- [289] Boudaiffa B, Cloutier P, Hunting D, Huels MA, Sanche L. Resonant formation of DNA strand breaks by low-energy (3 to 20 eV) electrons. *L. Science.* 2000; 287, 1658.

- [290] Huels, MA. Single, Double, and Multiple Double Strand Breaks Induced in DNA by 3–100 eV Electrons. *Journal of the American Chemical Society*. 2003; 125(15):4467-77.
- [291] Bordage M, et al. Implementation of new physics models for low energy electrons in liquid water in Geant4-DNA. *Physica Medica*. 2016; 32, 1833–1840.
- [292] Tran HN, El Bitar Z, Champion C, Karamitros M, Bernal MA, Francis Z, et al. Modeling proton and alpha elastic scattering in liquid water in Geant4-DNA *Nucl Instrum Methods Phys Res B*. 2015; 343, pp. 132-137.
- [293] Lampe N, Karamitros M, Breton V, Brown JMC, Sakata D, Sarramia D, et al. Mechanistic DNA damage simulations in geant4-DNA Part 1: a parameter study in a simplified geometry *Phys Med*. 2017; Volume 48, Pages 135-145.
- [294] Lampe N, Karamitros M, Breton V, Brown JMC, Sakata D, Sarramia D, et al. Mechanistic DNA damage simulations in Geant4-DNA Part 2: Electron and proton damage in a bacterial cell. *Phys Med* 2018; 48:146–55.
- [295] Bordes J, Incerti S, Lampe N, Bardiès M, Bordage MC. Low-energy electron dose-point kernel simulations using new physics models implemented in Geant4-DNA *Nucl. Instrum. Methods Phys. Res.* 2017; Sect. B 398, 13.
- [296] Francis Z, Incerti S, Capra R, Mascialino B, Montarou G, Stepan V, Villagrasa C. Molecular scale track structure simulations in liquid water using the Geant4-DNA Monte-Carlo processes. *Appl. Rad. Isotopes*. 2011; vol. 69, pp. 220–226.
- [297] Gomes PJ, et al. Energy Thresholds of DNA Damage Induced by UV Radiation: An XPS Study. *The Journal of Physical Chemistry B* 2015; 119 (17), 5404-5411.

- [298] Champion C, et al. Electron and proton elastic scattering in water vapour. *Nuclear Instruments and Methods in Physics Research B*. 2012; 273, 98.
- [299] Champion C, et al. A free-parameter theoretical model for describing the electron elastic scattering in water in the Geant4 toolkit. *Radiat. Phys. Chem.* 2009; 78, 745–750.
- [300] Kuncic Z. Advances in computational radiation biophysics for cancer therapy: simulating nano-scale damage by low-energy electrons *Biophys. Rev. Lett.* 2015; 10 25–36.
- [301] Kyriakou I, et al. Technical Note: improvements in GEANT4 energy-loss model and the effect on low-energy electron transport in liquid water. *Med Phys.* 2015; 42, pp. 3870-3876.
- [302] Ivanchenko VN, et al. Combination of electromagnetic physics processes for microdosimetry in liquid water with the Geant4 Monte Carlo simulation toolkit. *Nucl Instrum Methods Phys Res B*. 2012; 273, pp. 95-97.
- [303] Friedland W, Jacob P, Paretzke HG, et al. Simulation of DNA fragment distributions after irradiation with photons, *Rad. Env. Bio.* 1999; 38, 39-47.
- [304] Friedland W, Schmitt E, Kunderát P, et al. Comprehensive track-structure based evaluation of DNA damage by light ions from radiotherapy-relevant energies down to stopping. *Sci Rep.* 2017; 7:45161.
- [305] Nikjoo H, Emfietzoglou D, Liamsuwan T, Taleei R, Liljequist D, Uehara S. Radiation track, DNA damage and response—a review. *Rep Prog Phys.* 2016; 79:116601.
- [306] Incerti S, et al. Comparison of GEANT4 very low energy cross section models with experimental data in water *Med Phys.* 2010; 37, pp. 4692-4708.

- [307] Allison J, et al. Geant4 developments and applications in IEEE Transactions on Nuclear Science. 2006; vol. 53, no. 1, pp. 270-278.
- [308] Agostinelli S, et al. GEANT4—a simulation toolkit. Nucl. Instrum. Meth. A. 2003; 506, p. 250.
- [309] Champion C, et al. Dose point kernels in liquid water: an intra-comparison between GEANT4-DNA and a variety of Monte Carlo codes. Appl Radiat Isot. 2014; 83, pp. 137-141.
- [310] André T, et al. Comparison of Geant4-DNA simulation of S-values with other Monte Carlo codes. Nucl Instrum Methods Phys Res B. 2014; 319, pp. 87-94.
- [311] Incerti S, et al. Simulating radial dose of ion tracks in liquid water simulated with Geant4-DNA: a comparative study Nucl Instrum Methods Phys Res B. 2014; 333, pp. 92-98.
- [312] Schalch T, Duda S, Sargent DF, Richmond TJ. X-ray structure of a tetranucleosome and its implications for the chromatin fibre. Nature 2005; 436: 138-141.
- [313] Delage E, et al. PDB4DNA: implementation of DNA geometry from the Protein Data Bank (PDB) description for Geant4-DNA Monte-Carlo simulations. Comput Phys Commun. 2015; 192, pp. 282-288.
- [314] M. Karamitros, et al. Diffusion-controlled reactions modeling in Geant4-DNA. J. Comput. Phys. 2014; 274, p. 841.
- [315] Kreipl MS, Friedland W, Paretzke HG. Interaction of ion tracks in spatial and temporal proximity. Radiat. Environ. Biophys. 2009; 48, pp. 349-359.
- [316] Tian Z, Jiang SB, Jia X. Accelerated Monte Carlo simulation on the chemical stage in water radiolysis using GPU. Phys Med Biol. 2017; 62:3081–3096.

- [317] Incerti S. Geant4-DNA Overview: 2015 Geant4-DNA Tutorial [PDF Document] Hiroshima, Japan August 24-25 Accessed 4/20/2019.
- [318] Pan et al. Metabolic characterization of a CHO cell size increase phase in fed-batch cultures. *Appl. Microbiol. Biotechnol.* 2017; 101, pp. 8101-8113.
- [319] Spiga J, Siegbahn EA, Bräuer-Krisch E, Randaccio P, Bravin A. Microdosimetry for microbeam radiation therapy (MRT): theoretical calculations using the Monte Carlo toolkit *IEEE Nuclear Science Symp. Conf. Record* 2016; (San Diego, CA) pp 1363-7.
- [320] Villagrasa, C. First results on DNA clustered damage combining direct and indirect effects with Geant4-DNA. *MCMA-2017*; Naples, Italy; IRSN representing the efforts of the Geant4-DNA Collaboration.
- [321] Mantero A. Modeling Radiation Chemistry and Biology in the Geant4 Toolkit. Geant4-DNA consortium MC2010, Tokyo.
- [322] Abolfath R, Peeler CR, Newpower M, Bronk L, Grosshans D, Mohan R. A model for relative biological effectiveness of therapeutic proton beams based on a global fit of cell survival data. *Sci Rep.* 2017; 7:8340.
- [323] Kase Y, et al. Biophysical calculation of cell survival probabilities using amorphous track structure models for heavy-ion irradiation. *Phys Med Biol*, 53 (2008), pp. 37-59.
- [324] Werner BL, Das IJ, Khan FM, Meigooni AS. Dose perturbations at interfaces in photon beams. *Medical Physics*, vol. 14, no. 4, pp. 585–595, 1987.

- [325] White PJ, Zwicker RD, Huang DT. Comparison of dose homogeneity effects due to electron equilibrium loss in lung for 6 MV and 18 MV photons. *International Journal of Radiation Oncology Biology Physics*, vol. 34, no. 5, pp. 1141–1146, 1996.
- [326] Malhotra H, Avadhani J, de Boer S, Podgorsak M. SU-FF-T-81: mixed beam energy for IMRT treatment of prostate carcinoma. *Medical Physics*, vol. 32, no. 6, p. 1968, 2005
- [327] Park JM, Kim JI, Heon Choi C, Chie EK, Kim IH, S.-J. Ye SJ. Photon energy-modulated radiotherapy: Monte Carlo simulation and treatment planning study. *Medical Physics*, vol. 39, no. 3, pp. 1265–1277, 2012.
- [328] Fogliata A, Nicolini G, Clivio A, Vanetti E, Cozzi L. Dosimetric evaluation of Acuros XB advanced dose calculation algorithm in heterogeneous media. *Radiat Oncol* 2011, 6:82.
- [329] Lewis EE, Miller WF. *Computational methods of neutron transport*. Wiley, New York, 1984.
- [330] Kraft G, Kramer M. “Microdosimetric Measurements of the Radial Dose Distribution,” (eds) Altman K, Lett JT. *Advances in Radiation Biology, Relative Radiation Sensitivities of Human Organ Systems*, 1994.
- [331] Santa Cruz GA. Microdosimetry: Principles and applications. *Rep Pract Oncol Radiother*. 2016; 21(2):135–139.

APPENDIX A

A.1 – PEGS4 Materials for BEAMnrc Models

```
MEDIUM=Air , STERNCID=Air
MIXT,RHO= 1.2048E-03,NE= 4, IUNRST=0, EPSTFL=1, IAPRIM=1
ASYM=C ,Z= 6.,A= 12.011,PZ= 1.03237E-05,RHOZ= 1.24000E-04
ASYM=N ,Z= 7.,A= 14.007,PZ= 5.39218E-02,RHOZ= 7.55267E-01
ASYM=O ,Z= 8.,A= 15.999,PZ= 1.44869E-02,RHOZ= 2.31781E-01
ASYM=AR,Z=18.,A= 39.948,PZ= 3.21092E-04,RHOZ= 1.28270E-02
```

```
MEDIUM=Beryllium , STERNCID=Beryllium
ELEM,RHO= 1.8480E+00,NE= 1, IUNRST=0, EPSTFL=1, IAPRIM=1
ASYM=BE,Z= 4.,A= 9.012,PZ= 1.00000E+00,RHOZ= 9.01220E+00
```

```
MEDIUM=Copper , STERNCID=Copper
ELEM,RHO= 8.9600E+00,NE= 1, IUNRST=0, EPSTFL=1, IAPRIM=1
ASYM=CU,Z=29.,A= 63.540,PZ= 1.00000E+00,RHOZ= 6.35400E+01
```

```
MEDIUM=Kapton , STERNCID=Kapton
MIXT,RHO= 1.4200E+00,NE= 4, IUNRST=0, EPSTFL=1, IAPRIM=1
ASYM=H ,Z= 1.,A= 1.008,PZ= 2.61536E-02,RHOZ= 2.63620E-02
ASYM=C ,Z= 6.,A= 12.011,PZ= 5.75410E-02,RHOZ= 6.91133E-01
ASYM=N ,Z= 7.,A= 14.007,PZ= 5.23107E-03,RHOZ= 7.32700E-02
ASYM=O ,Z= 8.,A= 15.999,PZ= 1.30777E-02,RHOZ= 2.09235E-01
```

```
MEDIUM=Mylar , STERNCID=Mylar
MIXT,RHO= 1.3800E+00,NE= 3, IUNRST=0, EPSTFL=1, IAPRIM=1
ASYM=H ,Z= 1.,A= 1.008,PZ= 4.16272E-02,RHOZ= 4.19590E-02
ASYM=C ,Z= 6.,A= 12.011,PZ= 5.20364E-02,RHOZ= 6.25017E-01
ASYM=O ,Z= 8.,A= 15.999,PZ= 2.08148E-02,RHOZ= 3.33025E-01
```

```
MEDIUM=Tungsten , STERNCID=Tungsten
ELEM,RHO= 1.9300E+01,NE= 1, IUNRST=0, EPSTFL=1, IAPRIM=1
ASYM=W ,Z=74.,A= 183.850,PZ= 1.00000E+00,RHOZ= 1.83850E+02
```

```
MEDIUM=Water , STERNCID=Water
MIXT,RHO= 1.0000E+00,NE= 2, IUNRST=0, EPSTFL=1, IAPRIM=1
ASYM=H ,Z= 1.,A= 1.008,PZ= 1.11009E-01,RHOZ= 1.11894E-01
ASYM=O ,Z= 8.,A= 15.999,PZ= 5.55087E-02,RHOZ= 8.88106E-01
```

```
MEDIUM=Graphite , STERNCID=Graphite
ELEM,RHO= 1.7600E+00,NE= 1, IUNRST=0, EPSTFL=0, IAPRIM=1
ASYM=C ,Z= 6.,A= 12.011,PZ= 1.00000E+00,RHOZ= 1.20112E+01
```

```
MEDIUM=Steel , STERNCID=Steel
MIXT,RHO= 8.0600E+00,NE= 6, IUNRST=0, EPSTFL=1, IAPRIM=1
ASYM=C ,Z= 6.,A= 12.011,PZ= 8.32560E-05,RHOZ= 1.00000E-03
ASYM=SI,Z=14.,A= 28.088,PZ= 2.49217E-04,RHOZ= 7.00000E-03
```

```

ASYM=CR,Z=24.,A= 51.998,PZ= 3.46167E-03,RHOZ= 1.80000E-01
ASYM=MN,Z=25.,A= 54.938,PZ= 1.82023E-04,RHOZ= 1.00000E-02
ASYM=FE,Z=26.,A= 55.847,PZ= 1.27491E-02,RHOZ= 7.12000E-01
ASYM=NI,Z=28.,A= 58.710,PZ= 1.53296E-03,RHOZ= 9.00000E-02

```

```

MEDIUM=Brass_360 ,STERNCID=Brass_360
MIXT,RHO= 8.4700E+00,NE= 2, IUNRST=0, EPSTFL=1, IAPRIM=1
ASYM=CU,Z=29.,A= 63.540,PZ= 1.03872E-02,RHOZ= 6.60000E-01
ASYM=ZN,Z=30.,A= 65.370,PZ= 5.20116E-03,RHOZ= 3.40000E-01

```

```

MEDIUM=Brass_365 ,STERNCID=Brass_365
MIXT,RHO= 8.6700E+00,NE= 2, IUNRST=0, EPSTFL=1, IAPRIM=1
ASYM=CU,Z=29.,A= 63.540,PZ= 1.25905E-02,RHOZ= 8.00000E-01
ASYM=ZN,Z=30.,A= 65.370,PZ= 3.05951E-03,RHOZ= 2.00000E-01

```

```

MEDIUM=Aluminum ,STERNCID=Aluminum
MIXT,RHO= 2.7000E+00,NE= 5, IUNRST=0, EPSTFL=1, IAPRIM=1
ASYM=MG,Z=12.,A= 24.312,PZ= 4.11319E-04,RHOZ= 1.00000E-02
ASYM=AL,Z=13.,A= 26.982,PZ= 3.62749E-02,RHOZ= 9.78750E-01
ASYM=SI,Z=14.,A= 28.088,PZ= 2.13614E-04,RHOZ= 6.00000E-03
ASYM=CR,Z=24.,A= 51.998,PZ= 4.80788E-05,RHOZ= 2.50000E-03
ASYM=CU,Z=29.,A= 63.540,PZ= 4.32798E-05,RHOZ= 2.75000E-03

```

A.2 – BEAMnrc Input Code for Trilogy Model

```

VTH CLinac Trilogy      20x20           Higher Accuracy
#!GUI1.0
Air
0, 0, 0, 0, 1, 1, 0,  IWATCH ETC.
1000000000, 127, 128, 72, 2, 29, 0, 0,  NCASE ETC.
10, 100, 2, 20, 0, 16.37582,  DIRECTIONAL BREM OPTIONS
-1, 0, 0.1, 0, 0, 0,  0.0, 0.0, 0.0, 0.0,  IQIN, ISOURCE + OPTIONS
0, MONOENERGETIC
6.0
0, 0, 0.02, 0.001, 0, 0, , 0 , ECUT,PCUT,IREJCT,ESAVE
0, 0, 0, 0, 0,  PHOTON FORCING
1, 7,  SCORING INPUT
0,1
0, DOSE COMPONENTS
0.0, Z TO FRONT FACE
***** start of CM FLATFILT with identifier PrimColl *****
3.4, RMAX
Primary Collimator
0, ZMIN
10, NUMBER OF LAYERS
1, 1.55, # CONES, ZTHICK OF LAYER 1
0.2889,
0.2889,
1, 0.834, # CONES, ZTHICK OF LAYER 2
0.2889,
1.45,
2, 0.0889, # CONES, ZTHICK OF LAYER 3
1.44, 1.45,
1.44, 1.45,

```

2, 0.1575, # CONES, ZTHICK OF LAYER 4
 1.44, 1.45,
 1.44, 1.45,
 1, 0.76, # CONES, ZTHICK OF LAYER 5
 1.45,
 0.8,
 1, 0.5036, # CONES, ZTHICK OF LAYER 6
 0.8,
 0.5778,
 1, 2.344, # CONES, ZTHICK OF LAYER 7
 0.5778,
 1.156,
 2, 3.776, # CONES, ZTHICK OF LAYER 8
 1.156, 2.25,
 2.09, 2.25,
 1, 1.03, # CONES, ZTHICK OF LAYER 9
 0,
 0,
 1, 0.0254, # CONES, ZTHICK OF LAYER 10
 3.4,
 3.4,
 0, 0, 0, 0,
 VACUUM
 3, 0.05, 0, 2,
 Tungsten
 0, 0, 0, 0,
 VACUUM
 1, 0.001, 0, 2,
 Tungsten
 0, 0, 0, 0,
 Tungsten
 0, 0, 0, 0,
 VACUUM
 1, 0.001, 0, 2,
 Tungsten
 0, 0, 0, 3,
 Copper
 0, 0, 0, 3,
 VACUUM
 1, 0.001, 0, 2,
 Tungsten
 0, 0, 0, 0,
 VACUUM
 1, 0.001, 0, 2,
 Tungsten
 0, 0, 0, 0,
 VACUUM
 3, 0.05, 0, 2,
 Tungsten
 0, 0, 0, 0,
 VACUUM
 3, 0.05, 0, 2,
 Tungsten
 0, 0, 0, 0,

```

VACUUM
0.3, 0.05, 0, 0,
Tungsten
0, 0, 0, 3,
VACUUM
0, 0, 0, 0,
VACUUM
0, 0, 0, 0,
VACUUM
0, 0, 0, 0,
Beryllium
0, 0, 0, 0,
VACUUM
***** start of CM FLATFILT with identifier FlatFilt *****
3.81, RMAX
Flattening Filter
14.166, ZMIN
19, NUMBER OF LAYERS
1, 0.02794, # CONES, ZTHICK OF LAYER 1
0,
0.0635,
1, 0.02794, # CONES, ZTHICK OF LAYER 2
0.0635,
0.127,
1, 0.0381, # CONES, ZTHICK OF LAYER 3
0.127,
0.1905,
1, 0.04064, # CONES, ZTHICK OF LAYER 4
0.1905,
0.254,
1, 0.07366, # CONES, ZTHICK OF LAYER 5
0.254,
0.381,
1, 0.13462, # CONES, ZTHICK OF LAYER 6
0.381,
0.508,
1, 0.10922, # CONES, ZTHICK OF LAYER 7
0.508,
0.635,
1, 0.10922, # CONES, ZTHICK OF LAYER 8
0.635,
0.762,
1, 0.11176, # CONES, ZTHICK OF LAYER 9
0.762,
0.889,
1, 0.10414, # CONES, ZTHICK OF LAYER 10
0.889,
1.016,
1, 0.20828, # CONES, ZTHICK OF LAYER 11
1.016,
1.27,
1, 0.1905, # CONES, ZTHICK OF LAYER 12
1.27,
1.524,

```



```

0.0005, 0, 0, 0, 5, 0
Copper
0.33, 0, 0, 0, 5, 0
Air
0.005, 0, 0, 0, 5, 0
Kapton
0.0005, 0, 0, 0, 5, 0
Kapton
0.11, 0, 0, 0, 5, 0
Air
0.005, 0, 0, 0, 5, 0
Kapton
0.0005, 0, 0, 0, 5, 0
Copper
0.82, 0, 0, 0, 5, 0
Air
0.013, 0, 0, 0, 5, 0
Kapton
0.0005, 0, 0, 0, 0, 0
Copper
0.82, 0, 0, 0, 5, 0
Air
0.005, 0, 0, 0, 5, 0
Kapton
0.0005, 0, 0, 0, 5, 0
Copper
0.12, 0, 0, 0, 5, 0
Air
0.005, 0, 0, 0, 5, 0
Kapton
0.0005, 0, 0, 0, 5, 0
Copper
0.32, 0, 0, 0, 5, 0
Air
0.013, 0, 0, 0, 5, 0
Kapton
0.0005, 0, 0, 0, 5, 0
Copper
***** start of CM MIRROR with identifier Mirr *****
7.1452, RMAX
Mirror
21.314, 8.5, ZMIN, ZTHICK
3.481, -2.4708, XFMIN, XBMIN
1, # LAYERS
0.00508, thickness of layer 1
0, 0, 0, 6,
Mylar
0, 0, 0, 0,
Air
0, 0, 0, 0,
Air
***** start of CM JAWS with identifier Jaw *****
11.5, RMAX
Secondary Collimator

```

```

2, # PAIRED BARS OR JAWS
Y
30.814, 38.584, 2.8, 3.58, -2.8, -3.58,
X
39.564, 47.364, 3.67, 4.45, -3.67, -4.45,
0, 0, 0, 0,
3, 0.05, 0, 7,
Tungsten
3, 0.05, 0, 7,
Tungsten
***** start of CM MLC with identifier Mlc *****
15, RMAX
MLC
0, IDMLFC
51.119, ZMIN
5.61, ZTHICK
64, 40, # LEAVES, TOTAL WIDTH
0, ZFOCUS(1)
0, ZFOCUS(2)
0, 0, 16
-10, 10, 32
0, 0, 16
0, 0, 0, 0,
Air
3, 0.05, 0, 0,
Tungsten
***** start of CM SLABS with identifier Window *****
14.3, RMAX
Exit Window
2, NSLABS
60.164, ZMIN
0.01016, 0, 0, 0, 8, 0
Mylar
0.5, 0, 0, 0, 0, 0
Air
*****end of all CMs*****

```

```
:Stop MC Transport Parameter:
```

```
#####
```

```
:Start DBS rejection plane:
```

```
Use a rejection plane= On
```

```
Z(cm) from zero reference plane= 57
```

```
:Stop DBS rejection plane:
```

```
#####
```

```
:Start BCSE:
```

```
Use BCSE= Off
```

```
Media to enhance= Copper
```

```
Enhancement constant= 100
```

```
Enhancement power= 0
```

```
Russian Roulette= off
```

```
:Stop BCSE:
#####
```

A.3 – BEAMnrc Input Code for Imaging Model

```
Carbon Target Robar et. al. PLEX
#!GUI1.0
Air
0, 0, 0, 0, 1, 1, 0, IWATCH ETC.
1000000000, 1, 2, 24, 1, 29, 0, 0, NCASE ETC.
-1, 0, 0.1, 0, 0, 0, 0.0, 0.0, 0.0, 0.0, IQIN, ISOURCE + OPTIONS
0, MONOENERGETIC
2.35
0, 0, 0.7, 0.01, 0, 0, , 0 , ECUT,PCUT,IREJCT,ESAVE
0, 0, 0, 0, 0, PHOTON FORCING
1, 6, SCORING INPUT
0,1
0, DOSE COMPONENTS
0.0, Z TO FRONT FACE
***** start of CM FLATFILT with identifier primcol *****
5, RMAX
PrimaryCollimation
0, ZMIN
4, NUMBER OF LAYERS
1, 1.6, # CONES, ZTHICK OF LAYER 1
4.6,
4.6,
1, 6, # CONES, ZTHICK OF LAYER 2
0.398925,
1.894893,
1, 1.4, # CONES, ZTHICK OF LAYER 3
4.9,
4.9,
1, 0.0254, # CONES, ZTHICK OF LAYER 4
4.9,
4.9,
0, 0, 0, 0,
VACUUM
0, 0, 0, 2,
Tungsten
0, 0, 0, 0,
VACUUM
0, 0, 0, 0,
Tungsten
0, 0, 0, 0,
VACUUM
0, 0, 0, 0,
VACUUM
0, 0, 0, 3,
Beryllium
0, 0, 0, 3,
Beryllium
***** start of CM FLATFILT with identifier lowztarg *****
```

```

5, RMAX
LowZ - Graphite
9.92, ZMIN
1, NUMBER OF LAYERS
1, 0.76, # CONES, ZTHICK OF LAYER 1
5,
5,
0, 0, 0, 4,
Graphite
0, 0, 0, 0,
Air
***** start of CM SLABS with identifier chamber *****
5, RMAX
IonChamber
16, NSLABS
14.2, ZMIN
0.629, 0, 0, 0, 0, 0
Air
0.013, 0, 0, 0, 5, 0
Kapton
0.229, 0, 0, 0, 0, 0
Air
0.005, 0, 0, 0, 5, 0
Kapton
0.234, 0, 0, 0, 0, 0
Air
0.005, 0, 0, 0, 5, 0
Kapton
0.229, 0, 0, 0, 0, 0
Air
0.013, 0, 0, 0, 5, 0
Kapton
0.229, 0, 0, 0, 0, 0
Air
0.005, 0, 0, 0, 5, 0
Kapton
0.234, 0, 0, 0, 0, 0
Air
0.005, 0, 0, 0, 5, 0
Kapton
0.229, 0, 0, 0, 0, 0
Air
0.013, 0, 0, 0, 5, 0
Kapton
0.629, 0, 0, 0, 0, 0
Air
0.0015, 0, 0, 0, 0, 0
Copper
***** start of CM MIRROR with identifier mirror *****
7.1452, RMAX
Mirror
18.5, 8.5, ZMIN, ZTHICK
4.9941, -7.1452, XFMIN, XBMIN
1, # LAYERS

```

```

0.0088567, thickness of layer 1
0, 0, 0, 6,
Mylar
0, 0, 0, 0,
Air
0, 0, 0, 0,
Air
***** start of CM JAWS with identifier jaws *****
11.5, RMAX
Secondary Collimation0
2, # PAIRED BARS OR JAWS
Y
28, 35.8, 2.8, 3.58, -2.8, -3.58,
X
36.7, 44.5, 3.67, 4.45, -3.67, -4.45,
0, 0, 0, 0,
0, 0, 0, 7,
Tungsten
0, 0, 0, 7,
Tungsten
***** start of CM SLABS with identifier window *****
14.3, RMAX
Mylar Exit Window
2, NSLABS
57.3, ZMIN
0.01016, 0, 0, 0, 8, 0
Mylar
42.68984, 0, 0, 0, 0, 0
Air
*****end of all CMs*****

```

A.4 – BEAMnrc Input Code for SARRP Model

```

Sarrp 5x5 mm
#!GUI1.0
Air_ICRU
0, 0, 0, 0, 0, 3, 1, IWATCH ETC.
1000000000, 125, 126, 24, 1, 300, 2, 0, NCASE ETC.
-1, 13, 0.28, 0.77, -1, 0, 0.0, 0.0, 0.0, 0.0, IQIN, ISOURCE + OPTIONS
0, MONOENERGETIC
0.225
0, 0, 0, 0, 0, 2, 10, 0, ECUT, PCUT, IREJCT, ESAVE
0, 0, 0, 0, 0, PHOTON FORCING
1, 2, SCORING INPUT
1, 1
0.2,
0, DOSE COMPONENTS
-3.0, Z TO FRONT FACE
***** start of CM XTUBE with identifier Target *****
5, RMAX
Target
-3.0, 6.0, ZMIN, ZTHICK
20, ANGLE

```

```

1, # LAYERS
0.1, 0
0, 0, 0, 1,
W
0, 0, 0, 0,
VACUUM
0, 0, 0, 2,
Cu
***** start of CM CONESTAK with identifier Housing *****
3.0, RMAX
Exit
3, 3, ZMIN, RBN
2, NUMBER OF LAYERS
0.1, 2.051, 2.051,
1.9, 2.051, 2.051,
10, 0, 0, 3, OUTER WALL
Be
0, 0, 0, 3,
Be
10, 0, 0, 4,
Steel
0, 0, 0, 0,
Air_ICRU
10, 0, 0, 4,
Steel
***** start of CM PYRAMIDS with identifier Collim1 *****
3.0, RMAX
Collim1
1, 0, #LAYERS, AIR OUTSIDE
5, 7.5, 1.45, 2.0, -1.45, -2.0, 1.45, 2.0, -1.45, -2.0, 3.0, 3.0,
0, 0, 0, 0, ECUT ETC. FOR AIR
10, 10, 0, 5,
Brass_365
***** start of CM CONESTAK with identifier Collim2a *****
2.0, RMAX
Collim2a
7.5, 0, ZMIN, RBN
2, NUMBER OF LAYERS
0.016, 0.25, 0.25,
3.484, 0.25, 0.25,
0, 0, 0, 6,
Cu
10, 10, 0, 7,
Brass_360
0, 0, 0, 0,
Air_ICRU
10, 0, 0, 7,
Brass_360
***** start of CM CONESTAK with identifier Collim2b *****
2, RMAX
Collim2b
11, 1, ZMIN, RBN
1, NUMBER OF LAYERS
1, 0.25, 0.25,

```

```

10, 0, 0, 7, OUTER WALL
Al_6061
0, 0, 0, 0,
Air_ICRU
0, 0, 0, 7,
Brass_360
***** start of CM CONESTAK with identifier CollSup3 *****
1.5875, RMAX
CollimSupport3
14.5, 0, ZMIN, RBN
1, NUMBER OF LAYERS
9, 1, 1,
0, 0, 0, 0,
Air_ICRU
10, 0, 0, 8,
Al_6061
***** start of CM CONESTAK with identifier CollSup4 *****
1.5875, RMAX
CollimSupport4
23.5, 1, ZMIN, RBN
1, NUMBER OF LAYERS
0.5, 0.635, 0.635,
10, 0, 0, 9, OUTER WALL
Al_6061
0, 0, 0, 0,
Air_ICRU
10, 0, 0, 9,
Brass_360
***** start of CM FLATFILT with identifier Collim3a *****
1.5875, RMAX
Collim3a
24, ZMIN
4, NUMBER OF LAYERS
2, 0.5, # CONES, ZTHICK OF LAYER 1
0.325, 1,
0.25, 1,
2, 2.04, # CONES, ZTHICK OF LAYER 2
0.325, 1.5,
0.325, 1.5,
2, 0.5, # CONES, ZTHICK OF LAYER 3
0.325, 1.25,
0.325, 1.25,
2, 0.42, # CONES, ZTHICK OF LAYER 4
0.325, 0.8,
0.325, 0.8,
10, 10, 0, 0,
Air_ICRU
10, 10, 0, 10,
Brass_360
10, 10, 0, 10,
Al_6061
0, 0, 0, 0,
Air_ICRU
10, 0, 0, 10,

```

```

Brass_360
10, 0, 0, 0,
Air_ICRU
0, 0, 0, 0,
Air_ICRU
10, 0, 0, 10,
Brass_360
10, 0, 0, 0,
Air_ICRU
0, 0, 0, 0,
Air_ICRU
10, 0, 0, 10,
Brass_360
10, 0, 0, 0,
Air_ICRU
***** start of CM PYRAMIDS with identifier Collim3b *****
0.8, RMAX
Collim3b
1, 0, #LAYERS, AIR OUTSIDE
27.46, 30, 0.22, 0.22, -0.22, -0.22, 0.22, 0.22, -0.22, -0.22, 0.8, 0.8,
0, 0, 0, 0, ECUT ETC. FOR AIR
0, 0, 0, 10,
Brass_360
*****end of all CMs*****

```

A.5 – PEGS4 File for DOSXYZnrc Simulations

```

MEDIUM=Copper1 , STERNCID=Copper1
MIXT,RHO= 1.7960E+00,NE= 3, IUNRST=0, EPSTFL=0, IAPRIM=1
ASYM=H ,Z= 1.,A= 1.008,PZ= 9.99087E-02,RHOZ= 1.00705E-01
ASYM=O ,Z= 8.,A= 15.999,PZ= 4.99578E-02,RHOZ= 7.99295E-01
ASYM=CU,Z=29.,A= 63.540,PZ= 1.57381E-03,RHOZ= 1.00000E-01

```

```

MEDIUM=Copper8E2 , STERNCID=Copper8E2
MIXT,RHO= 1.6368E+00,NE= 3, IUNRST=0, EPSTFL=0, IAPRIM=1
ASYM=H ,Z= 1.,A= 1.008,PZ= 1.02128E-01,RHOZ= 1.02942E-01
ASYM=O ,Z= 8.,A= 15.999,PZ= 5.10680E-02,RHOZ= 8.17058E-01
ASYM=CU,Z=29.,A= 63.540,PZ= 1.25905E-03,RHOZ= 8.00000E-02

```

```

MEDIUM=Copper5E2 , STERNCID=Copper5E2
MIXT,RHO= 1.3980E+00,NE= 3, IUNRST=0, EPSTFL=0, IAPRIM=1
ASYM=H ,Z= 1.,A= 1.008,PZ= 1.05458E-01,RHOZ= 1.06299E-01
ASYM=O ,Z= 8.,A= 15.999,PZ= 5.27333E-02,RHOZ= 8.43701E-01
ASYM=CU,Z=29.,A= 63.540,PZ= 7.86906E-04,RHOZ= 5.00000E-02

```

```

MEDIUM=Copper2E2 , STERNCID=Copper2E2
MIXT,RHO= 1.1592E+00,NE= 3, IUNRST=0, EPSTFL=0, IAPRIM=1
ASYM=H ,Z= 1.,A= 1.008,PZ= 1.08789E-01,RHOZ= 1.09656E-01
ASYM=O ,Z= 8.,A= 15.999,PZ= 5.43985E-02,RHOZ= 8.70344E-01
ASYM=CU,Z=29.,A= 63.540,PZ= 3.14762E-04,RHOZ= 2.00000E-02

```

```

MEDIUM=Copper2 , STERNCID=Copper2
MIXT,RHO= 1.0796E+00,NE= 3, IUNRST=0, EPSTFL=0, IAPRIM=1
ASYM=H ,Z= 1.,A= 1.008,PZ= 1.09899E-01,RHOZ= 1.10775E-01

```

ASYM=O ,Z= 8.,A= 15.999,PZ= 5.49536E-02,RHOZ= 8.79225E-01
ASYM=CU,Z=29.,A= 63.540,PZ= 1.57381E-04,RHOZ= 1.00000E-02

MEDIUM=Copper8E3 ,STERNCID=Copper8E3
MIXT,RHO= 1.0637E+00,NE= 3, IUNRST=0, EPSTFL=0, IAPRIM=1
ASYM=H ,Z= 1.,A= 1.008,PZ= 1.10121E-01,RHOZ= 1.10999E-01
ASYM=O ,Z= 8.,A= 15.999,PZ= 5.50646E-02,RHOZ= 8.81001E-01
ASYM=CU,Z=29.,A= 63.540,PZ= 1.25905E-04,RHOZ= 8.00000E-03

MEDIUM=Copper5E3 ,STERNCID=Copper5E3
MIXT,RHO= 1.0398E+00,NE= 3, IUNRST=0, EPSTFL=0, IAPRIM=1
ASYM=H ,Z= 1.,A= 1.008,PZ= 1.10455E-01,RHOZ= 1.11335E-01
ASYM=O ,Z= 8.,A= 15.999,PZ= 5.52311E-02,RHOZ= 8.83665E-01
ASYM=CU,Z=29.,A= 63.540,PZ= 7.86906E-05,RHOZ= 5.00000E-03

MEDIUM=Copper2E3 ,STERNCID=Copper2E3
MIXT,RHO= 1.0159E+00,NE= 3, IUNRST=0, EPSTFL=0, IAPRIM=1
ASYM=H ,Z= 1.,A= 1.008,PZ= 1.10787E-01,RHOZ= 1.11670E-01
ASYM=O ,Z= 8.,A= 15.999,PZ= 5.53977E-02,RHOZ= 8.86330E-01
ASYM=CU,Z=29.,A= 63.540,PZ= 3.14762E-05,RHOZ= 2.00000E-03

MEDIUM=Copper3 ,STERNCID=Copper3
MIXT,RHO= 1.0080E+00,NE= 3, IUNRST=0, EPSTFL=0, IAPRIM=1
ASYM=H ,Z= 1.,A= 1.008,PZ= 1.10898E-01,RHOZ= 1.11782E-01
ASYM=O ,Z= 8.,A= 15.999,PZ= 5.54532E-02,RHOZ= 8.87218E-01
ASYM=CU,Z=29.,A= 63.540,PZ= 1.57381E-05,RHOZ= 1.00000E-03

MEDIUM=Copper4 ,STERNCID=Copper4
MIXT,RHO= 1.0008E+00,NE= 3, IUNRST=0, EPSTFL=0, IAPRIM=1
ASYM=H ,Z= 1.,A= 1.008,PZ= 1.10998E-01,RHOZ= 1.11883E-01
ASYM=O ,Z= 8.,A= 15.999,PZ= 5.55031E-02,RHOZ= 8.88017E-01
ASYM=CU,Z=29.,A= 63.540,PZ= 1.57381E-06,RHOZ= 1.00000E-04

MEDIUM=Copper5 ,STERNCID=Copper5
MIXT,RHO= 1.0001E+00,NE= 3, IUNRST=0, EPSTFL=0, IAPRIM=1
ASYM=H ,Z= 1.,A= 1.008,PZ= 1.11008E-01,RHOZ= 1.11893E-01
ASYM=O ,Z= 8.,A= 15.999,PZ= 5.55081E-02,RHOZ= 8.88097E-01
ASYM=CU,Z=29.,A= 63.540,PZ= 1.57381E-07,RHOZ= 1.00000E-05

MEDIUM=Gold1 ,STERNCID=Gold1
MIXT,RHO= 2.8320E+00,NE= 3, IUNRST=0, EPSTFL=0, IAPRIM=1
ASYM=H ,Z= 1.,A= 1.008,PZ= 9.99087E-02,RHOZ= 1.00705E-01
ASYM=O ,Z= 8.,A= 15.999,PZ= 4.99578E-02,RHOZ= 7.99295E-01
ASYM=AU,Z=79.,A= 196.987,PZ= 5.07648E-04,RHOZ= 1.00000E-01

MEDIUM=Gold8E2 ,STERNCID=Gold8E2
MIXT,RHO= 2.4656E+00,NE= 3, IUNRST=0, EPSTFL=0, IAPRIM=1
ASYM=H ,Z= 1.,A= 1.008,PZ= 1.02128E-01,RHOZ= 1.02942E-01
ASYM=O ,Z= 8.,A= 15.999,PZ= 5.10680E-02,RHOZ= 8.17058E-01
ASYM=AU,Z=79.,A= 196.987,PZ= 4.06118E-04,RHOZ= 8.00000E-02

MEDIUM=Gold5E2 ,STERNCID=Gold5E2
MIXT,RHO= 1.9160E+00,NE= 3, IUNRST=0, EPSTFL=0, IAPRIM=1
ASYM=H ,Z= 1.,A= 1.008,PZ= 1.05458E-01,RHOZ= 1.06299E-01

ASYM=O ,Z= 8.,A= 15.999,PZ= 5.27333E-02,RHOZ= 8.43701E-01
ASYM=AU,Z=79.,A= 196.987,PZ= 2.53824E-04,RHOZ= 5.00000E-0

MEDIUM=Gold2E2 ,STERNCID=Gold2E2
MIXT,RHO= 1.3664E+00,NE= 3, IUNRST=0, EPSTFL=0, IAPRIM=1
ASYM=H ,Z= 1.,A= 1.008,PZ= 1.08789E-01,RHOZ= 1.09656E-01
ASYM=O ,Z= 8.,A= 15.999,PZ= 5.43985E-02,RHOZ= 8.70344E-01
ASYM=AU,Z=79.,A= 196.987,PZ= 1.01530E-04,RHOZ= 2.00000E-02

MEDIUM=Gold2 ,STERNCID=Gold2
MIXT,RHO= 1.1832E+00,NE= 3, IUNRST=0, EPSTFL=0, IAPRIM=1
ASYM=H ,Z= 1.,A= 1.008,PZ= 1.09899E-01,RHOZ= 1.10775E-01
ASYM=O ,Z= 8.,A= 15.999,PZ= 5.49536E-02,RHOZ= 8.79225E-01
ASYM=AU,Z=79.,A= 196.987,PZ= 5.07648E-05,RHOZ= 1.00000E-02

MEDIUM=Gold8E3 ,STERNCID=Gold8E3
MIXT,RHO= 1.1466E+00,NE= 3, IUNRST=0, EPSTFL=0, IAPRIM=1
ASYM=H ,Z= 1.,A= 1.008,PZ= 1.10121E-01,RHOZ= 1.10999E-01
ASYM=O ,Z= 8.,A= 15.999,PZ= 5.50646E-02,RHOZ= 8.81001E-01
ASYM=AU,Z=79.,A= 196.987,PZ= 4.06118E-05,RHOZ= 8.00000E-03

MEDIUM=Gold5E3 ,STERNCID=Gold5E3
MIXT,RHO= 1.0916E+00,NE= 3, IUNRST=0, EPSTFL=0, IAPRIM=1
ASYM=H ,Z= 1.,A= 1.008,PZ= 1.10455E-01,RHOZ= 1.11335E-01
ASYM=O ,Z= 8.,A= 15.999,PZ= 5.52311E-02,RHOZ= 8.83665E-01
ASYM=AU,Z=79.,A= 196.987,PZ= 2.53824E-05,RHOZ= 5.00000E-03

MEDIUM=Gold2E3 ,STERNCID=Gold2E3
MIXT,RHO= 1.0366E+00,NE= 3, IUNRST=0, EPSTFL=0, IAPRIM=1
ASYM=H ,Z= 1.,A= 1.008,PZ= 1.10787E-01,RHOZ= 1.11670E-01
ASYM=O ,Z= 8.,A= 15.999,PZ= 5.53977E-02,RHOZ= 8.86330E-01
ASYM=AU,Z=79.,A= 196.987,PZ= 1.01530E-05,RHOZ= 2.00000E-03

MEDIUM=Gold3 ,STERNCID=Gold3
MIXT,RHO= 1.0183E+00,NE= 3, IUNRST=0, EPSTFL=0, IAPRIM=1
ASYM=H ,Z= 1.,A= 1.008,PZ= 1.10898E-01,RHOZ= 1.11782E-01
ASYM=O ,Z= 8.,A= 15.999,PZ= 5.54532E-02,RHOZ= 8.87218E-01
ASYM=AU,Z=79.,A= 196.987,PZ= 5.07648E-06,RHOZ= 1.00000E-03

MEDIUM=Gold4 ,STERNCID=Gold4
MIXT,RHO= 1.0018E+00,NE= 3, IUNRST=0, EPSTFL=0, IAPRIM=1
ASYM=H ,Z= 1.,A= 1.008,PZ= 1.10998E-01,RHOZ= 1.11883E-01
ASYM=O ,Z= 8.,A= 15.999,PZ= 5.55031E-02,RHOZ= 8.88017E-01
ASYM=AU,Z=79.,A= 196.987,PZ= 5.07648E-07,RHOZ= 1.00000E-04

MEDIUM=Gold5 ,STERNCID=Gold5
MIXT,RHO= 1.0002E+00,NE= 3, IUNRST=0, EPSTFL=0, IAPRIM=1
ASYM=H ,Z= 1.,A= 1.008,PZ= 1.11008E-01,RHOZ= 1.11893E-01
ASYM=O ,Z= 8.,A= 15.999,PZ= 5.55081E-02,RHOZ= 8.88097E-01
ASYM=AU,Z=79.,A= 196.987,PZ= 5.07648E-08,RHOZ= 1.00000E-05

MEDIUM=Silver1 ,STERNCID=Silver1
MIXT,RHO= 1.9490E+00,NE= 3, IUNRST=0, EPSTFL=0, IAPRIM=1
ASYM=H ,Z= 1.,A= 1.008,PZ= 9.99087E-02,RHOZ= 1.00705E-01

ASYM=O ,Z= 8.,A= 15.999,PZ= 4.99578E-02,RHOZ= 7.99295E-01
ASYM=AG,Z=47.,A= 107.870,PZ= 9.27042E-04,RHOZ= 1.00000E-01

MEDIUM=Silver2 ,STERNCID=Silver2
MIXT,RHO= 1.1898E+00,NE= 3, IUNRST=0, EPSTFL=0, IAPRIM=1
ASYM=H ,Z= 1.,A= 1.008,PZ= 1.09899E-01,RHOZ= 1.10775E-01
ASYM=O ,Z= 8.,A= 15.999,PZ= 5.49536E-02,RHOZ= 8.79225E-01
ASYM=AG,Z=47.,A= 107.870,PZ= 9.27042E-05,RHOZ= 1.00000E-02

MEDIUM=Silver3 ,STERNCID=Silver3
MIXT,RHO= 1.0095E+00,NE= 3, IUNRST=0, EPSTFL=0, IAPRIM=1
ASYM=H ,Z= 1.,A= 1.008,PZ= 1.10898E-01,RHOZ= 1.11782E-01
ASYM=O ,Z= 8.,A= 15.999,PZ= 5.54532E-02,RHOZ= 8.87218E-01
ASYM=AG,Z=47.,A= 107.870,PZ= 9.27042E-06,RHOZ= 1.00000E-03

MEDIUM=Silver4 ,STERNCID=Silver4
MIXT,RHO= 1.0009E+00,NE= 3, IUNRST=0, EPSTFL=0, IAPRIM=1
ASYM=H ,Z= 1.,A= 1.008,PZ= 1.10998E-01,RHOZ= 1.11883E-01
ASYM=O ,Z= 8.,A= 15.999,PZ= 5.55031E-02,RHOZ= 8.88017E-01
ASYM=AG,Z=47.,A= 107.870,PZ= 9.27042E-07,RHOZ= 1.00000E-04

MEDIUM=Gadolinium1 ,STERNCID=Gadolinium1
MIXT,RHO= 1.6900E+00,NE= 3, IUNRST=0, EPSTFL=0, IAPRIM=1
ASYM=H ,Z= 1.,A= 1.008,PZ= 9.99087E-02,RHOZ= 1.00705E-01
ASYM=O ,Z= 8.,A= 15.999,PZ= 4.99578E-02,RHOZ= 7.99295E-01
ASYM=GD,Z=64.,A= 157.250,PZ= 6.35930E-04,RHOZ= 1.00000E-01

MEDIUM=Gadolinium2 ,STERNCID=Gadolinium2
MIXT,RHO= 1.0690E+00,NE= 3, IUNRST=0, EPSTFL=0, IAPRIM=1
ASYM=H ,Z= 1.,A= 1.008,PZ= 1.09899E-01,RHOZ= 1.10775E-01
ASYM=O ,Z= 8.,A= 15.999,PZ= 5.49536E-02,RHOZ= 8.79225E-01
ASYM=GD,Z=64.,A= 157.250,PZ= 6.35930E-05,RHOZ= 1.00000E-02

MEDIUM=Gadolinium3 ,STERNCID=Gadolinium3
MIXT,RHO= 1.0069E+00,NE= 3, IUNRST=0, EPSTFL=0, IAPRIM=1
ASYM=H ,Z= 1.,A= 1.008,PZ= 1.10898E-01,RHOZ= 1.11782E-01
ASYM=O ,Z= 8.,A= 15.999,PZ= 5.54532E-02,RHOZ= 8.87218E-01
ASYM=GD,Z=64.,A= 157.250,PZ= 6.35930E-06,RHOZ= 1.00000E-03

MEDIUM=Gadolinium4 ,STERNCID=Gadolinium4
MIXT,RHO= 1.0007E+00,NE= 3, IUNRST=0, EPSTFL=0, IAPRIM=1
ASYM=H ,Z= 1.,A= 1.008,PZ= 1.10998E-01,RHOZ= 1.11883E-01
ASYM=O ,Z= 8.,A= 15.999,PZ= 5.55031E-02,RHOZ= 8.88017E-01
ASYM=GD,Z=64.,A= 157.250,PZ= 6.35930E-07,RHOZ= 1.00000E-04

A.6 – DOSXYZnrc Sample Input File

DU PLEX Gold concentrated E-1 in SW from 3cm to 4cm in Z 0.5mm
resoluti#!GUI1.0
3
H2O
Air
Gold1

```

0.02, 0.001, 0, 0, 0, 0
-1, -1, -1, 0
-15
0.5, 60
-15
0.5, 60
0
0.05, 160
0, 60, 0, 60, 60, 80, 3,
0, 0, 0, 0, 0, 0, 0, 0
0, 0, 0, 0, 0, 0, 0, 0
0, 0, 0, 0, 0, 0, 0, 0
0, 2, 0, 0, 0, 180, 0, 0, 0, 1, 10, 100, 57, 0
2, 0, 2, 0, 0, 0, 0, 0
/projects/skmartin@colostate.edu/EGSnrc-
new/egs_home/dosxyznrc/DU2X.egsphsp1
1665773503, 0, 24, 84, 26, 20, 0, 0, 2, 0, , 1, 0, 0, 1, 0, 0

```

A.7 – Silver and Gadolinium Dose Enhancement Factors

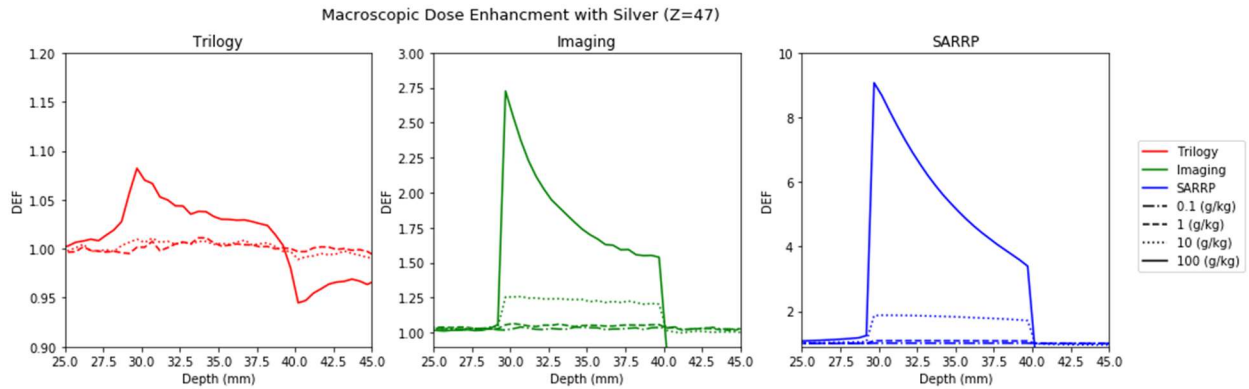


Figure A.1 - Dose enhancement evaluation of silver (Z=47) by concentration.

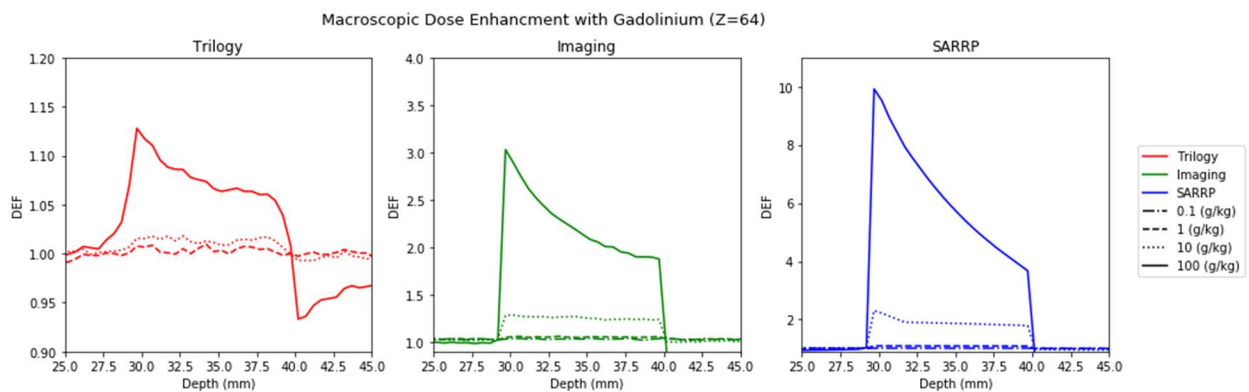


Figure A.2 - Dose enhancement evaluation of gadolinium (Z=64) by concentration.

A.8 – Maximum DEF for Non-radioactive Metals with Imaging Beam

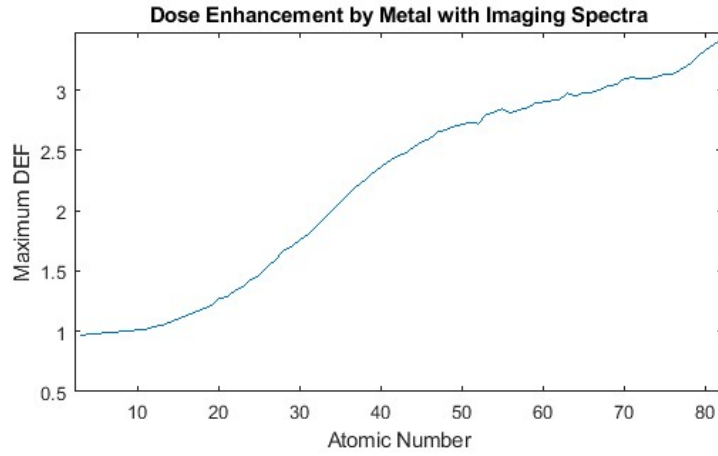


Figure A.3 – Maximum DEF versus atomic number for all non-radioactive metals with Imaging beam.

A.9 – Silver and Gadolinium DEF with Depth

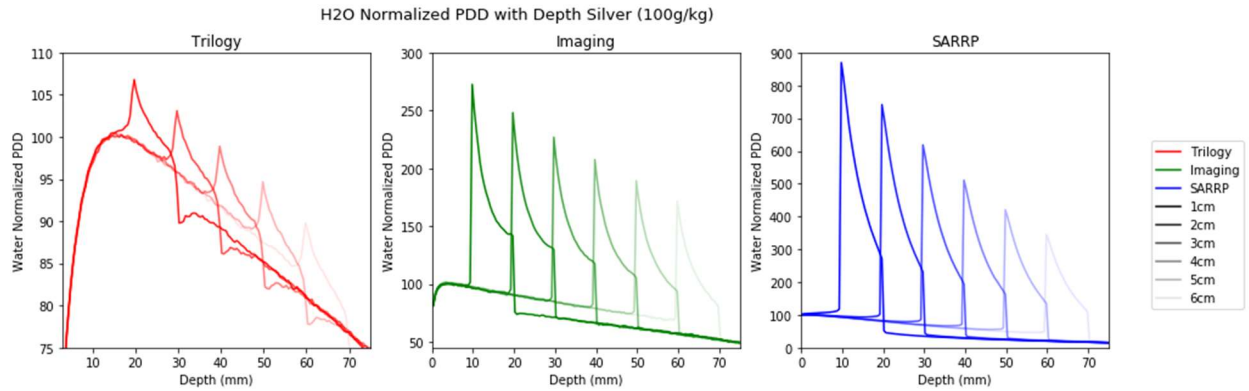


Figure A.4 - Evaluation of maximum DEF for a silver solution layer (concentration 100 g/kg) at increasing depths within a water phantom.

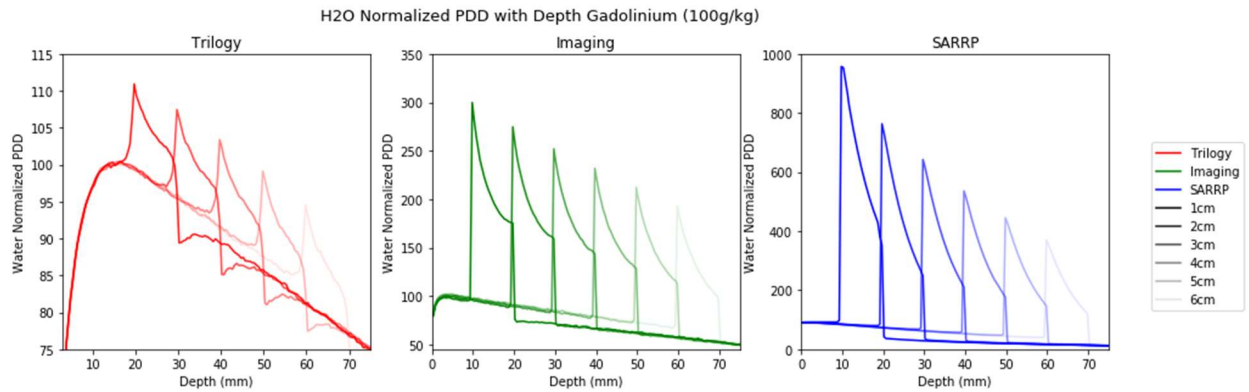


Figure A.5 - Evaluation of maximum DEF for a gadolinium solution layer (concentration 100 g/kg) at increasing depths within a water phantom.

A.10 – FLURZnrc Sample Input File

```
TITLE= Gold PLEX

#####
:start I/O control:

IWATCH= off
STORE INITIAL RANDOM NUMBERS= no
IRESTART= first
STORE DATA ARRAYS= no
PRINT FLUENCE SPECTRA= none
IPRIMARY= electron primaries
SLOTE= 0.0
TOPS OF ENERGY BINS= 0.001, 0.002, 0.003, 0.004, 0.005, 0.006, 0.007,
0.008, 0.009, 0.01, 0.011, 0.012, 0.013, 0.014, 0.015, 0.016, 0.017,
0.018, 0.019, 0.02, 0.021, 0.022, 0.023, 0.024, 0.025, 0.026, 0.027,
0.028, 0.029, 0.03, 6

:stop I/O control:
#####

#####
:start Monte Carlo inputs:

NUMBER OF HISTORIES= 1056795026
INITIAL RANDOM NO. SEEDS= 4, 33
MAX CPU HOURS ALLOWED= 24
IFULL= dose and stoppers
STATISTICAL ACCURACY SOUGHT= 0.05

:stop Monte Carlo inputs:
#####

#####
:start geometrical inputs:

METHOD OF INPUT= groups
Z OF FRONT FACE= 0
NSLAB= 40, 20, 80
SLAB THICKNESS= 0.05, 0.05, 0.05
RADII= 5, 10, 15
MEDIA= Water, Gold1;

DESCRIPTION BY= planes
MEDNUM= 1, 2, 1
START ZSLAB= 1, 40, 60
STOP ZSLAB= 40, 60, 140
START RING= 1, 1, 1
STOP RING= 3, 3, 3

:stop geometrical inputs:
```

```

#####

#####
:start source inputs:

INCIDENT PARTICLE= photon
SOURCE NUMBER= 21
SOURCE OPTIONS= 0, 1, 0, 0
FILSPC= /scratch/summit/skmartin@colostate.edu/PLEX.egspspl

:stop source inputs:
#####

#####
:start variance reduction:

BREM SPLITTING= off
NUMBER OF BREMS PER EVENT= 1
CHARGED PARTICLE RUSSIAN ROULETTE= off
ELECTRON RANGE REJECTION= off
ESAVEIN= 10000.
PHOTON FORCING= off
START FORCING= 0
STOP FORCING AFTER= 0

:stop variance reduction:
#####

#####
:start plot control:

PLOTTING= on
EXTERNAL PLOT TYPE= Point
PLOT RADIAL REGION IX= 1,2,3
PLOT PLANAR REGION IZ= 0
DRAW FLUENCE PLOTS= Primaries
PLOTS FOR ELECTRONS= on
PLOTS FOR POSITRONS= off
PLOTS FOR PHOTONS= off
PLOTS FOR E- AND E+= off
START SPECTRAL PLOT IN REGION= 41
STOP SPECTRAL PLOT IN REGION= 59

:stop plot control:
#####

```

A.11 – Electron Spectra Output for Silver and Gadolinium

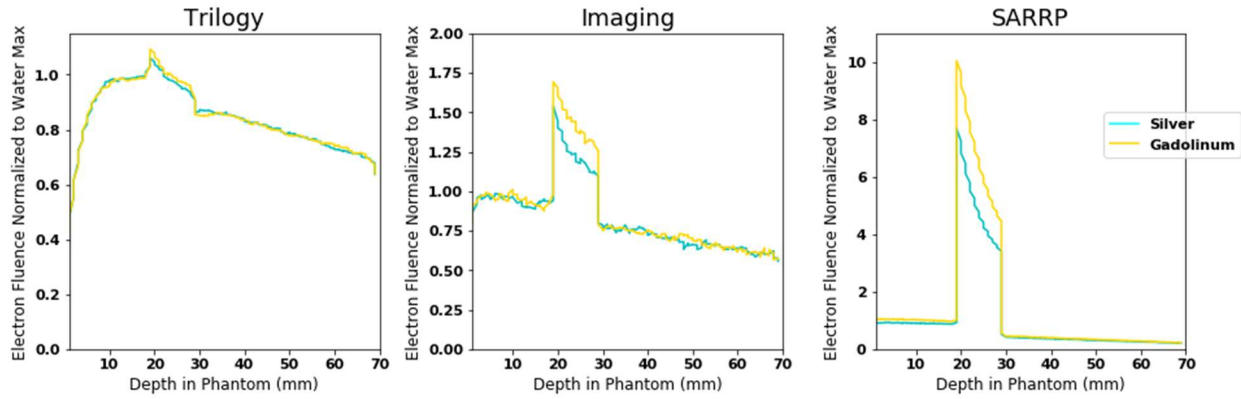


Figure A.6 – Silver and gadolinium electron fluence as a function of depth in phantom with metal solution layer at between 20mm and 30mm.

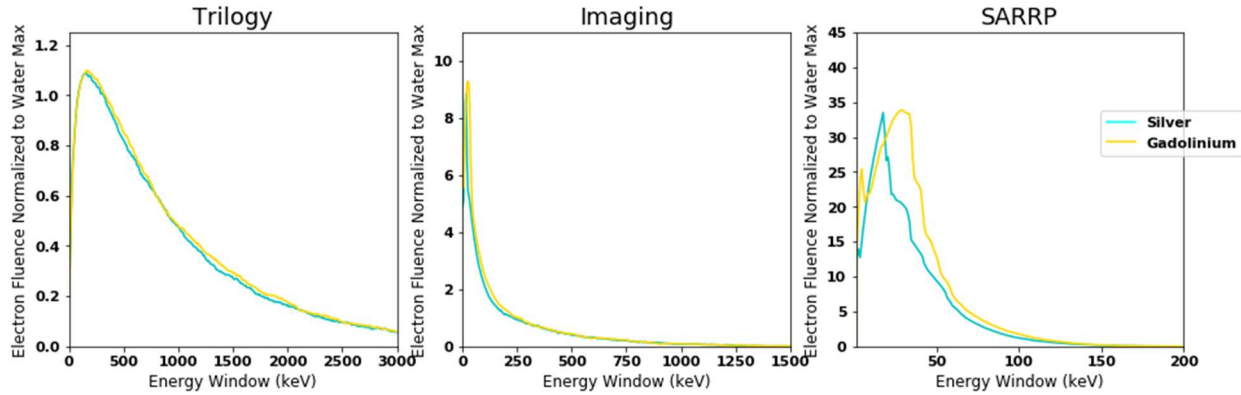


Figure A.7 - Three photon beam models are used as the input to evaluate electron yield amplification in silver and gadolinium solution layer.

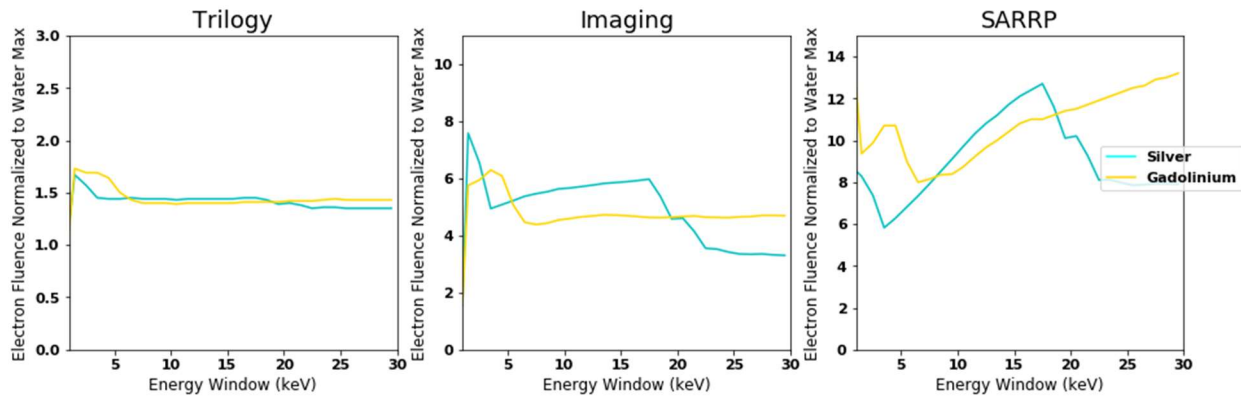


Figure A.8 – Low energy electron yield (<30 keV) amplification in silver and gadolinium solution layer.

A.12 – Electron Origin Output for Gold, Silver, Gadolinium

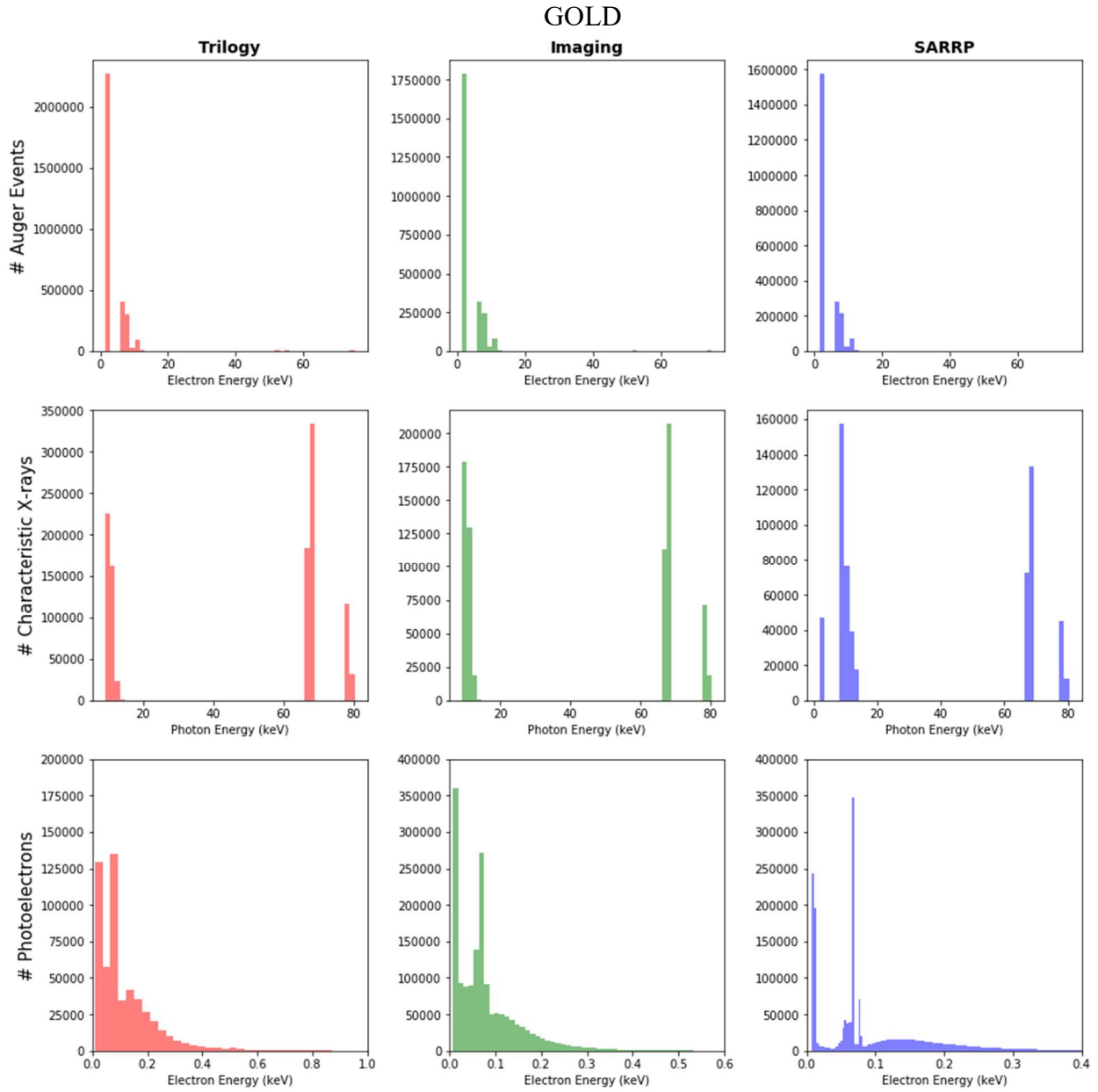


Figure A.9 – Gold electron and photon origin tracking with modified DOSXYZnrc code 10^6 histories.

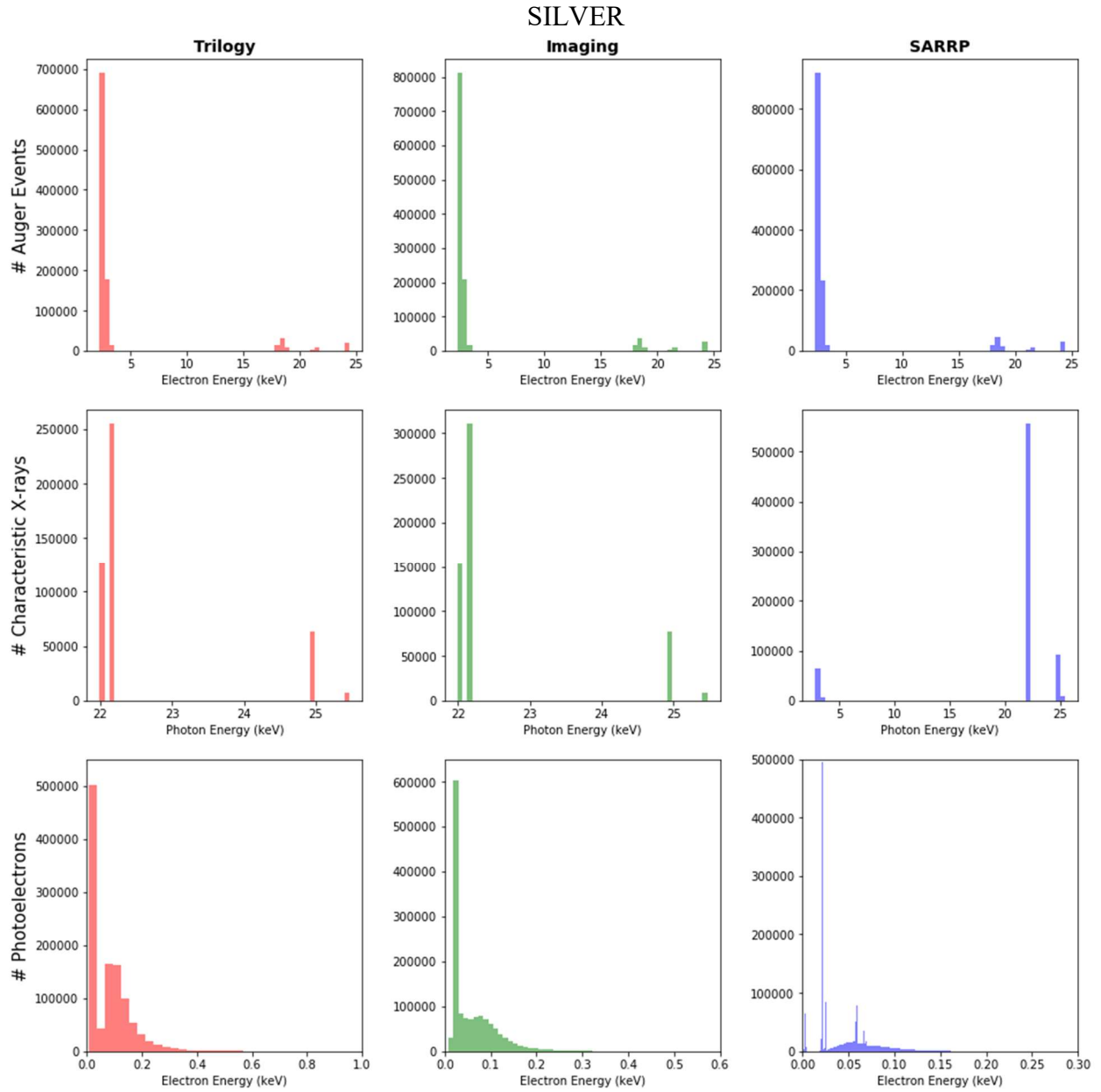


Figure A.10 – Silver electron and photon origin tracking with modified DOSXYZnrc code 10^6 histories.

GADOLINIUM

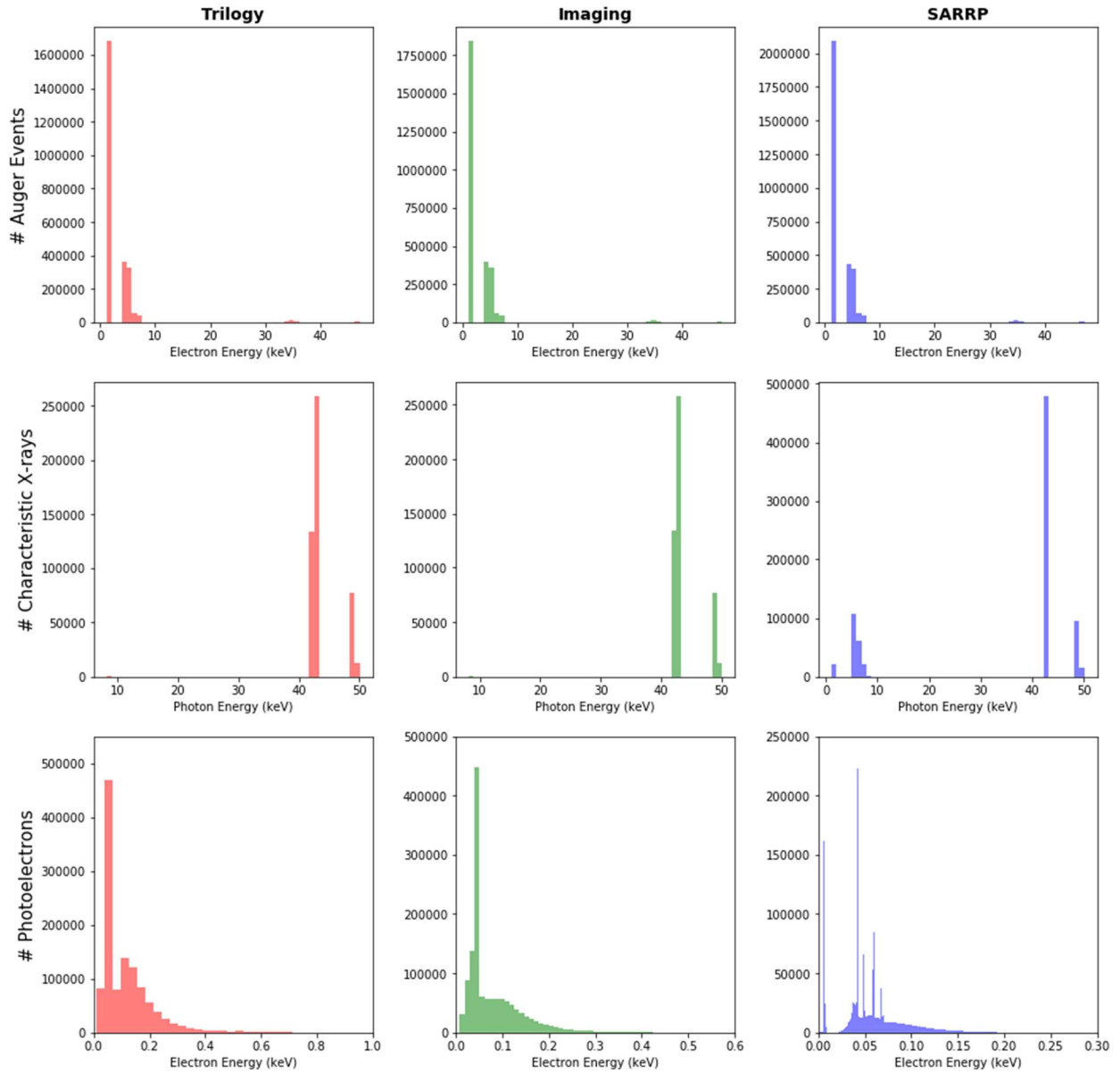


Figure A.11 – Gadolinium electron and photon origin tracking with modified DOSXYZnrc code 10^6 histories.

APPENDIX B

B.1 – Percentage Depth Dose in Tissues with differing Effective Atomic Numbers

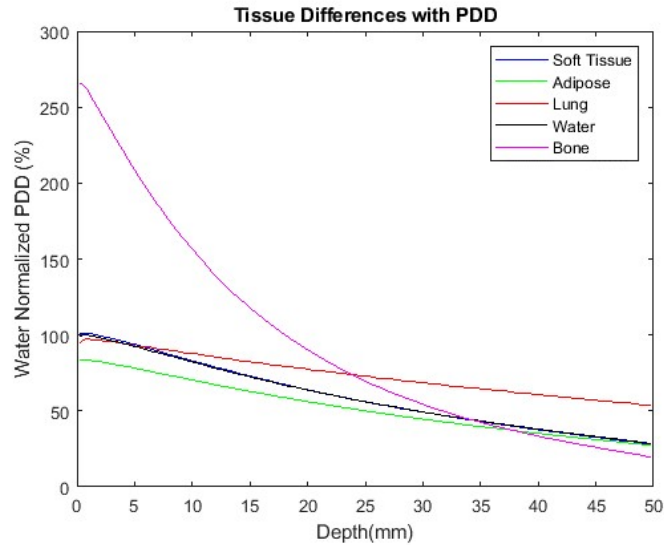


Figure B.1 – Percentage depth dose of tissues normalized to D_{max} for water.

B.2 – PEGS4 File for Hypoxic Tumor Model Simulations

```
MEDIUM=LowNormoxic , STERNCID=LowNormoxic
MIXT,RHO= 1.0002E+00,NE= 3, IUNRST=0, EPSTFL=0, IAPRIM=1
ASYM=H ,Z= 1.,A= 1.008,PZ= 1.11007E-01,RHOZ= 1.11892E-01
ASYM=O ,Z= 8.,A= 15.999,PZ= 5.55076E-02,RHOZ= 8.88089E-01
ASYM=CU,Z=29.,A= 63.540,PZ= 3.10041E-07,RHOZ= 1.97000E-05
```

```
MEDIUM=LowHypoxic , STERNCID=LowHypoxic
MIXT,RHO= 1.0014E+00,NE= 3, IUNRST=0, EPSTFL=0, IAPRIM=1
ASYM=H ,Z= 1.,A= 1.008,PZ= 1.10989E-01,RHOZ= 1.11874E-01
ASYM=O ,Z= 8.,A= 15.999,PZ= 5.54989E-02,RHOZ= 8.87949E-01
ASYM=CU,Z=29.,A= 63.540,PZ= 2.78565E-06,RHOZ= 1.77000E-04
```

```
MEDIUM=MedNormoxic , STERNCID=MedNormoxic
MIXT,RHO= 1.0005E+00,NE= 3, IUNRST=0, EPSTFL=0, IAPRIM=1
ASYM=H ,Z= 1.,A= 1.008,PZ= 1.11001E-01,RHOZ= 1.11886E-01
ASYM=O ,Z= 8.,A= 15.999,PZ= 5.55050E-02,RHOZ= 8.88046E-01
ASYM=CU,Z=29.,A= 63.540,PZ= 1.05760E-06,RHOZ= 6.72000E-05
```

```
MEDIUM=MedHypoxic , STERNCID=MedHypoxic
MIXT,RHO= 1.0048E+00,NE= 3, IUNRST=0, EPSTFL=0, IAPRIM=1
ASYM=H ,Z= 1.,A= 1.008,PZ= 1.10942E-01,RHOZ= 1.11826E-01
ASYM=O ,Z= 8.,A= 15.999,PZ= 5.54751E-02,RHOZ= 8.87569E-01
ASYM=CU,Z=29.,A= 63.540,PZ= 9.52156E-06,RHOZ= 6.05000E-04
```

MEDIUM=HighNormoxic , STERNCID=HighNormoxic
MIXT,RHO= 1.0022E+00,NE= 3, IUNRST=0, EPSTFL=0, IAPRIM=1
ASYM=H ,Z= 1.,A= 1.008,PZ= 1.10979E-01,RHOZ= 1.11864E-01
ASYM=O ,Z= 8.,A= 15.999,PZ= 5.54937E-02,RHOZ= 8.87866E-01
ASYM=CU,Z=29.,A= 63.540,PZ= 4.24929E-06,RHOZ= 2.70000E-04

MEDIUM=HighHypoxic , STERNCID=HighHypoxic
MIXT,RHO= 1.0193E+00,NE= 3, IUNRST=0, EPSTFL=0, IAPRIM=1
ASYM=H ,Z= 1.,A= 1.008,PZ= 1.10739E-01,RHOZ= 1.11622E-01
ASYM=O ,Z= 8.,A= 15.999,PZ= 5.53738E-02,RHOZ= 8.85948E-01
ASYM=CU,Z=29.,A= 63.540,PZ= 3.82436E-05,RHOZ= 2.43000E-03

MEDIUM=VeryNormoxic , STERNCID=VeryNormoxic
MIXT,RHO= 1.0108E+00,NE= 3, IUNRST=0, EPSTFL=0, IAPRIM=1
ASYM=H ,Z= 1.,A= 1.008,PZ= 1.10859E-01,RHOZ= 1.11743E-01
ASYM=O ,Z= 8.,A= 15.999,PZ= 5.54338E-02,RHOZ= 8.86907E-01
ASYM=CU,Z=29.,A= 63.540,PZ= 2.12465E-05,RHOZ= 1.35000E-03

MEDIUM=VeryHypoxic , STERNCID=VeryHypoxic
MIXT,RHO= 1.0967E+00,NE= 3, IUNRST=0, EPSTFL=0, IAPRIM=1
ASYM=H ,Z= 1.,A= 1.008,PZ= 1.09660E-01,RHOZ= 1.10534E-01
ASYM=O ,Z= 8.,A= 15.999,PZ= 5.48343E-02,RHOZ= 8.77316E-01
ASYM=CU,Z=29.,A= 63.540,PZ= 1.91218E-04,RHOZ= 1.21500E-02

MEDIUM=GNPNormoxic , STERNCID=GNPNormoxic
MIXT,RHO= 1.0247E+00,NE= 3, IUNRST=0, EPSTFL=0, IAPRIM=1
ASYM=H ,Z= 1.,A= 1.008,PZ= 1.10859E-01,RHOZ= 1.11743E-01
ASYM=O ,Z= 8.,A= 15.999,PZ= 5.54338E-02,RHOZ= 8.86907E-01
ASYM=AU,Z=79.,A= 196.987,PZ= 6.85324E-06,RHOZ= 1.35000E-03

MEDIUM=GNPReduced , STERNCID=GNPReduced
MIXT,RHO= 1.0073E+00,NE= 3, IUNRST=0, EPSTFL=0, IAPRIM=1
ASYM=H ,Z= 1.,A= 1.008,PZ= 1.10966E-01,RHOZ= 1.11850E-01
ASYM=O ,Z= 8.,A= 15.999,PZ= 5.54866E-02,RHOZ= 8.87753E-01
ASYM=AU,Z=79.,A= 196.987,PZ= 2.01566E-06,RHOZ= 3.97059E-04

MEDIUM=CopperMix , STERNCID=CopperMix
MIXT,RHO= 1.0373E+00,NE= 3, IUNRST=0, EPSTFL=0, IAPRIM=1
ASYM=H ,Z= 1.,A= 1.008,PZ= 1.10489E-01,RHOZ= 1.11370E-01
ASYM=O ,Z= 8.,A= 15.999,PZ= 5.52489E-02,RHOZ= 8.83950E-01
ASYM=CU,Z=29.,A= 63.540,PZ= 7.36544E-05,RHOZ= 4.68000E-03

B.3 – Hypoxic Tumor Model DOSXYZnrc Sample File

SARRP Tumor High Copper RN1#!GUI1.0
4
Water
Air
HighNormoxic
HighHypoxic

```

0.001, 0.001, 0, 0, 0, 0
-1, -1, -1, 0
-2.5
0.05, 100
-2.5
0.05, 100
0
0.05, 100
45, 55, 45, 55, 45, 55, 3,
48, 52, 48, 52, 48, 52, 4,
0, 0, 0, 0, 0, 0, 0, 0
0, 0, 0, 0, 0, 0, 0, 0
0, 0, 0, 0, 0, 0, 0, 0
0, 2, 0, 0, 0, 180, 0, 4, 0, 0, 10, 100, 57, 0
2, 2, 2, 0, 0, 0, 0, 0
/scratch/summit/skmartin@colostate.edu/SARX.egsphsp1
2000000000, 0, 24, 86, 28, 20, 0, 0, 0, 0, , 1, 0, 0, 1, 0, 0

```

B.4 – Dose Enhancement in Hypoxic Tumor Model with Imaging Beam Spectra

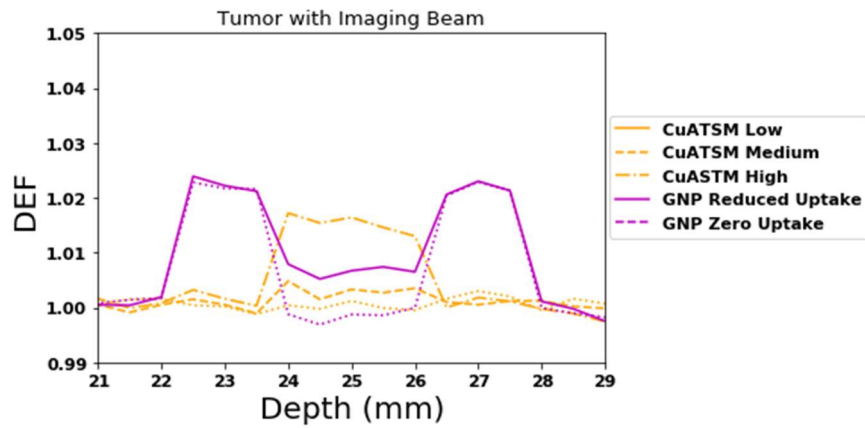


Figure B.2 – Tumor DEF with modified Imaging beam spectra.

B.5 – Dose Enhancement of Various Tissues with CuATSM High and SARRP

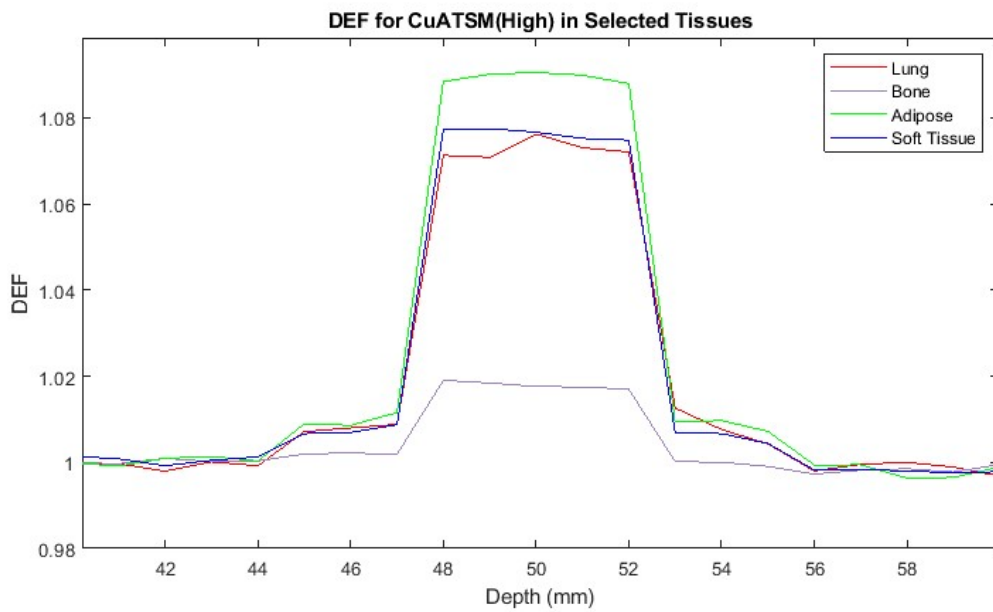


Figure B.3 – DEF with various tissue; CuATSM High with SARRP.

B.6 – Isodose Comparison of Boost Treatments

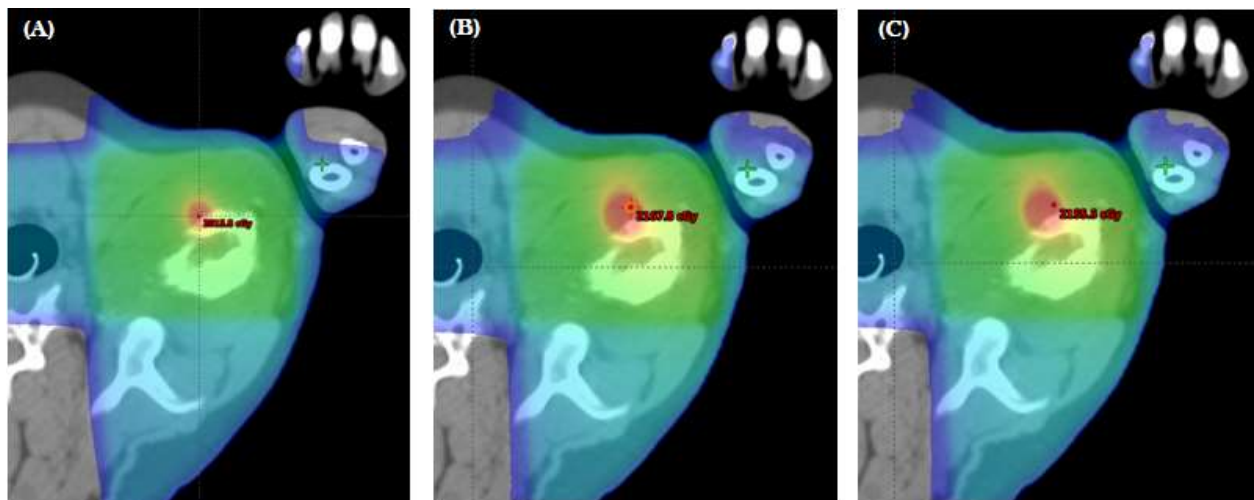


Figure B.4 – Dose wash comparison at an axial plane for boosted treatments. (A) MV boost. (B) Copper boost. (C) Ortho boost.

APPENDIX C

C.1 – Benchmarking Data for Examples

PDB4DNA

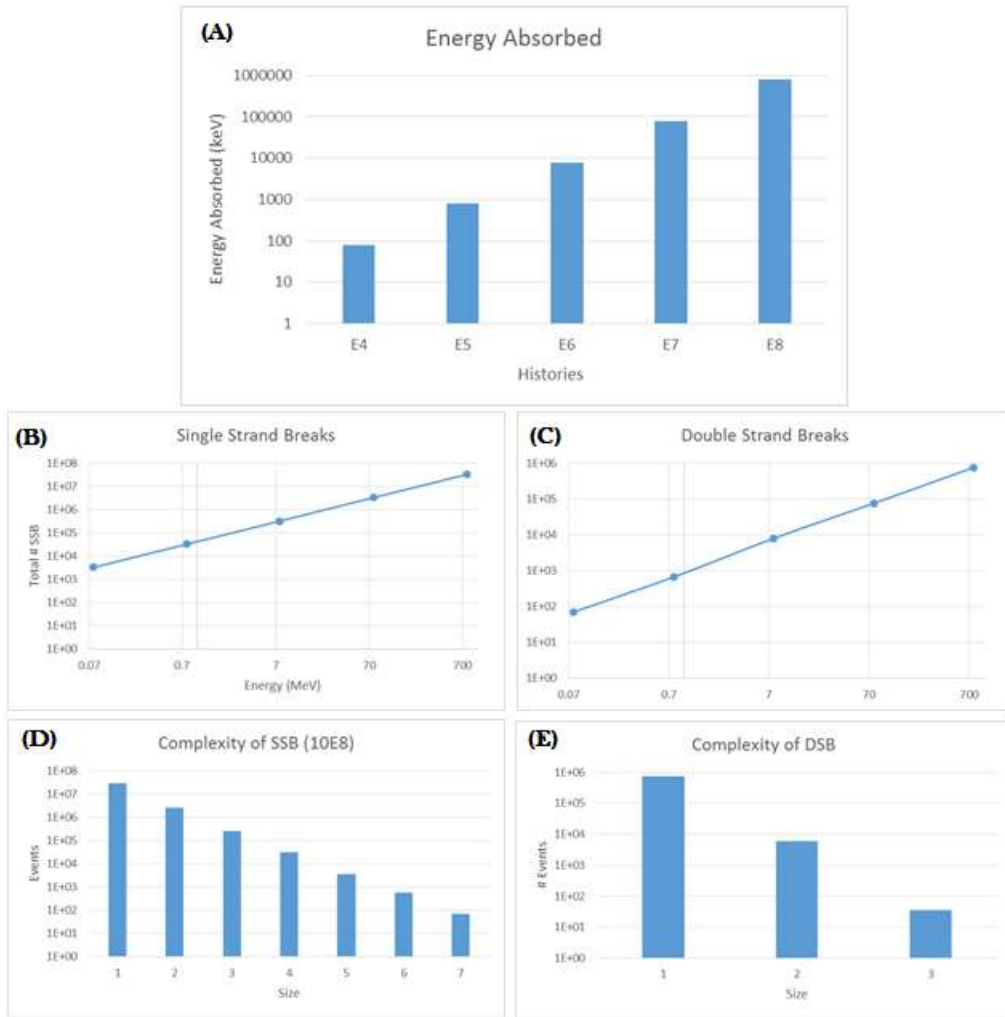


Figure C.1 – Total energy deposited from CuATSM High spectra (50/50) 10^8 total histories, forced interaction with DNA volume. (A) Energy deposited. (B) SSB vs. energy. (C) DSB vs. energy. (D) Complexity of SSB. (E) Complexity of DSB.

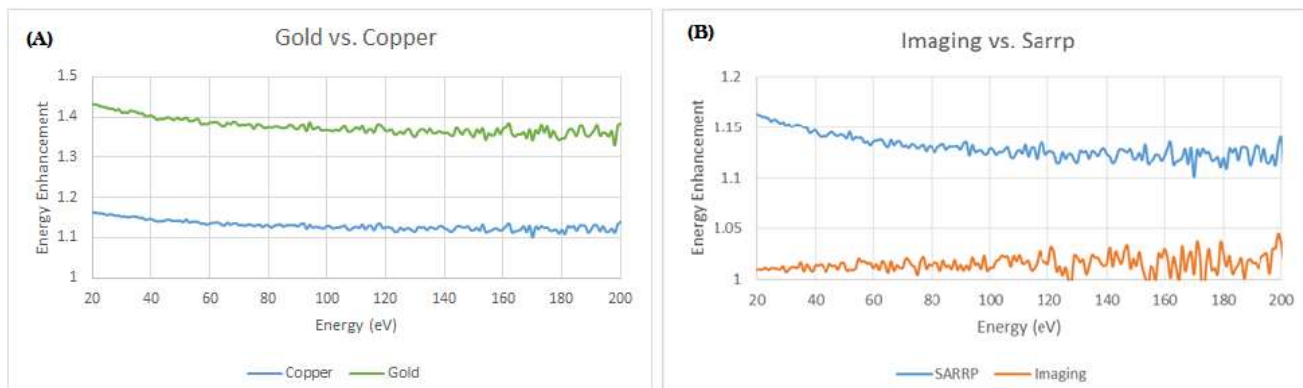


Figure C.2 – Metal and spectra energy enhancement from CuATSM High spectra (50/50) 10^8 total histories, forced interaction with DNA volume. (A) Gold vs. copper energy enhancement. (B) Imaging spectra vs. SARRP spectra energy enhancement.

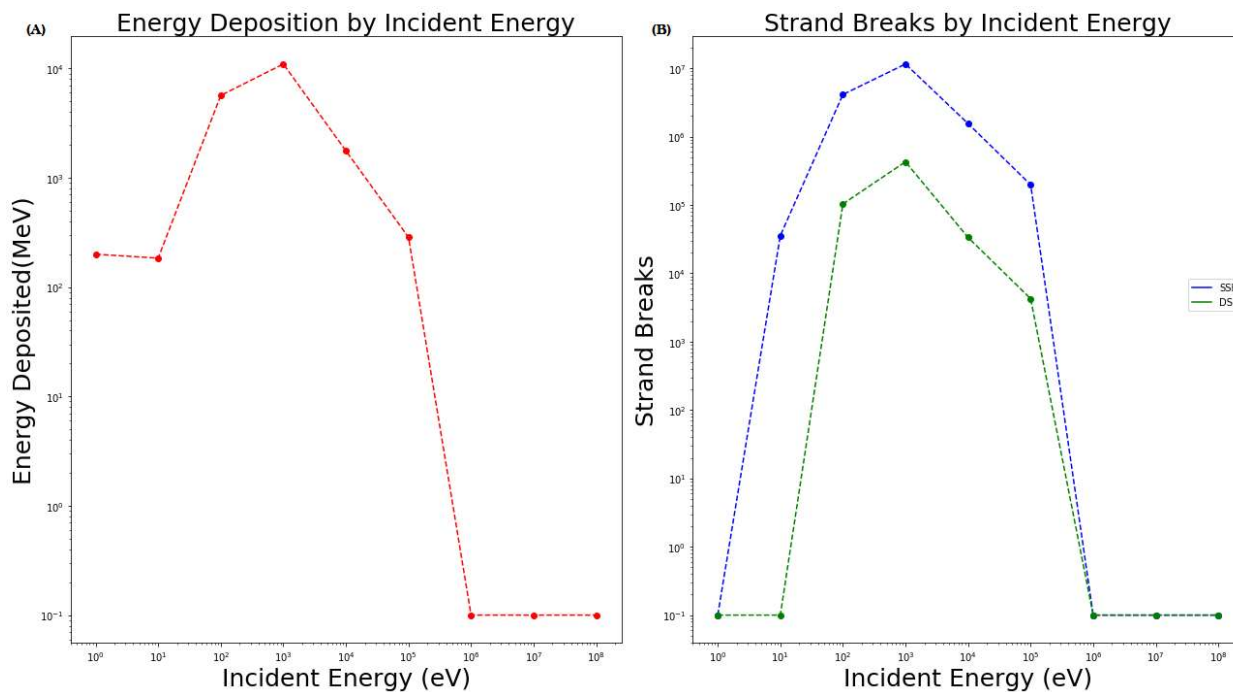


Figure C.3 – Incident energy effect on energy deposited and strand breaks. (A) Energy deposited. (B) Strand breaks.

CHEM4

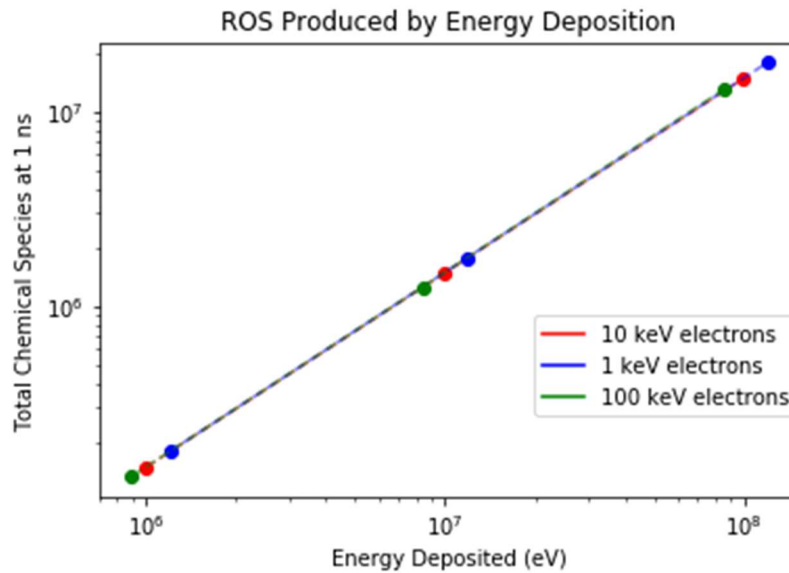


Figure C.4 – Linearity of chemical species yield with energy incident and history number.

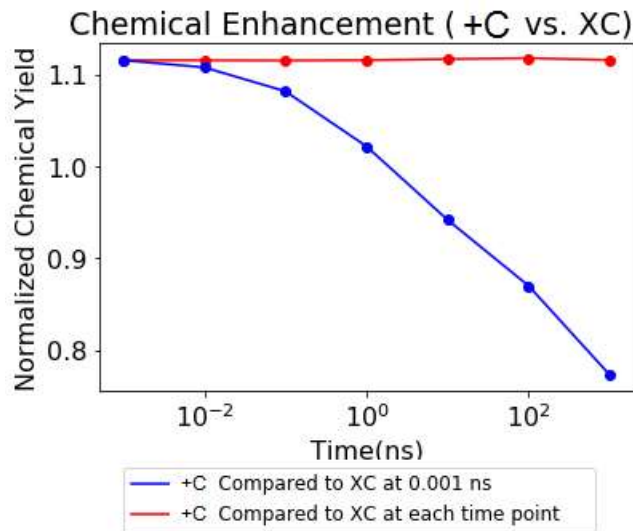


Figure C.5 – Time tabulated chemical yield comparison between copper containing cell with equal distribution of copper in nucleus and cytoplasm (+C) and the no copper case (XC). Copper results in chemical enhancement; the relative enhancement is consistent across time (red). The maximum chemical yield occurs at 1 ps, therefore, chemical yields at subsequent time points are reduced compared to the maximum (blue).

C.2 – PEGS4 Data for Electron Spectra

```

MEDIUM=Nucleus , STERNCID=Nucleus
MIXT,RHO= 1.0300E+00,NE= 6, IUNRST=0, EPSTFL=1, IAPRIM=1
ASYM=H , Z= 1.,A= 1.008,PZ= 1.05575E-01,RHOZ= 1.06416E-01
ASYM=C , Z= 6.,A= 12.011,PZ= 7.50969E-03,RHOZ= 9.02000E-02
    
```

ASYM=N ,Z= 7.,A= 14.007,PZ= 2.29890E-03,RHOZ= 3.22000E-02
ASYM=O ,Z= 8.,A= 15.999,PZ= 4.63195E-02,RHOZ= 7.41084E-01
ASYM=P ,Z=15.,A= 30.974,PZ= 8.52333E-04,RHOZ= 2.64000E-02
ASYM=S ,Z=16.,A= 32.064,PZ= 1.15394E-04,RHOZ= 3.70000E-03

MEDIUM=CuNu15 ,STERNCID=CuNu15
MIXT,RHO= 1.0329E+00,NE= 7, IUNRST=0, EPSTFL=0, IAPRIM=1
ASYM=H ,Z= 1.,A= 1.008,PZ= 1.05537E-01,RHOZ= 1.06378E-01
ASYM=C ,Z= 6.,A= 12.011,PZ= 7.50698E-03,RHOZ= 9.01675E-02
ASYM=N ,Z= 7.,A= 14.007,PZ= 2.29807E-03,RHOZ= 3.21884E-02
ASYM=O ,Z= 8.,A= 15.999,PZ= 4.63028E-02,RHOZ= 7.40817E-01
ASYM=P ,Z=15.,A= 30.974,PZ= 8.52027E-04,RHOZ= 2.63905E-02
ASYM=S ,Z=16.,A= 32.064,PZ= 1.15353E-04,RHOZ= 3.69867E-03
ASYM=CU,Z=29.,A= 63.540,PZ= 5.66572E-06,RHOZ= 3.60000E-04

MEDIUM=CuNu30 ,STERNCID=CuNu30
MIXT,RHO= 1.0357E+00,NE= 7, IUNRST=0, EPSTFL=0, IAPRIM=1
ASYM=H ,Z= 1.,A= 1.008,PZ= 1.05498E-01,RHOZ= 1.06339E-01
ASYM=C ,Z= 6.,A= 12.011,PZ= 7.50429E-03,RHOZ= 9.01351E-02
ASYM=N ,Z= 7.,A= 14.007,PZ= 2.29724E-03,RHOZ= 3.21768E-02
ASYM=O ,Z= 8.,A= 15.999,PZ= 4.62861E-02,RHOZ= 7.40550E-01
ASYM=P ,Z=15.,A= 30.974,PZ= 8.51720E-04,RHOZ= 2.63810E-02
ASYM=S ,Z=16.,A= 32.064,PZ= 1.15311E-04,RHOZ= 3.69734E-03
ASYM=CU,Z=29.,A= 63.540,PZ= 1.13314E-05,RHOZ= 7.20000E-04

MEDIUM=CuNu50 ,STERNCID=CuNu50
MIXT,RHO= 1.0395E+00,NE= 7, IUNRST=0, EPSTFL=0, IAPRIM=1
ASYM=H ,Z= 1.,A= 1.008,PZ= 1.05448E-01,RHOZ= 1.06288E-01
ASYM=C ,Z= 6.,A= 12.011,PZ= 7.50068E-03,RHOZ= 9.00918E-02
ASYM=N ,Z= 7.,A= 14.007,PZ= 2.29614E-03,RHOZ= 3.21614E-02
ASYM=O ,Z= 8.,A= 15.999,PZ= 4.62639E-02,RHOZ= 7.40195E-01
ASYM=P ,Z=15.,A= 30.974,PZ= 8.51310E-04,RHOZ= 2.63683E-02
ASYM=S ,Z=16.,A= 32.064,PZ= 1.15256E-04,RHOZ= 3.69556E-03
ASYM=CU,Z=29.,A= 63.540,PZ= 1.88857E-05,RHOZ= 1.20000E-03

MEDIUM=CuNu75 ,STERNCID=CuNu75
MIXT,RHO= 1.0443E+00,NE= 7, IUNRST=0, EPSTFL=0, IAPRIM=1
ASYM=H ,Z= 1.,A= 1.008,PZ= 1.05384E-01,RHOZ= 1.06224E-01
ASYM=C ,Z= 6.,A= 12.011,PZ= 7.49617E-03,RHOZ= 9.00376E-02
ASYM=N ,Z= 7.,A= 14.007,PZ= 2.29476E-03,RHOZ= 3.21420E-02
ASYM=O ,Z= 8.,A= 15.999,PZ= 4.62361E-02,RHOZ= 7.39750E-01
ASYM=P ,Z=15.,A= 30.974,PZ= 8.50800E-04,RHOZ= 2.63525E-02
ASYM=S ,Z=16.,A= 32.064,PZ= 1.15187E-04,RHOZ= 3.69334E-03
ASYM=CU,Z=29.,A= 63.540,PZ= 2.83286E-05,RHOZ= 1.80000E-03

MEDIUM=CuNu85 ,STERNCID=CuNu85
MIXT,RHO= 1.0462E+00,NE= 7, IUNRST=0, EPSTFL=0, IAPRIM=1
ASYM=H ,Z= 1.,A= 1.008,PZ= 1.05359E-01,RHOZ= 1.06199E-01
ASYM=C ,Z= 6.,A= 12.011,PZ= 7.49437E-03,RHOZ= 9.00160E-02
ASYM=N ,Z= 7.,A= 14.007,PZ= 2.29421E-03,RHOZ= 3.21343E-02
ASYM=O ,Z= 8.,A= 15.999,PZ= 4.62250E-02,RHOZ= 7.39572E-01
ASYM=P ,Z=15.,A= 30.974,PZ= 8.50593E-04,RHOZ= 2.63461E-02

ASYM=S ,Z=16.,A= 32.064,PZ= 1.15159E-04,RHOZ= 3.69245E-03
ASYM=CU,Z=29.,A= 63.540,PZ= 3.21058E-05,RHOZ= 2.04000E-03

MEDIUM=Cytoplasm ,STERNCID=Cytoplasm

MIXT,RHO= 1.0000E+00,NE=13, IUNRST=0, EPSTFL=0, IAPRIM=1
ASYM=H ,Z= 1.,A= 1.008,PZ= 1.03646E-01,RHOZ= 1.04472E-01
ASYM=C ,Z= 6.,A= 12.011,PZ= 1.93312E-02,RHOZ= 2.32190E-01
ASYM=N ,Z= 7.,A= 14.007,PZ= 1.77629E-03,RHOZ= 2.48800E-02
ASYM=O ,Z= 8.,A= 15.999,PZ= 3.93914E-02,RHOZ= 6.30238E-01
ASYM=NA,Z=11.,A= 22.990,PZ= 4.91522E-05,RHOZ= 1.13000E-03
ASYM=MG,Z=12.,A= 24.312,PZ= 5.34715E-06,RHOZ= 1.30000E-04
ASYM=P ,Z=15.,A= 30.974,PZ= 4.29395E-05,RHOZ= 1.33000E-03
ASYM=S ,Z=16.,A= 32.064,PZ= 6.20634E-05,RHOZ= 1.99000E-03
ASYM=CL,Z=17.,A= 35.453,PZ= 3.77965E-05,RHOZ= 1.34000E-03
ASYM=K ,Z=19.,A= 39.102,PZ= 5.08925E-05,RHOZ= 1.99000E-03
ASYM=CA,Z=20.,A= 40.080,PZ= 5.73852E-06,RHOZ= 2.30000E-04
ASYM=FE,Z=26.,A= 55.847,PZ= 8.95303E-07,RHOZ= 5.00000E-05
ASYM=ZN,Z=30.,A= 65.370,PZ= 4.58926E-07,RHOZ= 3.00000E-05

MEDIUM=CuCy15 ,STERNCID=CuCy15

MIXT,RHO= 1.0029E+00,NE=14, IUNRST=0, EPSTFL=0, IAPRIM=1
ASYM=H ,Z= 1.,A= 1.008,PZ= 1.03608E-01,RHOZ= 1.04434E-01
ASYM=C ,Z= 6.,A= 12.011,PZ= 1.93242E-02,RHOZ= 2.32106E-01
ASYM=N ,Z= 7.,A= 14.007,PZ= 1.77565E-03,RHOZ= 2.48710E-02
ASYM=O ,Z= 8.,A= 15.999,PZ= 3.93772E-02,RHOZ= 6.30011E-01
ASYM=NA,Z=11.,A= 22.990,PZ= 4.91344E-05,RHOZ= 1.12959E-03
ASYM=MG,Z=12.,A= 24.312,PZ= 5.34510E-06,RHOZ= 1.29950E-04
ASYM=P ,Z=15.,A= 30.974,PZ= 4.29240E-05,RHOZ= 1.32952E-03
ASYM=S ,Z=16.,A= 32.064,PZ= 6.20409E-05,RHOZ= 1.98928E-03
ASYM=CL,Z=17.,A= 35.453,PZ= 3.77830E-05,RHOZ= 1.33952E-03
ASYM=K ,Z=19.,A= 39.102,PZ= 5.08741E-05,RHOZ= 1.98928E-03
ASYM=CA,Z=20.,A= 40.080,PZ= 5.73653E-06,RHOZ= 2.29920E-04
ASYM=FE,Z=26.,A= 55.847,PZ= 8.94945E-07,RHOZ= 4.99800E-05
ASYM=ZN,Z=30.,A= 65.370,PZ= 4.58773E-07,RHOZ= 2.99900E-05
ASYM=CU,Z=29.,A= 63.540,PZ= 5.66572E-06,RHOZ= 3.60000E-04

MEDIUM=CuCy25 ,STERNCID=CuCy25

MIXT,RHO= 1.0050E+00,NE=14, IUNRST=0, EPSTFL=0, IAPRIM=1
ASYM=H ,Z= 1.,A= 1.008,PZ= 1.03581E-01,RHOZ= 1.04407E-01
ASYM=C ,Z= 6.,A= 12.011,PZ= 1.93192E-02,RHOZ= 2.32046E-01
ASYM=N ,Z= 7.,A= 14.007,PZ= 1.77519E-03,RHOZ= 2.48645E-02
ASYM=O ,Z= 8.,A= 15.999,PZ= 3.93668E-02,RHOZ= 6.29846E-01
ASYM=NA,Z=11.,A= 22.990,PZ= 4.91218E-05,RHOZ= 1.12930E-03
ASYM=MG,Z=12.,A= 24.312,PZ= 5.34382E-06,RHOZ= 1.29919E-04
ASYM=P ,Z=15.,A= 30.974,PZ= 4.29127E-05,RHOZ= 1.32917E-03
ASYM=S ,Z=16.,A= 32.064,PZ= 6.20247E-05,RHOZ= 1.98876E-03
ASYM=CL,Z=17.,A= 35.453,PZ= 3.77731E-05,RHOZ= 1.33917E-03
ASYM=K ,Z=19.,A= 39.102,PZ= 5.08608E-05,RHOZ= 1.98876E-03
ASYM=CA,Z=20.,A= 40.080,PZ= 5.73495E-06,RHOZ= 2.29857E-04
ASYM=FE,Z=26.,A= 55.847,PZ= 8.94746E-07,RHOZ= 4.99689E-05
ASYM=ZN,Z=30.,A= 65.370,PZ= 4.58642E-07,RHOZ= 2.99814E-05
ASYM=CU,Z=29.,A= 63.540,PZ= 9.77967E-06,RHOZ= 6.21400E-04

MEDIUM=CuCy50 , STERNCID=CuCy50
 MIXT,RHO= 1.0095E+00,NE=14, IUNRST=0, EPSTFL=0, IAPRIM=1
 ASYM=H ,Z= 1.,A= 1.008,PZ= 1.03522E-01,RHOZ= 1.04347E-01
 ASYM=C ,Z= 6.,A= 12.011,PZ= 1.93080E-02,RHOZ= 2.31911E-01
 ASYM=N ,Z= 7.,A= 14.007,PZ= 1.77416E-03,RHOZ= 2.48501E-02
 ASYM=O ,Z= 8.,A= 15.999,PZ= 3.93441E-02,RHOZ= 6.29482E-01
 ASYM=NA,Z=11.,A= 22.990,PZ= 4.90931E-05,RHOZ= 1.12864E-03
 ASYM=MG,Z=12.,A= 24.312,PZ= 5.34057E-06,RHOZ= 1.29840E-04
 ASYM=P ,Z=15.,A= 30.974,PZ= 4.28879E-05,RHOZ= 1.32840E-03
 ASYM=S ,Z=16.,A= 32.064,PZ= 6.19888E-05,RHOZ= 1.98761E-03
 ASYM=CL,Z=17.,A= 35.453,PZ= 3.77511E-05,RHOZ= 1.33839E-03
 ASYM=K ,Z=19.,A= 39.102,PZ= 5.08314E-05,RHOZ= 1.98761E-03
 ASYM=CA,Z=20.,A= 40.080,PZ= 5.73154E-06,RHOZ= 2.29720E-04
 ASYM=FE,Z=26.,A= 55.847,PZ= 8.94229E-07,RHOZ= 4.99400E-05
 ASYM=ZN,Z=30.,A= 65.370,PZ= 4.58314E-07,RHOZ= 2.99600E-05
 ASYM=CU,Z=29.,A= 63.540,PZ= 1.88857E-05,RHOZ= 1.20000E-03

MEDIUM=CuCy75 , STERNCID=CuCy75
 MIXT,RHO= 1.0133E+00,NE=14, IUNRST=0, EPSTFL=0, IAPRIM=1
 ASYM=H ,Z= 1.,A= 1.008,PZ= 1.03472E-01,RHOZ= 1.04297E-01
 ASYM=C ,Z= 6.,A= 12.011,PZ= 1.92988E-02,RHOZ= 2.31801E-01
 ASYM=N ,Z= 7.,A= 14.007,PZ= 1.77329E-03,RHOZ= 2.48380E-02
 ASYM=O ,Z= 8.,A= 15.999,PZ= 3.93253E-02,RHOZ= 6.29182E-01
 ASYM=NA,Z=11.,A= 22.990,PZ= 4.90652E-05,RHOZ= 1.12800E-03
 ASYM=MG,Z=12.,A= 24.312,PZ= 5.34715E-06,RHOZ= 1.30000E-04
 ASYM=P ,Z=15.,A= 30.974,PZ= 4.28749E-05,RHOZ= 1.32800E-03
 ASYM=S ,Z=16.,A= 32.064,PZ= 6.19698E-05,RHOZ= 1.98700E-03
 ASYM=CL,Z=17.,A= 35.453,PZ= 3.77401E-05,RHOZ= 1.33800E-03
 ASYM=K ,Z=19.,A= 39.102,PZ= 5.08158E-05,RHOZ= 1.98700E-03
 ASYM=CA,Z=20.,A= 40.080,PZ= 5.73852E-06,RHOZ= 2.30000E-04
 ASYM=FE,Z=26.,A= 55.847,PZ= 8.93513E-07,RHOZ= 4.99000E-05
 ASYM=ZN,Z=30.,A= 65.370,PZ= 4.57396E-07,RHOZ= 2.99000E-05
 ASYM=CU,Z=29.,A= 63.540,PZ= 2.63613E-05,RHOZ= 1.67500E-03

MEDIUM=CuCy85 , STERNCID=CuCy85
 MIXT,RHO= 1.0162E+00,NE=14, IUNRST=0, EPSTFL=0, IAPRIM=1
 ASYM=H ,Z= 1.,A= 1.008,PZ= 1.03435E-01,RHOZ= 1.04259E-01
 ASYM=C ,Z= 6.,A= 12.011,PZ= 1.92917E-02,RHOZ= 2.31716E-01
 ASYM=N ,Z= 7.,A= 14.007,PZ= 1.77267E-03,RHOZ= 2.48292E-02
 ASYM=O ,Z= 8.,A= 15.999,PZ= 3.93110E-02,RHOZ= 6.28952E-01
 ASYM=NA,Z=11.,A= 22.990,PZ= 4.90518E-05,RHOZ= 1.12769E-03
 ASYM=MG,Z=12.,A= 24.312,PZ= 5.33605E-06,RHOZ= 1.29730E-04
 ASYM=P ,Z=15.,A= 30.974,PZ= 4.28520E-05,RHOZ= 1.32729E-03
 ASYM=S ,Z=16.,A= 32.064,PZ= 6.19367E-05,RHOZ= 1.98594E-03
 ASYM=CL,Z=17.,A= 35.453,PZ= 3.77195E-05,RHOZ= 1.33727E-03
 ASYM=K ,Z=19.,A= 39.102,PZ= 5.07887E-05,RHOZ= 1.98594E-03
 ASYM=CA,Z=20.,A= 40.080,PZ= 5.72680E-06,RHOZ= 2.29530E-04
 ASYM=FE,Z=26.,A= 55.847,PZ= 8.93513E-07,RHOZ= 4.99000E-05
 ASYM=ZN,Z=30.,A= 65.370,PZ= 4.58008E-07,RHOZ= 2.99400E-05
 ASYM=CU,Z=29.,A= 63.540,PZ= 3.21058E-05,RHOZ= 2.04000E-03

C.3 – Plot of Copper Compartment Concentration with CuATSM

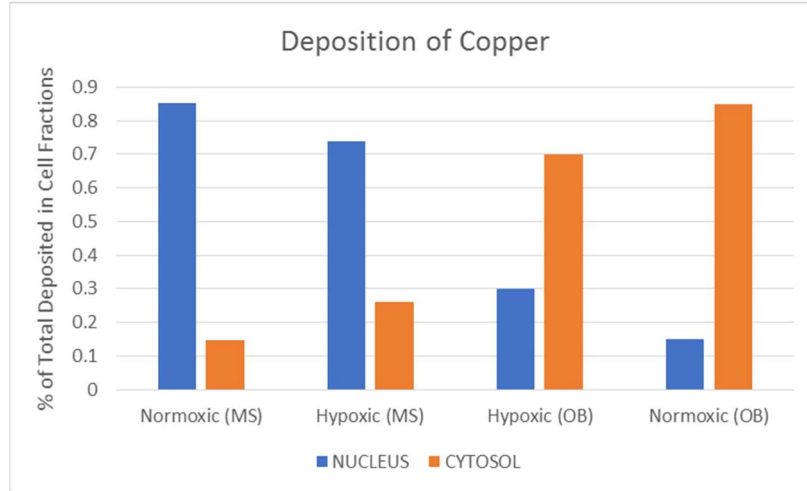


Figure C.6 – Rationale for CuATSM compartment uptake and electron spectra.

C.4 – Example Run File for Microdosimetry

```
/run/initialize

/tracking/verbose 0

/PDB4DNA/det/loadPDB 1ZBB.pdb
/PDB4DNA/det/buildBoundingV

/PDB4DNA/event/setEnergyThres 8.22 eV #default value: 8.22 eV
/PDB4DNA/event/setDistanceThres 10 #default value: 10

/gun/particle e-

/run/initialize

/gun/energy 3.5 keV
/run/beamOn 4355531
/run/printProgress 1000
/gun/energy 7.5 keV
/run/beamOn 4530573
/run/printProgress 1000
/gun/energy 12.5 keV
/run/beamOn 4612951
/run/printProgress 1000
...
/gun/energy 212.5 keV
/run/beamOn 27
/run/printProgress 1000
/gun/energy 217.5 keV
/run/beamOn 0
```

```
/run/printProgress 1000
/gun/energy 222.5 keV
/run/beamOn 0
/run/printProgress 1000
```

C.5 – Example Run File for Chemical Species

```
/primaryKiller/eLossMax 1 keV
/primaryKiller/eLossMin 20 keV # primary is killed if deposited E is
greater than this value
/gun/particle e-

/gun/energy 3.5 keV
/run/beamOn 871
/gun/energy 7.5 keV
/run/beamOn 906
/gun/energy 12.5 keV
/run/beamOn 923
...
/gun/energy 212.5 keV
/run/beamOn 0
/gun/energy 217.5 keV
/run/beamOn 0
/gun/energy 222.5 keV
/run/beamOn 0
```

LIST OF ABBREVIATIONS

N	Number of particles
μ	Linear attenuation coefficient (cm^{-1})
L, l	Length (m)
K_c	Collisional kinetic energy deposited in matter (KERMA)
X	Exposure (Ckg^{-1})
\bar{W}	Mean energy expended in gas per ion pair formed (J)
e	Charge of electron ($1.602 * 10^{-19}$ C)
Q	Total charge (C)
m	Mass (kg)
ρ	Density (gcm^{-3})
t	Time (s)
L_Δ, LET	Linear energy transfer
E_Δ	Energy cutoff
LEE	Low energy electron
C	Coulomb
D	Dose (Gy) (Jkg^{-1})
CPE	Charged particle equilibrium
kVp	Peak kilovoltage
MV	Megavoltage
E	Energy (J, eV)
Z	Atomic number
eV	Electronvolt
τ	Photoelectric cross-section
σ	Compton cross-section
κ	Pair-production cross-section
σ_R	Rayleigh cross-section
h	Planck's constant ($6.63 * 10^{-34}$ $\text{m}^2\text{kgs}^{-1}$)
ν	Frequency (Hz)
μ_{eff}	Effective linear attenuation coefficient
w	Weighting factor
Z_{eff}	Effective atomic number
a_i	Fraction of electrons present in the mixture that belong to atoms with atomic number i
f_i	Weight fraction of element i
ψ	Energy fluence (Jm^{-2})
μ_{en}	Energy absorption coefficient (cm^{-1})
$x\text{-ray}$	Energy range of electromagnetic radiation
$\gamma\text{-ray}$	Gamma: energy range of electromagnetic radiation

δ -ray	Secondary electron with enough energy to produce further ionization
r	Radius
A	Area
Ω	Solid Angle
sr	Steradian
Ci	Curie, unit for radioactivity
K -edge	Binding energy of the K-shell electron
L -edge	Binding energy of the L-shell electron
K -shell	Principle atom electron shell
L -shell	Secondary atom electron shell
RBE	Relative biological effectiveness
$linac$	Linear accelerator
MLC	Multi-leaf collimator
PDD	Percentage depth dose
$EMRT$	Energy modulated radiation therapy
$IMRT$	Intensity modulated radiation therapy
$HIG-IMRT$	Hypoxia image guided intensity modulated radiation therapy
SSD	Source surface distance
D_{max}	Depth of maximum dose
AAA	The Analytical Anisotropic Algorithm
DVH	Dose volume histogram
$CBCT$	Cone-beam computed tomography
$DICOM$	Digital Imaging and Communications in Medicine
GTV	Gross tumor volume
PTV	Planning target volume
HTV	Hypoxic tumor volume
TCP	Tumor control probability
$NTCP$	Non-target control probability
CT	Computed tomography
PET	Positron-emission tomography
MRI	Magnetic resonance imaging
$SmART$	Small Animal Radiation Therapy platform
VTH	Colorado State University Veterinary Teaching Hospital
$SARRP$	Small Animal Radiation Research Platform
$Imaging$	Megavoltage carbon-target imaging linac from Dalhousie University
$Trilogy$	Varian Trilogy linac
TPS	Treatment planning system
$SmART-ATP$	SmART-Advanced Treatment Planning system
MC	Monte Carlo
EGS	Electron gamma shower Monte Carlo code
$C++$	Programming code
$MORTRAN$	More formula translation (FORTRAN) programming code

<i>Geant4</i>	Geometry and Tracking Monte Carlo code
<i>G4DNA</i>	Geant4 – DNA low energy package
<i>CuATSM</i>	Copper diacetyl-bis N4-methylthiosemicarbazone
<i>GNP</i>	Gold nanoparticle
<i>SLAC</i>	Stanford Linear Accelerator Center
<i>PEGS4</i>	EGSnrc program for creating materials
<i>CM</i>	Component module
<i>BEAMnrc</i>	EGSnrc utility for linac modeling
<i>BEAMdp</i>	BEAMnrc utility for spectral data
<i>DOSXYZnrc</i>	EGSnrc utility for dosimetric evaluation in rectilinear phantom
<i>FLURZnrc</i>	EGSnrc utility for fluence evaluation in cylindrical phantom
<i>HU</i>	Hounsfield unit
<i>addphsp</i>	EGSnrc utility for combining phase spaces
<i>ECUT</i>	EGSnrc energy cutoff for electrons
<i>PCUT</i>	EGSnrc energy cutoff for photons
<i>DEF</i>	Dose enhancement factor
<i>DEF_{macro}</i>	Macroscopic dose enhancement factor
<i>mDEF, DEF_{micro}</i>	Microscopic dose enhancement factor
<i>G4DNA</i>	Low energy extension to Geant4
<i>G</i>	Radiochemical yield
<i>dep</i>	Deposited
<i>ICRP</i>	International Commission on Radiological Protection
<i>ICRU</i>	International Commission on Radiation Units and Measurements
<i>SSBEF</i>	Single-strand break enhancement factor
<i>DSBEF</i>	Double-strand break enhancement factor
<i>CEF</i>	Individual chemical species enhancement factor
<i>TCEF</i>	Total chemical yield enhancement factor
<i>EEF</i>	Energy enhancement factor
<i>XC</i>	Zero copper added
<i>NXC</i>	Zero copper added, normoxic
<i>HXC</i>	Zero copper added, hypoxic
<i>H+C</i>	Copper added, hypoxic
<i>N+C</i>	Copper added, normoxic
<i>50/50</i>	50% distribution of CuATSM in nucleus and 50% in cytoplasm
<i>ANOVA</i>	Analysis of variance
<i>Tukey HSD</i>	Honestly significant difference, post-hoc statistical test
<i>Paired-TTest</i>	Statistic to determine whether the mean difference between two sets of observations is zero
α	Statistical significance level, the probability of making a Type I error
<i>OSA</i>	Osteosarcoma
<i>ppm</i>	Parts-per-million
<i>DMSO</i>	Dimethyl sulfoxide

$CuCl_2$	Copper chloride
<i>SSB</i>	Single-strand break
<i>DSB</i>	Double-strand break
<i>CHO</i>	Chinese hamster ovary cell line
<i>ROS</i>	Reactive oxygen species
<i>p53</i>	Tumor suppressor gene
<i>mmHg</i>	Millimeter of mercury
<i>HIF</i>	Hypoxia inducible factor
<i>PHP</i>	Prolyl hydroxylase enzyme
<i>EMT</i>	Epithelial-mesenchymal transition
<i>VEGF</i>	Vasculature endothelial growth factor
<i>in vivo</i>	Performed or taking place in a living organism
<i>in vitro</i>	Biological molecules outside normal biological context
<i>DNA</i>	Deoxyribonucleic acid
<i>EGFR-ras</i>	Epidermal growth factor receptor
<i>ECM</i>	Extracellular matrix
<i>FDA</i>	US Food and Drug Administration
<i>NAD</i>	Nicotinamide adenine dinucleotide coenzymes
<i>F18</i>	Fluorine 18 (PET radionuclide)
<i>MISO</i>	^{18}F -Fluoromisonidazole
<i>FAZA</i>	^{18}F - Fluoroazomycin arabinoside
^{64}Cu	Copper 64 (PET radionuclide / radiotheranostic)
<i>Tris-HCL</i>	Buffer, Tris (hydroxymethyl) aminomethane (THAM) hydrochloride
<i>TAE</i>	Buffer, a mixture of Tris base, acetic acid and EDTA
<i>OD</i>	Optical density
<i>bp</i>	Base pair
<i>PE</i>	Plating efficiency
<i>SF</i>	Surviving fraction
<i>M</i>	Molarity
<i>GIV</i>	Growth inhibition value
α -MEM	Growth media
FBS	Fetal bovine serum
Anti-Anti	Antimycotic & Antibiotic
PBS	Phosphate buffered saline
Trypsin-EDTA	Protease + chelating agent for cell detachment
<i>n</i>	Growth rate
(v/v)	Volume per volume
e_{aq}^-	Aqueous electron
$H\bullet$	Atomic hydrogen
H_2	Molecular hydrogen
$\bullet OH$	Hydroxyl radical
H_3O^+	Hydronium

H_2O_2	Hydrogen peroxide
OH^-	Hydroxyl ion
<i>BIM</i>	Biologically important molecule